Theoretical Study on Reaction Dynamics in Gas and Solution(Dissertation_全文)

AUTHOR(S):

Morita, Akihiro

THEORETICAL STUDY ON REACTION DYNAMICS IN GAS AND SOLUTION

Doctoral Thesis

Akihiro Morita [1]

December 7, 1994

[1]Department of Chemistry, Faculty of Science, Kyoto University

Contents

Chapter 1

Introduction for Gas-Phase Reactions

Recent study on the chemical reaction dynamics in gas phase has been extensively developed and sophisticated [1, 2, 3, 4]. We are now confronting the situation to be overcome that further advances require a breakthrough. In this chapter I discuss the present situation with considering the history of research for gas-phase reactions, to delineate the background of my work described in Chap. 3.

The rapid advances on the gas-phase study has been greatly owed to state-selected information of isolated molecules. Actually, state-selected information prompted us to interpret reaction dynamics on the basis of the first principles. Such detailed information is attributed to a couple of technologies: supersonic jet and laser spectroscopy [5]. Supersonic jet is able to provide isolated molecules under extremely low temperature about a few Kelvin [6]. The molecules prepared under the condition are mostly populated in the ground rovibronic state. Other states than the ground rovibronic state can be also prepared selectively using monochromatic lasers. These specimens at a specific state are utilized to extract state-selected information on gas-phase reactions, including unimolecular and bimolecular ones. Electronically excited states are particularly remarkable objects, since they often cause subsequent unimolecular reactions for themselves with much more variety than the electronically ground states, *e.g.* dissociation, ionization, and internal conversion [7]. Bimolecular reactions as a result of single collsions have been also investigated in detail using the state-selected samples in crossed beam experiments [8].

Moreover, various laser techniques have been developed to progress the laser spectroscopy, which has been provided clear information on microscopic behaviors of molecules [5]. In this paragraph I give a brief survey of these experimental techniques. Use of pulse lasers is quite popular for these experiments, since pulse lasers are suitable for experiments using pulse-injected supersonic jet. In addition to that, it enables us to measure directly time-

dependent properties such as lifetimes, and it facilitates pump-probe method as mentioned below. One of the most important techniques is laser induced fluorescence (LIF) to find the internal state distribution of either reactant or product [9], where a specific internal state is selectively excited by a laser pulse and the amount of subsequent fluorescence is detected to find the population distribution. Use of multiple lasers further extends the experimental ability. In particular, it makes possible the pump-probe method, which is one of the most fundamental forms of laser experiments. In this method, a first laser pulse (pump) prepares a certain internal state, and a second delayed pulse (probe) monitors the following dynamics or the result of dynamics. The pump-probe technique has been widely implemented to pursue the reaction dynamics and further improved with various devices in the following. Multiphoton spectroscopy, which takes advantage of multiphoton processes for either pump or probe, enables us to deal with internal states not accessible or detectable by a single photon. Another device comes from use of polarization of light, since a polarized laser manifests transition moments of molecules. Vector information reflecting spatial anisotropy in a reaction has been gained by use of polarized lasers as well as angular distribution and Doppler spectroscopy. Duration of laser pulses has been shortened to reach subpicosecond order, which enables us to gain the information on ultrafast phenomena. These kinds of laser spectroscopic techniques have greatly contributed to recent progress in the gas-phase reactions.

Fine information obtained by these experiments gives suitable clues to understand the chemical reactions theoretically. Since the isolated systems in gas phase are free from intermolecular interaction, they are amenable to theoretical treatments. Chemical reactions are ultimately regarded as nuclear dynamics on adiabatic potential energy surfaces (PESs), sometimes accompanied with nonadiabatic transitions [10, 11]. Though the principle of the chemical reaction dynamics has been established, there remain a number of difficulties to understand it virtually. First, it is not easy to obtain reliable PESs. Those of electronically excited states are particularly hard to be calculated so that they have come to be available only for the last decade. Recent progress in elctronic structure theory as well as computer technology has provided efficient methods to evaluate PESs [12, 2, 10]. Particularly, muliticonfigurational self-consistent field (MCSCF) and multireference single-double CI (MR-SDCI) have enabled us to obtain reliable PESs not only for ground states but also for electronically excited states. It has become widely known that nonadiabatic transitions often play an important role in reactions on excited PESs. Secondly, even if the PESs are obtained, the relation to the nuclear dynamics is not obvious. In many cases nuclear dynamics is approximately treated by the classical mechanics [14, 15, 16], but quantitative description requires more accurate calculation based on the quantum mechanics. There often appear some phenomena that call for the quantum

mechanics even for the qualitative understanding, namely "quantum effect". For instance, tunnelling effect manifests itself in proton transfer and in reaction rates under low temperature [17]. Another instance of quantum effect is the resonance observed in cross sections with varying collision energy [18]. The two general issues for theoretical understanding noted above, *i.e.* obtaining reliable PESs and elucidating reaction dynamics on PESs, are crucially relevant also to my work in Chap. 3, where a single example of gas-phase reaction will be considered from these viewpoints.

On the early study to establish the relation between PESs and reaction dynamics, the key property was vibrational/rotational state distribution of product, since it was then available owing to the LIF experiments. The internal state distribution was interpreted on the basis of the PESs particularly from a viewpoint of their topological features. Polanyi made a great contribution to relate their topological features to the internal state distribution, by proposing a concept of "barrier location" during the reaction processes on the PESs. Let us consider a three-atom substitution reaction: $AB + C \longrightarrow A + BC$. His idea is that location of the potential barrier in reaction path governs the effect of vibration. Note that reaction path changes its direction at the intermediate region $A \cdots B \cdots C$. If the barrier is located near the entrance channel, the direction of the reaction path changes significantly after passing over the barrier, so that vibrational excitation of the product BC is enhanced due to the curvature of the reaction path. Contrary to the above, if the barrier is located near the exit channel, barrier passage occurs after significant change in the curvature of the reaction path. Thus vibrational excitation of product BC is not so enhanced while that of reactant AB is expected to be fairly effective to pass over the barrier. His work as well as the development of the transition state theory [19, 20, 21] yielded a definite concept for elucidating reaction dynamics on PESs. Reaction path was later defined analytically to discuss energy disposal during reactions [22]. Further, a system of curvilinear coordinates including the reaction path was introduced to describe the Hamiltonian [23, 24]. The coordinate system facilitates to grasp reaction dynamics involving many degrees of freedom, since it can be essentially described by the reaction path and a few other coordinates.

These concepts noted above have now been established to understand the reaction dynamics qualitatively, though they are insufficient to bear the quantitative comparison with experimental results. The vibrational/rotational distribution of the product states is still hard to be predicted theoretically. The inherent reasons are that (i) the distribution is sensitive to the accuracy of PESs at not only the transition state region but also the exit region of a reaction, and (ii) quantum mechanical calculation for realistic nuclear dynamics is in general a difficult task [25]. The second reason comes from the basic fact that heavy nuclei open a great number of channels concerned in considering their dynamics quantum mechanically. Even in the present,

there remain some unsolved problem in the vibrational distribution of the product HF in a benchmark reaction $F+H_2 \rightarrow HF+H$, despite of intensive studies both from experimental and theoretical sides [13]. Thus alternative methods have been widely adopted to estimate the internal state distribution more roughly but concisely, including the classical trajectory method [14, 15, 16], approximated quantum methods [26] or Franck-Condon model [27, 28, 29, 30]. The Franck-Condon model estimates the distribution using Franck-Condon overlaps between initial and final states, by projecting the wave function initially prepared to those of the product eigenstates. The above model assumes that the characteristics of wavefunction for internal states approximately preserve during the reaction. The characteristics and direction of angular momenta, *e.g.* orbital angular momentum and internal rotation, also tends to preserve so that rotational distribution was found to be restricted by correlation of angular momenta between reactant and product.

At present we are standing on a further stage where other useful information than the vibrational/rotational state distribution is available, allowing us to discuss the reaction mechanism more directly. In a case of photodissociation reactions, which have thoroughly studied to form a major field in the gas-phase reactions [31, 32], two properties are worth noting besides the vibrational/rotational distribution, since they have been markedly exploited so far. One of them is vector correlation, and the other is fine-structure distribution. The former means correlation of each pair among three vectors relevant to the photodissociation: transition moment of parent molecule $\vec{\mu}$, rotational vetor of product fragment $\vec{J}$, and recoil velocity $\vec{v}$. These correlations can be measured using polarized lasers and Doppler spectroscopy, by taking advantage of the fact that their observed values depend on spatial geometry of experimental equipment, *e.g.* (both pump and probe) laser polarization and direction of incident probe. They facilitate to specify the directions of these vector properties as well as their amounts, which provide useful information for anisotropic shape of PES. Much work on the vector correlation have been reported to date for various photodissociation systems, including ICN [50], H_2O [43], HONO [35], H_2O_2 (references are in Chap. 3), and $(CHO)_2$ [36]. In my work in Chap. 3, experimental finding about $\vec{v} - \vec{J}$ correlation of H_2O_2 will be utilized to corroborate a conclusion.

On the other hand, fine-structure distribution means population distribution among fine structure levels of product fragment, which are inherent to open-shell species [37]. Since a manifold of fine structure levels are distinguished in fine splitting of spectral lines by moderately high-resolution spectroscopy, population distribution among the manifold is detected from their intensity ratio. Fine structure comes from minite perturbation, such as spin-orbit or spin-rotation coupling, splitting nearly degenerate eigenstates. Λ-type doubling is a kind of the fine structures currently seen in $^2\Pi$ diatomic radicals, *e.g.* $OH(\tilde{X}^2\Pi)$ and $NO(\tilde{X}^2\Pi)$ [44]. Λ-type doubling is attributed to

the coupling between electronic angular momentum and rotational one. (Distinguish Λ-type doubling from another kind of fine structure due to spin-orbit couping [$J = 3/2, 1/2$ for $^2\Pi_J$]. Energy splitting of Λ-doublet is generally much less than that due to spin-orbit coupling, whereas the two eigenstates of Λ-type doubling have different parities.) Although a manifold of fine-structure levels are nearly degenerated, preferential population among them often results from photodissociation reactions. Such a preferential population does not come from energetics of the PESs, because the energy levels does not necessarily correlate to the preference of population. The interpretation of the non-statistical distribution among fine-structure levels brings a new light upon reaction mechanisms. In the case of Λ-type doubling, the origin is relatively definite in terms of spatial geometry [39]. The splitting due to Λ-doubling is observed in a rotating $^2\Pi$ radical. The Λ-doublet manifolds of product radicals refer to the orientational relation between the odd $p\pi$ orbital and the plane of rotation; one of them to in-plane relation (denoted by A'), and the other to out-of-plane (A'') [40]. Thus the preferential distribution in the Λ-type levels gives a direct information on the following two factors: direction of the rotational excitation during the recoil process and correlation of the electronic structures between parent molecule and product radical.

My work described in Chap. 3 deals with the photodissociation reaction of hydrogen peroxide H_2O_2:

$$H_2O_2 + h\nu \longrightarrow OH(\tilde{X}^2\Pi) + OH(\tilde{X}^2\Pi), \tag{1.1}$$

where the Λ-type polarization observed in the product $OH(\tilde{X}^2\Pi)$ is elucidated theoretically. This reaction has been most widely studied among photodissociation of tetraatomic molecules, because of its simplicity. This reaction is a typical direct dissociation, not predissociation, and the lifetime of the photoexcited species is found to be less than 60fs at 266 nm excitation [41, 42]. The energy disposal of this reaction is fairly simple; almost 90 % of the exothermic available energy is disposed to the translational motion, but vibrational excitation is scarcely observed. The vector correlation on this reaction has also been extensively studied, partially because this reaction is quite suitable for the Doppler spctroscopy, owing to a large amount of translational energy and small mass of the fragment OH. One of the distinct features revealed is that the v-J correlation shows a tendency of $\vec{v} \parallel \vec{J}$, where $\vec{v}$ is the recoil velocity and $\vec{J}$ is the rotational vector of the fragment. Since the recoil vector reflects the O-O direction of the parent, such a tendency of $\vec{v} \parallel \vec{J}$ indicates that the rotational excitation is strongly correlated with torsional motion of the parent H_2O_2 during the recoil process. As to the fine-structure distribution, the population ratio of the Λ-type doublet has a bias toward A''-component (out-of-plane) rather than A'-component (in-plane), while the population ratio between $^2\Pi_{1/2}$ and $^2\Pi_{3/2}$ states is nearly statistical. However, the origion of the non-statistical distribution in the Λ-

type doublet has not been clear so far. This is because the electronic state just after the photoexcitation is $\tilde{A}n\sigma^*$ or $\tilde{B}n\sigma^*$ [43], either of which does not correlate to products having a preferential distribution of the Λ-doublet. In Chap. 3, we discuss the origin of the preferential population, by considering not only the $\tilde{A}$ and $\tilde{B}$ state but all the states correlating to $OH(\tilde{X})+OH(\tilde{X})$ at the dissociation limit. The origin is ascribed to intersystem crossing near the exit channel, as discussed later.

Besides the Λ-type doublet, preferential population as a result of photodissociation reactions were found in other kind of fine-structure manifolds. In particular, fine-structure manifolds due to spin-rotation coupling possibly involve dynamical information because they may reflect the rotational motions. Such kind of non-statistical distribution was experimentally observed in some radical products including $NH(^3\Sigma^-)$, $SO(^3\Sigma^-)$, and $CN(^2\Sigma^+)$. However, its interpretation is less obvious than that of the Λ-type doubling, because the spin-rotation coupling has to be considered in spin space as well as actual space. I will mention two studies that successfully gave its interpretation. Alexander et al. [44] argued a photodissociation reaction following multiphoton infrared absorption:

$$HN_3(\tilde{X}) \longrightarrow N_2(\tilde{X}^1\Sigma_g^+) + NH(\tilde{X}^3\Sigma^-,\ or\ \tilde{a}^1\Delta), \tag{1.2}$$

to elucidate the non-statistical distrubution among the three spin manifolds of $NH(\tilde{X}^3\Sigma^-)$. Experiments by multiphoton infrared absorption [45, 46] showed that F_1 and F_3 levels are preferentially produced while F_2 level are little. Note that the former two levels are symmetric with respect to reflection of the spatial and spin spaces while the latter is anti-symmetric. They found the transition state to be planar on the basis of CASSCF and MCSCF-CI calculations, and further predicted to preserve planar geometry during the dissociation process. They conclusively attributed the preferential population to the conservation of mirror symmetry possessed by the electronic and roational wavefunction. On the other hand, Zare, Child and co-workers [47] gave another explanation for a non-statistical distribution in the fine-structure manifolds of $CN(\tilde{X}^2\Sigma^+)$, observed in the photodissociation reaction with a UV photon:

$$ICN \longrightarrow I(^2P_{3/2,1/2}) + CN(\tilde{X}^2\Sigma^+). \tag{1.3}$$

The population ratio between $F_1(J = N + 1/2)$ and $F_2(J = N - 1/2)$ of the product $CN(\tilde{X}^2\Sigma^+)$ strangely oscillates with the rotational quantum number N of the product CN [48, 49, 50]. They concluded that the ocillatory pattern comes from interference effect dependent on N. Let us consider a coupling scheme of angular momenta as

$$\vec{J}_{12} = \vec{j} + \vec{S}; \tag{1.4}$$

where $\vec{j}$ stands for the angular momentum of the I atom, and $\vec{S}$ for that of CN spin. We further define Λ_{12} as the component of $\vec{J_{12}}$ along the interfragment axis, $\vec{l}$ as the orbital angular momentum between the two fragments, and $\vec{N}$ as the rotational angular momentum of CN. It is assumed that the spin-orbit interaction particularly due to the I atom makes Λ_{12} a good quantum number. When the total Hamiltonian including mutual rotation is written as

$$H = H_0 + \frac{l^2}{2\mu R^2}, \tag{1.5}$$

a coupling term H' is derived from the second term of Eq. (1.5), *i.e.*

$$H' = \frac{\vec{N} \cdot \vec{J_{12}}}{\mu R^2} \tag{1.6}$$

on condition that $\vec{l}+\vec{N}+\vec{J_{12}} \approx 0$. Thus the above coupling Hamiltonian mixes the different Λ_{12} states to interfere each other during the reaction dynamics, which emerges in the final population ratio of the fine-structure levels.

In the remainder of this section, I will discuss some promising seeds for future research. Recent studies based on potential energy calculations have clearly demonstrated that transition states and their vicinities are often crucial to reaction mechanisms. However, direct information relevant to the dynamics near the transition states is rather hard to be obtained experimentally. The above-mentioned properties, such as vibrational or rotational state distribution, vector correlation, and fine-structure population, refer to detailed knowledge of either product or reactant. Most of other available properties such as lifetime are also obtained by measureing either reactant or product. Though they often provide useful evidences to infer the intermediate dynamics near the transition states, more direct information will greatly facilitate comparison with theory and further understanding reaction mechanisms. I mention two avenues along this line with spectroscopic means: the transition state spectroscopy and the femtosecond spectroscopy. The transition state spectroscopy aims to analyze transition states by spectroscopic means. It is quite challenging, since usual spectroscopy for stable molecules is useless for the unstable species. Neumark and his co-workers developed a new device to finesse their transient characters, by use of photodetachment of corresponding anions [51, 52, 53]. Their device is based on the fact that such anion complexes as $[\mathrm{I}\cdots\mathrm{H}\cdots\mathrm{I}]^-$, $[\mathrm{F}\cdots\mathrm{H}\cdots\mathrm{I}]^-$, and $[\mathrm{F}\cdots\mathrm{H}\cdots\mathrm{H}]^-$ are stable and thus amenable to spectroscopic treatment while the equivalent neutral complexes are unstable. The neutral complexes are prepared by removing excess electrons from the anion complexes, and consequently the resultant unstable complexes break into a couple of fragments. Since the unstable complexes prepared as such mimic the species at transition states of three-atom bimolecular collisions, the photodetachment spectra exhibit

the information on the transition states of bimolecular reactions. In the case of a benchmark system $F+H_2$, for instance, the transition-state spectroscopy was utilized to yield useful information on the reactive complex $[F\cdots H\cdots H]$ by Neumark et al. They prepared state-selected complexes of $[F\cdots H\cdots H]$ using a polarized laser, and related the peaks observed in the photodetachment spectra to the resonance effect in the reactive scattering. Such comparison between the spectroscopic and scattering results is, if possible, remarkably effective to confirm the PESs near the transition states. However, the above-mentioned method seems to be limited in its applicability. The photodetachment method can be applied only to the reacive complexes whose anions are stable, but they are rather few. This problem is not specific to the transition-state spectroscopy, but a general problem that has been faced by the spectroscopy so far. Usual spectroscopy permits us to access only the Franck-Condon region in PESs. In order to extend the accessible regions on PESs, some special devices have been developed. Such devices include not only the use of the photodetachment, but stimulated emission pumping for the study on highly-excited vibrational states [54, 55], other multi-photon/multi-color spectroscopy, etc [56]. Despite the difficulties to be overcome by further development of such a device, the transition-state spectroscopy opens a new avenue to seek for the transition state regions.

Femtosecond spectroscopy is another promising seed for future research. It utilizes pulse lasers capable to provide a pulse with ultrashort duration of femtosecond order, sometimes shorter than the vibrational period of molecules. It achieves the time resolution of femtosecond order to trace reaction dynamics. This technique has a wide applicability to detect reaction dynamics directly in time-domain. Its applicability is beyond the gas-phase reactions; it is rather suitable for condensed-phase studies where definite information is less available in frequency-domain. It probably casts new light onto ultrashort phenomena incorporating some quantum effects, since some of the vibrational or electronical dephasing rates becomes comparable to the laser pulse duration. However, we are not completely optimistic about future of the femtosecond spectroscopy. This is because (i) it also suffers the common problem to the spectroscopy as mentioned above that accessible regions of PESs are rather limited, and (ii) it is hard to gain definite information against the multi-demensionality of the PESs, as discussed later. I then focus on the present situation and posiibility of the femtosecond spectroscopy.

There already exists much work on the pump-probe experiments using the femtosecond lasers. These studies have been cited and introduced in recent reviews by Zewail, a pioneer in this field [57, 58]. On the earliest stage of the research, he and his co-workers implemented this technique to the predissociation of the photoexcited NaI [59], drawing much attention of other researchers. They utilized a femtosecond pump laser to prepare NaI on the quasi-bound excited state and detected the dissociatied products by another

femtosecond probe laser. Through this experiment, they first demonstrated the vibration of wave packet on the quasi-bound excited state, by showing a damped-oscillating signal as a function of the delay time between the two pulses. Moreover, they found an unexpected recurrence of the signal at 30 to 40 ps after it decays out for a few ps through the predissociation channel. The time profile of the recurrence signal was found to be sensitive to the wavelength and duration of the pump laser. Chapman et al. elucidated the phenomenon theoretically from a semiclassical viewpoint, by considering that the predissociation lifetimes vary with the rovibronic levels on the quasi-bound state over several orders of magnitude [60]. They attributed the recurrence to the presence of extremely long-lived levels and the interference among these levels. The recurrence phenomena provide a sensitive probe for the distribution of the quasi-bound levels and their lifetimes.

Besides diatomic molecules such as NaI, simple polyatomic molecules, *e.g.* IHgI and CH_3I [61, 62], and van der Waals clusters, *e.g.* $IH \cdots CO_2$ [63], have been studied by the femtosecond spectroscopy. These studies deal with dissociating dynamics along both the reaction coordinates and other internal coordinates. However, further application to more complex molecules seems to be difficult along this line, because of increasing degrees of freedom. The usual pump-probe method has only a few variable parameters, including the laser wavelength, polarization, and delay time. Thus the available information obtained by varying these parameters is apparently too little to analyze multi-dimensional PESs. One possibility to extract more information lies in the use of phase coherence. The pulse duration of the femtosecond lasers is comparable to the vibrational or electronical dephasing times. Hence the femtosecond spectroscopy can potentially be utilized to detect and research the dephasing processes. Though the long-time recurrence of NaI as noted above is one instance of the dephasing, most of the dephasing processes have not been explored yet. There has been appearing pioneering work to exploit the phase coherence by femtosecond lasers [64, 65, 66]. The importance of the dephasing will be also stressed in Chap. 4, where the electronic dephasing rate is discussed in relation to the intersystem crossing rate of a biradical in solution.

On the future stage of theoretical research on the gas-phase reaction dynamics, more accuate and reliable potential energy surfaces will become available for various molecules and electronic states, owing to the progress of electronic structure theory and computing ability. Qualitative characteristics of PESs will be taken full advantage of to understand reaction mechanisms. Nevertheless, accurate quantum-mechanical calculation on reaction dynamics is still hard to incorporate realistic molecules. Thus alternatively, semi-quantitative theory based on reliable PESs will be probably developed and sophisticated. As to treat the nonadiabatic transition theoretically, surface hopping method proposed by Tully et al. has been currently adopted

along with the classical trajectory method [67]. Recently Kosloff et al. [68, 69] offered multiconfigurational-TDSCF (time-dependent self-consistent-field) method to deal with the nonadiabatic effect on dynamics. Quantum effects on dynamics require futher refined description not only in the gas-phase reaction, but also in the other fields of chemical reaction dynamics.

Bibliography

[1] R. Levine and R. B. Bernstein *"Molecular Reaction Dynamics and Chemical Reactivity"*, Oxford, New York, 1987.

[2] *"The Theory of Chemical Reaction Dynamics"*, ed. M. Baer, CRC Press, Boca Raton, Fla., 1985.

[3] S. R. Leone, Ann. Rev. Phys. Chem. **35**, 109 (1984).

[4] R. N. Zare and R. B. Bernstein, Phys. Today, **33**, 43 (1980).

[5] R. B. Bernstein *"Chemical Dynamics via Molecular Beam and Laser Techniques"*, Oxford, New York, 1982.

[6] J. B. Anderson, R. P. Andres and J. B. Fenn, Adv. Chem. Phys. **10**, 275 (1966).

[7] R. E. Smalley, Ann. Rev. Phys. Chem. **34**, 129 (1983).

[8] Faraday Discuss. Chem. Soc. **55**, (1973).

[9] R. N. Zare and P. J. Dagdigian, Science, **185**, 739 (1974).

[10] *"Potential Energy Surfaces and Dynamics Calculations"*, ed. D. G. Truhler, Plenum, New York, 1981.

[11] D. M. Hirst, *"Potential Energy Surfaces: Nolecular Structures and Reaction Dynamics"*, Taylor & Francis, London, 1985.

[12] *"Ab initio Methods in Quantum Chemistry"*, Part I, II, ed. K. P. Lawley, Adv. Chem. Phys. **67**, (1987).

[13] Chap. 7 in [Levine:1987].

[14] R. N. Porter, Ann. Rev. Phys. Chem. **25**, 317 (1974).

[15] D. L. Bunker, Method Comput. Phys. **10**, 287 (1971).

[16] J. T. Muckerman, in *"Theoretical Chemistry: Theory of Scattering"*, ed. D. Henderson, Academic, New York, 1981.

[17] J. C. Light, Adv. Chem. Phys. **19**, 1 (1971).

[18] V. Aquilanti, in *"The Theory of Chemical Reaction Dynamics"*, ed. D. C. Clary, Boston, 1986.

[19] H. Eyring, J. Chem. Phys. **3**, 107 (1935).

[20] K. J. Laidler and M. C. King, J. Phys. Chem. **87**, 2657 (1983).

[21] D. G. Truhler, W. L. Hase, and J. T. Hynes, J. Phys. Chem. **87**, 2664 (1983).

[22] (a) K. Fukui, J. Phys. Chem. **74**, 4161 (1970). (b) K.Fukui, S. Kato, and H. Fujimoto, J. Am. Chem. Soc. **97**, 1 (1975). (c) K. Fukui, Acc. Chem. Res., **14**, 363 (1981).

[23] W. H. Miller, N. C. Handy, and J. E. Adams, J. Chem. Phys. **72**, 99 (1980).

[24] W. H. Miller, J. Phys. Chem. **87**, 3811 (1983).

[25] A. Kuppermann, in [Henderson,1981].

[26] J. M. Bowman, G. -Z. Ju, and K. T. Lee, J. Phys. Chem. **86**, 2232 (1982).

[27] R. Schinke, J. Phys. Chem. **92**, 3195 (1988).

[28] K. C. Kulander and E. J. Heller, J. Chem. Phys. **69**, 2439 (1978).

[29] G. G. B.-Kurti, J. Chem. Phys. **84**, 4443 (1986).

[30] R. D. Coalson and M. Karplus, J. Chem. Phys. **93**, 3919 (1990).

[31] P. Brumer and M. Shapiro, Adv. Chem. Phys. **60**, 371 (1984).

[32] M. Shapiro and R. Bersohn, Ann. Rev. Phys. Chem. **33**, 409 (1982).

[33] I. Nadler, D. Mahgerefteh, H. Reisler, and C. Wittig, J. Chem. Phys. **82**, 3885 (1985).

[34] A. U. Grunewald, K. -H. Gericke, and F. J. Comes, Chem. Phys. Lett. **133**, 501 (1987).

[35] R. Vasudev, R. N. Zare, and R. N. Dixon, J. Chem. Phys. **80**, 4863 (1984).

[36] I. Burak, J. W. Hepburn, N. Sivakuruar, G. E. Hall, G. Chawla, and P. L. Houston, J. Chem. Phys. **86**, 1258 (1987).

[37] G. Herzberg, *"Molecular Spectra and Molecular Structure"*, Vol. II, Van Nostrand, New York, 1945.

[38] M. H. Alexander et al., J. Chem. Phys. **89**, 1749 (1988).

[39] P. Andresen and E. W. Rothe, J. Chem. Phys. **82**, 3634 (1985).

[40] M. H. Alexander and P. J. Dagdigian, J. Chem. Phys. **80**, 4325 (1984).

[41] K. -H. Gericke, S. Klee, and F. J. Comes, J. Chem. Phys. **85**, 4463 (1986).

[42] S. Klee, K. -H. Gericke, and F. J. Comes, J. Chem. Phys. **85**, 40 (1986).

[43] A. U. Grunewald, K. -H. Gericke, and F. J. Comes, J. Chem. Phys. **87**, 5709 (1987).

[44] M. H. Alexander, H. -J. Werner, and P. J. Dagdigian, J. Chem. Phys. **89**, 1388 (1988).

[45] J. C. Stephenson, M. P. Casassa, D. S. King, J. Chem. Phys. **89**, 1378 (1988).

[46] B. R. Foy, M. P. Casassa, J. C. Stephenson, D. S. King, J. Chem. Phys. **89**, 608 (1988).

[47] H. Joswig, M. A. O'Halloran, R. N. Zare, and M. S. Child, Faraday Discuss. Chem. Soc. **82**, 79 (1986).

[48] I. Nadler, H. Reisler, C. Wittig, Chem. Phys. Lett. **103**, 451 (1984).

[49] F. Shokoohi, S. Hay, and C. Wittig, Chem. Phys. Lett. **110**, 1 (1984).

[50] I. Nadler, D. Nahgereften, H. Reisler, and C. Wittig, J. Chem. Phys. **82**, 3885 (1985).

[51] R. B. Metz, A. Weaver, S. E. Bradforth, T. N. Kitsopoulos, and D. M. Neumark, J. Phys. Chem. **94**, 1377 (1990).

[52] S. E. Bradforth, A. Weaver, D. W. Arnold, R. B. Metz, and D. M. Neumark, J. Chem. Phys. **92**, 7205 (1990).

[53] A. Weaver and D. M. Neumark, Faraday Discuss. Chem. Soc. **91**, 5 (1991).

[54] C. E. Hamilton, J. L. Kinsey, and R. W. Field, Annu. Rev. Phys. Chem. **37**, 493 (1986).

[55] F. J. Northrup and T. J. Sears, Annu. Rev. Phys. Chem. **43**, 127 (1992).

[56] M. Brouard, M. T. Martinez, C. J. Milne, J. P. Simons, and J. -X. Wang, Chem. Phys. Lett. **165**, 423 (1990).

[57] L. R. Khundkar and A. H. Zewail, Ann. Rev. Phys. Chem. **41**, 15 (1990).

[58] A. H. Zewail, Faraday DIscuss. Chem. Soc. **91**, 207 (1991).

[59] T. S. Rose, M. J. Rosker and A. H. Zewail, J. Chem. Phys. **88**, 6672 (1988).

[60] S. Chapman and M. S. Child, J. Phys. Chem. **95**, 578 (1991).

[61] M. Dantus, R. M. Bowman, and A. H. Zewail, J. Chem. Phys. **91**, 7437 (1989).

[62] M. Dantus, M. H. M. Janssen, and A. H. Zewail, Chem. Phys. Lett. **181**, 281 (1991).

[63] N. F. Scherer, C. Sipes, R. B. Bernstein, and A. H. Zewail, J. Chem. Phys. **92**, 5239 (1990).

[64] A. M. Weiner, D. E. Leaird, G. P. Wiederrecht, and K. A. Nelson, Science **247**, 1317 (1990).

[65] S. Mukamel and Y. -J. Yan, J. Phys. Chem. **95**, 1015 (1991).

[66] K. A. Nelson and E. P. Ippen, Adv. Chem. Phys. **75**, 1 (1989).

[67] R. K. Preston and J. C. Tully, J. Chem. Phys. **54**, 4297 (1971).

[68] A. D. Hammerich, R. Kosloff, M. A. Ratner, Chem. Phys. Lett. **171**, 97 (1990).

[69] Z. Kotler, A. Nitzan, and R. Kosloff, Chem. Phys. Lett. **153**, 483 (1988).

Chapter 2

Introduction for Chemical Reactions in Solutions

2.1 Introduction

Solution has been the most popular field for chemical reactions. Most of organic chemical reactions occur in solution. It is a common aim for many chemists to understand molecular behavior during the chemical reactions in solution. At this point, recent advance in pico- or subpicosecond spectroscopy has made a great contribution to obtain microscopic information on reaction dynamics in solution [1]. The solution chemistry, owing to this technique, became a main field of molecular science, since usual spectroscopy at frequency domain is not capable of extracting fine information from liquids, unlike gas-phase samples. Computer simulation is proved to be another useful technique, for it brought us detailed molecular knowledge about the liquid chemistry beyond experimental limitations. Molecular-dynamics simulation is a particularly powerful method for local phenomena in solutions (both spatially and temporally) that are suited for modelling in terms of a finite number of molecules, e.g., dielectric relaxation dynamics [2, 3] .

In the present stage of research where microscopic information about the liquid chemistry can be obtained to some extent, we have to reflect on future development in this field. Then a principal problem emerges; what does it mean to understand the molecular behavior in solution? If one puts an ultimate purpose to estimate precise reaction rate *ab initio* for a given system, it will hardly be achieved. This would become apparent in considering barrier crossing reactions. The Arrhenius factor $e^{-\Delta G/kT}$ indicates that alteration in the activation free energy by $0.6 kcal/mol$ is sufficient to change the reaction rate about three times. We cannot expect to realize such a precise estimation of free energy even in the near future. Therefore, we consider relative rates of reactions rather than absolute ones, when the latters are inadequate to be argued. For example, we have usually compared reaction rates of the same system under gas-phase and liquid-phase conditions, or compared an actual

rate to a predicted value from the transition state theory. Such comparisons are useful to obtain characteristics of reaction rates in solution. In particular, the comparison of an actual rate to the corresponding expectation value by the transition state theory provides a clue to argue the effect of solvation dynamics on the reaction rates, as is discussed later. Microscopic dynamics of solvation itself has been studied extensively, because it is particularly suitable for the molecular dynamics simulation (see Chap. 6) [2, 3]. Therefore, we intend to clarify the relation between the reaction rates in solution and the solvation dynamics. This problem has a long history of research since Kramers, and some useful theories have been proposed to elucidate the relation [4]. However, all of these theories deal with quite simplified models, so that the validity for real systems remains unclear.

Chemical reactions in solutions are full of variety, so that it is difficult to discuss them in general even within their kinetic aspect. Thus we will focus on barrier crossing reactions as a most typical case, where a reaction proceeds from reactant to product over a potential barrier along a (mostly one-dimensional) reaction coordinate. Such reactions, called activation reactions, are ubiquitous both in gas-phase and in liquid-phase, and are suitable to be applied by the transition state theory [5, 6, 7]. Typical examples of the activation reactions are photoisomerization of trans-stilbene, bimolecular nucleophilic substitution (S_N2), etc. We often observe that the same reactions of this activation type occur both in gas and in solution; the comparison enables us to draw purely the effects of solvation on reaction rates, provided that the other factors inherent to reaction system, such as potential energy surfaces, are identical in the two conditions. It is noted that there are other sorts of reactions specific to solution; *e.g.*, radical- or ion-recombination [8], which belong to the "diffusion-controlled" reactions, and electon-transfer in polar solvents where the solvation itself defines the reaction coordinates [9]. The other sorts of reactions mentioned above are characterized by a common feature that the coupling between reaction coordinates and solvation is so strong that the reaction rates are dominantly affected by the relaxation times of solvation. The kinetics of these reactions are thus treated usually as another category, because the mechanism to determine the reaction rates is rather different. However, from a microscopic point of view, the solvation affecting these reactions is analogous to it affecting the activation reactions; it seems useful to argue the similarity and difference in the solvation mechanism of these "solvation-controlled" reactions and the activation ones.

The activation reactions with potential barrier crossings have gained a great interest of many theoreticians as well as experimentalists since Kramers' theory in 1940 [10], which first formulated the dynamical effect of solvation on the reaction rates. His theory gave rise to consequent examinations and critiques, which made a great contribution to the advancement of the study of chemical reactions in solutions [11, 12]. In this section we firstly survey

the theoretical advancement since Kramers. However, if we deal with actual reactions in solutions instead of simplified models, it is in fact very hard to extract definitely the effect of solvation dynamics on observable reaction rates, because various factors besides the solvation dynamics affect the reaction rates and reactivities. Therefore, many studies have been focused on limited samples that seem amenable to simplified models, avoiding more complicated systems that may concern the other factors seriously, such as multidimensional shapes of potential energy surfaces, specific solute-solvent interactions, etc. Then, as a most typical example of the activated reactions, we next discuss the photoisomerization reaction of trans-stilbene. This system has been one of the most popular for the picosecond spectroscopy, and a great amount of experimental results have been accumulated. These results indicate that actually a number of factors have to be considered to understand the reaction mechanism even for such an apparently simple reaction. We will argue this point later on the basis of the experimental findings.

2.2 Kramers' theory and the consequent development

2.2.1 Kramers' original theory

Kramers described the microscopic reaction dynamics in solutions in terms of a Brownian motion over a potential energy barrier, by projecting the whole dynamics onto a one-dimensional reaction coordinate. Therefore, the reaction rates are estimated in terms of the stationary fluxes from reactant to product over the barrier. It is noted that this model takes into account the effect of solvent fluctuations on the motion along the reaction coordinates, while the transition state theory neglects such dynamical fluctuations. His theory showed that this dynamical effect can alter the overall reaction rates significantly.

There are two ways to describe the Brownian motion on the reaction coordinate. One way is the use of a Langevin equation,

$$\dot{p} = K(q) - \eta p + f(t), \tag{2.1}$$

$$K(q) = -\frac{\partial U(q)}{\partial q}. \tag{2.2}$$

Here $U(q)$ stands for a potential energy function, and $f(t)$ denotes a white Gaussian random force whose average is 0. The mass of the particle was set to be 1. The other way, equivalent to the above, is to express time propagation of a distribution function $\rho(q, p, t)$ on the phase space using the following

equation (called Kramers' equation),

$$\frac{\partial \rho}{\partial t} = -K(q)\frac{\partial \rho}{\partial p} - p\frac{\partial \rho}{\partial q} + \eta \frac{\partial}{\partial p}(p\rho + T\frac{\partial \rho}{\partial p}); \tag{2.3}$$

where the Bolzmann constant was set to be 1. In a special case where Maxwell-Bolzmann momentum distribution holds at each point of the reaction coordinate, the phase-space distribution function $\rho(q,p,t)$ is separated into two parts as a function of each variable, q and p:

$$\rho(q,p,t) \;=\; \sigma(q,t)\cdot\sqrt{\frac{1}{2\pi T}}\exp(-\frac{p^2}{2T}). \tag{2.4}$$

$\sigma(q,t)$ is a distribution function in q-space, and $\sqrt{1/(2\pi T)}\exp(-p^2/(2T))$ denotes the Maxwell-Bolzmann distribution in p-space. This leads to the Smolchowski's diffusion equation for $\sigma(q,t)$, a reduced form of the Kramers' equation for $\rho(q,p,t)$, *i.e.*

$$\frac{\partial \sigma}{\partial t} = -\frac{\partial}{\partial q}(\frac{K}{\eta}\sigma - \frac{T}{\eta}\frac{\partial \sigma}{\partial q}). \tag{2.5}$$

This reduction is valid only when the frictional force in Eq. (2.1), $-\eta p + f(t)$, dominates the potential force $K(q)$. This means that the friction coefficient η is so large that momentum relaxation between the reaction coordinate and the residual bath occurs much more rapidly than time propagation of the distribution function ρ along q. The diffusional flux along q is given according to Eq. (2.5),

$$w = \frac{K}{\eta}\sigma - \frac{T}{\eta}\frac{\partial \sigma}{\partial q}. \tag{2.6}$$

Let us obtain the reaction rate $r = w/n_A$ using Eq. (2.3) and the following formulas; where w is the stationary diffusional flux at the top of the barrier and n_A is the consentration at the reactant region. The ratio w/n_A gives the probability to pass over the barrier within a unit time, if the activation barrier Q is far larger than T so that the equilibriation within the reactant region A is achieved much faster than the barrier passage. Suppose that the shape of the potential energy surface $U(q)$ near the barrier top is smooth (see Fig. 2.1) and approximated to be inverse parabolic,

$$U \approx Q - \frac{1}{2}(2\pi\omega')^2(q-q_c)^2; \tag{2.7}$$

where Q is the barrier height between A and C, and $2\pi\omega'$ is the curvature at the barrier top C. In addition, we put the curvature at the bottom of the reactant A to be $2\pi\omega$. Then one can derivate analytically the probability r of the barrier passage using Eq. (2.7). The result is

$$r = \frac{\omega}{2\pi\omega'}(\sqrt{\frac{\eta^2}{4} + (2\pi\omega')^2} - \frac{\eta}{2})e^{-Q/T}. \tag{2.8}$$

Figure 2.1: Schematic picture of a potential energy surface with smooth barrier [10]

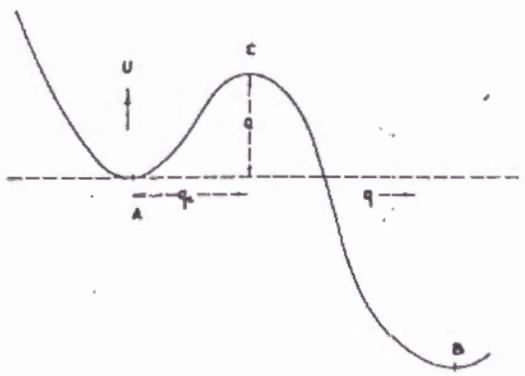

We mention here the limiting behaviors of Eq. (2.8). When the friction coefficient η is sufficiently large ($\eta/2 \gg 2\pi\omega'$), Eq.(2.8) is reduced as

$$r = \frac{2\pi\omega\omega'}{\eta} e^{-Q/T}. \tag{2.9}$$

The above equation indicates that the reaction rate r is inversely proportional to the friction coefficient η in the large friction limit. It is noted that Eq.(2.9) can also be derivated directly from the Smolchowski's equation (Eq.(2.5)) and its diffusional flux (Eq.(2.6)). On the other hand, when the friction coefficient η is sufficiently small ($\eta/2 \ll 2\pi\omega'$), Eq.(2.8) leads to

$$r = \omega e^{-Q/T}. \tag{2.10}$$

This is equal to the reaction rate given by the one-dimensional transition state theory. It is evident that the reaction rate of Eq.(2.8) decays monotoniously with increasing η and coincides with that of the transition state theory at $\eta = 0$.

However, it is important to note that the probability of the barrier passage described by Eq. (2.8) can deviate from the reaction rate when the friction coefficient η is small enough. It would be obvious in considering implicit assumption involved in Eq. (2.8). As discussed above, we obtained Eq. (2.8) by estimating the stationary flux at the local region around the barrier top where the potential function $U(q)$ is reasonably approximated with Eq. (2.7). In the other region of the potential energy surface, thermal equilibrium is assumed due to the relaxation of solvation (Remember the previous assumption that the activation barrier Q is so high that the equilibriation within the reactant region A is much more rapid than the barrier passage). However, this assumption might break down in the small friction limit when

the coupling between the solvation and the reaction coordinate is inefficient. In this situation the motion along the reaction coordinate becomes nearly isoenergetic within the reaction coordinate, because of the weak influence of the solvation. Therefore, the rate of energy relaxation over the barrier passage must be very slow besides the "friction" experienced around the barrier top is also very small. Thus the energy relaxation becomes rate-determining step of the reaction instead of the barrier passage itself. (We note that the above discussion has to be modified in an extended multidimensional vergion of the Kramers' theory, because in the multidimensional situation a number of coordinates can participate in the energy relaxation without the solvation.) In the case that the energy relaxation is rate-determining, the reaction rate is naturally described in terms of energy distribution function $\rho(E,T)$ rather than the phase-space one $\rho(q,p,t)$. Then let us derivate the equation for $\rho(E,t)$ and consequently the reaction rate in the low friction limit. We assume here that periodic motions would be realized on the reaction coordinate if the solvent friction does not influence, and introduce $I(E)$ as the area of the phase space enclosed by the periodic trajectory,

$$I(E) = \oint p dq. \tag{2.11}$$

On averaging Eq. (2.3) over one period in the low friction limit, we can obtain the equation for $\rho(E,t)$, provided that the change in energy is negligible within one period. In the average the first and second terms in the right-hand side of Eq. (2.3) vanish and only the third term with respect to the frictional force remains, *i.e.*

$$\begin{aligned}
\frac{\partial \bar{\rho}}{\partial t} &= \eta \overline{\frac{\partial}{\partial p}(p\rho + T\frac{\partial \rho}{\partial p})} \\
&= \eta(\bar{\rho} + p\overline{\frac{\partial \rho}{\partial p}} + \overline{\frac{\partial}{\partial p}(T\frac{\partial \rho}{\partial p})}) \\
&= \eta(1 + \bar{p^2}\frac{\partial}{\partial E})(\bar{\rho} + T\frac{\partial \bar{\rho}}{\partial E}) \\
&= \eta\frac{\partial}{\partial I}(I\bar{\rho} + TI\frac{\partial \bar{\rho}}{\partial E});
\end{aligned} \tag{2.12}$$

where $\overline{\rho(E)}dI$ denotes the probability fragment, averaged over an isoenergetic surface in the phase space. In the above derivation to Eq. (2.12), we used the following equations:

$$\frac{\partial E}{\partial p} = p, \quad \overline{p^2} = I\frac{\partial E}{\partial I}. \tag{2.13}$$

It is noted that Eq. (2.12) is a diffusion equation in energy; the diffusional flux in Eq. (2.12) is given by

$$w = -\eta(I\bar{\rho} + TI\frac{\partial \bar{\rho}}{\partial E}). \tag{2.14}$$

Provided that the reaction rate r is determined by energy activation and is regarded as the rate to supply activated species at the energy level of the transition state E_C, it can be shown that r is represented approximately by

$$r \approx \eta \frac{Q}{T} e^{-Q/T}. \tag{2.15}$$

(Note an assumption that once a particle is excited over E_C it never returns to the reactant region A. When considering the effect of reentering, Eq. (2.15) is reduced by some factor; *e.g.* in a case of symmetric double-well potential, a factor 1/2 is needed.) Eq. (2.15) indicates that the reaction rate r is proportional to the friction coefficient η in the low friction limit.

According to Eqs.(2.15) and (2.8), there are two factors of solvation dynamics on the reaction rate. One is the effect of energy relaxation, and the other is the "friction" to disturb the barrier passage. The former affects the rate seriously in the low friction limit, where the deficiency of energy relaxation lowers the reaction rate than the prediction of the transition state theory, and the latter emerges in higher friction to lower the reaction rate in a seemingly similar manner. Both factors thus make a maximum of the reaction rate as a function of the friction coefficient; the behavior of the reaction rate is called "Kramers' turnover". This means that the transition state theory may hold good only in the intermediate region of the friction coefficient. The Kramers' theory elucidated the validity and limitation of the transition state theory, by considering stochastic processes on the reaction coordinate explicitly. His theory also gave a unified picture about the effect of solvation dynamics on reaction rates over a wide range of friction coefficient.

2.2.2 Grote-Hynes theory

One can point out three problems inherent to the Kramers' theory. Firstly, it is a purely classical theory, neglecting quantum-mechanical effects on the barrier passage such as tunnelling [13]. The neglection causes a crucial defect in some cases including proton-transfer reactions. Secondary, it regards the motion on a reaction coordinate as one-dimensional. However in actual reactions of polyatomic molecules, *e.g.* dissociation or isomerization, the coupling with other intramolecular vibrational modes often plays an important role on the reaction dynamics. We have to examine whether an explicit treatment for other degrees of freedom is necessary in such cases. Thirdly, it takes into account the effect of solvation dynamics in terms of Brownian motion, described by a Langevin equation. The Langevin equation assumes that the correlation time of random force is neglibibly small compared to the motion along the reaction coordinate [14]. This assumption is surely valid in a case that a Brownian particle is much heavier and thus moves much slower than a solvent molecule, but it is quite doubtful in another case

that a solute molecule (Brownian particle) has a mass of the same order as a solvent molecule so that the time scales of solute and solvent motions are nearly equivalent. These three problems noted above, already pointed out by Kramers himself, have been remaining to be central issues for the following development after Kramers. Here we omit the first problem and focus on the classical dynamics relevant to the latter two.

The third problem among them was solved by Grote-Hynes theory [15], which is a natural extension of the Kramers' one. The Grote-Hynes theory expresses the stochastic motion on a reaction coordinate in terms of a generalized Langevin equation [14, 16] as follows:

$$\ddot{x} = -\frac{\partial G}{\partial t} - \int_0^t d\tau \zeta(\tau)\dot{x}(t-\tau) + R(t); \tag{2.16}$$

where $G(x)$ denotes a potential function, $\zeta(t)$ a generalized friction coefficient, and $R(t)$ a random force. $R(t)$ and $\zeta(t)$ relate each other by the fluctuation-dissipation theorem,

$$\zeta(t) = \frac{1}{k_B T} < R(0)R(t) > . \tag{2.17}$$

This relation means that finite duration of the correlation of the random force requires a generalized form of the friction coefficient $\zeta(t)$ involving delayed response. In particular when the correlation time of the random force is infinitely short, Eq. (2.16) is reduced to the original Langevin equation. The correlation time of $\zeta(t)$ as well as its functional form is the most crucial character of the system in quetion, according to the Grote-Hynes theory. $G(x)$ is usually taken as a free-energy function, namely a "potential of mean force", so that the first term of the right-hand side of Eq. (2.16) refers to the mean force which involves static contribution of solvent. Grote and Hynes derived the reaction rate of the barrier passage using the generalized Langevin equation, Eq. (2.16). Provided that the free-energy function around the barrier top ($x \sim 0$) is approximated in inverse parabolic form,

$$G(x) = G(0) - \frac{1}{2}\omega_{eq}^2 x^2, \tag{2.18}$$

and that $R(t)$ and $\zeta(t)$ are independent of the reaction coordinate x, then the reaction rate of the barrier passage is derived analytically as,

$$k = \frac{\lambda_r}{\omega_{eq}} k^{TST}; \tag{2.19}$$

where λ_r is the positive solution of the following equation,

$$\lambda_r^2 - \omega_{eq}^2 + \lambda_r \int_0^\infty e^{-\lambda_r t}\zeta(t)dt = \lambda_r^2 - \omega_{eq}^2 + \lambda_r^2 \frac{1}{2\pi}\int_{-\infty}^{\infty} \frac{\tilde{\zeta}(\omega)}{\lambda_r^2 + \omega_2} d\omega = 0. \tag{2.20}$$

In the above equation Eq. (2.20), the Fourier transformation of the friction coefficient

$$\tilde{\zeta}(\omega) = \int_{-\infty}^{\infty} e^{i\omega t}\zeta(t) \tag{2.21}$$

was employed for later discussion, instead of the Laplace transformation

$$\mathcal{L}(\zeta)(\lambda) = \int_{0}^{\infty} e^{-\lambda t}\zeta(t)dt. \tag{2.22}$$

k^{TST} in Eq. (2.19) denotes the prediction of the reaction rate by the transition state theory on the same free-energy surface. Without the friction, Eqs.(2.19) and (2.20) indicate that the Grote-Hynes theory reproduces the rate of the transition state theory k^{TST} because λ_r becomes identical to ω_{eq}. (Note that we treat here the local dynamics at the barrier passage, not the dynamics of energy relaxation explicitly.) The fact of $\mathcal{L}(\zeta)(\lambda) \geq 0$ leads to $\lambda_r/\omega_{eq} \leq 1$, which means the transition state theory gives an upper bound of the reaction rate for the Grote-Hynes theory. An interpretation of λ_r comes from the asymptotic form of Eq. (2.16), *i.e.* $x(t) \sim e^{\lambda_r t}$. The asymptotic form implies that λ_r^{-1} may be regarded as a characteristic time scale to pass over the barrier.

The reward for the above formulations is an insight how the characteristics of the friction coefficient affect the reaction rate. Here we delineate some typical cases of the friction coefficients and further argue correspondence to a realistic instance. One typical case is that λ_r^{-1} (the time scale to pass over the barrier) is extremely shorter than the time scale of solvent motion, which is called "non-adiabatic limit". This means that the barrier passage occurs so suddenly that the solvent is nearly frozen during the passage. As to the friction spectrum $\tilde{\zeta}(\omega)$, it consists of very low-frequency components alone in comparison to λ_r (see Fig. 2.2(a)). If we put $\tilde{\zeta}(\omega) = \tilde{\zeta}_0\delta(\omega)$ in the extreme case, the reaction rate k is given in the following:

$$k = \frac{\omega_{na}}{\omega_{eq}} k^{TST}, \tag{2.23}$$

where

$$\omega_{na}^2 = \omega_{eq}^2 - \frac{\tilde{\zeta}_0}{2\pi} = \omega_{eq}^2 - \zeta(t=0). \tag{2.24}$$

The deviation from the transition state theory is expressed via a factor ω_{na}/ω_{eq}. ω_{eq} denotes a curvature of the free energy surface along the reaction coordinate x at the barrier top ($x = 0$) on condition that equilibrium solvation is invoked at each point of x, while ω_{na} refers to a curvature at $x = 0$ on condition that the solvation is equilibriated and fixed at the barrier top ($x = 0$). The latter means that solvation does not adjust itself to any other points than $x = 0$. Solvation energy is thus more stabilized in the former situation than in the latter at other points than $x = 0$, though at the top of

Figure 2.2: Three typical cases of friction spectra $\tilde{\zeta}(\omega)$ in Grote-Hynes theory: (a) non-adiabatic limit, (b) adiabatic limit (Kramers' case), (c) transition state theory.

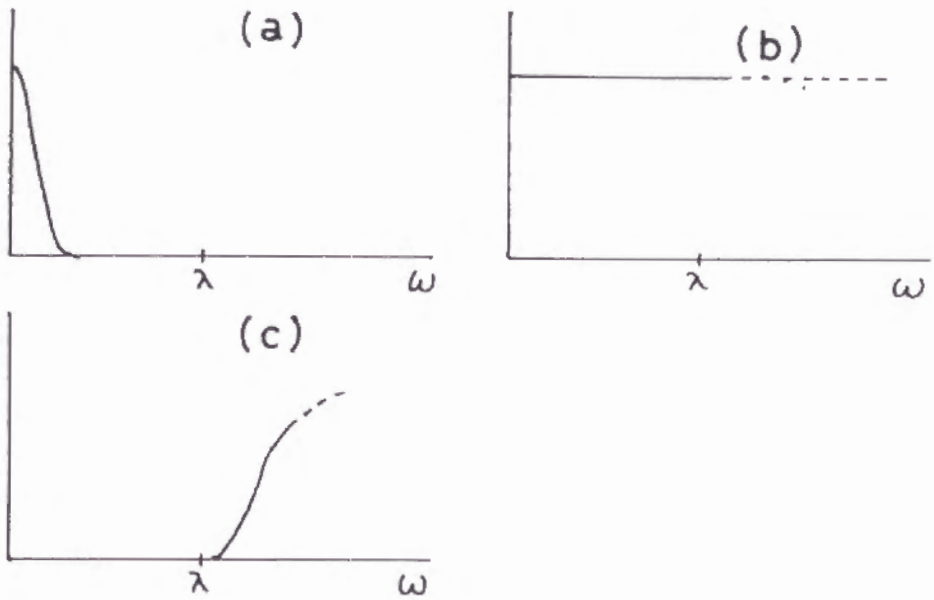

the barrier ($x = 0$) both situations are equal in solvation. Therefore, the curvature of the former ω_{eq} is invariably larger than that of the latter ω_{na}, which is also shown quantitatively in Eq. (2.24). In a special case of Eq. (2.24) that large friction coefficient causes $\omega_{na}^2 < 0$, ω_{na} becomes imaginary so that the rate expression of Eq. (2.23) breaks down. This indicates that the barrier "top" becomes minimum in frozen solvent of the latter situation, which refers to typical caging.

In opposite to the above non-adiabatic case that the friction spectrum $\tilde{\zeta}(\omega)$ is a δ-function in frequency domain, there is another case that the friction coefficient $\zeta(t)$ is represented with a δ-function in time domain (*i.e.* $\zeta(t) = 2\zeta_0\delta(t)$, called "adiabatic limit"). Since the adiabatic limit involves only an instantaneous response of the friction, the generalized Langevin equation Eq. (2.16) is reduced to the original Langevin equation,

$$\ddot{x}(t) = -\frac{\partial G}{\partial x} - \zeta_0\dot{x}(t) + R(t). \tag{2.25}$$

Furthermore, the fluctuation-dissipation theorem Eq. (2.17) results that the instantaneous response of the friction requires negligible duration of the correlation function of the random force $R(t)$, $< R(0)R(t) > \sim \delta(t)$. Therefore, the Grote-Hynes theory in the adiabatic limit is identical to the Kramers'

theory. The adiabatic limit is represented in terms of the friction spectrum $\tilde{\zeta}(\omega)$ in Fig. 2.2(b), where the friction is independent of frequency. In general however, the friction is frequency-dependent. Whereas both theory is equal in the adiabatic limit, we argue here the difference in the other situations. The usual friction coefficient ζ involving no delayed response is expressed using a generalized friction coefficient $\zeta(t)$ as an integral in time,

$$\zeta = \int_0^\infty \zeta(t)dt = \tilde{\zeta}(\omega = 0) = \mathcal{L}(\zeta)(\lambda = 0). \tag{2.26}$$

Since Kramers' theory considers neither delayed response nor frequency-dependence of the friction, it regards the friction coefficient as ζ which is independent of frequency. Therefore, the rate of barrier passage predicted by Kramers' theory is invariably smaller than that by Grote-Hynes one, according to Eq. (2.20) and $\mathcal{L}(\zeta)(\lambda > 0) < \mathcal{L}(\zeta)(\lambda = 0)$. This can be interpreted that the frequency-dependence of the friction reduces the effective friction experienced at the barrier top $\mathcal{L}(\zeta)(\lambda_r)$ from $\mathcal{L}(\zeta)(\lambda = 0)$. It is expected that the discrepancy between the two theory becomes inconspecuous in small curvature ω_{eq}, because Eq. (2.20) implies that λ_r tends to approach 0 in small ω_{eq}.

We discuss here a third situation where the transition state theory holds good. The difference of the reaction rates between Grote-Hynes theory and the transition state theory is given in the following using Eqs.(2.19) and (2.20):

$$\begin{aligned} k - k^{TST} &= (\frac{\lambda_r}{\omega_{eq}} - 1)k^{TST} \\ &= -\frac{k^{TST}}{\omega_{eq}(\lambda_r + \omega_{eq})}\frac{1}{\pi}\int_0^\infty \frac{\lambda_r^2}{\lambda_r^2 + \omega^2}\tilde{\zeta}(\omega)d\omega. \end{aligned} \tag{2.27}$$

Eq. (2.27) involves a factor $\lambda_r^2/(\lambda_r^2+\omega^2)$ within the integral in frequency. Since the factor $\lambda_r^2/(\lambda_r^2 + \omega^2)$ works as a low-pass filter having the characteristic frequency of λ_r, low-frequency components of the friction spectrum relative to λ_r contributes greatly to make the difference. Its physical meaning is obvious; an assumption under the transition state theory breaks down particularly due to the low-frequency components of the friction. In the transition state theory for reactions in solutions, the effect of solvation is involved only energetically in the potential functions (free energy surfaces) via a thermal average. It thus assumes that transient behavior of solvation is negligible. However, the transient behavior toward equilibrium solvation manifests itself in the low-frequency components, because the low-frequency components cannot follow the motion on the reaction coordinate whose time scale is about λ_r^{-1}. We now conclude that the transition state theory holds good on condition that solvation dynamics is sufficiently faster than the time scale to pass over

the barrier λ_r^{-1} and that the frequency spectrum $\tilde{\zeta}(\omega)$ includes negligible components in the frequency range of $0 \sim \lambda_r$ (see Fig. 2.2(c)).

Hynes and co-workers tried to adopt the Grote-Hynes theory to realistic systems to check its applicability. For example, one of the most intensively studied systems is a nucleophilic bimolecular substitution (S_N2) reaction as follows [17, 18, 19] :

$$CH_3Cl + Cl^- \longrightarrow Cl^- + CH_3Cl, \tag{2.28}$$

which is a symmetric and one-dimensional activated reaction. Its potential energy surface and free energy one had been calculated before [20, 21]. They performed molecular-dynamics simulations for this system in aqueous solution to find out the friction spectra $\tilde{\zeta}(\omega)$ and the transmission coefficients of the reaction rates $\chi = k/k^{TST}$. The friction spectra obtained above and the free energy surface were also utilized to estimate the reaction rate in another way using the Grote-Hynes theory. The two reaction rates obtained in different ways, *i.e.* directly from molecular-dynamics simulation and by the Grote-Hynes theory, were compared to examine the theory. As a result, the rate of this S_N2 reaction can be well described by the Grote-Hynes theory. In particular, this is found to be close to the non-adiabatic limit (see Fig. 2.2(a)), because most components of the friction spectrum lie below $\lambda_r(\approx 500cm^{-1})$ at room temperature. Therefore, it was found that the S_N2 reaction in aqueous solution is suitable to neither the transition state theory nor the Kramers theory.

What is the reason that the Grote-Hynes theory is able to gain a wide applicability to realistic systems? In order to elucidate it, we introduce another way of description than the generalized Langevin equation for the dynamics in solutions. The reward of the following description is a convenience to treat explicitly the solvent dynamics and solute-solvent interaction. We now define a model Hamiltonian for the whole solute-solvent system such as

$$H = \frac{1}{2}p^2 + G(x) + \sum_{j=1}^{N}\{\frac{1}{2}P_j^2 + \frac{1}{2}(\omega_j Q_j + \frac{C_j}{\omega_j}x)^2\}, \tag{2.29}$$

In Eq. (2.29), Q_j and P_j denote the conjugated coordinate and momentum of the j-th harmonic mode of the solvent respectively, and the reaction coordinate x is coupled linearly to the solvent coordinates Q_j. The equations of motions based on the Hamiltonian of Eq. (2.29) are projected onto the reaction coordinate x to obtain the generalized Langevin equation Eq.(2.16). Thus the model Hamiltonian of Eq. (2.29) delineates the dynamics on the reaction coordinate equivalently to the generalized Langevin equation [22].

The generalized friction coefficient $\zeta(t)$ and random force $R(t)$ are expressed using the notations in Eq.(2.29) as follows:

$$\zeta(t) = \sum_j \frac{C_j^2}{\omega_j^2}\cos\omega_j t, \tag{2.30}$$

$$R(t) = -\sum_j \{C_j(\frac{C_j}{\omega_j^2}x(0) + Q_j(0))\cos\omega_j t + C_j\frac{P_j(0)}{\omega_j}\sin\omega_j t\}. \quad (2.31)$$

Furthermore, the reaction rate of the Grote-Hynes theory can be reproduced not using the generalized Langevin equation but directly from the Hamiltonian of Eq.(2.29). It is proved that the Grote-Hynes theory defined on the reaction coordinate x is equivalent to an extended transition state theory defined in the whole configuration space of the solute-solvent system (x, Q_j) [22]. In the latter theory, dividing surface between reactant and product is not necessarily the plane of $x = 0$, but is optimized among all the planes that involve the origin $(x, Q_j) = (0, 0)$ so that the flux passing the plane should be minimum. This procedure of optimization permits the dividing surface of the transition state to involve solvent coordinates explicitly, and consequently it improves the usual transition state theory to reproduce the Grote-Hynes theory. It is also noted that the potential curvature normal to the optimized dividing plane is shown to be λ_r.

In the above Hamiltonian of the whole solute-solvent system, the solvent dynamics and solute-solvent interaction are simply described under two assumptions; the solvent dynamics is represented by a set of harmonic oscillators and the solute-solvent interaction by linear coupling. We have to consider the validity of these two assumptions, for the Grote-Hynes theory also holds the assumptions equivalently. As for the first assumption, the harmonic approximation for the solvent dynamics is appropriate only in a short time during which coherence of motions continues (typically about subpicoseconds) [23]. Thus the harmonic approximation would be valid provided that such a short time is sufficient to describe crucial dynamics to determine reaction rates. The other assumption, linear coupling of solute-solvent interaction, defines a character of the solvent friction. It indicates that both the friction coefficient $\zeta(t)$ and random force $R(t)$ in the generalized Langevin equation are independent of the reaction coordinate x, because higher-order coupling should inevitably cause x-dependent friction $\zeta(x, t)$ or random force $R(x, t)$. However, the assumption of linear coupling does not seem to hold good generally to actual situations. For example, let us consider the S_N2 reaction mentioned above,

$$CH_3Cl + Cl^- \rightarrow Cl^- + CH_3Cl. \quad (2.32)$$

Since a negative charge transfers from one chlorine atom to the other rather suddenly when passing the transition state [17, 18, 19], the electrostatic interaction probably shows a striking change near the barrier top. If it is true, the assumption of linear coupling breaks down, because the friction coefficient or the random force should be dependent on the reaction coordinate x. Thus the assumption of linear coupling holds only within a quite local region on the reaction coordinate where the friction and the random force

are safely regarded as constant. Therefore, the above two assumptions of the model Hamiltonian of Eq. (2.29) indicate that the model Hamiltonian can be applied only in a quite local region at the barrier top both temporally and spatially. Thus a wide applicability of the Grote-Hynes theory results that the dynamics crucial to reaction rates is quite local at the barrier top both temporally and spatially in general. This assumption of local dynamics seems more appropriate in a liquid-phase reaction than in a gas-phase one, since the coherence of motion is more easily destroyed in liquids that a deterministic description of global motion becomes invalid. We will discuss this point further in the next section.

2.2.3 Multidimensionality of reaction coordinates

Multidimensionality of reaction coordinates is another important problem, though it is omitted in the Kramers theory. Besides a reaction coordinate, there often exist other intramolecular coordinates strongly coupled to it so that they are not amenable to a treatment as a bath. However, a general argument for searching an appropriate treatment is difficult, because situations of the intramolecular coupling are quite various due to the shape of potential energy surface of each system. Thus we argue here two typical cases as examples in the followings.

Curvature effect of potential energy surface — an application of variational transition state theory —

Among gas-phase reactions, some systems demonstrate a breakdown of the transition state theory owing to the multidimensionality. One of the most notorious instances is a triatomic substitution reaction of a heavy-light-heavy system,

$$HL + H' \longrightarrow H + LH', \tag{2.33}$$

where H and H' stand for relatively heavy atoms, and L for a relatively light atom. Provided that the three atoms are constrained collinear, the system has two internal degrees of freedom: the distance between HL and H', $x(HL-H')$, and that between H and LH', $y(H-LH')$. Both axes meet at a skew angle as seen in Fig. 2.3, when the kinetic energy should be expressed to be diagonal on the potential energy surface. The angle becomes more acute as the difference of masses between the center atom and the side atoms is augmented. If the skew angle is acute enough due to the large mass ratio, the intrinsic reaction coordinate (IRC) [24, 25] has a large curvature in the vicinity of the suddle point of the potential energy surface. (IRC is defined using the steepest descent path drawn from the suddle point toward each side of reactant and product.) Such a large curvature stresses the "recrossing" effect that a considerable amount of the incident flux upon the suddle

Figure 2.3: Schematic picture of a potential energy surface for three-atom substitution reaction: $HL + H' \longrightarrow H + LH'$. Bold line denotes the intrinsic reaction path, and broken line is the dividing surface of the transition state crossing the suddle point.

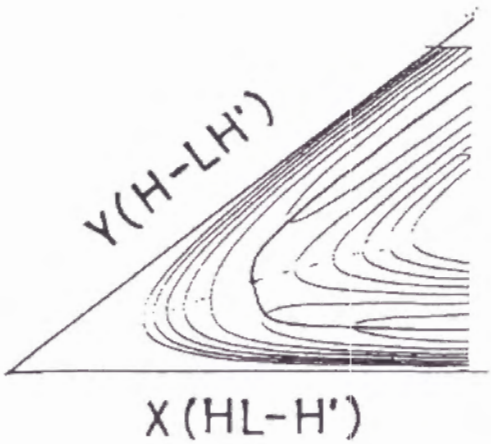

point from reactant is reflected to be unable to reach the product region. The recrossing effect causes the transition state theory to overestimate the reaction rate, because it estimates the rate by the incident flux itself and does not take account of the recrossing effect. However, the Hamiltonian of Eq. (2.29) is useless to describe such effect of curvature-induced recrossing, since it includes second-order derivatives and no higher-order ones with respect to coordinates, though the curvature along the reaction coordinate is expressed using third-order derivatives. Thus the Grote-Hynes theory omitts the effect of curvature-induced recrossing, while it deals with the effect of solvent-induced recrossing. It is rather apparent that the Grote-Hynes theory is not capable of describing the former effect, because it can describe only a quite local dynamics at the barrier top as discussed previously while the curvature of IRC is refered to a more global property near the barrier top. However, it is not obvious whether the former effect may be safely omitted due to the latter effect in liquid-phase reactions.

In gas-phase reactions, the former effect has been well studied for the latter is absent. One of the most valuable theories to describe the former effect is variational transition state theory, an extended vergion of the transition state theory [26]. The term "variational" means that location of the dividing surface is optimized to minimize the incident flux. The theory is based on the fact that an incident flux into a dividing surface is always larger than the net reactive flux by the amount of recrossing regardless of the location of a dividing surface, as far as it certainly divides the reactant and product regions of the phase space. This variational transition state theory is more general than the Grote-Hynes theory (or equivalently the ex-

tended transition state theory discussed in Sec. 2.2.2), since the variational transition state theory permits more flexible optimization, constrainted by neither the saddle point nor the origin $(x, Q_j) = (0, 0)$. If the dividing surface optimized variationally deviates from the saddle point, the variational transition state theory gives an improved estimate of the reaction rate than the original transition state theory. In particular when the skew angle between the axes $x(HL-H')$ and $y(H-LH')$ is small, the variational transition state theory manifest its efficiency by giving an optimized dividing surface not to involve the suddle point. This is because a normal dividing surface involving the suddle point has particularly wide entrance available to the incident flux (due to a small angle, see Fig. 2.3), which is unfavorable to reduce the flux.

Garrett and co-workers discussed the effect of curvature-induced recrossing in liquid-phase reactions on the basis of a model system of Eq. (2.33), by utilizing molecular-dynamics simulation and the variational transition state theory [27]. The model potential employed by them is

$$V(\boldsymbol{q}, \boldsymbol{Q}) = V_0(\boldsymbol{q}) + \frac{1}{2}(\boldsymbol{Q} - \boldsymbol{C}\boldsymbol{q})^T \cdot \boldsymbol{\Omega}^2 \cdot (\boldsymbol{Q} - \boldsymbol{C}\boldsymbol{q}); \tag{2.34}$$

where $\boldsymbol{q}$ and $\boldsymbol{Q}$ stand for the coordinates of solute and solvent, respectively. $\boldsymbol{q}$ is a two-dimensional vector whose components denote $x(HL - H')$ and $y(H - LH')$, and $V_0(\boldsymbol{q})$ is an empirical LEPS potential [28] to describe the three-atom reaction of Eq. (2.33). The second term in Eq. (2.34) is inherent to solution; it includes a set of harmonic potentials for solvent and linear coupling between the solute and solvent. Note that the second term involves no higher-order derivatives than second-order by coordinates and only the first term $V_0(\boldsymbol{q})$ involves them within the internal degrees of freedom $\boldsymbol{q}$. Apparently Eq. (2.34) is equivalent to Eq. (2.29) except for the dimension of the internal space as seen in the difference of notations, $\boldsymbol{q}$ and q. Therefore, one can easily prove that Eq. (2.34) leads to a multidimensional vergion of the Grote-Hynes theory [29] in the same way as that Eq. (2.29) leads to the original Grote-Hynes theory. The multidimensional friction coefficient $\boldsymbol{\zeta}(t)$ and random force $\boldsymbol{R}(t)$ are given as

$$\boldsymbol{\zeta}(t) = \boldsymbol{C}^T \cdot \boldsymbol{\Omega}^2 \cdot \cos(\boldsymbol{\Omega} t) \cdot \boldsymbol{C}, \tag{2.35}$$

$$\begin{aligned} \boldsymbol{R}(t) = {} & \boldsymbol{C}^T \cdot \boldsymbol{\Omega}^2 \cdot \cos(\boldsymbol{\Omega} t) \cdot (\boldsymbol{Q}(0) - \boldsymbol{C}\boldsymbol{q}(0)) \\ & + \boldsymbol{C}^T \cdot \boldsymbol{\Omega} \cdot \sin(\boldsymbol{\Omega} t) \cdot \boldsymbol{P}(0). \end{aligned} \tag{2.36}$$

Garrett and co-workers estimated the reaction rate of Eq. (2.33) using molecular-dynamics simulation on the basis of the Hamiltonian of Eq. (2.34). The rates obtained by the simulation were compared to those by the transition state theory for the whole solute-solvent system (which is equivalent to the multidimensional Grote-Hynes theory) or by the variational transition state theory, to evaluate the effect of curvature-induced recrossing. They examined some

Figure 2.4: Transmission coefficients of the reaction rates of $CH_3 + H \longrightarrow H + CH_3$ [27].

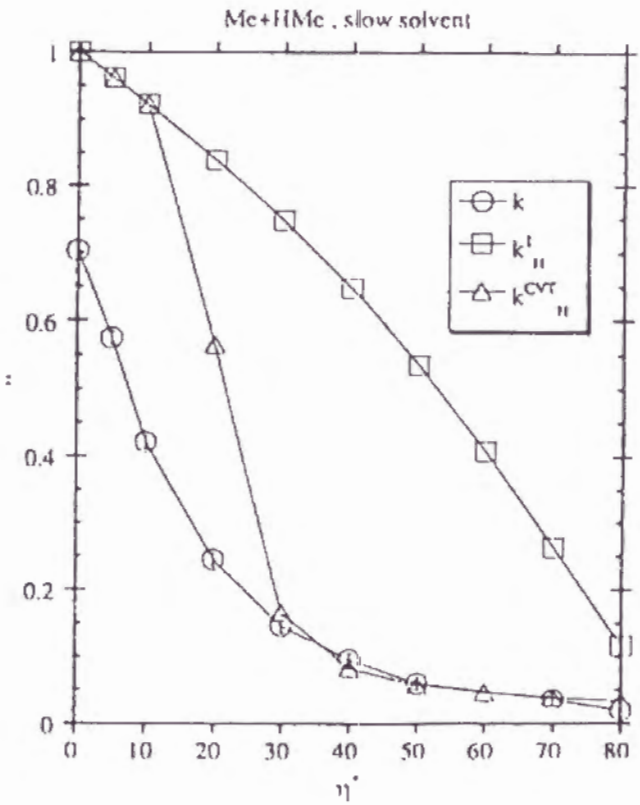

situations with varying parameters for the mass ratio and relaxation time of solvent; one of their results is displayed here in Fig. 2.4. In this figure, the axis of abscissas denotes reduced friction coefficient and that of ordinates the transmission coefficient which means the ratio of reaction rate to the expectation value by the transition state theory in gas-phase (without friction). ○ refers to the simulation; □ to the multidimensional Grote-Hynes theory; △ to the variational transition state theory. Figure 2.4 shows a considerable discrepancy between the results of the simulation and the multidimensional Grote-Hynes theory in low friction region, while the discrepancy is diminished with increasing friction. This indicates a competition between the effect of curvature-induced recrossing and that of solvent-induced one. As noted before, the Grote-Hynes theory involves no former effect but only the latter one. Thus in the low friction region where the solvent exerts little friction the former effect apparently manifests the defect of the Grote-Hynes theory, while in the high friction region where the latter effect is dominant the defect does not emerge clearly.

Figure 2.4 also shows that the variational transition state theory reproduces the results of the simulation better than the Grote-Hynes theory except for low friction region. We can obtain further insight by comparing their results of Fig. 2.4 to a realistic system, *e.g.* the S_N2 reaction in water discussed previously,

$$Cl^- + CH_3Cl^- \longrightarrow CH_3Cl^- + Cl^-. \tag{2.37}$$

Note that the above reaction in aqueous solution belongs to the adiabatic case (see Sec. 2.2.2), to which Fig. 2.4 also refers. The reduced friction coefficient for this system is estimated approximately that $\eta^* \approx 6$ using the molecular-dynamics results by Hynes et al.[17, 18, 19], which falls under the low friction region in Fig. 2.4 where the curvature effect emerges in the reaction rate. In this region not only the Grote-Hynes theory but also the variational transition state theory is useless to reproduce the results of the simulation. (We should also note that in the S_N2 reaction the mass ratio $M(Cl)/M(CH_3)$ is about 2.4. This value is rather smaller than that in the Fig. 2.4, $M(CH_3)/M(H) \approx 15$, so that the curvature effect is not so magnified in the S_N2 reaction as in Fig. 2.4.) Generally speaking, however, the solvent friction is fairly large in the S_N2 reaction in aqueous solution because of the dielectric friction, which comes from the fact that the ionic species involved in the reaction system strongly interacts with the polar solvent (water) during the reaction. Therefore, it is rather appropriate to say that the variational transition state theory is valid only in the cases of very high friction among realistic systems. Such high friction tends to cause so-called cage effect, where the reaction system $H \cdots L \cdots H'$ is temporary enclosed in a solvent cage. Under such situation the usual transition state theory particularly overestimates the reaction rate, because the cage confines the three particles

together to cause many recrossings. The variational transition state theory, on the other hand, possibly gives an improved rate by moving the dividing surface toward either reactant or product, so that the dividing surface is crucially relevant to creation of annihilation of the cage. As a conclusion, the effect of curvature-induced recrossing may influence liquid-phase reactions, even if it is not described by the variational transition state theory. This effect is favored by the following conditions: that (i) the mass ratio is large, (ii) the solvent friction is small, and (iii) the relaxation time of solvent is slow relative to the motion on the reaction coordinate. The latter two conditions support to keep the coherence of motion on the reaction coordinate.

Solvation dynamics and intramolecular vibrations — Sumi-Marcus theory —

In the preceding section we argued the multidimensionality of the reaction dynamics for a simple three-particle substitution reaction. In this section we argue the multidimensionality for another situation on the basis of Sumi-Marcus theory [30, 31]. Though it originally deals with electron-transfer reactions, its treatment is not specific so that it is probably useful for other reactions relevant to both solvation dynamics and intramolecular vibration. First we give a brief survay on the electron-transfer reactions to delineate its background. The most famous theory to deal with them is the Marcus theory [32], which regards them as activated processes on free energy surfaces, since electron-transfer reactions in solutions are driven by fluctuation of solvation. Although electron-transfer reactions and usual activated reactions discussed previously are commonly regarded as activated processes, a principal difference exists in reaction coordinate; in the former the Marcus theory defines it with dielectric polarization exerting on solute while in the latter it is usually defined with a intramolecular coordinate of solute. Therefore, the electron-transfer reactions are in general more influenced by diffusive and collective motions of solvent than the usual activated reactions. If the solvation dynamics alone determines the electron-transfer rates and it may be described by Debye's dielectric continuum model, the electron-transfer rates should be predicted by the longitudinal dielectric relaxation times of solvents. Thus in order to examine the assumptions, the correlation between the electron-transfer rates and the longitudinal relaxation times of solvents has been particularly studied both from experimental and theoretical sides [33, 34, 35, 36, 37]. When considering the microscopic processes during the electron-transfer reactions, we have to take account of the following three factors. One point is the relevant free energy surface as well as the nonadiabatic coupling element that is crucial to the electronic transition [38]. Another point is the dielectric relaxation process involved in the reactions. Though it is often described by a single exponential decay as Debye did,

Figure 2.5: Schematic picture of two-dimensional potential energy surface by Sumi-Marcus theory [30]

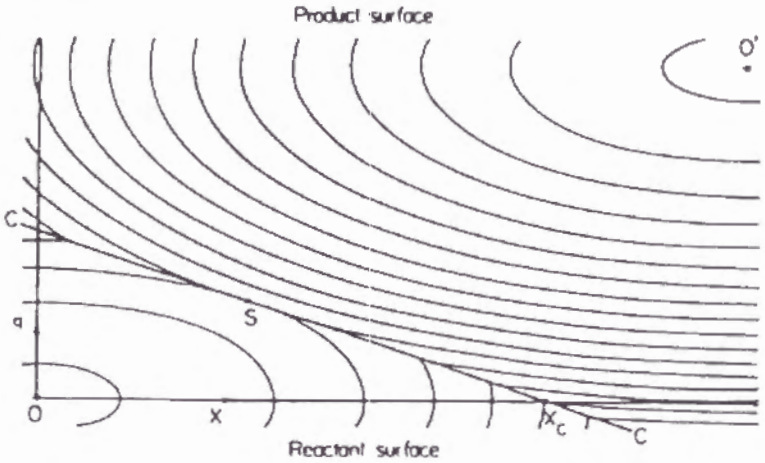

recent studies by molecular-dynamics simulation imply that it is not necessarily true for realistic systems [2, 3]. The other point refers to the reaction coordinate. As noted above, the original Marcus theory defines it with the dielectric polarization exerting on solute and omitts the intramolecular coordinates of solute. However, it is doubtful to omit the latter if the solute changes in stable structure between reactant and product (experimental evidence was found [39]). Sumi-Marcus theory elucidated that the latter is also able to play an important role to the electron-transfer rates.

There exists a qualitative difference in dynamics between the dielectric polarization and the intramolecular vibration. The former is essentially diffusive and particularly couples to slow motion (vibration) of solute, *e.g.* about an order of $1 \sim 10cm^{-1}$ for a large molecule, while the latter is much more rapid in the order of magnitude. To describe both the dynamics in a simple manner, let us introduce a two-dimensional space as seen in Fig. 2.5, where the two kinds of dynamics correspond to two coordinates, X and x. X refers to the dielectric polarization, and x to the intramolecular vibration. Figure 2.5 shows a schematic picture of free energy surfaces of reactant and product, both of which are expressed harmonically. Note that each coordinate has different values at the stable configurations of reactant and product, which is a necessary condition for both the coordinates to participate in the reaction rate. If the above condition is satisfied, the dividing line between reactant and product, defined with the seam of the free energy surfaces, is not paralell to either axis as seen in Fig. 2.5. Thus the barrier passage is achieved by the dynamics along either axis, while the original Marcus theory considers the diffusive dynamics along the X axis alone. If the x axis

contributes to the reaction rate substantially, it deviates from the original Marcus theory, since the diffusive slow dynamics along the X axis is not necessarily the rate-determining step any more. We will formulate the dynamics using a probability distribution function of reactant, $P(X;t)$. The dynamics along the X axis is described by a diffusion equation, while transient behavior along the x axis is much more rapid so that reaction rate to escape through the x axis $k(X)$ can be well defined at each point of X. Therefore, the time development of $P(X;t)$ is expressed by a diffusion-reaction equation as follows:

$$\frac{\partial P}{\partial t} = D\frac{\partial^2 P}{\partial X^2} + \frac{D}{k_B T}\frac{\partial}{\partial X}(P\frac{dV}{dX}) - k(X)P. \tag{2.38}$$

The first and second terms of the right-hand side denote the diffusional motion along X, which is equivalent to the high friction limit (Smoluchowski limit) of the Kramers theory. The third term refers to reaction, where the back reaction from product to reactant is omitted. As the above two-dimensional model was proposed by an extension of the conventional theory, it is reduced to one-dimensional models in some extreme situations. We give here a brief discussion on the four extreme cases. Two of them are defined with the normal direction of the dividing surface. If the normal direction is almost parallel to the X axis (narrow reaction window) or the x axis (wide reaction window), the other axis becomes irrelevant to the reaction. Thus the reaction is described using a single coordinate in both cases, though they are quite different each other. The other two extreme cases are defined with the ratio of time scales of motions along the two axes. If the diffusional motion is extremely slower than the intramolecular vibration to be regarded as frozen, the diffusional motion does not contribute to the reaction rate and the X coordinate will be merely regarded as inhomogeneous distribution. Contrary to the above, if the diffusional motion is sufficiently faster than the intramolecular vibration, the reaction rate appears to be independent to the diffusional motion except for the narrow reaction window limit. In that case the reaction is proceeded with keeping equilibrium distribution on the X axis. Thus X axis need not be treated explicitly, since the effect of non-equilibrium solvation does not emerge in this limiting case. Except for the narrow reaction window limit, both the extreme cases does not affected by the motion along X axis. The Sumi-Marcus theory permits to deal with general situation besides these limiting cases by using Eq. (2.38). It derives some possible features of reaction rate attributed to the intramolecular vibration; *e.g.* reaction rate may be faster than the dielectric longitudinal relaxation of solvent even if the dielectric polarization is diffusionally relaxed, or reaction rate may be proportional to a fractional power of the dielectric longitudinal relaxation time τ_L, $k \sim \tau_L^{-\alpha}$ $(\alpha < 1)$. Such fractional dependence had been experimentally observed, although it had not been elucidated theoretically until the Sumi-Marcus theory. (Such fractional dependence to the solvent

friction was also found in other activated reactions including photoisomerization ones. We will discuss this point further in the following section.) The Sumi-Marcus theory gives a definite picture to multidimensional dynamics of reactions, by remarking the difference in time scale between diffusional motions and intramolecular vibrations. This picture is probably useful to other reactions that have been regarded as merely diffusive ones to date.

However, the above theory has a crucial problem; it assumes a harmonic shape of the free energy surfaces, for the actual shape is not a matter of discussion. Obviously this assumption is not always approriate. In an intramolecular charge transfer reaction of N,N-dimethylaminobenzonitrile (DMABN) in aqueous solution, the free energy surface of the charge transfer state was found to be far from harmonic, by Kato et al. using *ab initio* MO calculation and Monte Carlo simulation [40]. In general, little is known about actual shapes of potential energy surfaces or free energy ones, especially about their multidimensional shapes, because their actual shapes become hard to be delineated with increasing dimensionality. Thus most of reactions in solutions have been treated using one-dimensional models in spite of much effort devoted to extend the models, which includes the two models of two-dimensional surfaces discussed in this subsection and the preceding one. The effort is certainly necessary; even in the photoisomerization reaction of stilbene, experimental findings suggest that one-dimensional treatment is quite doubtful. We have to gain realistic information on potential energy surfaces or free energy ones reliable enough to interpret experiments. Many experiments have been carried out using ultrashort pulse lasers and observed transient dynamics on excited states. Such experiments require further difficulty of theoreticians, because the potential energies at excited states are much harder to be calculated than those at ground states. Under the present stage of the research, it is particularly important to obtain accurate and detailed knowledge for a few typical systems as much as possible. Therefore, we will argue the photoisomerization reaction of stilbene, one of the most popular systems in this field, on the basis of experimental findings.

2.3 The photoisomerization reaction of stilbene

Stilbene $(C_6H_5)HC = CH(C_6H_5)$ has two stable isomers on the electronic ground state, cis and trans isomers with respect to the center C=C bond. The two isomers are easily transformed to each other by absorbing a UV photon having shorter wavelength than *c.a.* 300nm. Figure 2.6 is a schematic picture of the potential energy surfaces of S_0 and S_1 states as a function of the torsional angle around the central C=C bond [41, 42]. This figure shows that the twisted geometry at 90° is unstable on the S_0 state while it

Figure 2.6: Potential energy surfaces of S_0 and S_1 states of stilbene as a function of the central C=C torsional angle

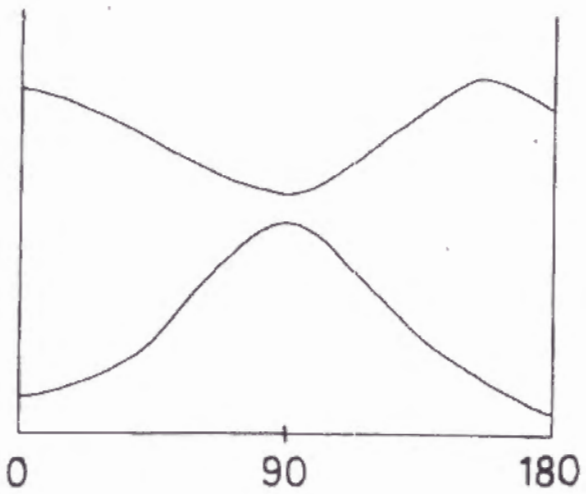

corresponds to a minimum geometry on the S_1 state. The energy difference between S_0 and S_1 is very small at this geometry so that effective internal conversion should take place at this point. Thus after photoabsorption to prepare excited stilbene, either trans or cis isomer goes toward the twisted geometry, where it experiences internal conversion into the S_0 state. Since the twisted geometry on the S_0 state corresponds to a suddle point on the potential energy surface, it stabilizes to either trans or cis isomer at a ratio of *c.a.* 1:1. The consequent processes on photoabsorption have been confirmed experimentally. Detailed experiments in gas phase revealed that the trans isomer has an activated barrier about 1200cm^{-1} on the S_1 state to go to the twisted geometry while the cis isomer has no barrier. They also revealed that it takes several 10 ps for the excited trans isomer to pass over the barrier though the time depends on the excitation energy. As mentioned previously, this barrier passage has been regarded as a typical instance of one-dimensional activated reactions. Besides, this system is quite suitable to time-resolved experiments using pump-probe technique. Thus a number of experiments have been performed both in gas phase and in solutions.

One of the central interests for the experiments in solutions was the examination of the Kramers theory. This issue was solved by experiments demonstrating the Kramers' turnover of the reaction rate with varying friction [41]. Changing friction is realized experimentally by changing solvent, but it must not accompany secondary effect besides changing friction. In the actual experiments, solvents with varying friction were prepared using a series of alkanes, from gaseous methane to viscous liquid paraffin. The

Figure 2.7: Reaction rate of isomerization of stilbene in alkane solvents. The axis of abscissa is the inverse of the diffusion coefficients; the axis of ordinate is the monoatomic reation rate [41].

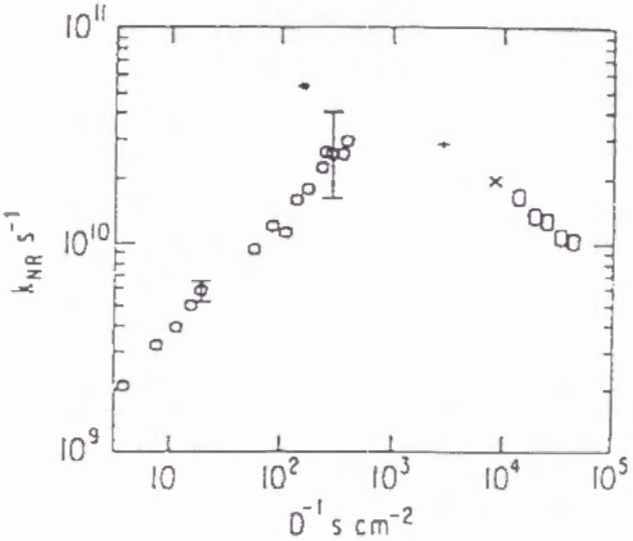

intermediate range of friction was prepared by supercritical ethane. These alkanes are chemically inert and nonpolar in common, so that secondary effect such as perturbation to the potential energy surface or dielectric friction [43] is likely to be negligible. The observed rates with varying alkanes are shown in Fig. 2.7, which indicates the Kramers' turnover at least qualitatively. The photoisomerization of stilbene played a crucial role to corroborate the Kramers' turnover as well as the chair-boat isomerization of cyclohexane [44]. Nevertheless, it has not been verified whether the Kramers theory is really valid to the photoisomerization reaction of stilbene or it is only Sapparently. This is because the entire picture of this photoisomerization has not been brought to light in spite of a number of studies. Further quantitative investigation on the reaction rate brings some unexpected findings that seem unable to be elucidated by the Kramers theory. For instance, the reaction rate k in liquid alkanes having long chains decays slowly with increasing viscosity η much more than the Kramers' expectation [42]. Provided that the friction ζ is proportional to the viscosity η according to the Stokes-Einstein law (see Sec. 2.3.2), the Kramers theory predicts the viscosity dependence of the reaction rate that $k \propto \eta^{-1}$ in the high friction limit, while experiments indicate that $k \propto \eta^{-\alpha}$ ($\alpha < 1$, $\alpha \simeq 0.2 \sim 1$). Some of the experimental results showing such an insensitive dependence as $\alpha \sim 0.2$ are not reproduced even by the Sumi-Marcus theory. This is not so surprising to note that the reaction in question is rather different from electron-transfer reactions of large

molecules; the dynamics of solvent fluctuation and intramolecular vibration are not definitely separated in time scale for this photoisomerization reaction. Another instance remaining unsolved is relevant to the absolute value of the reaction rate; there seems to lie inconsistency in the reaction rate between in gas phase and in solutions [41]. The above instances make it evident that fundamental theories on reactions in solutions discussed in the previous section are in fact quite unsatisfactory to interpret the actual behavior of a stilbene molecule. In order to utilize or examine those theories, following two factors have to be understood: potential energy surfaces of the solute (stilbene molecule) and microscopic friction due to solvation. The former is also relevant to the gas-phase reaction. First we argue the former factor in the following.

2.3.1 Potential energy surfaces of stilbene

Figure 2.6 showed a rough scheme of the potential energy surfaces relevant to the photoisomerization as well as the barrier height at the S_1 state. These features were certainly corroborated by experimental evidences, but little is known about further details including potential crossing, shape of the potential energy surfaces on other degree of freedom, and solvent effect on the potential energy surfaces. These three points are crucial to the photoisomerization process; thus we will give a discussion on them as follows. Since the former two points among them are commonly crucial to the gas-phase reaction, we will also mention the gas-phase studies when considering the two points.

Before discussing these points, we first survey previous work done by molecular-orbital calculations for obtaining the potential energy surfaces. Since *ab initio* calculations were hardly performed for the excited state due to fairly large size of the stilbene molecule [47], most previous were carried out using semiempirical calculations [48, 49]. However, semiempirical calculations are less reliable for excited states than for ground states, because empirical parameters involved were usually determed to reproduce ground-state properties. All of these semiempirical calculations made use of π-electron approximation, where wavefunctions of the excited states are expressed by configuration interaction restricted within π-electron space. However, π-electron approximation is quantitatively inaccurate for $\pi\pi^*$ excited states of conjugated polyenes including the stilbene. This comes from the fact that ion-pair character of $\pi\pi^*$ states induces a considerable σ polarization that reduces their excited energies about an order of 1eV [9], while the σ polarization is not involved in the π-electron approximation. Even if some semiempirical calculations demonstrate excite excitation energies of $\pi\pi^*$ states, they are scaled to involve the σ polarization. Such scaling is not necessarily appropriate to other states or other geometries far from the equilibrium one. We

have to be cautious of previous results on molecular-orbital calculations.

One of the crucial features of the potential energy surfaces is potential crossing, as mentioned previously. Avoided crossing of ^1A and ^1B states is currently believed to be the origin to make the barrier on the S_1 state [51], though there remains some contradiction [49]. Zewail and co-workers studied the gas-phase reaction and insisted that nonadiabatic coupling between ^1A and ^1B states is so small that nonadiabatic transition affects the probability of the barrier passage [45]. If it is true, the nonadiabaticity imposes a serious modification on the current picture of simple (adiabatic) barrier passage. They also suggested that in liquid-phase reaction adiabaticity at the electronic transition may increase due to the solvent fluctuation [52, 53]. The amount of the nonadiabatic coupling should be estimated by a molecular-orbital calculation, but it remains to be a future problem. Before estimating the nonadiabatic coupling, one has to describe the two excited states ^1A and ^1B with even accuracy and examine the avoided crossing. When an accurate description for the excited states is achieved, it will also make possible to yield useful information about the potential shape on other degrees of freedom.

Among the other degrees of freedom besides the central C=C torsion, two coordinates are worth noting: the torsions around C-C_6H_5 and the central C=C stretching. The torsions around C-C_6H_5 is stable at planer geometry, but is very loose. Experimentally, large amplitude motion of the torsions is observed at room temperature in gas or solutions, while trans-stilbene molecules in crystal phase take rigid planer structure [54]. Such loose coordinates probably play a role during the photoisomerization process, as expected by many people. If the nonadiabatic transition actually affect the reaction rate, the loose coordinates become more important from a viewpoint of electronic structure. This is because molecular deformation along the C-C_6H_5 torsions reduces the molecular symmetry from C_2 to C_1. Thus a reactive trajectory can bypass the conical intersection to diminish the nonadiabatic transition. We also propose another inference from a viewpoint of solvent friction. In actual dynamics in solutions, the rotation around the central C=C bond experiences strong frictional resistance due to the bulky phenyl rings, but the torsions around the C-C_6H_5 moieties feel less friction to occur more easily. The twisted C-C_6H_5 moieties turn to lessen the solvent friction during the central C=C rotation. Thus it is plausible that the C-C_6H_5 torsions are involved in the photoisomerization path. We anticipate that the first step of the deformation is out-of-plane motions of the central two carbon atoms into opposite direction each other, which lead to an intermidiate geometry with both the C-C_6H_5 moieties twisted. This step is little influenced by solvent friction, since the bulky phenyl rings do not move particularly. Then the central C=C rotation follows with keeping the twisted C-C_6H_5 configuration. Similar dynamics of isomerization was observed by

molecular-dynamics simulations for saturated hydrocarbon chains (namely "kink motion") [55].

The other coordinate worth noting is the central C=C stretching. In the S_1 state, the central C=C bond weakens while the C-C_6H_5 bonds gain some double-bond character in comparison to the ground state. Since the equilibrium distances are rather different between S_0 and S_1, the photoisomerization causes marked vibrational excitation of these stretching modes [56], which may affect the subsequent dynamics. A previous semiempirical molecular-orbital calculation for styrene ($(C_6H_5)HC = CH_2$) reported that the crossing seam of ^1A and ^1B is strikingly dependent on the coordinate of the C=C stretching [57]. This result suggests an analogous dependence also for the stilbene.

We then turn to the final point, the effect of solvent perturbation on potential energy surfaces. Troe and co-workers insisted that the barrier height itself is diminished by solvent [58, 59]. Their contention is based on the experimental results that actual rate in nonpolar solvents exceeded the expected value from canonical transition state theory $k(T)$, which was derived by thermal average of microcanonical rate $k(E)$ observed in gas phase. This result is hardly understood unless the barrier height is altered, because the rate expected from the canonical transition state theory gives a classical upper bound of the actual rate. We should note, however, that their ground is not necessarily certain, since the density of states is virtually unknown though it is indispensable to the thermal average. There is another evidence of the solvent perturbation on the potential energy surfaces; the reaction rate in alcohol solution is strikingly enhanced than in nonpolar solution [41]. Besides, the rate in alcohol solutions decays proportionally to inverse diffusion coefficient D^{-1} (which is equivalent to the solvent friction in high friction limit) as expected by the Kramers theory. This behavior in alcohol differs qualitatively from that in nonpolar solutions showing an marked deviation from the Kramers theory. Such different behaviors can be elucidated by assuming a barrierless transition in alcohol solution [41]. This is not surprising since polar solvent exerts a strong influence on the solute by its electrostatic force. The solute molecule on the excited state, on the other hand, is fairly sensitive to the solvent perturbation. Generally, a solute molecule on a electronically excited state has a larger polarizability than on a ground state; in particular, an ion-pair state such as the $\pi\pi^*$ states of conjugated polyenes probably has a strong interaction to polar solvents. However, detailed and accurate knowledge is quite insufficient at present about the intermolecular interactions between solute on electronically excited states and solvents.

2.3.2 Microscopic features of solvent friction

In Sec. 2.2 we discussed some fundamental theories about reactions in solutions developed since Kramers. They are useful to predict reaction rates if solvent friction as well as potential energy surface is given, but they are invalid to predict solvent friction. Note the previous argument for a model S_N2 reaction in Sec. 2.2.2 to verify the Grote-Hynes theory. In the discussion, the friction spectrum $\tilde{\zeta}(\omega)$ utilized by the Grote-Hynes theory was not evaluated until a molecular-dynamics simulation was implemented. Such a theory is virtually unsatisfactory to predict reaction rates in solutions. Thus we have to explore a further theory to understand the solvent friction itself. A number of theoretical studies have been performed for isomerization dynamics of molecular chains in solutions [60, 61]. Here we will focus on microscopic features of solvent friction exerted on the photoisomerization reaction of stilbene. As noted previously, this system shows an odd behavior that the reaction rate decays more slowly with increasing solvent viscosity than the Kramers' expectation at high friction limit. This issue has given rise to a number of hypotheses, but none of those predominates over the others. In order to solve this issue, it is certainly necessary to understand the solvent friction exactly.

One of the potent hypotheses comes from the time-dependent friction [62]; this idea is essentially the same as that of extension from the Kramers theory to the Grote-Hynes one. The latter theory gives a larger reaction rate than the former in general, as discussed in Sec. 2.2.2. This fact was utilized to explain the deviation from the Kramers theory. Physically speaking, most part of a friction spectrum $\tilde{\zeta}(\omega)$ of viscous solvent belongs to quite low-frequency components that do not couple to rapid motion of the barrier passage. Thus the effective friction exerted on the barrier passage is thought to increase not so much as solvent viscosity does. The above story consistently explains why the photoisomerization rate in viscous solvent decays more slowly with increasing viscosity than the Kramers' expectation, on the basis of the general feature of solvent friction. However, it is hardly corroborated by a quantitative evidence, because a quantitative argument should inevitably involve a number of parameters relevant to the solvent friction and the potential barrier that are very difficult to be specified and, unfortunately, the reaction rate was found to be quite sensitive to these parameters [62]. Thus, instead of a quantitative discussion, we seek another clue to understand the solvent friction by investigating other analogous systems.

There are many other molecules showing photoisomerization in solutions when bulky substituent groups change their positions induced by photoabsorption, *e.g.* 1,4-diphenylbutadiene, DODCI, 1,1'-binaphthalene [41]. Some of those molecules manifest similar behavior that the photoisomerization rates in viscous solutions deviate from the Kramers' expectation in

high friction limit. For instance, Eisenthal et al. [63] observed such a deviated behavior of 1,1'-binaphthalene, which is made of two naphthalene rings connected at 1,1- sites and has two isomers with respect to the torsional angle between the two rings. Nevertheless, they insisted that the Kramers theory reproduces its reaction rates fairly well if intermediated region of friction is considered and the original formula Eq. (2.8) (not the Smoluchowski version at high friction limit, Eq. (2.9)) is adopted. Hochstrasser et al. [64] demonstrated a photoisomerization reaction of a remarkable molecule, 1,1'-biindanylidene (namely "stiff stilbene"), whose compound formula is

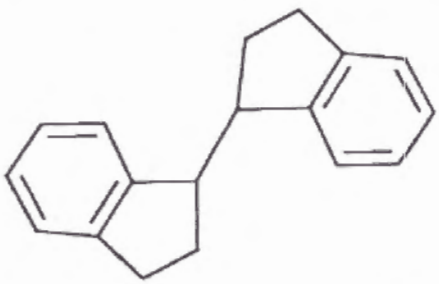

Consider the difference between the so-called stiff stilbene and usual stilbene; both C-C_6H_5 torsions of the former are fixed to be nearly planer by $(CH_2)_2$ alkyl chains, while those of the latter are very loose. Thus the comparison of these two systems is quite useful to extract the effect of the C-C_6H_5 torsions on the photoisomerization of stilbene. Hochstrasser et al. [64] reported that the Kramers theory is well applicable to the photoisomerization rates of the "stiff stilbene" in alkane solutions, unlike those of the normal stilbene. Their result suggests that the odd behavior of stilbene in question is attributed to the C-C_6H_5 torsions. Large amplitude motion along the C-C_6H_5 torsions makes the reaction path multidimensional, though it is not properly involved in the Kramers theory. It is worth noting that the photoisomerization reaction of 1,1'-binaphthalene, which obeys the Kramers theory, is likely to be one-dimensional, because there is no other coordinate relevant to large amplitude motion except for the central torsion. The result of 1,1'-binaphthalene is at least consistent to the hypothesis that multidimensionality of reaction path actually causes a breakdown of the Kramers theory, and moreover it is probably a dominant reason of the odd behavior of stilbene [65].

However, the above idea has not been confirmed any more; we have to point out a matter to support another possibility noted previously, the time-dependent friction. The activated barriers of 1,1'-binaphthalene and the "stiff stilbene" were found to be 1.3kcal/mol and 1.5kcal/mol respectively, while that of stilbene is 3.5kcal/mol. The former two systems obeying the Kramers theory have considerably lower barriers than stilbene. Several experiments imply a tendency that photoisomerization reactions having low barriers are amenable to the Kramers theory. This tendency seems reasonable by considering that a low activation barrier generally reduces the potential

curvature at barrier top (ω_{eq} in Eq. 2.18) so that the deviation of the Kramers theory from the Grote-Hynes one becomes less distinctive, as mentioned in Sec. 2.2.2. However, limited information available at present prevents us from judging which hypothesis, the multidimensionality of reaction path or the time-dependent friction, is more appropriate.

Is it possible to evaluate the time-dependent (frequency-dependent) friction of solvents without performing molecular-dynamics simulation? The answer is unknown, though some attempts have been made. One useful method to evaluate it is a hydrodynamic approach. Although hydrodynamics originally describes macroscopic dynamics of fluids with neglecting their molecularity, empirically it has turned out to be fairly valid to microscopic motions at molecular scale if certain modification is made [66]. In rapid motions at an order of $10^{-13} sec$, even a usual liquid shows viscoelastic behavior so that the assumption of incompressibility breaks down. On the basis of a modified hydrodynamics, Zwanzig and co-workers [67] gave an analytical formula for frequency-dependent friction coefficient exerted on a spherical molecule using the linearized Navier-Stokes equation. In their derivation, Maxwell's viscoelastic relaxation time and velocity of sound were utilized to characterize fluids besides density and viscosity coefficients (both shear and bulk ones). Their theory was further modified by Metiu et al. [68], and the modified vergion has been implemented because of its simplicity. However, their hydrodynamic theory does not incorporate in ultrashort dynamics at a subpicosecond order [67, 68]. Since subpicosecond dynamics is rather crucial to determine the probability of barrier passage, hydrodynamic description of solvation dynamics seems to be doubtful.

Use of solvent viscosity is also doubtful, because it is a rather macroscopic property negecting the molecularity of fluids. Nonetheless, previous studies have often evaluated friction exerted on a solute molecule with viscosity of solvent, based on the Stokes' law. The Stokes' law is derived from the hydrodynamics at law Stokes numbers, which represents a friction coefficient exerted on a spherical particle ζ as

$$\zeta = \begin{cases} 6\pi\eta a & \text{(stick boundary)} \\ 4\pi\eta a & \text{(slip boundary),} \end{cases} \tag{2.39}$$

where η stands for shear viscosity coefficient of solvent, and a is a radius of the particle. The friction coefficient ζ is related to the diffusion coefficient D by Einstein's relation:

$$\zeta = k_B T / D. \tag{2.40}$$

Eq. (2.40) enable us to evaluate ζ by a observed value of D. Note that ζ in Eqs. (2.39)-(2.40) is frequency-independent. In a case of rotational Brownian motion, corresponding formula is given by (Stokes-Einstein-Debye rule)

$$\tau_2 = \frac{V_p}{k_B T}\eta \quad \text{(stick boundary)}, \tag{2.41}$$

where V_p stands for a volume of a solute particle. τ_2 denotes a correlation time of Legendre second-order polynomials refering to solute orientation, which is a usual measure of orientational relaxation. When a solute particle is not spherical or the boundary condition on the surface of the solute is not stick, Eq. (2.41) is multiplied by certain factors [69]. Furthermore, the orientational relaxation time τ_2 and the rotational friction coefficient ζ are connected by a equivalent formula to Eq. (2.40) [70]:

$$\zeta = \frac{6k_BT}{I}\tau_2, \tag{2.42}$$

where I stands for a moment of inertia of a solute. Eqs. (2.41) and (2.42) derive a proportionality between ζ and η in rotational motions in solutions also. However, since the above argument is based on the hydrodynamics, it is also doubtful to apply these equations to the behavior of a single solute molecule. Actually some experiments on rotational relaxation demonstrated that the proportionality of τ_2 and η predicted by Eq. (2.41) breaks down when observing a single molecule in solutions [71, 72, 73]. The deviation becomes conspecious when a solvent molecule is of equal size or larger than a solute one, if a solute is not ionic. In this situation, molecularity of solvent should not at all omitted in considering the behavior of a solute molecule. The deviation at a non-ionic solute exhibits that the Stokes-Einstein-Debye rule usually overestimates τ_2. This means that molecularity of solvent reduces effective friction exerted on the rotational motion of a solute. The effect attributed to solvent molecularity has been described by extending hydrodynamics in various ways, *e.g.* "free volume model" [69], Gierer-Wirtz model that considers a effect of spatial descreteness on intramolecular angular momentum transfer [74], or a model modifying boundary condition on the surface of a solute (stick $\sim$ slip) [75]. All of the above-mentioned models reproduces the deviation from the Stokes-Einstein-Debye rule with at least semiquantitative accuracy. Hochstrasser and co-workers [76, 77] attributed the odd behavior of stilbene to this deviation. Their idea is based on the fact that microscopic friction coefficient ζ utilized in the Kramers theory or other is not proportional to solvent viscosity η. They estimated the friction coefficient ζ not using solvent viscosity η but by observed values of rotational relaxation time τ_2 on the basis of Eq. (2.42), since the friction exerted on stilbene during the photoisomerization is thought to be essentially similar to rotational friction. Their attempt succeeded in explaining the odd behavior of stilbene within the framework of the Kramers theory. They insisted that the Kramers theory is valid to reproduce even the odd behavior of stilbene if the microscopic friction ζ is accurately estimated.

In this section we discussed three hypotheses to explain the strange behavior of stilbene: time-dependent friction, multidimensionality of reaction path, and artifact due to the use of macroscopic viscosity. These argument

is of course one example not resolved yet in liquid-phase reactions. Even in such a seemingly simple reaction as the photoisomerization of stilbene, many complicated factors are involved. In particular, potential energy surfaces (or free energy surfaces) and microscopic friction due to solvation are crucial to examine or apply the basic theories including the Kramers one and Grote-Hynes one. Although these information is insufficient at present, future progress at experimental technique and computational ability will enable us to explore futher insight into these factors. Such progress does not only increase our knowledge about realistic systems, but also urge us to reexamine these fundamental theories for chemical reactions in solutions.

Bibliography

[1] G. R. Fleming, Ann. Rev. Phys. Chem. **37**, 81 (1986).

[2] M. Maroncelli and G. R. Fleming, J. Chem. Phys. **89**, 5044 (1988).

[3] M. Maroncelli, J. Chem. Phys. **94**, 2084 (1991), and references therein.

[4] for example, J. T. Hynes, "*Theory of Chemical Reaction Dynamics*", edited by M. Baer (CRC, Boca Raton, Fl, 1985), Vol. 4, p171.

[5] P. Pechukas, "*Dynamics of Molecular Collisions*", Part B, edited by W. H. Miller (Plenum, New York, 1976), Chap. 6.

[6] P. Pechukas, Ann. Rev. Phys. Chem. **32**, 159 (1981).

[7] D. G. Truhler, W. L. Hase, and J. T. Hynes, J. Phys. Chem. **87**, 2664 (1983).

[8] R. I. Cukier, J. Stat. Phys. **42**, 69 (1986).

[9] G. R. Fleming and P. G. Wolynes, Phys. Today **43**(5), 36 (1990).

[10] H. A. Kramers, Physica, **7**, 284 (1940).

[11] A. Nitzan, Adv. Chem. Phys. **70**, 489 (1988).

[12] "*Rate Processes in Dissipative Systems: 50 years after Kramers*", Ber. Bunsenges. Phys. Chem. **95**, No. 3 (1991).

[13] P. Hanggi, J. Stat. Phys. **42**, 105 (1986).

[14] R. Kubo, M. Toda, N. Hashizume, N. Saito, "*Toukei-butsurigaku (Statistical Physics)*", (Iwanami, Tokyo, 1972) (in Japanese).

[15] R. F. Grote and J. T. Hynes, J. Chem. Phys. **73**, 2715 (1980).

[16] S. A. Adelman and C. L. Brooks, III, J. Phys. Chem. **86**, 1511 (1982).

[17] J. P. Bergsma, B. J. Gertner, K. R. Wilson, and J. T. Hynes, J. Chem. Phys. **86**, 1356 (1987).

[18] B. J. Gertner, J. P. Bergsma, K. R. Wilson, S. Lee, and J. T. Hynes, J. Chem. Phys. **86**, 1377 (1987).

[19] B. J. Gertner, K. R. Wilson, and J. T. Hynes, J. Chem. Phys. **90**, 3537 (1989).

[20] J. Chandrasekhar, S. F. Smith, and W. L. Jorgensen, J. Am. Chem. Soc. **106**, 3049 (1984).

[21] J. Chandrasekhar, S. F. Smith, and W. L. Jorgensen, J. Am. Chem. Soc. **107**, 154 (1985).

[22] E. Pollak, J. Chem. Phys. **85**, 865 (1986).

[23] M. Buchner, B. N. Ladanyi, and R. M. Stratt, J. Chem. Phys. **97**, 8522 (1992).

[24] K. Fukui, J. Phys. Chem. **74**, 4161 (1970).

[25] W. H. Miller, N. C. Handy, and J. E. Adams, J. Chem. Phys. **72**, 99 (1980).

[26] D. G. Truhlar, A. D. Isaacson, and B. C. Garrett, "*Theory of Chemical Reaction Dynamics*", edited by M. Baer (CRC, Boca Raton, Fl, 1985), Vol. 4, p65.

[27] G. K. Schenter, R. P. McRae, and B. C. Garrett, J. Chem. Phys. **97**, 9116 (1992).

[28] C. A. Parr and D. G. Truhlar, J. Phys. Chem. **75**, 1844 (1971).

[29] R. F. Grote and J. T. Hynes, J. Chem. Phys. **74**, 4465 (1981).

[30] H. Sumi and R. A. Marcus, J. Chem. Phys. **84**, 4894 (1986).

[31] W. Nadler and R. A. Marcus, J. Chem. Phys. **86**, 3906 (1987).

[32] R. A. Marcus, Ann. Rev. Phys. Chem. **15**, 155 (1964).

[33] P. F. Barbara, W. Jarzeba, Acc. Chem. Res. **21**, 195 (1988).

[34] E. M. Kosower and D. Huppert, Ann. Rev. Phys. Chem. **37**, 127 (1986).

[35] D. F. Calef and P. G. Wolynes, J. Phys. Chem. **87**, 3387 (1983).

[36] D. F. Calef and P. G. Wolynes, J. Chem. Phys. **78**, 470 (1983).

[37] G. van der Zwan and J. T. Hynes, J. Phys. Chem. **89**, 4181 (1985).

[38] L. D. Zusman, Chem. Phys. **49**, 295 (1980).

[39] S. -G. Su, and J. D. Simon, J. Chem. Phys. **89**, 908 (1988).

[40] S. Kato and Y. Amatatsu, J. Chem. Phys. **92**, 7241 (1990).

[41] J. Schroeder and J. Troe, Ann. Rev. Phys. Chem. **38**, 163 (1987).

[42] G. R. Fleming, S. H. Courtney, and M. W. Balk, J. Stat. Phys. **42**, 83 (1986).

[43] P. G. Wolynes, Ann. Rev. Phys. Chem. **31**, 345 (1980).

[44] D. L. Hasha, T. Eguchi, and J. Jonas, J. Chem. Phys. **75**, 1571 (1981).

[45] P. M. Felker and A. H. Zewail, J. Phys. Chem. **89**, 5402 (1985).

[46] J. Schroeder and J. Troe, J. Phys. Chem. **90**, 4215 (1986).

[47] G. Orlandi, P. Palmiere, and G. Poggi, J. Am. Chem. Soc. **101**, 3492 (1979).

[48] P. Tavan and K. Schulten, Chem. Phys. Lett. **56**, 200 (1978).

[49] J. Troe and K. -M. Weitzel, J. Chem. Phys. **88**, 7030 (1988).

[50] R. J. Cave and E. R. Davidson, J. Phys. Chem. **91**, 4481 (1987), *ibid.* **92**, 2173 (1988).

[51] G. Orlandi and W. Siebrand, Chem. Phys. Lett. **30**, 352 (1975).

[52] H. Frauenfelder and P. G. Wolynes, Science, **229**, 337 (1985).

[53] J. N. Onuchic and P. G. Wolynes, J. Phys. Chem. **92**, 6495 (1988).

[54] A. Hoekstra, P. Meertens, and A. Vos, Acta Crystallogr. Sect. **B 31**, 2813 (1975).

[55] (a) R. W. Pastor, R. M. Venable, and M. Karplus, J. Chem. Phys. **89**, 1112 (1988). (b) R. W. Pastor, R. M. Venable, M. Karplus, and A. Szabo, J. Chem. Phys. **89**, 1128 (1988).

[56] K. Iwata and H. Hamaguchi, Chem. Phys. Lett. **196**, 462 (1992).

[57] G. L. Bendazzoli, G. Orlandi, P. Palmieri, and G. Poggi, J. Am. Chem. Soc. **100**, 392 (1978).

[58] G. Maneke, J. Schroeder, J. Troe, and F. Voß, Ber. Bunsenges. Phys. Chem. **89**, 896 (1983).

[59] J. Schroeder and J. Troe, Chem. Phys. Lett. **116**, 453 (1985).

[60] (a) M. Fixman and J. Kovac, J. Chem. Phys. **61**, 4939, 4950 (1974). (b) M. Fixman, J. Chem. Phys. **69**, 1527, 1538 (1978). (c) M. Fixman, Faraday Discuss. Chem. Soc. **83**, 199 (1987).

[61] (a) G. T. Evans, Mol. Phys. **36**, 1199 (1978). (b) G. T. Evans, J. Chem. Phys. **72**, 3849 (1980). (c) G. T. Evans, J. Chem. Phys. **74**, 4621 (1981). (d) G. T. Evans and D. C. Knauss, J. Chem. Phys. bf 75, 4647 (1981).

[62] B. Bagchi and D. W. Oxtoby, J. Chem. Phys. **78**, 2735 (1983).

[63] D. P. Millar and K. B. Eisenthal, J. Chem. Phys. **83**, 5078 (1985).

[64] G. Rothenberger, D. K. Negus, and R. M. Hochstrasser, J. Chem. Phys. **79**, 5360 (1983).

[65] N. S. Park and D. H. Waldeck, J. Chem. Phys. **91**, 943 (1989).

[66] J. P. Hansen and L. R. McDonald, "*Theory of Simple Liquids*", 2nd ed., (Academic Press, Florida, 1986), Chap. 8.

[67] R. Zwanzig and M. Bixon, Phys. Rev. **A 2**, 2005 (1970).

[68] H. Metiu, D. W. Oxtoby, and K. F. Freed, Phys. Rev. **A 15**, 361 (1977).

[69] J. L. Dote, D. Kivelson, and R. N. Schwartz, J. Phys. Chem. **85**, 2169 (1981).

[70] P. S. Habbard, Phys. Rev. **131**, 1155 (1963).

[71] T. J. Chuang and K. B. Eisenthal, Chem. Phys. Lett. **11**, 368 (1971).

[72] S. A. Rice and G. A. Kenney-Wallace, Chem. Phys. **47**, 161 (1980).

[73] L. A. Philips, S. P. Webb, and J. H. Clark, J. Chem. Phys. **83**, 5810 (1985).

[74] A. Gierer and K. Wirtz, Z. Naturforsch. **A, 8**, 532 (1953).

[75] M. Ahn, Chem. Phys. Lett. **52**, 135 (1977).

[76] M. Lee, A. J. Bain, P. J. McCarthy, C. H. Han, J. N. Hasltine, A. B. Smith III, and R. M. Hochstrasser, J. Chem. Phys. **85**, 4341 (1986).

[77] M. Lee, N. N. Haseltine, A. B. Smith III, and R. M. Hochstrasser, J. Am. Chem. Soc. **111**, 5044 (1989).

Chapter 3

The Potential Energy Surfaces and the Spin-Orbit Coupling for H_2O_2 Photodissociation : The Importance of the Intersystem Crossing for Λ -type Polarization of Product OH.

In order to elucidate the mechanism of H_2O_2 photodissociation, especially the origin of the Λ-type preference of product OH, we calculated the potential energy surfaces containing the singlet and triplet states with MRCI method and the spin-orbit coupling on the basis of the Breit-Pauli Hamiltonian. We discussed the results with considering the electronic character of the parent H_2O_2 and its correlation to the Λ-type components of the fragment OH. Consequently, it is proposed that the intersystem crossing from $\tilde{A}^1A$ to ^3B exerts the branching ratio of the Λ-type components. The relation of the Λ-component ratio with the product rotation J is consistent with the recent experimental findings of vector correlation.

3.1 Introduction

In the recent development of the photodissociation dynamics, hydrogen peroxide has been extensively studied as a benchmark molecule [1, 2, 3, 4, 5, 6, 7, 8, 9, 10]. In particular, the measurements of vector correlation using a polarized laser [2, 3, 4, 5, 6, 7, 8, 9, 10] enable us to obtain much information about the dynamics of H_2O_2 photodissociation. Stimulated by these

experiments, theoretical studies have been also progressed to understand the photodissociation dynamics [21, 12]. However, some of the experimental findings are not yet explained theoretically. One of the most important topics is the cause of the Λ-type ratio of Λ-type components deviates from unity and that the A''-component of Λ-type doublet becomes dominant with increasing J in case of 248nm or 266nm excitation [2, 8].

Recently several theoretical studies have been advanced to consider the Λ-type doubling of products in the photodissociation and collision processes to obtain a deeper insight into the dynamics [13, 14, 15, 16, 17]. The origin of the Λ-type preference has been also discussed in relation to the electronic properties of dissociating molecules [17]. In the photodissociation of H_2O_2, the $\tilde{A}^1A(n\sigma^*)$ or $\tilde{B}^1B(n\sigma^*)$ state is prepared by the light absorption. However, it seems hard to interpret the experimentally observed preference of Λ-type components in the product OH solely by considering the dynamics on these potential energy surfaces. It is therefore worthwhile to perform detailed studies of the potential energy surfaces and the nonadiabatic electronic transition between these surfaces.

In the present work, we carried out the configuration interaction (CI) calculations for the potential energy surfaces of eight states leading to the product $OH(\tilde{X}^2\Pi)$+$OH(\tilde{X}^2\Pi)$. The matrix elements of spin-orbit coupling between the singlet and triplet states were also calculated on the basis of the full Breit-Pauli Hamiltonian. Although some theoretical calculations have been performed for the potential energy surfaces of H_2O_2 [18, 19, 20], calculation including the triplet surfaces and the spin-orbit coupling is, to our knowledge, virtually nonexistent. The purpose of the present work is to examine the importance of nonadiabatic transition in the photodissociation process on the basis of potential energy characteristics and give a qualitative discussion on the origin of Λ-type preference. The potential energy surfaces and the spin-orbit coupling obtained here will also give important information for the calculation of photodissociation dynamics in a further stage.

3.2 Method of Calculations

3.2.1 Potential Energy Surfaces

Among the electronic states of H_2O_2 there are four singlet states and four triplet states correlated to $OH(\tilde{X}^2\Pi)$+$OH(\tilde{X}^2\Pi)$ in the dissociation limit. We calculated the potential energy surfaces for these states as a function of four coordinates: the O-O distance R, the torsional angle of OH-OH τ and two OOH bending angles, θ_1 and θ_2 (Fig. 3.1(a)). The OH distance was fixed to be $0.967\mathring{A}$. We did not take account of the vibrational excitation of the fragment OH, because the fragment OH was found to show little vibrational excitation in H_2O_2 photodissociation [1, 2]. The distance in the equilibrium

geometry of H_2O_2 is very close to that of isolated OH radical ($r_{OH} = 0.967\mathring{A}$ in H_2O_2 [22], $r_e = 0.970\mathring{A}$ for OH [23]). We mainly focused the potential energy surfaces in C_2 symmetry ($\theta_1 = \theta_2 \equiv \theta$), because C_1 geometry requires more expensive calculations. As described later, the torsional dependence of the potential energy surfaces is more crucial in the photodissociation dynamics than the bending dependence. We think that the characteristics of this dynamics can be understood in terms of C_2 geometry, although more general geometries are neccessary for quantitative calculations of the dynamics. We first performed the complete active space SCF (CASSCF) calculation [24]. For example, the main configuration of the electronic ground state $\tilde{X}^1A$ at the equilibrium geometry is represented by

$$\tilde{X}^1A \quad (1a)^2(1b)^2(2a)^2(2b)^2(3a)^2(3b)^2(4a)^2(5a)^2(4b)^2(5b)^0;$$

the last four MO's are denoted to be σ, n(syn-phase), n(anti-phase), σ^*, respectively (see Fig. 3.1(b)). In order to describe qualitatively all the states correlated to OH($\tilde{X}$)+OH($\tilde{X}$), it is enough to take account of four valence MO's mentioned above. We therefore regarded these four orbitals as the active orbitals in constructing the CASSCF wave functions and obtained 6-in-4 CASSCF wave fuctions for the average state of four singlet states. We used the Huzinaga-Dunning-Raffenetti (9s5p1d/3s1p)/[3s2p1d/2s1p] basis set [25]. The exponents of polarization functions were taken to be 0.85 for the d function of O atom and 1.0 for the p function of H atom, respectively.

We next carried out the multi-reference single and double CI (MRCI) calculations [26]. The natural orbitals obtained from the CASSCF calculations were used as the one-particle basis functions. As the reference configurations of MRCI, we took all the configuration state functions (CSF's) generated within the space of six orbitals: the four valence orbitals mentioned above and two inner orbitals. The perturbation selection procedure with the threshold value of 5μ hartree was applied to reduce the number of configurations in the CI wave functions and the energy extrapolation was performed. The number of CSF's was thus reduced to be about 30,000. We further employed the multi-reference Davidson's correction to obtain the full CI energy estimates.

3.2.2 Spin-Orbit Coupling

The spin-orbit coupling between the singlet and triplet states were calculated using the full microscopic Breit-Pauli Hamiltonian [27];

$$\begin{aligned} H_{so} &= \frac{e^2\hbar}{2m^2c^2}\{\sum_k \sum_\alpha \frac{z_\alpha}{r_{\alpha k}^3}[(\vec{r}_k - \vec{r}_\alpha) \times \vec{p}_k)] \cdot \vec{s}(k) - \\ &\quad \sum_k \sum_{j(\neq k)} \frac{1}{r_{kj}^3}[(\vec{r}_k - \vec{r}_j) \times \vec{p}_k] \cdot [\vec{s}(k) + 2\vec{s}(j)]\}. \end{aligned} \tag{3.1}$$

The first and the second terms refer to spin-same-orbit and spin-other-orbit interaction respectively. The algorithm to calculate the Breit-Pauli spin-orbit integrals for Gaussian-type basis functions was developed by H.F.King et al [28]. We modified the CI wave functions obtained by MRCI for the use to calculate the spin-orbit coupling. We selected only the reference components out of the original CI wave functions in order to reduce the CI dimension and then renormalized them. The approximated wave functions consist of all symmetry-adapted CSF's within the active space of the six orbitals, and it has been confirmed that they have more than 90% overlap to the original CI wave functions. Using the spin-orbit integrals and the truncated CI wave functions, we calculated the spin-orbit coupling with varying the internal coordinates in the same way as the case of the potential energy surfaces.

3.3 Results and Discussion

Before proceeding the calculations we will give a brief discussion on the correlation between the electronic character of the precursor H_2O_2 and the Λ-type components of the fragment OH and define the conditions for the electronic structures of H_2O_2 that cause the Λ-type polarization. It is well known that the branching of the Λ-doublet is determined by neither the energy splitting nor the total parity, but by the direction of the unpaired electron orbitals relative to the plane of rotation of the fragments [14]. $OH(\tilde{X}^2\Pi)$ has a rather small $\lambda(=-7.4)$, i.e. the ratio of the spin-orbit constant A to the rotational constant B ($\lambda = A/B = -139.2\text{cm}^{-1}/18.9\text{cm}^{-1}$) [23]. This means that the eigenstates approach Hund's case (b) even in low J [29]. Thus since the unpaired electron orbitals of the eigenstates tend to have large asymmetry around the molecular axis, the eigenstates of Λ-type doubling can be classified by the orbital orientation of the molecule. In the photodissociation of H_2O_2, recent experiments of $v-J$ correlation gave detailed information about the plane of rotation of the fragment OH [4, 7]. According to the results, the rotation vector J of OH tends to be parallel to the relative velocity v, which indicates that the O-O axis is nearly perpendicular to the plane of rotation. In view of these circumstances, it is thought that among the valence orbitals of the parent H_2O_2 the σ orbitals correlate to the unpaired electron orbitals of A''-component (out-of-plane) and the n orbitals correlate to those of A'-component (in-plane) with the C_2 geometry, provided that the orbital orientation does not so significantly change during the photodissociation process. Hence, one can imagine that a state consisting mainly of $\sigma\sigma^*$ configuration causes the preference of A''-component in the dissociation limit, and that a state consisting mainly of $n\sigma^*$ shows no preference of Λ-type components.

The potential energy curves along the O-O distance R and the torsional angle τ are given in Fig. 3.2. All the potential curves except the ground state

$\tilde{X}$ are strongly repulsive with respect to R. The energies at the equilibrium geometry as well as the dissociation limit are summarized in Table 3.6. The dissociation energy for the $\tilde{X}$ state was calculated to be 2.05eV, which is in good agreement with the experimental value, $17300 \pm 800 cm^{-1} (= 2.14 \pm 0.10 eV)$ [30]. It is apparent from Fig. 3.2(b) that the potentials of both $\tilde{A}^1A$ and $\tilde{B}^1B$, the states yielded after light absorption, have torsional dependence much more prominent than that of the $\tilde{X}$ state; this causes strong torsional torque. Figure 3.3 represents the potential energy surfaces of the ground state $\tilde{X}$ as a function of R and τ. The surface near the equilibrum configuration is very flat, and one can see that the Franck-Condon region is fairly wide, considering the zero-point vibration and the thermal distribution. The vertical excitation energies at the equilibrium geometry were calculated to be 5.97eV for the $\tilde{X} - \tilde{A}$ transition and 7.51eV for the $\tilde{X} - \tilde{B}$ transition, respectively. Since the potential energy surface of the excited state is strongly repulsive, it is supposed that the absorption band is considerably wide until longer wavelength. The branching ratio $P(\tilde{A})/P(\tilde{B})$ after light absorption was estimated $P(\tilde{A})/P(\tilde{B}) \cong 0.62/0.38$, according to the experiments of 193nm (6.42eV) excitation [7]. However, if the excitation light has a longer wavelength like 248nm (5.00eV) or 266nm (4.66eV), such a photon energy is insufficient to the vertical excitation so that the ratio $P(\tilde{A})/P(\tilde{B})$ might become larger. This is confirmed by the dependence of translational anisotropy β on excitation wavelength [3, 4, 5, 9]. Thus we will focus on the photodissociation from the $\tilde{A}^1A$ surface below.

According to Fig. 3.2(b), the surface of $\tilde{A}^1A$ crosses over that of the lowest ^3B. We also show the potential energy curves along the bending angle θ in Fig. 3.4. From these figures one can see that the $\tilde{A}^1A$ state only crosses over the $\tilde{B}^1B$ and the lowest ^3B states except near the linear configuration. In the actual dynamics of photodissociation such linear geometries are not important unless both fragments go far apart. Then we show Fig. 3.5 and Fig. 3.6 referring to the potential energy map of $\tilde{A}^1A$ and ^3B as a function of $R - \tau$ and $R - \theta$, respectively. One can also find from the figures that the $\tilde{A}^1A - ^3B$ seam is located to cross the Franck-Condon region. The deviation of the Franck-Condon region from the minimum energy configuration of the excited states $\tilde{A}^1A$ and ^3B is considerably less for the bending angle than for the torsional angle. This supports the idea that the fragment rotation tends to be excited along the torsional direction more than the bending direction.

In order to gain deeper insight into the photodissociation, we now discuss the electronic structure of the excited states including $\tilde{A}^1A$ and the lowest ^3B. The $\tilde{A}^1A$ and $\tilde{B}^1B$ states, generated by the light absorption, are represented by $n\sigma^*$ configuration(s) over almost all the nuclear geometries. The lowest ^3A state also keeps strong $n\sigma^*$ character over the potential energy surface. When observing the four states with strong $n\sigma^*$ character in Fig. 3.2(b), we notice that the potential energies of $\tilde{A}^1A$ and ^3A states

decrease and those of $\tilde{B}^1B$ and ^3B states increase as the torsional angle τ raises from 0° to 180° and that the states of each pair indicate very similar τ-dependence. This behavior comes from the τ-dependence of the non-bonding orbital energies. The opposite behavior of the two pairs is due to the difference between the anti-phase n orbital and the syn-phase one.

However, the lowest ^3B state has the strong $n\sigma^*$ character only in a finite region of the potential energy surface. The lowest ^3B state is composed of two main electronic configurations, $n\sigma^*$ and $\sigma\sigma^*$, and they alternate with each other through an avoided crossing. Figure 3.7 represents the electronic character of the lowest ^3B state by showing contribution of $n\sigma^*$ and $\sigma\sigma^*$ CSF's accounting for the CI wave functions. With regard to the τ-dependence of it, it is apparent that the lowest ^3B state tends to show the $n\sigma^*$ character on the side of $\tau = 0°$ and $\sigma\sigma^*$ on the side of $\tau = 180°$. This is because the $n\sigma^*$ configuration of ^3B is more stable on the side of $\tau = 0°$. Moreover, Fig. 3.7 shows that the avoided crossing region moves to the side of $\tau = 0°$ with increasing O-O distance. And at the region of $R > 1.6\mathring{A}$, the lowest ^3B state has strong $\sigma\sigma^*$ character in the crossing region with $\tilde{A}^1A$ (in the vicinity of $\tau = 120°$). Provided that the ^3B state has $\sigma\sigma^*$ character, the spin-orbit coupling between the ^3B and $\tilde{A}^1A$ $n\sigma^*$ is expected to be rather large, by considering the orientations of n and σ orbitals [31].

We display the spin-orbit coupling elements between the $\tilde{A}^1A$ and ^3B states in Fig. 3.8 as a function of R and τ. The contributions of one- and two-electron components at $R = 1.6\mathring{A}$ and the dissociation limit are also tabulated in Table 3.6, where these two terms are opposite in sign and the magnitude of two-electron term is about 1/3 of the one-electron part. These trends are observed at all geometries considered. The spin-orbit coupling at the dissociation limit was calculated to be 96.764cm^{-1} between $\tilde{A}^1An\sigma^*$ and $^3B\sigma\sigma^*$. Thus the fine-structure constant of OH($\tilde{X}^2\Pi$) was derived: $|A| = \sqrt{2}\cdot 96.764cm^{-1} = 136.84cm^{-1}$. This is in good agreement with the experimental value; $A = -139.21cm^{-1}$. [23]. As seen in Fig. 3.8, the spin-orbit coupling increases with the torsional angle. This behavior is rationalized by the ratio of the $\sigma\sigma^*$ configuration accounting for the lowest ^3B state (see Fig. 3.7). In the region of the small O-O distance, the τ-dependence shows a rather different behavior, attributed to mixing an inner-excited configuration $(3b)^1(5b)^1$ into the $\tilde{A}^1A$ state. The result indicates that the spin-orbit coupling on the $\tilde{A}^1A - ^3B$ seam is distributed over about 50~90 cm^{-1}. Table 3.6 represents the spin-orbit coupling elements along the seam of Fig. 3.6 referring to the potential energy surfaces as a function of R and θ.

On the basis of the above discussion, we turn to consider the intersystem crossing from $\tilde{A}^1A$ to ^3B. Figure 3.4 shows the potential energy surfaces along the bending angle θ, where R and τ are fixed to be $1.6\mathring{A}$ and 120.2°. The region near the bottom of $\tilde{X}$ and/or $\tilde{A}$ in this figure ($\theta \approx 90°$) corresponds to the tail of the Franck-Condon region. According to the Fig. 3.4, the ^3B curve

crosses over $\tilde{A}^1A$ in the vicinity of the bottom of $\tilde{A}^1A$ curve. Furthermore, the $\tilde{A}^1A - {}^3B$ seam is given in Fig. 3.6 as a function of R and θ. One can see from this figure that the bending angle does not vary much ($\theta \approx 100°$) along the crossing seam with changing the O-O distance and that the crossing seam is located near the bottom of the $\tilde{A}^1A$ surface for all the O-O distance considered here.

We estimate the transition probability on the basis of the Landau-Zener model:

$$p = 1 - \exp(-\frac{2\pi V^2}{\hbar v \Delta F}); \tag{3.2}$$

where p indicates the probability of the intersystem crossing; V, the spin-orbit coupling element on the crossing seam; v, the velocity normal to the crossing seam; and ΔF, the gradient difference of the two diabatic potentials, respctively. As for v, the initial velocity distribution is hard to be determined when the excitation wavelength is rather longer than that of $\tilde{X} - \tilde{A}$ vertical excitation ($\approx$ 208nm) like 266nm or 248nm. Thus the velocity v on the crossing seam was estimated approximately as the relative angular velocity of the two fragments; $v \simeq 2\omega$, where ω is the angular velocity of the product free rotor at $J = 6$, the mode of the rotational distribution in 266nm excitation [8], i.e.,

$$\omega = \frac{2B}{\hbar} J \approx 4.3 \times 10^{13} rad/sec. \tag{3.3}$$

Therefore

$$v \simeq 2\omega \approx 8.6 \times 10^{13} rad/sec. \tag{3.4}$$

The gradient difference at the crossing seam ΔF was represented with R-dependence in the following:

$$\Delta F = Ae^{-\alpha R}; \tag{3.5}$$

where $A = 300 eV/rad$, and $\alpha = 3.1 \mathring{A}^{-1}$. Using the above values and spin-orbit coupling elements, the transition probabilities were estimated with varying R:

$$p = \begin{cases} 0.0016 & \text{for } R = 1.6\mathring{A} \\ 0.019 & 2.0\mathring{A} \\ 0.12 & 2.5\mathring{A} \\ 0.44 & 3.0\mathring{A}. \end{cases} \tag{3.6}$$

One can easily see that the transition probabilities increase with R. The above results indicate very small probabilities in the small-R region, but the actual values must be greater than the above estimations, because the angular velocities v on the seam of the small-R region are not so excited as that of the final fragments. We then estimate the angular velocity just after the photoabsorption from the initial vibrational energy at the ground state $\tilde{X}$. The initial vibrational energy correlating to the product rotation was

estimated to be $85cm^{-1}$ for zero-point and thermally excited torsion [2]. This corresponds to the classical angular velocity: $v_\tau \approx 1.5 \times 10^{13} rad/sec$ along the torsional mode. The actual transition probability in small-R region must not be much greater than the above estimation using the angular velocity of the free rotors.

The dominant factor that governs the R-dependence of the transition probability is the gradient difference of the potential surfaces ΔF. As the potential energy surfaces become flat along the internal angles with increasing R, the transition between $\tilde{A}^1A$ and ^3B becomes easy to occur. We think that the exit-channel interaction derived from the potential crossing of $\tilde{A}^1A$ and ^3B plays a central role for the intersystem crossing of the system. However, it is noted that the potential crossing between the two states, $\tilde{A}^1A$ and ^3B, can be treated in the above manner as far as a certain O-O separation. When the O-O distance R increases, the eight electronic states correlated to $OH(\tilde{X}^2\Pi)+OH(\tilde{X}^2\Pi)$ degenerate so that their energy splittings come to be comparable to the spin-rotation and spin-orbit interaction of the fragment $OH(\tilde{X}^2\Pi)$. In that region these interactions become important and mix the eight states to form the final states that consist of the fragment eigenstates detectable by usual experiments. Such a state mixing to form the final eigenstates requires very large separation ($R \geq 3.5\AA$); the $\tilde{A}^1A - ^3B$ crossing affects the Λ-type branching until that separation. In order to ascertain whether the trajectories cross over the seam on the exit channel before dissociating, rough classical trajectory calculations were performed on the $R - \tau$ space, where other internal coordinates are fixed to be the equilibrium values. The initial species were prepared on the $\tilde{A}^1A$ potential in the Franck-Condon region ($R = 1.4 \sim 1.6\AA$ and $\tau = 110° \sim 130°$ with the kinetic energy $E_k = 0 \sim 500cm^{-1}$) and the trajectories after that were pursued. In observing them, the initial species on $\tilde{A}^1A$ in the Franck-Condon region move toward the side of $\tau = 180°$ so that the species prepared on the $\tau = 0°$ side of the $\tilde{A}^1A - ^3B$ seam cross over the seam immediately after the light absorption. And it was confirmed that most trajectories cross over the seam on the opposite side ($\tau \approx 240°$) once before dissociating. Among the two kind of the crossings, the later observed near the exit channel is dominant for the intersystem crossing to affect the photodissociation dynamics. However, it is difficult to estimate the rate of the intersystem crossing quantitatively, because some quantum effects might influence the dynamics. For example, we cannot neglect the tunnelling effect with regard to the nonadiabatic transition, since the moment of inertia along the torsional or bending angle is very small. From the figures of the potential energy surfaces shown above (Fig.'s 3.2(b),3.4,3.5,3.6), one can find that the excited $\tilde{A}^1A$ and ^3B states are nearly bound with discrete levels along the torsional or bending angle. Thus the condition of energy matching and resonance might have influence on the transition. As mentioned previously, when the excitation wavelength

is rather longer than that of the $\tilde{X} - \tilde{A}$ vertical excitation (≈208nm) like 266nm or 248nm, such a case is inappropriate to be treated classically. In order to confirm the result of this work quantitatively, we must perform quantum mechanical calculations of the dynamics using the potential energy surfaces and the spin-orbit coupling obtained in this work.

Considering that the intersystem crossing from $\tilde{A}^1A$ to ^3B has influence on the photodissociation dynamics, one can explain the propensity of Λ-type components as follows. As discussed above, the $\sigma\sigma^*$ configuration of the ^3B is correlated to the dissociated state with two unpaired electron orbitals both of which are pointed to the direction of the O-O axis in high J limit. This causes strong preference to A''-components. In the experimental results, the revised degree of electron alignment (DEA) [14]

$$DEA = \frac{\Pi(A'') - \Pi(A')}{\Pi(A'') + \Pi(A')}, \tag{3.7}$$

which indicates the deviation from unity of the branching ratio of the Λ- type doubling, is about $0.4 \sim 0.5$ for high J ($J \geq 6$) products [8]. $DEA \sim 0.5$ means that the $\tilde{A}^1A$ state and the lowest ^3B state are comparably generated, considering that the $\tilde{A}^1An\sigma^*$ state leads to the products with the branching ratio of $\Pi(A') : \Pi(A'') = 1 : 1$ and the $\sigma\sigma^*$ configuration of the lowest ^3B state leads with the ratio of $\Pi(A') : \Pi(A'') = 0 : 2$ in high J limit. This large probability of the intersystem crossing can be understood in terms of the $\tilde{A}^1A - ^3B$ interaction near the exit channel, as described previously. It is noted that the J dependence of the Λ-doublet ratio is affected by the transition from Hund's case (a) to (b). In low J case, the fragment OH is described by case (a) and has little anisotropy of the unpaired electron orbital along the molecular axis. This is consistent with the experimental findings that high J species tend to show strong propensity for the A''-component, while low J species show little propensity. The correlation of the Λ-doublet branching ratio to the product J is also consistent with the experimental results of $v - J$ correlation, reporting that in low J species $\beta_0^0(22) \approx 0$, which indicates little $v - J$ correlation, but in high J case $\beta_0^0(22) > 0$, the distinct tendency of $v \| J$ [7, 8]. It is worth noting that in low J of D_2O_2 photodissociation $\beta_0^0(22) < 0$, which indicates $v \perp J$, and A'-component is dominant [8]. The $v - J$ correlation $\beta_0^0(22)$ and the dominant component of Λ-type doubling are reversed with increasing J in D_2O_2.

The above discussion about the correlation between the electronic character of the parent H_2O_2 and the Λ-type components of the fragment OH has a basic assumption that the direction of the valence orbitals in the parent H_2O_2 is conserved during the photodissociation process. Therefore we must examine the assumption, by considering the other final state interactions. One possible factor to break the correlation is spin-orbit coupling that rotates the orbital direction. We display in Fig. 3.9 the spin-orbit coupling

between $\tilde{A}^1A$ and all the nearly degenerate triplet states at large O-O distance $R = 2.5\mathring{A}$, where the energy splittings of these states are within 0.5eV. The second excited ^3B state as well as the lowest ^3B state has a large spin-orbit coupling with $\tilde{A}^1A$. The second excited ^3B state is characterized by the excitation of two electrons from the two different n orbitals to the σ^*, which also causes the Λ-type polarization. However, since the eigenstates of $OH(\tilde{X}^2\Pi)$ approach Hund's case (b) even in fairly low J, the energy splitting of the eigenstates in the dissociation limit is due dominantly to the spin-rotation interaction rather than to the spin-orbit interaction. Thus the state mixing by the spin-orbit coupling is thought to have little influence to break the correlation. Another possible factor is potential crossing near the exit channel besides the $\tilde{A}^1A -^3 B$ crossing. Among the eight states correlated to $OH(\tilde{X}^2\Pi)+OH(\tilde{X}^2\Pi)$ in the dissociation limit, a conspicious crossing of $\sigma\sigma^*$ and $n\sigma^*$ is seen in ^3B states (see Fig. 3.7). As discussed previously, the crossing region moves to the side of $\tau = 0°$ with increasing O-O distance R and the region of $\sigma\sigma^*$ character accounting for the lowest ^3B state expands. Figure 3.7 shows that even when R is as long as $2.5\mathring{A}$, the lowest ^3B has strong $n\sigma^*$ character in the vicinity of $\tau = 0°$ and that the avoided crossing is still observed. This avoided crossing near the exit channel may affect the branching ratio of the Λ-type doubling. The $n\sigma^*$ configuration causes no preference of Λ-type components, according to the previous discussion. Thus the actual dissociation limit from the lowest ^3B state possibly shows less preference than expected from $^3\sigma\sigma^*$ configuration. On the other hand, it is found that the states that correlate preferentially to A'-component, i.e. the states consisting mainly of the configuration(s) with two electron holes at the non-bonding orbitals ($(4a)^2(5a)^0(4b)^2(5b)^2$, $(4a)^2(5a)^2(4b)^0(5b)^2$, or $(4a)^2(5a)^1(4b)^1(5b)^2$) cross over neither $\tilde{A}^1A$, $\tilde{B}^1B$, nor the lowest ^3B. This supports our discussion that the Λ-type prefernce is attributed to the $\sigma\sigma^*$ character of the lowest ^3B state and not else. Ondrey et al. [1] suggested that $nn \rightarrow \sigma^*\sigma^*$ configurations cause the Λ-type propensity, mixing into the excited singlet states at large O-O separations. However, according to our calculations, the weight of the $nn \rightarrow \sigma^*\sigma^*$ configurations accounting for the $\tilde{A}^1A$ state was estimated to be about 5% at $R = 2.5\mathring{A}$ and $\tilde{A}^1A$ state keeps distinct $n\sigma^*$ character. Furthermore, the $nn \rightarrow \sigma^*\sigma^*$ configurations correlate preferentially the A'-component under the condition of $v \parallel J$, which is contrary to the experiments. This possibility seems to be quite small.

3.4 Conclusion

In the photodissociation of H_2O_2, fairly large preference of Λ-type components is observed in the product OH, although the $\tilde{A}^1A(n\sigma^*)$ or $\tilde{B}^1B(n\sigma^*)$

states of H_2O_2 is yielded by light absorption. In order to elucidate the origin we considered the electronic structure of the excited states, calculating the potential energy surfaces containing of singlet and triplet states and the spin-orbit coupling elements between them. The potential energy surfaces were obtained using MRCI method and the spin-orbit coupling was calculated on the basis of the full microscopic Breit-Pauli Hamiltonian. It is found that the $\tilde{A}^1A$ state crosses over the lowest ^3B state. The ^3B state has strong $\sigma\sigma^*$ character on the $\tilde{A}^1A - ^3B$ seam when the O-O distance $R > 1.6\mathring{A}$, where the spin-orbit coupling between $\tilde{A}^1A$ and ^3B has rather large value of $50\sim90\text{cm}^{-1}$. Using the potential energy surfaces and the spin-orbit coupling elements, we estimated the probability of the $\tilde{A}^1A - ^3B$ intersystem crossing in terms of the Landau-Zener model. The transition probability is fairly large when the trajectories cross over the $\tilde{A}^1A - ^3B$ seam near the exit channel. It was also confirmed that most of the trajectories cross over the seam near the exit channel before dissociating by rough classical trajectory calculations.

Considering that the intersystem crossing from $\tilde{A}^1A$ to ^3B affects the photodissociation dynamics appreciably, one can explain the preference of Λ-type components and its correlation to the product rotation. The product OH dissociated from the lowest ^3B is thought to show the preference of Λ-type components, because the ^3B state has strong $\sigma\sigma^*$ character, which correlates to the fragments with unpaired electron orbitals pointing toward the O-O axis in high J. Moreover, the correlation of the ratio $P(A'')/P(A')$ and the product rotation J is consistent with the experimental finding about $v - J$ correlation that in low J $\beta_0^0(22)\approx0$, which indicates little $v - J$ correlation, but that in high J $\beta_0^0(22) > 0$, the distinct tendency of $v \parallel J$.

Now we are planning to define the potential energy surfaces on the general configuration by removing the restriction of C_2 symmetry and to perform the calculation of quantum mechanical dynamics.

3.5 Acknowlegment

We would like to thank Professor Morokuma for valuable comments on this topic. We also thank Dr. Fujimura for stimulating discussion. Numerical calculation was performed at IMS Computer Center and Data Processing Center of Kyoto University. This work was supported by the Grant in Aid for Scientific Research from the Ministry of Education.

3.6 Figures and Tables

Figure 3.1: The schematic pictures of the geometry of (a)H_2O_2 molecule and (b)four valence orbitals of H_2O_2. See the text.

Figure 3.2: Potential energy curves of H_2O_2. (a)The dependence of the O-O distance R. The OH-OH torsional angle $\tau = 120.2°$ and the bending angle $\theta_1 = \theta_2 = 99.3°$ fixed. (b)The dependence of the torsional angle τ. $R = 1.463\mathring{A}$, and $\theta_1 = \theta_2 = 99.3°$ fixed. The energy standard is defined at the dissociation limit.

Figure 3.3: Potential energy surface of the ground electronic state $\tilde{X}$ as a function of both the O-O distance R and the torsional angle τ. The bending angle θ is fixed to 99.3°. The contour spacings of the dotted lines and of the solid lines are 0.2eV and 1.0eV, respectively.

Figure 3.4: Potential energy curves along the bending angle. $\theta_1 = \theta_2$, $R = 1.6\mathring{A}$ and $\tau = 120.2°$ fixed.

Figure 3.5: Potential energy surfaces of the $\tilde{A}^1A$ state and the lowest ^3B state as a function of R and τ. $\theta_1 = \theta_2 = 99.3°$ fixed. The contour spacing is 0.5eV. The $\tilde{A}^1A - ^3B$ seam is also given.

Figure 3.6: Potential energy surfaces of the $\tilde{A}^1A$ state and the lowest ^3B state as a function of R and θ. $\theta \equiv \theta_1 = \theta_2$ and $\tau = 120.2°$ fixed. The contour spacing is 0.5eV.

Figure 3.7: Contribution of $n\sigma^*$ and $\sigma\sigma^*$ configurations accounting for the lowest ^3B state. The $n\sigma^*$ character is defined by summing the squares of the coefficients of $(4a)^1(4b)^1$ and $(5a)^1(5b)^1$ CSF's. The $\sigma\sigma^*$ character is the square of the coefficient of $(4a)^1(5b)^1$. The solid lines and the broken lines indicate $n\sigma^*$ and $\sigma\sigma^*$ characters, respectively. *a*, *b*, *c*, *d* and *e* in the figure refer to the cases of $R = 1.463\mathring{A}$, $1.6\mathring{A}$, $1.8\mathring{A}$, $2.0\mathring{A}$ and $2.5\mathring{A}$, respectively.

Figure 3.8: Contour map of the spin-orbit coupling element between $\tilde{A}^1A$ and the lowest ^3B. The root mean square values are indicated. The contour spacing is $10cm^{-1}$.

Figure 3.9: The spin-orbit coupling near the exit channel ($R = 2.5\mathring{A}$) between the $\tilde{A}^1A$ state and all the triplet states correlated to $OH(\tilde{X}^2\Pi)+OH(\tilde{X}^2\Pi)$, consisting of one ^3A and three ^3B states. The solid line refers to ^3A, and the broken lines refer to ^3B. 1, 2 and 3 are denoted to the lowest ^3B, the first excited ^3B and the second excited ^3B, respectively. The root mean square values are indicated.

Figure 3.1(a)

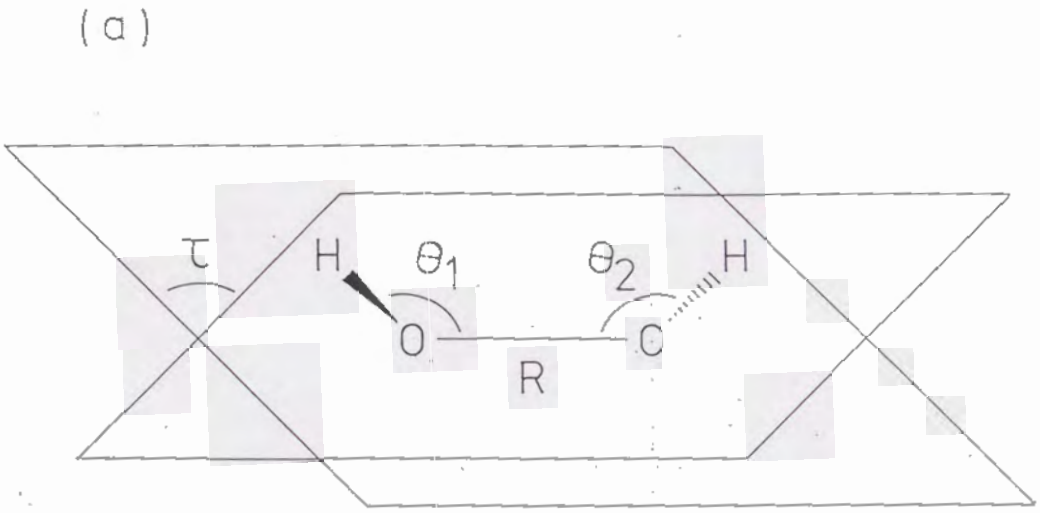

Figure 3.1(b)

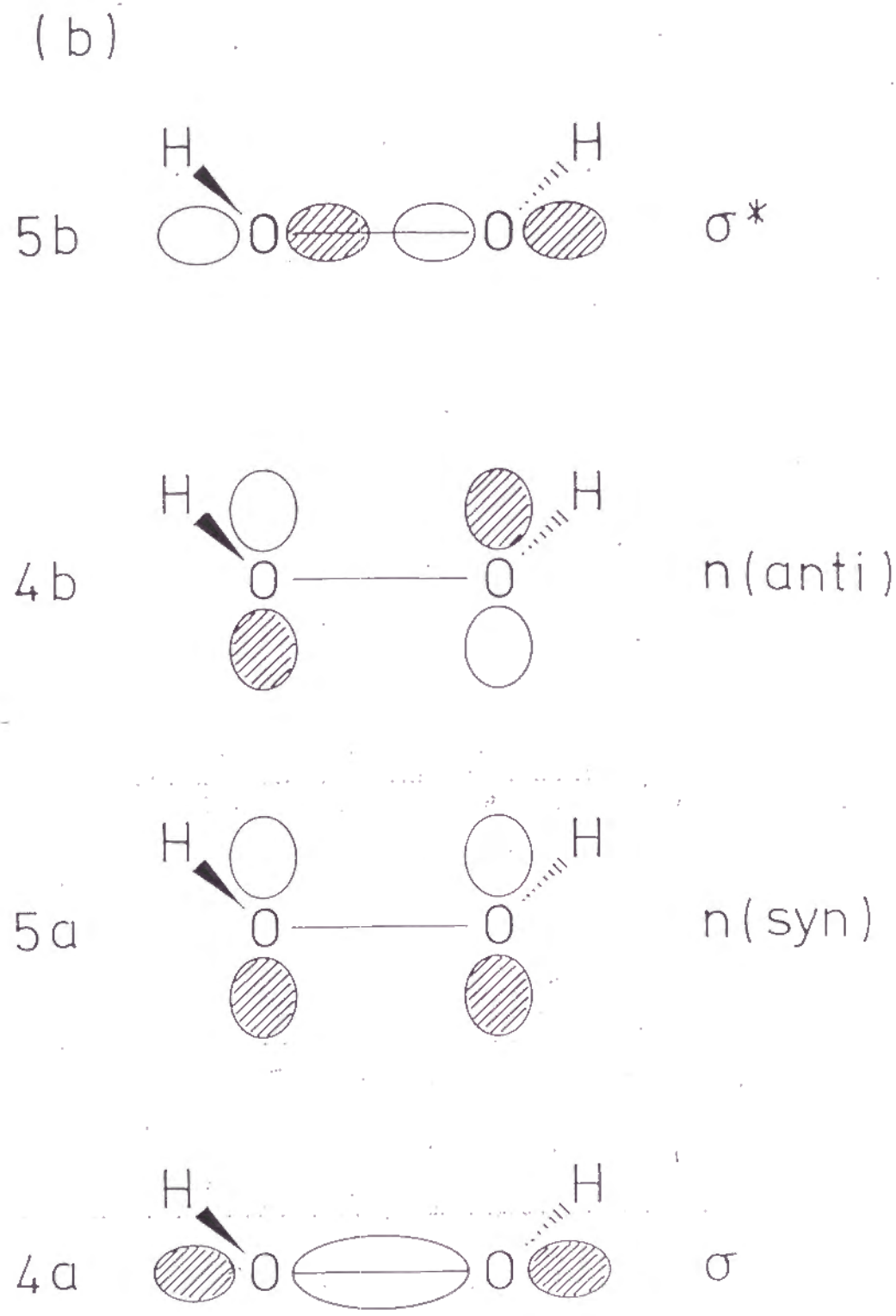

Figure 3.2(a)

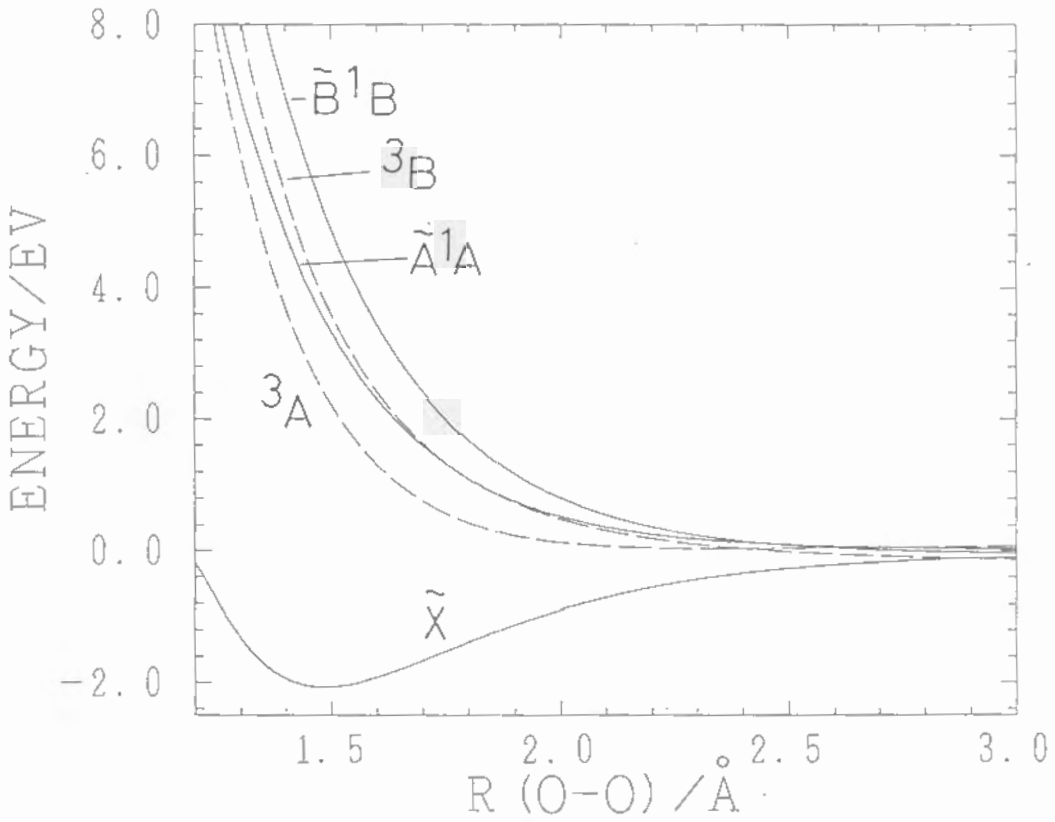
8.0
6.0
4.0
2.0
0.0
−2.0
ENERGY/EV
$\tilde{B}^1B$
^3B
$\tilde{A}^1A$
^3A
$\tilde{X}$
1.5
2.0
2.5
3.0
R (O−O) /Å

Figure 3.2(b)

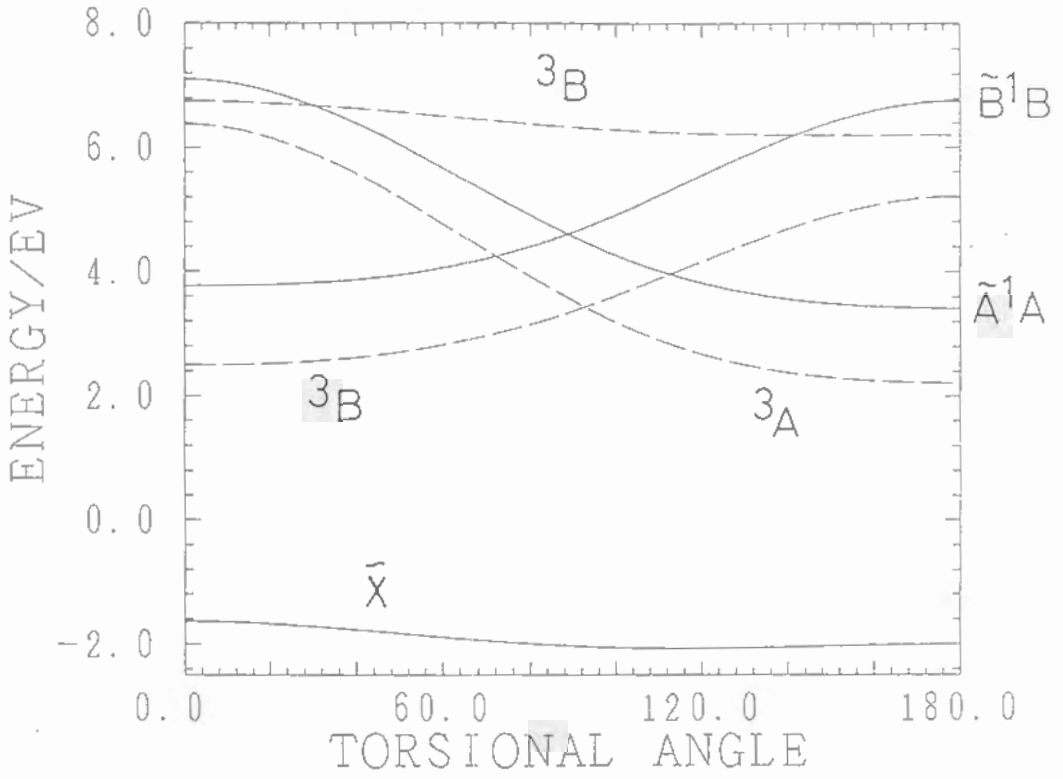
8.0
6.0
4.0
2.0
0.0
-2.0
ENERGY/EV
0.0
60.0
120.0
180.0
TORSIONAL ANGLE
^3B
$\tilde{B}^1B$
$\tilde{A}^1A$
^3B
^3A
$\tilde{X}$

Figure 3.3

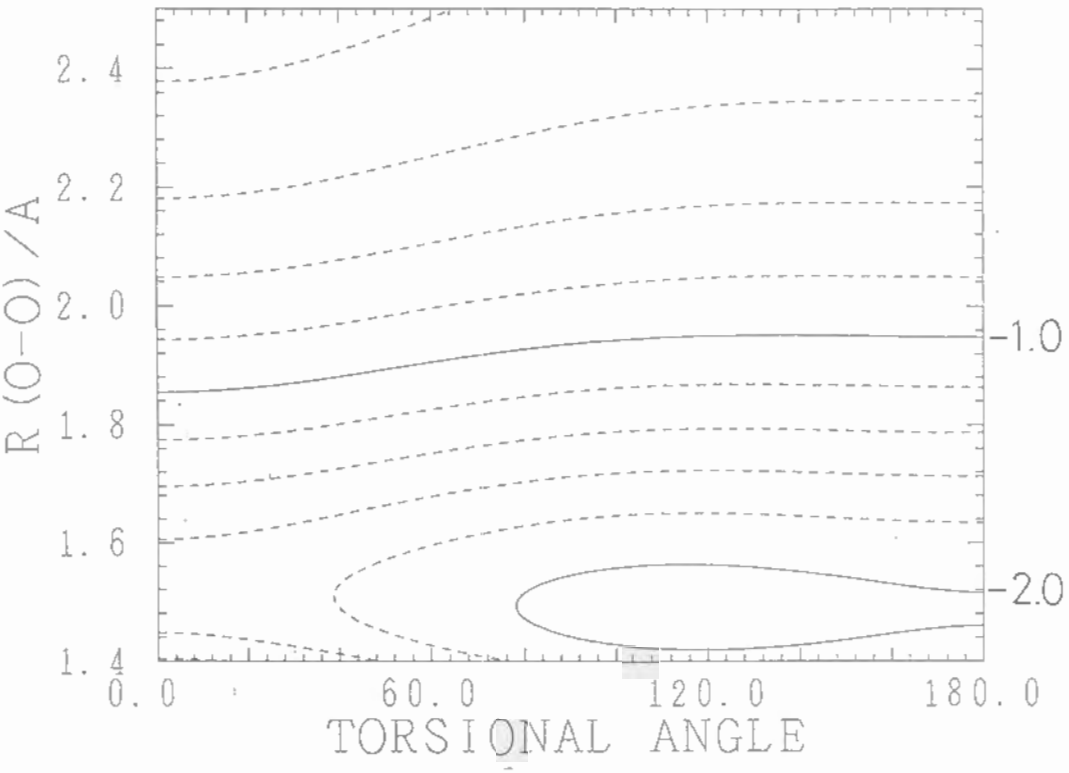

Figure 3.4

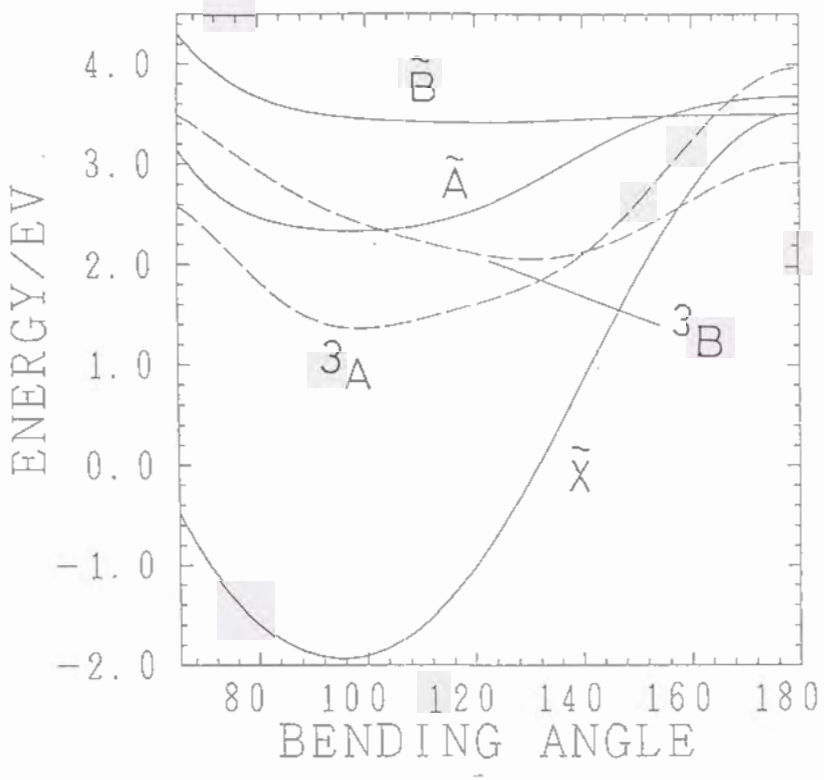
4.0
3.0
2.0
1.0
0.0
−1.0
−2.0
ENERGY/EV
80
100
120
140
160
180
BENDING ANGLE
$\tilde{B}$
$\tilde{A}$
^3B
^3A
$\tilde{X}$

Figure 3.5

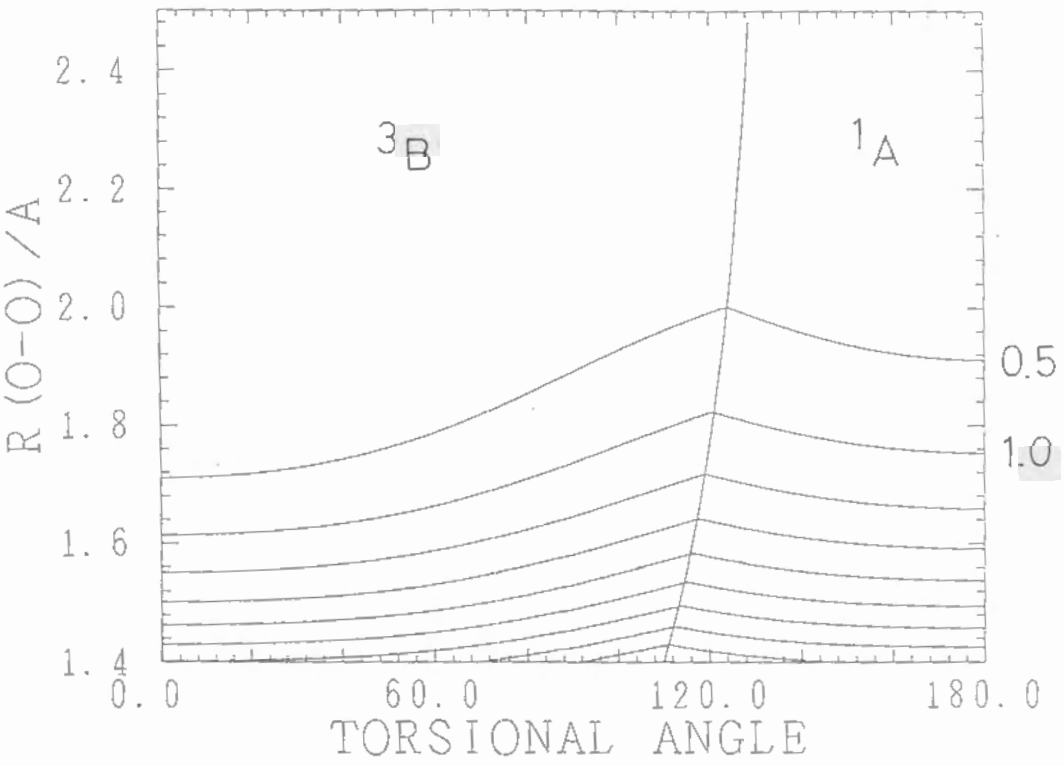
2.4
2.2
2.0
1.8
1.6
1.4
R (O-O) / Å
3B
1A
0.5
1.0
0.0
60.0
120.0
180.0
TORSIONAL ANGLE

Figure 3.6

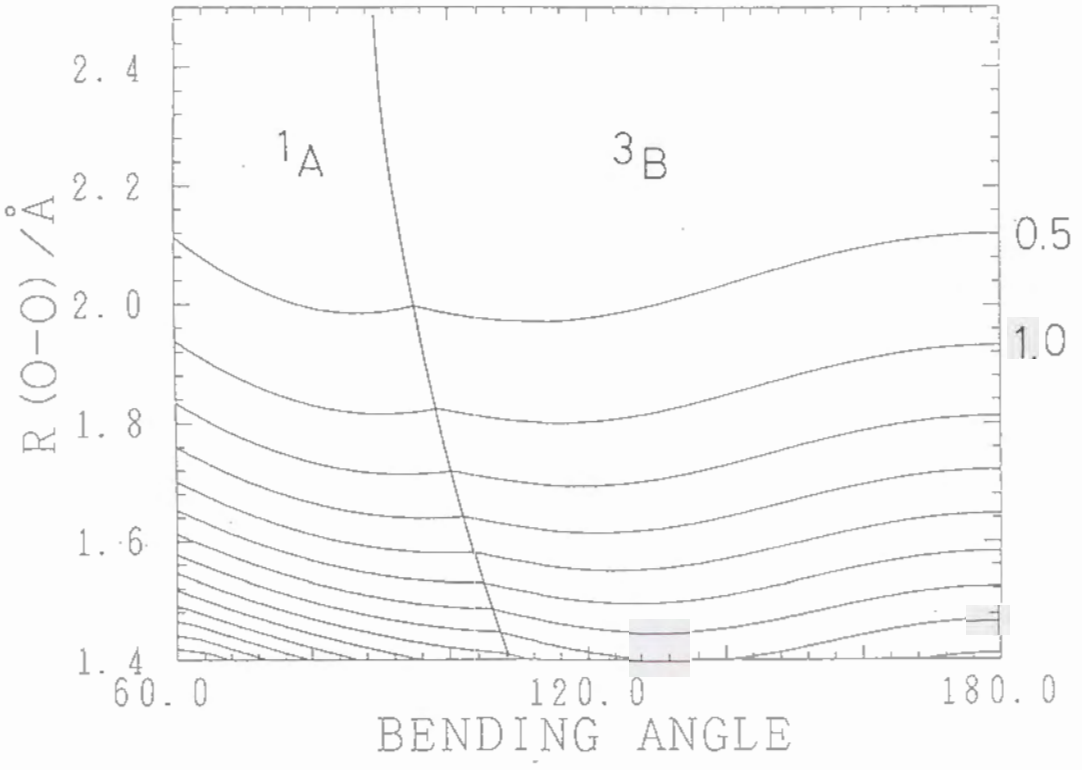

Figure 3.7

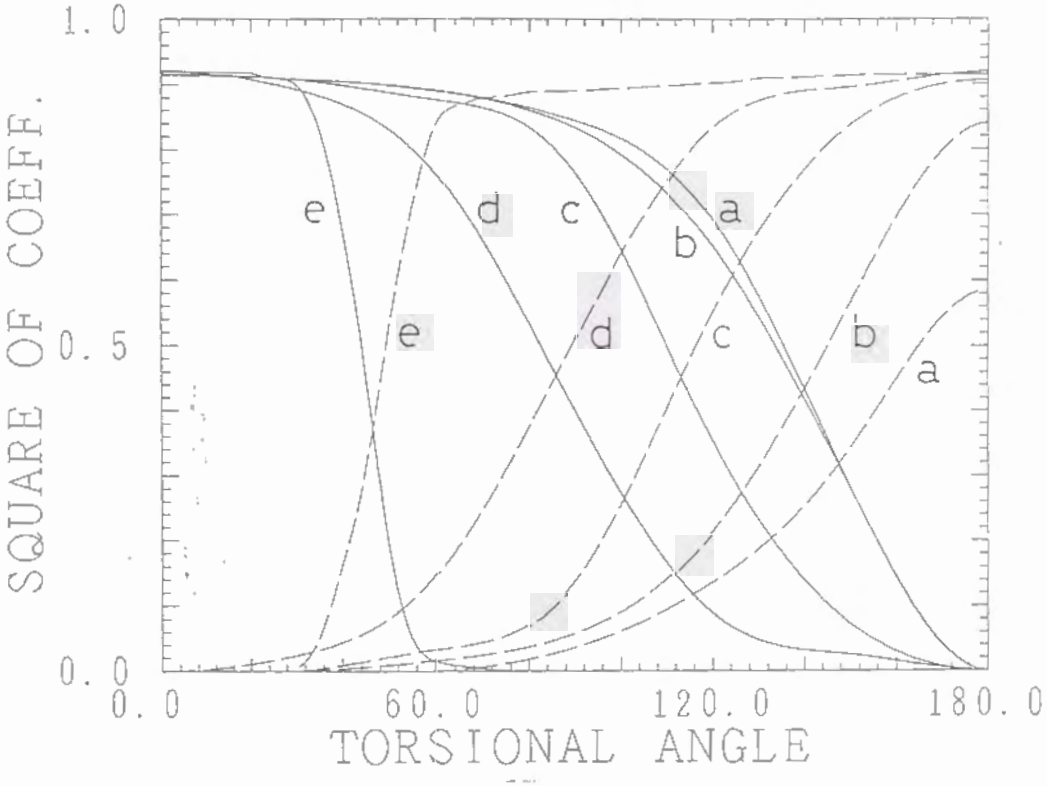
1.0
0.5
0.0
SQUARE OF COEFF.
0.0
60.0
120.0
180.0
TORSIONAL ANGLE
e
d
c
b
a
e
d
c
b
a

Figure 3.8

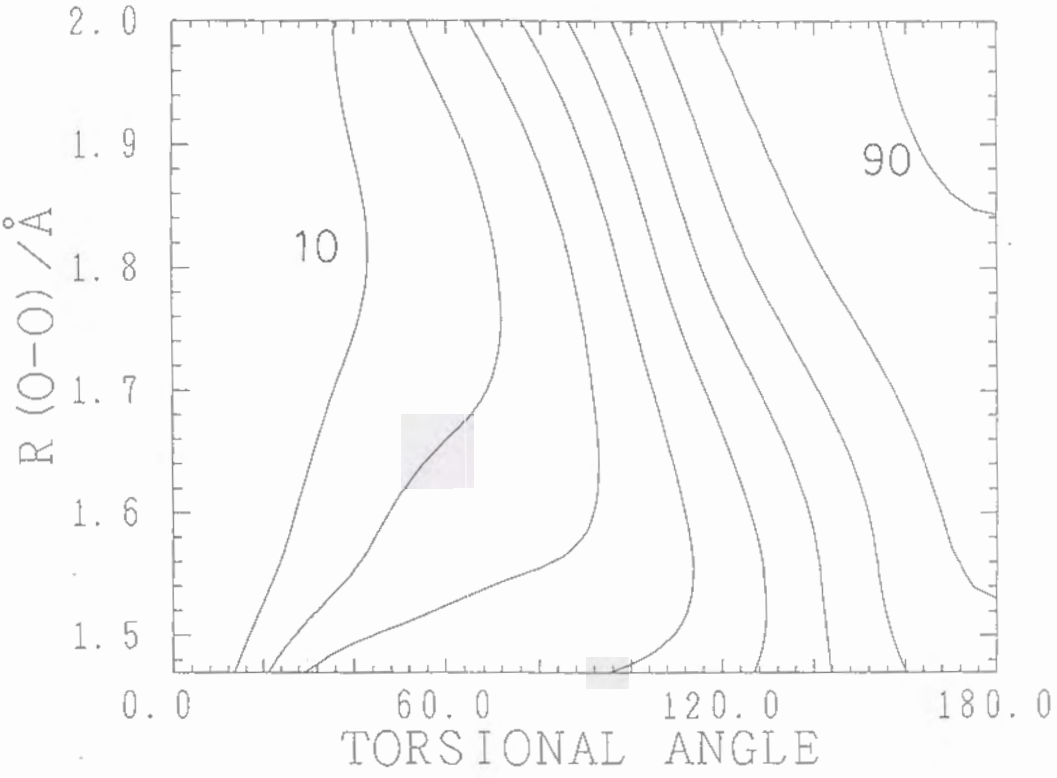

Figure 3.9

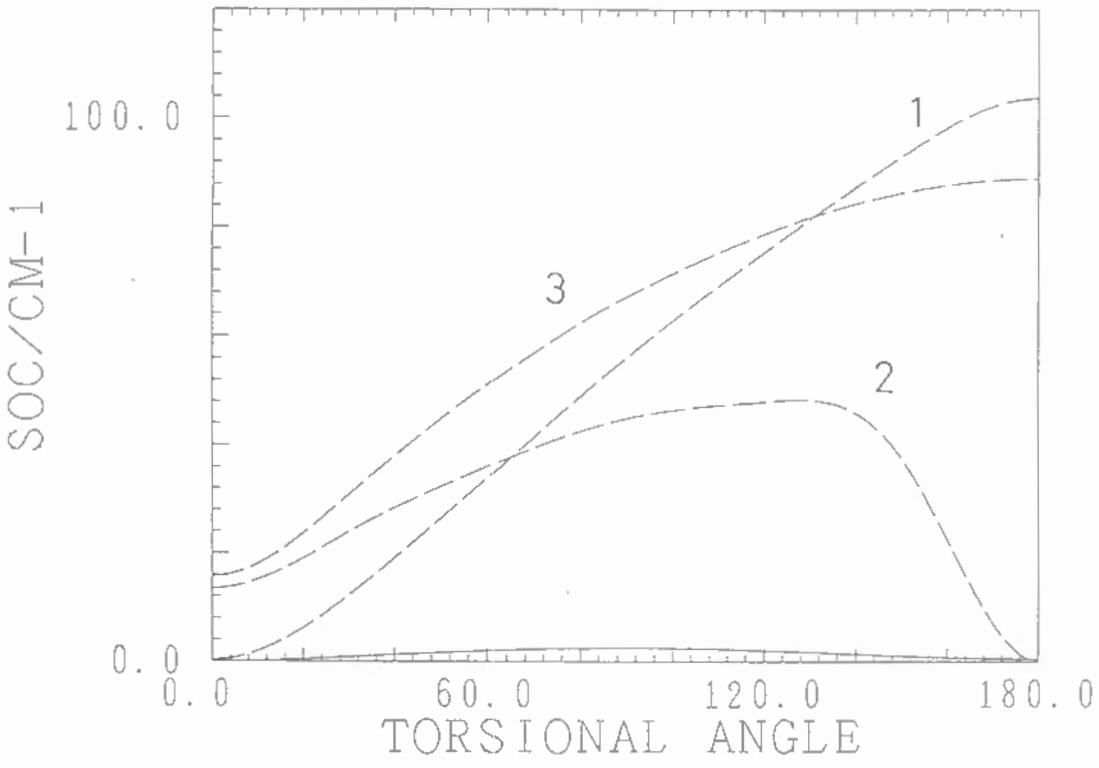

Table 3.1: Ab initio energies of the electronic states of H_2O_2 at the equilibrium geometry[a]

state	energy(eV)
$\tilde{X}^1A$	0.00
$\tilde{A}^1A$	5.97
$\tilde{B}^1B$	7.51
$\tilde{C}^1A$	11.48
^3A	4.90
^3B	6.19
^3B	8.28
^3B	11.93
$OH(\tilde{X})$+$OH(\tilde{X})$	2.05

[a] $R = 1.463\mathring{A}, \tau = 120.2°, \theta_1 = \theta_2 = 99.3°$.[21]

[b] The total energy of the ground state is -151.2075 hartree.

Table 3.2: The spin-orbit coupling between $\tilde{A}^1A$ and the lowest ^3B

	one-electron[a]	two-electron[b]	total
$R = 1.600\mathring{A}$			
$\tau = 0.0°$	1.305	-0.519	0.786
30.0°	18.574	-7.160	11.415
60.0°	39.639	-15.346	24.300
90.0°	48.009	-18.594	29.422
120.2°	73.261	-27.607	45.666
150.0°	109.303	-40.612	68.697
180.0°	131.997	-48.881	83.120
Dissociation limit			
	151.587	-54.824	96.764

[a] One-electron contribution referring to the first term of eq. 3.1.

[b] Two-electron contribution referring to the second term of eq. 3.1.

[c] All the above values are root mean squares:

$$SOC_{rms} = \sqrt{\sum_{M_s} |< \tilde{A}^1A \mid H_{so} \mid^3 B(M_s) >|^2}.$$

[d] The unit is cm^{-1}.

Table 3.3: The spin-orbit coupling between $\tilde{A}^1A$ and the lowest ^3B states along the crossing seam of Fig. 3.6.

R^a	θ^b	one-electron[c]	two-electron[c]	total[c]
1.463	107.2	81.055	-31.450	49.623
1.600	103.6	78.337	-29.401	48.945
1.800	99.3	101.831	-37.092	64.739
2.000	95.5	127.953	-46.277	81.676

[a]unit/$\mathring{A}$. [b]unit/degree.

[c]the root mean squares of the spin-orbit coupling. unit/cm^{-1}.

Bibliography

[1] G. Ondrey, N. van Veen, and R. Bersohn, J. Chem. Phys. **78**, 3792 (1983).

[2] K. -H. Gericke, S. Klee, F. J. Comes, and R. N. Dixon, J. Chem. Phys. **85**, 4463 (1986).

[3] S. Klee, K. -H. Gericke, and F. J. Comes, J. Chem. Phys. **85**, 40 (1986).

[4] M. P. Docker, A. Hodgson, and J. P. Simons, Chem. Phys. Lett. **128**, 264 (1986).

[5] A. U. Grunewald and K. -H. Gericke, F. J. Comes, Chem. Phys. Lett. **132**, 121 (1986).

[6] M. P. Docker, A. Hodgson, and J. P. Simons, Faraday Discuss. Chem. Soc. **82**, 25 (1986).

[7] A. U. Grunewald, K. -H. Gericke, and F. J. Comes, J. Chem. Phys. **87**, 5709 (1987).

[8] S. Klee, K. -H. Gericke, and F. J. Comes, Ber. Bunsenges. Phys. Chem. **92**, 429 (1988).

[9] M. Brouard, M. T. Martinez, C. J. Milne, J. P. Simons, and J. -X. Wang, Chem. Phys. Lett. **165**, 423 (1990).

[10] K. -H. Gericke, H. G. Gläser, C. Maul, and F. J. Comes, J. Chem. Phys. **92**, 411 (1990).

[11] R. Schinke and V. Staemmler, Chem. Phys. Lett. **145**, 486 (1988).

[12] R. Schinke, J. Phys. Chem. **92**, 4015 (1988).

[13] M. H. Alexander and P. J. Dagdigian, J. Chem. Phys. **80**, 4325 (1984).

[14] P. Andresen and E. W. Rothe, J. Chem. Phys. **82**, 3634 (1985).

[15] G. G. Balint-Kurti, J. Chem. Phys. **84**, 4443 (1986).

[16] G. C. Corey and M. H. Alexander, J. Chem. Phys. **88**, 6931 (1988).

[17] M. H. Alexander, H. -J. Werner, and P. J. Dagdigian, J. Chem. Phys. **89**, 1388 (1988).

[18] C. Chevaldonnet, H. Cardy, and A. Dargelos, Chem. Phys. **102**, 55 (1986).

[19] L. B. Harding, J. Phys. Chem. **93**, 8004 (1989).

[20] U. Meier, V. Staemmler, and J. Wasilewski, to be published. (cited in

[21])

[22] D. Cremer, J. Chem. Phys. **69**, 4440 (1978).

[23] K. P. Huber and G. Herzberg, In *Molecular Spectra and Molecular Structure*; vol.4 *Constants of Diatomic Molecules* ; Van Nostrand, New York, 1979.

[24] We used the HONDO7 program by Dupuis et al. to obtain the CASSCF wave functions.

[25] T. H. Dunning,Jr. and P. J. Hay, in *Modern Electronic Structure Theory* ; H. F. Schaefer, Eds.; Plenum, New York, 1977.

[26] (a)R. J. Buenker, in *Proceeding of Workshop on Quantum Chemistry and Molecular Physics in Wollongong*, Australia, 1980. (b) R. J. Buenker and R. A. Philips, J. Mol. Struct. THEOCHEM. **123**, 291 (1985).

[27] S. R. Langhoff, in *Applications of Electronic Structure Theory* ; H. F. Schaefer, Eds.; Vol.4 of *Modern Theoretical Chemistry*; Plenum, New York, 1977; p.384

[28] H. F. King and T. R. Furlani, J. Comp. Chem. **9**, 771 (1988).

[29] for example, R. N. Zare, In *Angular Momentum*; Chap.6; John Wiley and Sons, New York, 1988.

[30] D. L. Baulch, R. A. Cox, R. F. Hampson, J. A. Kerr, J. Troe, and R. T. Watson, J. Phys. Chem. Ref. Data **9**, 295 (1980).

[31] L. Salem and C. Rowland, Angew. Chem. internat. Edit. **11**, 92 (1972).

Chapter 4

Theoretical Study on the Intersystem Crossing Mechanism of a Diradical in Norrish Type II Reactions in Solution

We studied theoretically the mechanism of intersystem crossing (ISC) of a diradical involved in Norrish type II reactions in solution, on the basis of *ab initio* molecular orbital calculations and molecular dynamics (MD) simulation. The *ab initio* calculations were performed for the simple 1,4-diradical C_4H_8O to obtain the potential energy surfaces and the spin-orbit coupling (SOC) elements. These results revealed that the energy splitting and the SOC element between the singlet and triplet states vary with the solute geometry in a complicated manner and have no correlation to the radical site distance, indicating that the through-bond interaction is dominant to characterize these properties. We constructed the analytical functions representing the potential energy surfaces, the energy splitting and the SOC element by considering the orbital interaction. Further the MD calculations were carried out for the diradical in methanol solvent, and the rate constant of ISC driven by SOC was calculated from the MD trajectories for each solute isomer. By analyzing the rate with microscopic dynamics, we found that localized transition is not realized for some conformers, but the transition state theory holds rather good to estimate the rate. The deviation does not come from the recrossing effect as commonly discussed, but from the fact that the coupling element varys with time during the transition. The solvent effect on the ISC rate was extensively discussed from both the dynamic and static viewpoints.

4.1 Introduction

Among the reactions of organic molecules, diradicals often play an important role as reaction intermediates [1]. In particular, the series of reactions initiated from the $n\pi*$ state of photoexcited ketones have diradical intermediates in general, and such reactions, named type I and II reactions by Norrish [2], have been extensively studied to form one of the major fields in organic photochemistry [3]. In the case of the type II reactions, the intersystem crossing (ISC) to the $n\pi*$ triplet state of ketones is followed by the hydrogen abstraction through a six-membered ring transition state to generate the 1,4-diradicals. This process is symmetry-allowed and can be efficient [4]. However, the triplet diradicals generated in this way have to experience the ISC to the singlet state before proceeding to the final singlet products. The ISC of the diradical intermediates is thus an important process commonly involved in the Norrish type II reactions [5]. In considering this process from a microscopic point of view, it consists in the nonadiabatic spin state transition and the molecular chain and solvent dynamics.

There have been many experimental studies to bring information about the diradical intermediates, using optical or magnetic means. The experiments of the transient absorption have been performed [6, 7, 8, 9, 10] with the flash photolysis technique, and the lifetime of the triplet diradicals has been measured under various conditions to throw light upon the effect of solvent, temperature, magnetic field, or derivatives. On the other hand, the CIDNP experiments have been brought other information [11, 12, 13], especially about the structural and electronic characteristics of the diradical intermediates.

In spite of the activity of experimental side, theoretical studies for the dynamic behavior of the diradical intermediates are rather limited. The magnetic field dependence on the ISC rate or the CIDNP spectrum has been mainly studied theoretically by Schulten et al. [14, 15, 16] and de Kanter et al. [17] in relation to the microscopic molecular motions. They have concerned with the diradicals with a longer chain length or the radical pairs where the hyperfine coupling (HFC) is responsible to the ISC. In such systems, the HFC constants can be regarded to be independent of the chain conformations, which is amenable to theoretical treatments. For the diradicals with a shorter chain length such as the Norrish type II diradicals, however, the spin-orbit coupling (SOC) plays an important role to the ISC [5], and their behavior is more complex because the SOC elements as well as the singlet-triplet energy splitting vary with the molecular geometry. One of the most current instruments to describe the ISC dynamics is the stochastic Liouville equation [14, 15, 17]. Although the treatment is adequate itself, there have been some assumptions too simplified to be a realistic model. For example, the chain conformation has been considered only from the distance of the

two radical sites, and the chain dynamics has been also projected on that dimension with a diffusional model or other. The exchange interaction and the SOC elements have often been assumed to be the simple functions of the radical site distance. Actually, these properties are quite sensitive to the chain conformation and behave in a rather complicated manner, because the relative orientation as well as the distance between the two radical orbitals is crucial to determine their magnitudes as discussed later. In the present work, we have carried out *ab initio* molecular orbital (MO) calculations of the 1,4-diradical $\dot{C}H_2CH_2CH_2\dot{C}HOH$ to construct a realistic molecular model for the Norrish type II diradical and estimated the ISC rate in methanol by the molecular dynamics (MD) simulations. This diradical, derived from butanal, is regarded to be the simplest type II reaction intermediate.

Recent theoretical studies on the chemical reactions in solutions based on the microscopic dynamics have been advanced to discuss certain classes of reactions [18], including electron transfer [19, 20, 21], proton transfer [22, 23], S_N2 reaction [24], isomerization [25, 26] and so on. However, theoretical calculations on the ISC of diradical intermediates driven by the SOC with taking into account the microscopic dynamics of the molecular chain and solvent are virtually nonexistent to our knowledge. One of the main reasons comes from difficulties to grasp the potential energy surfaces and the electronic properties in the multi-dimensional configuration space. It is noted that this ISC process has some different aspects from the nonadiabatic electron transfer. The exchange interaction of diradicals is small in general and the singlet and triplet states are nearly degenerate each other. Thus the nonadiabatic transition between the states is not necessarily localized, and the surviving time at the potential crossing region is possibly longer than the usual nonadiabatic electron transfer. Further, the reaction rate is actually about $10^7 \sim 10^9 sec^{-1}$, which is quite slow to pursue the whole process with MD simulation. Thus we have to estimate the reaction rate using the simulation results during a short time scale.

The purposes of the present study are (i) to provide theoretical information on the features of the singlet-triplet energy splitting and the SOC as well as the relevant potential energy surfaces themselves, the ingredient essential to understand the ISC dynamics; and (ii) to evaluate the ISC rate constant by carrying out the MD calculations. The mechanism of ISC is discussed on the basis of the characteristics of the potential energy and dynamics. In the next section, we will discuss the formal rate of the ISC adequate to the MD simulation. We also develop the transition state theory (TST) to estimate the ISC rate and compare with the dynamics results. In Sec. 4.3 the *ab initio* calculations for the potential energy surfaces and the SOC are described, and the characteristics of them in terms of the chain conformation are discussed. On the basis of these results, we construct the analytical functions representing the potential energies, the triplet-singlet energy splitting and the SOC

element for the use of MD calculations. Sec. 4.4 describes the MD calculations. After a brief explanation of the MD trajectory method employed in the present paper, we will present the trajectory results and the ISC rate constants. In Sec. 4.5 we intend to characterize the mechanism of ISC of the diradical by analyzing the MD trajectories. The dynamic and static solvent effects on the ISC rate in solution are also discussed. A brief summary and conclusion are given in Sec. 4.6.

4.2 Theoretical Model

4.2.1 Formal Rate of the Intersystem Crossing.

We discuss the formula for the ISC rate in order to estimate it by the MD trajectory calculations. Actually, the lifetime of the triplet diradicals has been found to be as long as $10 \sim 100 nsec$ for the Norrish type II reactions; which indicates that the transition can be regarded as the weak coupling case due to the small SOC elements. For the case it is adequate to calculate the transition rate by the perturbation theory. The ISC rate from the triplet to the singlet is thus expressed on the basis of the Fermi's golden rule [27]:

$$k = \frac{2\pi}{\hbar} \sum_{i,j} \frac{e^{-\beta E_{it}}}{Q} \frac{1}{3} \sum_{M_s=-1}^{1} |< \Psi_{it}(M_s) \mid H' \mid \Psi_{js} >|^2 \, \delta(E_{it} - E_{js}); \qquad (4.1)$$

where H' is the coupling Hamiltonian; $\Psi_{it}(M_s)$ and E_{it} are the state vector and the total energy, respectively, of the triplet state including the solute and solvent, and Ψ_{js} and E_{js} are of the singlet; Q is the partition function. We considered here only the SOC Hamiltonian H_{so} for H', because the HFC is much smaller than the SOC in the present system, as discussed in Sec. 4.3 (c). The triplet manifolds ($M_s = -1, 0, 1$) are prepared in even probabilities by the hydrogen abstraction, and they are degenerate under no magnetic field. Although Eq. (4.1) is exact within the full quantum mechanics, it is convenient to derive the semiclassical form suited for the MD calculations, where the motion of nuclei is treated classically. For this purpose, we first introduced the Born-Oppenheimer approximation:

$$\begin{aligned} H &= H_0(\vec{r}) + H_B(\vec{R}) + V(\vec{r}, \vec{R}), \\ \mid \Psi_{it}(M_s)(\vec{r}, \vec{R}) > &= \mid \varphi_t(M_s)(\vec{r}, \vec{R}) > \mid \psi_{it}(\vec{R}) >, \\ \mid \Psi_{js}(\vec{r}, \vec{R}) > &= \mid \varphi_s(\vec{r}, \vec{R}) > \mid \psi_{js}(\vec{R}) >, \end{aligned} \qquad (4.2)$$

and

$$\begin{aligned} (H_0(\vec{r}) + V(\vec{r}, \vec{R})) \mid \varphi_{t,s}(\vec{r}, \vec{R}) > &= U_{t,s}(\vec{R}) \mid \varphi_{t,s}(\vec{r}, \vec{R}) >, \\ (H_B(\vec{R}) + U_{t,s}(\vec{R})) \mid \psi_{it,js}(\vec{R}) > &= E_{it,js} \mid \psi_{it,js}(\vec{R}) >; \end{aligned} \qquad (4.3)$$

where $\vec{r}$ is the coordinate of the electrons and $\vec{R}$ is that of the nuclei including the solute and the solvent molecules. $U_{t,s}(\vec{R})$ are the adiabatic potentials of the triplet and singlet states, respectively. $\varphi_{t,s}$ are the electronic wave functions, and $\psi_{it,js}$ the wave functions for the nuclear motion.

Using the Born-Oppenheimer approximation, the ISC rate k is represented as follows:

$$\begin{aligned} k &= \frac{2\pi}{\hbar}\sum_{i,j}\frac{e^{-\beta E_{it}}}{Q}\frac{1}{3}\sum_{M_s=-1}^{1}|<\psi_{it}|<\varphi_t(M_s)\mid H_{so}\mid\varphi_s>|\psi_{js}>|^2 \\ &\quad \frac{1}{2\pi\hbar}\int_{-\infty}^{\infty}dt\exp(\frac{i(E_{it}-E_{js})t}{\hbar}) \\ &= \frac{1}{\hbar^2}\sum_{i,j}\frac{e^{-\beta E_{it}}}{Q}\frac{1}{3}\sum_{M_s=-1}^{1}\int_{-\infty}^{\infty}dt<\psi_{it}\mid\exp(\frac{i(H_B+U_t)t}{\hbar})<\varphi_t(M_s)\mid H_{so}\mid\varphi_t> \\ &\quad \exp(\frac{-i(H_B+U_s)t}{\hbar})\mid\psi_{js}><\psi_{js}|<\varphi_s\mid H_{so}\mid\varphi_t(M_s)>|\psi_{is}> \\ &= \frac{1}{3\hbar^2}\int_{-\infty}^{\infty}dt<\exp(\frac{i(H_B+U_t)t}{\hbar})\vec{J}\exp(\frac{-i(H_B+U_s)t}{\hbar})\vec{J}>_{eq}; \end{aligned} \tag{4.4}$$

where $\vec{J}$ is a vector quantity of the SOC elements which are $J(M_s) =< \varphi_t(M_s)\mid H_{so}\mid\varphi_s>$ for $M_s=-1,0,1$; $<>_{eq}$ denotes the thermal average. The elements of $\vec{J}$ can be expressed in another way:

$$\begin{aligned} J_x &= -\frac{1}{\sqrt{2}}(J(M_s=1)+J(M_s=-1)), \\ J_y &= -\frac{i}{\sqrt{2}}(J(M_s=1)-J(M_s=-1)), \\ J_z &= J(M_s=0). \end{aligned} \tag{4.5}$$

The root mean square $J_{rms}=\sqrt{\sum_{M_s=-1}^{1}\mid J(M_s)\mid^2}=\sqrt{J_x^2+J_y^2+J_z^2}$ is a scalar quantity invariant to the space rotation. It is noted that the last form of Eq. (4.4) is expressed only with the nuclear coordinates explicitly. Further, the time evolution operators $\exp(\frac{i(H_B+U_{t,s})t}{\hbar})$ are splitted in the following:

$$\begin{aligned} \exp(\frac{i(H_B+U_t)t}{\hbar}) &= e^{i(A+B)t}, \\ \exp(\frac{i(H_B+U_s)t}{\hbar}) &= e^{i(-A+B)t}; \end{aligned} \tag{4.6}$$

where

$$\begin{aligned} A &= \frac{1}{\hbar}(H_B+\frac{U_t+U_s}{2}), \\ B &= \frac{1}{2\hbar}(U_t-U_s). \end{aligned}$$

Therefore, the rate constant can be rewritten as

$$\begin{aligned} k &= \frac{1}{3\hbar^2}\int_{-\infty}^{\infty} dt < e^{i(A+B)t}\vec{J}e^{i(-A+B)t}\vec{J} >_{eq} \\ &= \frac{1}{3\hbar^2}\int_{-\infty}^{\infty} dt < \exp_-[i\int_0^t \tilde{B}(\tau)d\tau]e^{iAt}\vec{J}e^{-iAt}\exp_+[i\int_0^t \tilde{B}(\tau)d\tau]\vec{J} >_{eq} \\ &= \frac{1}{3\hbar^2}\int_{-\infty}^{\infty} dt < \exp_-[i\int_0^t \tilde{B}(\tau)d\tau]\tilde{J}(t)\exp_+[i\int_0^t \tilde{B}(\tau)d\tau]\tilde{J}(0) >_{eq}; \end{aligned} \quad (4.7)$$

where $\tilde{X}(t) = e^{iAt}Xe^{-iAt}$ for an arbitary operator X. In deriving Eq. (4.7) the Feynman's formula was used, and $\exp_\pm$ denote the time-ordered exponential functions [28]. Then we introduce the semiclassical approximation for the nuclear dynamics, by replacing $\tilde{X}(t)$ by the expectation value $X(t) = X(\vec{R}(t))$, which can be estimated in terms of the classical mechanics. The final form of the ISC rate is thus given by

$$\begin{aligned} k &= \frac{1}{3\hbar^2}\int_{-\infty}^{\infty} dt < \vec{J}(t)\vec{J}(0)\exp(\frac{i}{\hbar}\int_0^t [U_t(\tau) - U_s(\tau)]d\tau) >_{eq} \\ &= \frac{2}{3\hbar^2}Re\int_0^{\infty} dt < \vec{J}(t)\vec{J}(0)\exp(\frac{i}{\hbar}\int_0^t \Delta U(\tau)d\tau) >_{eq}; \end{aligned} \quad (4.8)$$

where $\Delta U(\tau) = U_t(\tau) - U_s(\tau)$. All the values in Eq. (4.8) can be calculated by the classical MD simulation on the averaged potential surface $\bar{U}(\vec{R}) = \frac{1}{2}(U_t(\vec{R}) + U_s(\vec{R}))$ and by the thermal average manipulation. This formula consists of an integral of a time correlation function, which is suitable to be estimated with the MD calculation during a short time scale.

4.2.2 Transition State Theory Approximation.

In this section we consider an approximation of the static limit for Eq. (4.8) because we intend to discuss the effect of the solute and solvent dynamics on the ISC rate in the following sections. Provided that the singlet-triplet energy splitting $\Delta U(t)$ and the spin-orbit coupling element $\vec{J}(t)$ change much more slowly than the time scale determined by the time correlation function in Eq. (4.8) the rate formula is reduced as follows:

$$k = \frac{2}{3\hbar^2}Re\int_0^{\infty} < J^2\exp(\frac{i}{\hbar}\Delta U t) >_{eq} . \quad (4.9)$$

The thermal average $< >_{eq}$ is carried out for the distribution of $\vec{J}$ and ΔU.

It is convenient to apply the TST in calculating the rate constants of reactions. For the ISC process as in the present case, the dividing surface separating the reactant and product is taken to be the potential crossing surface [29]. The reaction flux passing through the dividing surface is given by

$$f(\vec{q}_0, \vec{p}) = \chi(\vec{q}_0, \vec{p})\frac{e^{-\beta H(\vec{q}_0,\vec{p})}}{3Q} \mid \vec{p}\cdot\vec{n} \mid;$$

where $\vec{q}_0$ is the mass-weighted Cartesian coordinate on the crossing surface, *i.e.* $\Delta U(\vec{q}_0) = U_t(\vec{q}_0) - U_s(\vec{q}_0) = 0$, and $\vec{p}$ the conjugate momentum to $\vec{q}$. Q denotes the partition function, and the factor 3 was derived from the triplet manifold of the reactant. $\vec{n}$ is the unit vector normal to the dividing surface and has the element

$$n_i = (\frac{\partial \Delta U}{\partial q_i})_{\vec{q}=\vec{q}_0} / \mid \frac{\partial \Delta U}{\partial \vec{q}} \mid_{\vec{q}=\vec{q}_0} .$$

If we employ the Landau-Zener formula to calculate the triplet-singlet transition probability, the characteristic funcition $\chi(\vec{q}_0, \vec{p})$ in the TST is written by

$$\begin{aligned} \chi(\vec{q}_0, \vec{p}) &= 1 - \exp(-\frac{2\pi J(\vec{q}_0)^2}{\hbar \mid \vec{p} \cdot \vec{n} \mid\mid \frac{\partial \Delta U}{\partial \vec{q}} \mid_{\vec{q}=\vec{q}_0}}) \\ &\simeq \frac{2\pi J(\vec{q}_0)^2}{\hbar \mid \vec{p} \cdot \vec{n} \mid\mid \frac{\partial \Delta U}{\partial \vec{q}} \mid_{\vec{q}=\vec{q}_0}}. \end{aligned} \tag{4.10}$$

For the present system it is adequate to take the formula of weak coupling limit, Eq. (4.10), in accordance with Eq. (4.1)

The ISC rate constant is given in the following:

$$\begin{aligned} k &= \int\int d\vec{q}d\vec{p} f(\vec{q},\vec{p}) \frac{e^{-\beta H(\vec{q},\vec{p})}}{3Q} \delta(\vec{q}-\vec{q}_0)(\vec{p}\cdot\vec{n}) \\ &= \frac{2\pi}{3\hbar} \int\int d\vec{q}d\vec{p} \frac{J(\vec{q})^2}{\mid \vec{p}\cdot\vec{n} \mid\mid \frac{\partial \Delta U}{\partial \vec{q}} \mid} \cdot \frac{e^{-\beta H(\vec{q},\vec{p})}}{Q} \delta(\vec{q}-\vec{q}_0)(\vec{p}\cdot\vec{n}) \\ &= \frac{2\pi}{3\hbar} \int d\vec{q} J(\vec{q})^2 \frac{e^{-\beta E(\vec{q})}}{Z} \delta(\Delta U(\vec{q})) \\ &= \frac{1}{3\hbar^2} \int d\vec{q} J(\vec{q})^2 \frac{e^{-\beta E(\vec{q})}}{Z} \int_{-\infty}^{\infty} dt \exp(\frac{i}{\hbar}\Delta U(\vec{q})t) \\ &= \frac{1}{3\hbar^2} \int_{-\infty}^{\infty} dt < J^2 \exp(\frac{i}{\hbar}\Delta U t) >_{eq} \\ &= \frac{2}{3\hbar^2} Re \int_0^{\infty} dt < J^2 \exp(\frac{i}{\hbar}\Delta U t) >_{eq}; \end{aligned} \tag{4.11}$$

where Z is the configuration integral:

$$Z = \int d\vec{q} \exp(-\beta U_t(\vec{q})).$$

The TST rate constant k^{TST} is thus determined by the distribution of $\vec{J}$ and ΔU in the thermal equilibrium. In evaluating the rate constant by the MD calculations, we have replaced $U_t(\vec{q})$ in Eq. (refeq:tstiscr) by the averaged potential of the triplet and singlet states to compare the results with those

of Eq. (4.8). This may be acceptable considering that the triplet surface is nearly degenerate to the singlet one.

It is noteworthy that the TST rate constant of ISC, Eq. (4.11), is regarded as the static limit, Eq. (4.10), as mentioned above. If the transition occurs in a short time enough to regard the molecular motion to be frozen during the correlation time of Eq. (4.8), the rate constant of Eq. (4.8) is reduced to the TST rate constant. The comparison of the rate constants by Eq. (4.8) and Eq. (4.9) is useful to examine the effect of dynamics on the ISC rate.

4.3 Calculation of Electronic States

4.3.1 Potential Energy Surface of the Averaged State.

The potential energies of the singlet state were calculated with the two-configuration self-consistent field (TCSCF) method, and those of the triplet state with the restricted open-shell Hartree-Fock (ROHF) method [30]. The TCSCF wavefunction was further transformed into the generalized valence bond (GVB) form [31] to have an intuitive description for the diradical electronic structure. These methods are rather simple and can adequately describe the diradical electronic states to the same extent of the approximation.

First we obtained the equilibrium geometries of various conformational isomers of the diradical $\dot{C}H_2CH_2CH_2\dot{C}HOH$. The geometry of the diradical C_4H_8O, as well as the serial numbers of the atoms to define the geometric parameters, is illustrated in Fig. 4.1. The isomers derived from the flexible chain are characterized by the two torsional angles around the C-C bonds (1-2-3-4 and 2-3-4-5), τ_1 and τ_2, and the rotational angle of OH (13-1-2-3). Each of the former torsional angles has three minima (gauche$^-$[g^-], gauche$^+$[g^+], and trans[t]), and the latter OH angle has two minima. The geometries of 18 conformers for the triplet state were optimized using the unrestricted Hartree-Fock (UHF) method with the 3-21G basis set [32]. We also optimized the geometries for the singlet state diradical using the TCSCF method, and found that the optimized geometries are very close to those of the triplet state. In Table 4.9 we show the nine optimized geometries among them and their energies where the OH rotational angle is at the minima near 180°. The other conformers with the different OH rotational angles have nearly the same geometric parameters except some bending angles (1-2-3 and 1-2-6); see the Appendix.

Next the potential energy surface of the averaged state was obtained. From the optimized geometries in Table 4.9, it is found that the other variables except the two torsional angles are not much changed among the equilibrium configurations. Thus we represented those variables by the analytic functions of the two angles, τ_1 and τ_2, to interpolate the equilibrium geome-

tries. We generated 144 geometries with varying the two angles: τ_1, τ_2 = $-150°$, $-120°$, $-90°$, $-60°$, $-30°$, $0°$, $30°$, $60°$, $90°$, $120°$, $150°$, $180°$, for which the potential energies of the singlet and triplet states were calculated. The 6-31G basis set [32] was used to obtain the potential energies. Additional calculations for smaller systems modelling the 1,4-diradical in quetion were performed to obtain more detailed information about the potential energy surface. We calculated the energies of a model radical $CH_3\dot{C}HOH$ with varying the OH rotational angle and the out-of-plane angle of the hydrogen connecting the radical carbon, and those of $CH_3\dot{C}H_2$ with varying the torsional and wagging angles of the radical CH_2 moiety. These calculations for the model systems were carried out using the UHF method with the 6-31G basis set. The potential energy characteristics obtained for these radicals were utilized to construct the potential function of the diradical C_4H_8O.

Using the calculated results, we determined the potential energy function of the averaged state. The potential energy function was assumed to have the following form

$$\begin{aligned} U &= U_{stret} + U_{bend} + U_{vdW} + U_{tors} + U_{wag} + U_{rot} + U_{CH_2} \\ &= \sum_{i=1}^{12} \frac{1}{2} k_i (r_i - r_i^{(0)})^2 + \sum_{i=1}^{19} \frac{1}{2} k_i' (\theta_i - \theta_i^{(0)})^2 \\ &\quad + \sum_{i=1}^{3} \epsilon_i [(\frac{\sigma_i}{R_i})^{12} - (\frac{\sigma_i}{R_i})^6] + \sum_{i=1}^{2} (a_i \cos\tau_i + b_i \cos 2\tau_i + c_i \cos 3\tau_i) \\ &\quad + U_{wag} + U_{rot} + U_{CH_2}. \end{aligned} \tag{4.12}$$

The stretching and bending terms, the first and second terms, are represented by the sum of harmonic potentials. The force constants k_i and k_i' were obtained by the UHF calculations for the triplet state at the equilibrium geometry of the trans-trans (*tt*, see Table 4.9) conformer, where the effect of intramolecular nonbonding interaction is small. These force constants were assumed to be independent of the chain conformation, and the equilibrium bond distance and angles, $r_i^{(0)}$ and $\theta_i^{(0)}$, were taken as the average values of the optimized geometries. It is noted that all the bending angles including the redundant ones were used to represent the bending motions. The intramolecular van der Waals (vdW) interaction and the torsional terms, the third and fourth terms, were determined with the energies of the 144 geometries interpolating the equilibrium configurations described above, for these terms represent the conformational dependency of the energy. These parameters included in the first four terms of the potential function were tabulated in Table 4.9. The out-of-plane wagging term of the 6-th hydrogen U_{wag} and the OH rotation term U_{rot} were determined using the *ab initio* results of the model system $CH_3\dot{C}HOH$, and the wagging and torsional terms of the -CH_2 moiety U_{CH_2} were determined with $CH_3\dot{C}H_2$. The detail forms and the parameters are described in the Appendix. The mean square deviation between

the analytic function and the *ab initio* energies was $0.5 kcal/mol$.

The contour map of the potential energy using the analytic function was displayed as a function of the two torsional angles in Fig. 4.2. The nine minima are clearly observed in the figure, and the energy differences of these minima are within $1.5 kcal/mol$. The energy barriers to change the conformations are $1.2 \sim 2.1 kcal/mol$ along the τ_1 axis and $2.6 \sim 4.1 kcal/mol$ along the τ_2 axis, except for the region near $(\tau_1, \tau_2) = (0°, 0°)$ which is not important to the dynamics. This indicates that the conformational transition can occur with the thermal energy, though the transition along the τ_1 coordinate is considerably easier than that along τ_2.

4.3.2 Singlet-Triplet Energy Splitting.

In general the energies of the singlet and triplet states are close in the diradical (see Table 4.9, for example), and the small splitting comes from the weak interaction between the two radical electrons. Considering the ISC rate given by Eq. (4.8) or Eq. (4.9), the singlet-triplet energy splitting ΔU is an important factor as well as the SOC element $\vec{J}$. We discuss here the feature of the energy splitting ΔU and represent the *ab initio* results by the analytic function for the use of MD calculations.

Looking at the *ab initio* results for the 144 geometries interpolating the equilibrium geometries, one can find that the energy splitting has *no* correlation to the radical site distance. This implies that the energy splitting mainly comes from the through-bond interaction besides the through-space interaction [33], because the chain length between the radical sites is not so long in this 1,4-diradical. This is a rather surprising result, and it is not easy to give a simple intuitive functional form for the energy splitting, such as an exponentially decaying function of the radical site distance. We therefore examined the electronic characteristics of the diradical to search a suitable form of the energy splitting function. Regarding this diradical as two valence electrons system simply, the wave functions of both the states are expressed as follows:

$$\Psi_s = \frac{1}{\sqrt{2+2S_{ab}^2}}[|| \varphi_1\overline{\varphi_1}\cdots\varphi_n\overline{\varphi_n}\psi_a\overline{\psi_b} || + || \varphi_1\overline{\varphi_1}\cdots\varphi_n\overline{\varphi_n}\psi_b\overline{\psi_a} ||],$$

$$\Psi_t(M_s=0) = \frac{1}{\sqrt{2-2S_{ab}^2}}[|| \varphi_1\overline{\varphi_1}\cdots\varphi_n\overline{\varphi_n}\psi_a\overline{\psi_b} || - || \varphi_1\overline{\varphi_1}\cdots\varphi_n\overline{\varphi_n}\psi_b\overline{\psi_a} ||], \quad (4.13)$$

where $\varphi_1 \sim \varphi_n$ are the doubly occupied core orbitals, and ψ_a and ψ_b are the GVB orbitals [31]. S_{ab} is the overlap between the two GVB orbitals. It is assumed here that the singlet and triplet orbitals are identical for simplicity. We thus obtain the energies of the two states $U_{s,t}$ and the splitting ΔU as

$$U_{s,t} = \frac{1}{1 \pm S_{ab}^2}[(E_{core} + h_{aa} + h_{bb}) \pm (h_{ab}S_{ab} + \frac{1}{2}(ab \mid ba)$$

$$+\sum_{i=1}^{n}(ab \mid ii)S_{ab}) + O(S_{ab}^2)], \tag{4.14}$$

$$\begin{aligned}\Delta U &= U_t - U_s \\ &= -(ab \mid ba) - 2(h_{ab} + \sum_{i=1}^{n}(ab \mid ii))S_{ab} + O(S_{ab}^2) \\ &= -(ab \mid ba) - 2\tilde{h}_{ab}S_{ab} + O(S_{ab}^2). \end{aligned} \tag{4.15}$$

The energy splitting ΔU consists of the two terms with the opposite signs, $(ab \mid ba)$ and $\tilde{h}_{ab}S_{ab}$; the former exchange term works the triplet state energy to lower while the latter term contributes to lower the singlet state. However, one can expect that both the terms have close relation to the square of the overlap of the GVB orbitals S_{ab}^2. As shown in Fig. 4.3, a linear relationship between the energy splitting ΔU and S_{ab}^2 are apparently observed, and the negative value of ΔU at $S^2 \approx 0$ can be interpreted from the Hund's rule. This correlation is crucial to construct the energy splitting function.

As mentioned above, the overlap S_{ab} also has a larger through-bond contribution S_{TB} than the through-space S_{TS}. The through-bond overlap S_{TB} consists of two components; one is the interaction through the C_3-C_4 σ-type orbital, S_σ, and the other through the pseudo π type orbital formed by the CH $\sigma*$ orbitals, S_π. Under these considerations, we gave an analytic function for the overlap S_{ab} in the following:

$$\begin{aligned} S_{ab} &= S_{TS} + S_{TB} \\ &= S_{TS} + S_\sigma + S_\pi \\ S_{TS} &= x_1(\vec{e}_{2p}\cdot\vec{e}_{25})(\vec{e}_{5p}\cdot\vec{e}_{25})e^{-x_2 r_{25}} + x_3(\vec{e}_{2p}\cdot\vec{e}_{15})(\vec{e}_{5p}\cdot\vec{e}_{15})e^{-x_4 r_{15}} \\ S_\sigma &= [x_5(\vec{e}_{2p}\cdot\vec{e}_{\sigma*}) + x_6](\vec{e}_{\sigma*}\cdot\vec{e}_{5p}) \\ S_\pi &= x_7(\vec{e}_{2p}\cdot\vec{e}_{3\pi*})(\vec{e}_{3\pi*}\cdot\vec{e}_{4\pi*})(\vec{e}_{4\pi*}\cdot\vec{e}_{5p}) \\ &\quad + x_8(\vec{e}_{2p}\cdot\vec{e}_{3\pi*})[-(\vec{e}_{75}\cdot\vec{e}_{5p})\cos^4(\theta_1/2)e^{-x_9 r_{75}} + (\vec{e}_{85}\cdot\vec{e}_{5p})\cos^4(\theta_2/2)e^{-x_9 r_{85}}]. \end{aligned} \tag{4.16}$$

This expression seems rather complicated, but each term has a clear physical meaning on the basis of the orbital interaction. $\vec{e}_{2p}$ and $\vec{e}_{5p}$ denote the unit vectors with the origins at the positions of the atoms 2 and 5 and normal to the planes (1,3,6) and (4,11,12), respectively, which represent the directions of the p oribital at the sp^2 radical carbons. The unit vector and the distance are defined as

$$\vec{e}_{ij} = \frac{\vec{r}_i - \vec{r}_j}{\mid \vec{r}_i - \vec{r}_j \mid}, \tag{4.17}$$

and

$$r_{ij} = \mid \vec{r}_i - \vec{r}_j \mid . \tag{4.18}$$

The three vectors have special notation:

$$\vec{e}_{\sigma*} = \frac{\vec{r}_4 - \vec{r}_3}{\mid \vec{r}_4 - \vec{r}_5 \mid};\ \vec{e}_{3\pi*} = \frac{\vec{r}_8 - \vec{r}_7}{\mid \vec{r}_8 - \vec{r}_7 \mid};\ \vec{e}_{4\pi*} = \frac{\vec{r}_{10} - \vec{r}_9}{\mid \vec{r}_{10} - \vec{r}_9 \mid}.$$

These three vectors refer to the orientation of the localized anti-bonding orbitals which are important to the through-bond interaction. $\vec{e}_{\sigma*}$ denotes the $\sigma*$ orbital of C_3-C_4 bond, and $\vec{e}_{3\pi*}$ and $\vec{e}_{4\pi*}$ the pseudo $\pi*$ orbitals of the C_3 and C_4 atoms (see Fig. 4.1), respectively. The scalar products included in the through-bond terms, S_σ and S_π, mean the overlaps between the localized orbitals, for these overlaps are determined mainly by the orbital orientation because the distances between the neighbor sites are nearly constant. The second term of S_π comes from the direct interaction between the radical orbital of the C_5 atom and the pseudo $\pi*$ orbital of the C_3 atom, which is strongly dependent on the distance. θ_1 and θ_2 are the torsional angle of 5-4-3-7 and 5-4-3-8, respectively. $x_1 \sim x_9$ are the parameters which have been determined by the least square fitting to the *ab initio* results of the 144 configurations. The values obtained are as follows:

$$\begin{array}{lll} x_1 = 21.97, & x_2 = 0.8100, & x_3 = -4.971, \\ x_4 = 0.6477, & x_5 = -0.1018, & x_6 = -2.848 \times 10^{-2}, \\ x_7 = -1.226 \times 10^{-2}, & x_8 = -7.896 \times 10^{3}, & x_9 = 2.489. \end{array}$$

(unit: $bohr^{-1}$ for x_2, x_4, x_9.)

Using the overlap function of the GVB orbitals, we expressed the energy splitting $\Delta U = U_T - U_S$ as

$$\Delta U = (A + Be^{-\alpha r_{25}})S_{ab}^2 + (C + De^{-\beta r_{25}}) \tag{4.19}$$

$$A = -10.672,\ B = 539.38,\ C = -0.23584,\ D = -7.4544 \times 10^7,$$

$$\alpha = 0.16273,\ \beta = 3.5320,$$

(unit; $kcal/mol$ for $A \sim D$, $bohr^{-1}$ for α, β);

where r_{25} is the radical site distance: $r_{25} = \mid \vec{r}_2 - \vec{r}_5 \mid$. This formula is based on the linear dependence of S_{ab}^2 as noted above. The parameters $A \sim D$ were determined by the least square fitting. The *ab initio* energy splitting is compared with those by the fitted function in Fig. 4.4(a); which is quite satisfactory. The contour of the energy splitting is also given in Fig. 4.5 as a function of the two torsional angles τ_1, τ_2. Although the behavior of the energy splitting ΔU seems to be complicated, it can be analyzed by considering both the through-space and through-bond interaction adequately.

4.3.3 Spin-Orbit Coupling.

The SOC is another important factor for the ISC rate. It should be noted that there are two mechanisms to cause the singlet-triplet mixing, the SOC and HFC. As shown below, the order of magnitude of the SOC element is

about $0.01 \sim 1.0 cm^{-1}$ for the present diradical, which is much larger than that of the typical HFC, about $0.001 cm^{-1}$. We therefore took into account only the SOC in the present treatment.

The SOC elements were calculated on the basis of the full Breit-Pauli Hamiltonian [34]:

$$H_{so} = \frac{e^2\hbar}{2m^2c^2}\{\sum_k \sum_\alpha \frac{z_\alpha}{r_{\alpha k}^3}[(\vec{r}_k - \vec{r}_\alpha) \times \vec{p}_k)] \cdot 1\vec{s}(k) - \sum_k \sum_{j(\neq k)} \frac{1}{r_{kj}^3}[(\vec{r}_k - \vec{r}_j) \times \vec{p}_k] \cdot [\vec{s}(k) + 2\vec{s}(j)]\}; \quad (4.20)$$

where α is the suffix of the nuclei, and j, k are of the electrons. The first and the second terms of H_{so} denote the spin-same-orbit and the spin-other-orbit interactions, respectively. The former corresponds to the one-electron term and the latter to the two-electron term. The algorithm to calculate the SOC integrals has been developed by King and Furlani [35], which ascribes the one-electron SOC integral to the nuclear attraction integral and the two-electron to the electron repulsion using the Gaussian-type basis sets. The wave functions in use have been already obtained in Sec. 4.3 (a), *i.e.* the TCSCF type for the singlet and the ROHF type for the triplet with the 6-31G basis set. These types of the wave functions have been confirmed to satisfy at least the minimal requirement to describe the SOC [36, 37]. Since the singlet and triplet orbitals are not necessarily identical, the corresponding orbital transformation [38] was applied to remove the non-orthogonality between these orbital sets. We calculated the SOC elements between the singlet and triplet states at the different 144 geometries.

As in the case of the energy splitting, the SOC elements were also found to exhibit quite complex behavior along the path of conformational change. However, we can interpret this behavior on the basis of the picture of the orbital interaction. According to the pioneering work of Salem et al. [39], the SOC elements of the diradicals can be expressed as a product of the two factors: the overlap $S_{ab} = < \psi_a \mid \psi_b >$ and the matrix element of the angular momentum $< \psi_a \mid \vec{l} \mid \psi_b >$, where ψ_a and ψ_b correspond to the GVB orbitals. The former S_{ab} represents the weight of the ionic character contained in the singlet state, which is one of the dominant factors in the diradical SOC. The latter $< \psi_a \mid \vec{l} \mid \psi_b >$, the angular momentum element, increases as the orientation of the orbitals approaches to be perpendicular to each other and as the distance becomes close. Such behavior of the vector property is similar to that of the vector product of the two orientations.

Since the overlap integral was already expressed by the analytic function above, we only discuss on the angular momentum term here. According to the above discussion on the overlap S_{ab} and the singlet-triplet splitting ΔU, the GVB orbitals of the diradical, ψ_a and ψ_b, are not necessarily localized

at the radical sites and spread onto the other atoms by the through-bond interaction. This implies that the angular momentum element originated from the through-bond interaction cannot be neglected in constructing the analytical function. Therefore, the functional form of the angular momentum element $\vec{L}$ between the two GVB orbitals was given in the following:

$$
\begin{aligned}
\vec{L} &= <\phi_1 \mid \vec{l} \mid \phi_2> = \vec{L}_{TS} + \vec{L}_{TB} + \vec{L}_{HE} \qquad (4.21)\\
\vec{L}_{TS} &= x_1(\vec{e}_{2p} \times \vec{e}_{5p})e^{-x_2 r_{25}} + x_3(\vec{e}_{2p} \times \vec{e}_{5p})e^{-x_4 r_{15}}\\
\vec{L}_{TB} &= x_5(\vec{e}_{2p} \times \vec{e}_{32})(\vec{e}_{\sigma*} \cdot \vec{e}_{5p}) + x_6(\vec{e}_{32} \times \vec{e}_{\sigma*})(\vec{e}_{\sigma*} \cdot \vec{e}_{5p})\\
&\quad + x_7(\vec{e}_{2p} \cdot \vec{e}_{\sigma*})(\vec{e}_{54} \times \vec{e}_{5p}) + x_8(\vec{e}_{2p} \cdot \vec{e}_{3\pi*})(\vec{e}_{3\pi*} \times \vec{e}_{\sigma*})(\vec{e}_{\sigma*} \cdot \vec{e}_{5p})\\
&\quad + x_9(\vec{e}_{2p} \cdot \vec{e}_{\sigma*})(\vec{e}_{\sigma*} \times \vec{e}_{4\pi*})(\vec{e}_{4\pi*} \cdot \vec{e}_{5p})\\
\vec{L}_{HE} &= x_{10}(\vec{e}_{5p} \cdot \vec{e}_{65})(\vec{e}_{62} \times \vec{e}_{2p})e^{-x_{11} r_{65}}\\
&\quad + x_{12}(\vec{e}_{5p} \cdot \vec{e}_{13,5})(\vec{e}_{13,1} \times \vec{e}_{2p})e^{-x_{13} r_{13,5}}\\
&\quad + x_{14}(\vec{e}_{5p} \cdot \vec{e}_{14,5})(\vec{e}_{14,1} \times \vec{e}_{2p})e^{-x_{15} r_{14,5}};
\end{aligned}
$$

where $x_1 \sim x_{15}$ are the parameters which have been determined using the *ab initio* results with the least square fitting as follows:

$$
\begin{array}{lll}
x_1 = 1.111 \times 10^3, & x_2 = 1.036, & x_3 = 3.480 \times 10^4,\\
x_4 = 1.873, & x_5 = 3.486, & x_6 = -0.7241,\\
x_7 = 1.546, & x_8 = 0.8841, & x_9 = -2.845,\\
x_{10} = -1.738 \times 10^3, & x_{11} = 1.327, & x_{12} = 21.14,\\
x_{13} = 0.3547, & x_{14} = -1.403 \times 10^3, & x_{15} = 2.100
\end{array}
$$

(unit: cm^{-1} for $x_1, x_3, x_5 \sim x_{10}, x_{12}, x_{14}$, $bohr^{-1}$ for $x_2, x_4, x_{11}, x_{13}, x_{15}$).

The suffixes of the unit vectors ($\vec{e}$) and the distance (r) are the same as Eq. (4.17) and (4.18). It is noted that we introduced the virtual 14-th atom in addition to the 13 real atoms to represent the back lobe of OH anti-bonding orbital (see Fig. 4.1). In Eq. (4.21), the angular momentum elements can be expressed by the sum of three components, i.e. the direct through-space interaction $\vec{L}_{TS}$, the through-bond interaction $\vec{L}_{TB}$ and the hydrogen-enhancing term $\vec{L}_{HE}$. The through-space component $\vec{L}_{TS}$ has the major 2-5 interaction term and minor 1-5 interaction term, as in the case of the overlap function. The vector products in this component correspond the angular momentum elements beween the two radical orbitals and the exponential factors represent the distance dependence. For the through-bond component $\vec{L}_{TB}$, five major terms were taken into account. Those terms consist of vector products and scalar products. The vector products mean the angular momentum elements between the localized orbitals on the atoms. All the vector products refer to the one-center elements on the carbon atoms, and we neglected the two-center elements in the through-bond component $\vec{L}_{TB}$. The scalar products represent the overlapping effect between the neighbor sites to borrow the

amplitudes of the GVB orbitals. The hydrogen-enhancing term $\vec{L}_{HE}$ comes from the enhancement effect of the SOC when the radical orbital on the C_5 atom directly interacts with the H_6 or H_{13} atom through the space. This effect becomes outstanding at some geometries where the radical orbital is oriented to either of the two hydrogen atoms, and has also been observed earlier for another system [36]. The mechanism can be understood by considering that the anti-bonding C_2-H_6 or O_1-H_{13} orbital intervenes between the two radicals. The third term of $\vec{L}_{HE}$ including the virtual atom is neccessary to express the interaction between the radical orbital of the C_5 atom and the back lobe of the OH anti-bonding orbital. This term is not negligible under some closely packed geometries because actually the SOC element on the oxygen atom is fairly large.

The final form of the SOC element is given by the product of the overlap S_{ab} and the angular momentum element $\vec{L}$:

$$\vec{J} = S_{ab} \cdot \vec{L}, \tag{4.22}$$

and the matrix elements of the spin-orbit Hamiltonian between the singlet and triplet states are now expressed as

$$\begin{aligned} < \Psi_S \mid H_{so} \mid \Psi_T(M_s = \pm 1) > &= -\frac{1}{\sqrt{2}}(J_x \pm iJ_y) \\ < \Psi_S \mid H_{so} \mid \Psi_T(M_s = 0) > &= J_z; \end{aligned} \tag{4.23}$$

It is noted that the matrix elements in Eq. (4.5) are complex conjugate to those in Eq. (4.23). The accuracy of the fitted results was shown in Fig. 4.4(b), where the root mean square values were compared. Actually the SOC is a vector quantity, and we determined the parameters $x_1 \sim x_{15}$ with the least square fitting to minimize the norm of the discrepancy vector $\sqrt{\sum_{i=x,y,z}(J_i^{cal} - J_i^{fit})^2}$, not the discrepancy of the norm $\sqrt{\sum_i (J_i^{cal})^2} - \sqrt{\sum_i (J_i^{fit})^2}$, where $\vec{J}^{cal}$ is the *ab initio* value, and $\vec{J}^{fit}$ is the fitting one. The SOC elements obtained from the fitted values were also displayed in Fig. 4.6 as a function of the two torsinal angles, τ_1, τ_2. The very high peak near $(\tau_1, \tau_2) = (0°, 0°)$ is not important to the actual dynamics, because the potential energy at the region is too high. The order of magnitude is about $0.01 \sim 1 cm^{-1}$. We can say that there is a general correlation between the singlet-triplet splitting and the SOC, because both the values are connected by the overlap S_{ab} of the radical orbitals. This means that large coupling elements tend to be distributed on the large splitting area on the potential energy surface and that the coupling elements at the potential crossing region are small in general. This situation is quite different to that of the usual non Born-Oppenheimer radial coupling, where the coupling elements are generally localized on the crossing region. This is possibly one of the factors to

make the ISC occur in the broad range of the potential energy surface, in addition to that the potential energy surfaces are nearly degenerated.

Recently Carlacci et al. [36] calculated the SOC of the trimethylene diradical and found that the geometrical dependence of the SOC is reproduced by a simple semiempirical formula based on the through-space interaction. They concluded that the through-bond coupling behaves in the similar way as the through-space coupling in the trimethylene diradical. Although their result seems to show distinct contrast with our finding for the 1,4-diradical, it is probably due to the difference of through-bond interaction between the 1,3- and 1,4- diradicals. In the 1,3-diradical, the scalar product terms in the through-bond interaction corresponding to Eq. (4.21) are those between one radical orbital and the $\sigma*$ orbital directly connected to the other radical carbon. Therefore, the scalar products can be represented simply by the function of distance between the two radical sites. Thus the complicated behaviors of through-bond interaction terms observed here are inherent to the 1,4- and more longer diradicals.

4.3.4 Intermolecular Interaction.

Finally we give the intermolecular potential functions both for the solute-solvent and solvent-solvent interactions to treat the reaction in solution by the MD calculations. We considered methanol as a typical polar solvent. The solvent model of methanol has been developed by Jorgensen [40], which can describe the hydrogen bonding adequately. The methanol molecule is regarded to be a rigid rotor consisting of three extended atoms: CH_3, O, and H. The geometry was defined as $r(\mathrm{O}-\mathrm{H}) = 0.945\ \mathring{A}$, $r(\mathrm{C}-\mathrm{O}) = 1.430\ \mathring{A}$ and $\angle \mathrm{C}-\mathrm{O}-\mathrm{H} = 108.5°$. The effective charges were taken to be $+0.265$ for CH_3, -0.70 for O and $+0.435$ for H, respectively, and the Lennard-Jones parameters were $\sigma = 3.775\ \mathring{A}$, $\epsilon = 0.207 kcal/mol$ for CH_3 and $\sigma = 3.070\ \mathring{A}$, $\epsilon = 0.170 kcal/mol$ for O. The solute molecule also brings the partial charges on all the nuclei of the 13 atoms and the Lennard-Jones parameters on the 5 united atoms: one OH, one CH and three CH_2 centered at the positions of the nuclei of the oxygen and carbon atoms. The Lennard-Jones parameters of these united atoms, which were determined using the values of Jorgensen et al. [41], are listed in Table 4.9. The partial charges on the solute atoms were determined by the least square fitting to reproduce the electrostatic potential around the solute, calculated with the electronic density matrix obtained from the *ab initio* ROHF wave function for the *tt* conformer (see Table 4.9). We assumed that these parameters are independent of the solute conformation. Those parameters of the solute were tabulated in Table 4.9. The Lennard-Jones parameters of the solute-solvent interaction were obtained by the geometric averages [42]:

$$\sigma_{solute-solvent} = \sqrt{\sigma_{solute} \cdot \sigma_{solvent}},$$

$$\epsilon_{solute-solvent} = \sqrt{\epsilon_{solute} \cdot \epsilon_{solvent}}. \tag{4.24}$$

4.4 Molecular Dynamics Simulation

4.4.1 Method.

On the basis of the averaged potential energy function determined in Sec. 4.3 (a), we carried out the classical MD calculations [43] for the 1,4-diradical C_4H_8O in methanol solvent in order to estimate the ISC rate. The integration of the equation of motion was performed by the velocity version of the Verlet method, with the RATTLE algorithm [44]. The constraint was introduced for all the bond lengths in the flexible solute molecule; that constraint had been confirmed to have little influence on the structure and dynamics [45]. We neglected the high-frequency intramolecular stretching vibrations to lengthen the step size of time in the integration, because the long-time simulation is preferable to consider the slow ISC. The time step of the integration was thus taken to be $0.5fsec$. The periodic boundary condition was applied with the box length of 25.9 $\mathring{A}$. Each cubic cell contains one C_4H_8O diradical and the 228 methanol molecules. The density is thus $0.70g/cm^3$.

The solvent molecule was regarded as a rigid rotor with a simple three-point model as noted above. Thus we introduced the quaternion parameters to describe the solvent rotation [46]. The potential tapering method [47] was employed to cut off the long-range Coulombic interactions between the solute and solvent molecules as well as the solvent and solvent. The interaction potentials were modified by multiplying the tapering function $\sigma(\xi)$:

$$\sigma(\xi) = \begin{cases} 1 & for \quad \xi < 0 \\ 1 - \xi^3(10 - \xi(15 - 6\xi)) & for \quad 0 < \xi < 1 \\ 0 & for \quad 1 < \xi; \end{cases} \tag{4.25}$$

where

$$\xi = (R_{CM} - R_T)/(R_C - R_T).$$

R_{CM} denotes the distance of the centers of mass, and we set the cut-off distance R_C to be a half of the box length and $R_T = 0.9R_C$. The tapering function damps the bare interaction potential in $R_{CM} > R_T$ and vanishes the interaction in $R_{CM} > R_C$ continuously both for the potential and for its derivative. This implementation greatly improves the condition of the energy conservation.

The procedure of the MD calculations is as follows. First we initiated the equilibration runs independently for the nine configurations of the solute fixed. After the equilibrium condition of $300K$ was achieved in the solvent, the solute was allowed to move and the equilibration runs were continued. In this way the equilibrium conditions of the whole solution were accomplished

for the nine different isomers of the solute. Then the nine different trajectories were calculated from these initial conditions during $35psec$. During these runs, some conformational transitions of the solute were observed. We split the sequential files of the configuration into the different solute isomers to analyze them separately.

4.4.2 Feature of MD Trajectories.

We now show the results of the MD trajectory calculations to characterize the solute molecular motion in the present systems. Figure 4.7 is the time profile of a typical trajectory as displayed by the time propagation of the two torsional angles τ_1 and τ_2. We discuss the conformational transition between the solute isomers, because the comparison between the rate of the conformational transition and that of the ISC gives one of the important characteristics of this reaction. As seen in Fig. 4.7, the conformational transitions are surely observed during the time scale of the MD calculations and it was found that the transition along τ_1 occurs much more frequently than that along τ_2. Using the trajectory results for the methanol solution, the transition probability was roughly estimated to be $0.13psec^{-1}$ along τ_1, but the probability along τ_2 is too small to be estimated during this simulation. Generally speaking, MD simulation is not suitable to the accurate estimation of such a small probability. Therefore, we estimated the order of the transition probability in another way with the transition state theory. The potential barriers were found to be $1.2 \sim 2.1kcal/mol$ along the torsional coordinate τ_1 and $2.6 \sim 4.1kcal/mol$ along the τ_2 except the region near $(\tau_1, \tau_2) = (0°, 0°)$. On the other hand, the vibrational frequencies along these torsional motions were calculated to be $530cm^{-1}$ for τ_1 and $720cm^{-1}$ for τ_2, respectively, from the normal mode analysis of the solute molecule presented in Sec. 4.3. Provided that the other force constants except those of the torsions are kept constant during the conformational transition, the rate constant of the isomerization was obtained as follows:

$$\begin{aligned} k(T) &= \nu \exp(-\frac{E^{\ddagger}}{k_B T}) \\ &= \begin{cases} 2.2 \times 10^{12} \sim 4.8 \times 10^{11} sec^{-1} & \text{for } \tau_1 \\ 2.8 \times 10^{11} \sim 2.3 \times 10^{10} sec^{-1} & \text{for } \tau_2 \end{cases} \\ &\quad (\mathrm{T} = 300\mathrm{K}), \end{aligned} \tag{4.26}$$

where ν is the vibrational frequency along the torsion and $E^{\ddagger}$ is the activation energy. This estimation is roughly consistent with the MD simulation. Thus it was confirmed that the transition probability between the solute isomers is much larger than the ISC rate, which is about $10^7 \sim 10^9 sec^{-1}$ for the Norrish type II diradicals [5, 6, 7]. This means that it is adequate to estimate the total ISC rate by thermally averaging the ISC rates of the isomers.

Next we describe the actual situation of the surface crossing on the basis of the MD trajectories. Table 4.9 represents the total statistics of the MD trajectories using the histgram of the solute potential energy. The histgram shows the proportion of the staying time for each the range of solute potential energy. Since we also obtained the observed numbers of the surface crossing for the corresponding energy ranges, we estimated the mean free time of the surface crossing using the ratio of the above two properties, which is also shown in the table. From the distribution of the mean free time, one can see that the surface crossing occurs nearly as frequently among all the accessible energy ranges. The situation is different obviously to some other reactions including the surface crossing such as the electron transfer, where the crossing is an activated process and can occur with the help of the solvent fluctuation. Table 4.9 also shows the distribution of the averaged SOC element, which surely shows some correlation to the solute potential energy but it is small. Under these considerations, the ISC is not an activated process in this system and it tends to occur uniformly for the solute potential energy. There is an experimental evidence that the ISC rates of the Norrish II diradicals have little temperature dependence [5, 6]. Further, the mean free time of the surface crossing is relatively short about $80fsec$, which is about the same order of the intramolecular vibration. We can imagine that a trajectory crosses over the crossing seam quite frequently for all the range of accessible energies.

4.4.3 Intersystem Crossing Rate Constants.

We analyzed the MD result to obtain the ISC rate on the basis of Eq. (4.8). Using the analytic functions of the singlet-triplet energy splitting ΔU and the SOC element $\vec{J}$ obtained in Sec. 4.3, the ISC rate was calculated for each solute isomer, on the basis of the time correlation function involved in Eq. (4.8), *i.e.* the reaction kernel $k_{tcf}(t)$

$$k_{tcf}(t) = \frac{2}{3\hbar^2} Re < \vec{J}(0)\vec{J}(t) \exp(\frac{i}{\hbar}\int_0^t \Delta U(\tau)d\tau) > . \qquad (4.27)$$

Further, in order to analyze the ISC rate, we examined the two properties involved in $k_{tcf}(t)$, the energy splitting ΔU and the SOC element $\vec{J}$. Thus we calculated the mean energy splitting, $< \Delta U >$, and the root mean square of the SOC, $\sqrt{<\mid \vec{J} \mid^2>}$, and the time correlation function of the energy splitting fluctuation, $< \Delta\delta U(0)\Delta\delta U(t) > = < \Delta U(0)\Delta U(t) > - < \Delta U >^2$. These results were represented in Table 4.9 for each conformer.

As seen in Table 4.9, the ISC rate distributes in the range of $2.3 \times 10^6 \sim 3.5 \times 10^7 sec^{-1}$. The resultant lifetime of triplet diradical, $30 \sim 430nsec$, is consistent with the experiments. As in the table, the conformers with the torsional angle of τ_1 around $-60°$, denoted g^-, have larger rate constants

than those with the angle around 60°, g^+. The rate constants of the trans isomers, denoted as t, lie between those of the two different gauche isomers. The conformational dependence of the ISC rate constants corresponds with the experimental result of Caldwell et al. [9] that the lifetime of gauche conformers is not necessarily smaller than that of trans conformers. Considering the ISC rate constant for each isomer, there seems a slight correlation between the calculated rate constant and the mean free time of the surface crossing given in Table 4.9. For example, the crossing interval of g^-g^+ is four times shorter than that of g^+t, and this result is consistent with the difference of the ISC rate between the two conformers. In order to gain more detailed information on the ISC rate, we analyzed the reaction kernel $k_{tcf}(t)$ and its power spectrum $\tilde{k}(\omega)$. Figure 4.8 shows $k_{tcf}(t)$ and $\tilde{k}(\omega)$ for two of the isomers, g^-t and g^+t (see Table 4.9). The two conformers were chosen as examples that show a distinct difference; the conformer g^-t has the smaller energy splitting while the conformer g^+t has the larger splitting on the average (see Table 4.9 and Fig. 4.5). The difference is clearly distinguished in the spectra $\tilde{k}(\omega)$ obtained by the Fourier transformation in Fig. 4.8. In general, the frequency of the reaction kernel increases with the average energy splitting $< \Delta U >$. The spectra for the g^-t isomer has a very sharp peak at $\omega = 0cm^{-1}$ and no component at the high frequency region, $\omega > 500cm^{-1}$. On the other hand, a broad peak is observed at the region of $0 \sim 1000cm^{-1}$ for the spectra of the g^+t isomer. The ISC rate constant is given by $\tilde{k}(0)$, the $\omega = 0$ component of the spectra, according to Eq. (4.8). When we consider the time profile of the reaction kernel $k_{tcf}(t)$ from Fig. 4.8, it is found that the reaction kernel of g^-t decays with the time scale of $0.1psec$ while that of g^+t damps very rapidly with oscillation. In order to characterize the time profile of the reaction kernel, we introduced its correlation time τ_k

$$\tau_k = \frac{1}{<|\vec{J}|^2>} \int_0^\infty < \vec{J}(0)\vec{J}(t) \exp(\frac{i}{\hbar}\int_0^t \Delta U(\tau)d\tau) > dt. \qquad (4.28)$$

The ISC rate constant is represented by the product of τ_k and averaged SOC element $<|\vec{J}|^2>$:

$$k = \frac{2}{3\hbar^2} <|\vec{J}|^2> \tau_k. \qquad (4.29)$$

Table 4.9 includes the τ_k and $\sqrt{<|\vec{J}|^2>}$ for each isomer. We found that the root mean square of the averaged SOC element $\sqrt{<|\vec{J}|^2>}$ does not so vary within $0.1 \sim 0.2cm^{-1}$ while the τ_k distributes in the range of $2.4 \sim 102.3fsec$.

We give a brief discussion on the behavior of $\Delta U(t)$ and $\vec{J}(t)$ characterizing the reaction rate. The mean energy splittings $< \Delta U >$ have the plus sign except for the g^-g^+ and tg^+ isomers, indicating that the singlet state is more stable than the triplet on the average. The magnitude of $|< \Delta U >|$ is about $0.01kcal/mol \sim 1.0kcal/mol$, which corresponds to the oscillation pe-

riod of $10 \sim 0.1 psec$ of the exponential function $\exp(\frac{i}{\hbar}\int_0^t \Delta U(\tau)d\tau)$. In particular the g^-g^+, g^-t and tt conformers have small values both for $<\Delta U>$ and the fluctuation $\sqrt{<\delta\Delta U^2>}$. Such small splitting and long period are apparently derived from the near degeneracy of the potential energy surfaces. It would be meaningful to compare the correlation times for the energy splitting fluctuation τ_U

$$\tau_U = \frac{1}{<\delta\Delta U^2>}\int_0^\infty <\delta\Delta U(0)\delta\Delta U(t)>dt \tag{4.30}$$

and the SOC element with τ_k, because the time dependent behaviors of these quantities within the time scale of τ_k appear in the ISC rate as seen in Eq. (4.8). The correlation time τ_U is rather longer than τ_k except for the conformers having the g^- form around the C_2-C_3 bond. It was also found that the correlation time of the SOC is generally longer than τ_U. Actually we have calculated the time correlation function of the SOC element $<\vec{J}(0)\vec{J}(t)>$ for all the conformers and observed that it declines very slowly with the time scale of $0.1 \sim 0.3 psec$. In the case of the energy splitting, it fluctuates around the mean value $<\Delta U>$ and the time correlation $<\delta\Delta U(0)\delta\Delta U(t)>$ shows relatively rapid damps, while in the case of the SOC its vector orientation is defined roughly with the skeleton of the solute molecule and is conserved to some extent to bring about the long-time tail of the time correlation function $<\vec{J}(0)\vec{J}(t)>$. The time correlation function of the energy splitting fluctuation is thus more sensitive to the dynamics of the solute molecule, although that of the SOC element also plays an important role to the rate as discussed in the following section.

Finally we have calculated the ISC rate constants on the basis of the TST approximation introduced in Sec. 4.2(b), and the resultant rate constants k^{TST} were summarized in Table 4.9. Compared with the rate constants obtained by Eq. (4.8), the TST approximation gives rather good estimates of the ISC rates, though the rates are overestimated except for the g^-g^+ and g^-t conformers. This result provides important insight to the dynamic effect on the ISC rates because such an effect is discarded in the TST approximation. We will discuss on the TST approximation in detail in the next section.

4.5 Discussion

4.5.1 Mechanism of Intersystem Crossing.

As discussed in Sec. 4.3 on the electronic structure of the diradical, the singlet and triplet energy surfaces are nearly degenerated and the SOC element tends to increase at the large energy splitting region. Since this system has such peculiar characters for the nonadiabatic transion, we have to elucidate how

these features influence the reaction rate, by considering the order of the time scales characterizing the nonadiabatic transition and the molecular motion.

Though the ISC rates are quite slow ($10^6 \sim 10^7 sec^{-1}$), the survival time at the transition region, which is a crucial factor to determine the rates, is much faster in the order of magnitude. We consider here the time profile of the reaction kernel $k_{tcf}(t)$ introduced in Sec. 4.4 (c), because $k_{tcf}(t)$ represents the time-dependent behavior of the transition. The exponential factor $\exp(\frac{i}{\hbar}\int_0^t \Delta U(\tau)d\tau)$ involved in the reaction kernel $k_{tcf}(t)$ of Eq. (4.27) is often used to express the off-diagonal element of the density matrix, which means the coherence between the two states. Thus extending the interpretation to the case of the variable coupling element $\vec{J}(t)$, we can regard the correlation time of the reaction kernel τ_k as the coherence time between the singlet and triplet states during the transition. The electronic transition is completed approximately within the time scale, about $2 \sim 100 fsec$ for various conformers. It should be noted that the correlation time τ_k was actually obtained by thermal average of the oscillating functions and the statistical "dephasing" is also crucial to determine the time scale besides the dynamical behavior at the transition region. Thus we will discuss the dynamics at the transition region more extensively in the following. In the expression of the reaction kernel $k_{tcf}(t)$ of Eq. (4.27), the dynamical factor manifests itself through the time propagation of the singlet-triplet energy splitting $\Delta U(t)$ and the SOC element $\vec{J}(t)$.

We consider first the energy splitting $\Delta U(t)$, since it is more sensitive to the molecular motions as noted previously. As seen in Eq. (4.27), the energy splitting ΔU is involved in the reaction kernel $k_{tcf}(t)$ as an exponential factor. We displayed the time profiles of the characteristic function of ΔU

$$\psi_U(t) = < \exp(\frac{i}{\hbar}\int_0^t \Delta U(\tau)d\tau) > \tag{4.31}$$

for the g^-t and g^+t conformers in Fig. 4.9. In order to examine whether $\Delta U(t)$ can be regarded as the Gaussian process in the present system, we performed the cumulant expansion for $\psi_U(t)$ and truncated it at the second order, *i.e.*

$$\begin{aligned}\psi_U^{cum}(t) &= \exp[\frac{i}{\hbar} < \Delta U > t - \frac{1}{\hbar^2}\int_0^t dt_1 \int_0^{t_1} dt_2 < \delta\Delta U(t_1)\delta\Delta U(t_2) >] \\ &= \exp[\frac{i}{\hbar} < \Delta U > t - \frac{1}{\hbar^2}\int_0^t d\tau (t-\tau) < \delta\Delta U(0)\delta\Delta U(\tau) >] \end{aligned} \tag{4.32}$$

where $< \Delta U >$ and $< \delta\Delta U(0)\delta\Delta U(\tau) >$ have been obtained already. In Fig. 4.9, the truncated characteristic functions $\psi_U^{cum}(t)$ are shown. Although the $\psi_U^{cum}(t)$ for the g^-t and g^+t seems to reproduce the initial decaying behavior of $\psi_U(t)$ to some extent, we found that the truncation at the second order leads to a significantly faster decay of the characteritic functions for

some conformers. These imply that dynamical behavior of $\Delta U(t)$ is not expressed adequately as the Gaussian process. Recently Borgis et al. [22] employed the cumulant expansion to the identical rate formula with Eq. (4.8) and successfully estimated the reaction rate by truncating it at the second order in a model nonadiabatic proton transfer, which shows a marked contrast with the present case. We can see that this difference is derived from that of the physical situations underlying the rate formula. In the nonadiabatic proton transfer treated by Borgis et al., the energy splitting between the reactant and product states is originated by the asymmetric configuration of the solvent molecules with respect to the solute, not by the solute geometry itself. Since the energy splitting is determined as the accumulation of the interaction energies between the solute and many solvent molecules, it is likely to be expressed as the Gaussian process adequately on the basis of the central limit theorem. Further, the correlation time of the energy splitting fluctuation $\delta\Delta U$ was reported to be of the order of $0.1psec$, which is much longer than that of the present case about the order of $10fsec$. Thus in the Borgis' system the time profile of the energy splitting is affected more strongly by the diffusional effect. In the ISC of the diradical, the time profile of the singlet-triplet energy splitting $\Delta U(t)$ is governed dominantly by the potential energy surfaces of the solute geometry itself. Thus there is no strong reason that the Gaussian process is realized in the present system. Actually we observed that the distribution of ΔU for each conformer significantly deviates from the Gaussian form.

When we pay an attention to the short-time behavior of ΔU, another expression is valid for $\psi_U(t)$ as a limiting case. Provided that the energy splitting is nearly constant within a short time scale, the characteristic function $\psi_U(t)$ can be expressed in the same way as the TST approximation presented in Sec. 4.2 (b) in the following form

$$\psi_U^{TST}(t) = < \exp(\frac{i}{\hbar}\Delta U t) >, \tag{4.33}$$

which is compared with the original $\psi_U(t)$ in Fig. 4.10. From the figure one can find that both the time profiles are almost coincident only in the short time range within $40fsec$, although the correlation times obtained by integration of time are apparently different from each other. This result indicates that the dynamics of ΔU does not affect the characteristic function $\psi_U(t)$ within such short time as $40fsec$, and that the decaying behavior of $\psi_U(t)$ is determined dominantly by the statistical distribution of ΔU.

On the basis of these dynamical behaviors, we now discuss the ISC rate in comparison with the TST approximation. As in Table 4.9, the TST reproduces the rates rather well in general, but underestimates the rates of g^-g^+ and g^-t conformers. The TST usually gives an upper limit of the reaction rate, and thus the above two conformers have quite peculiar characteristics.

The TST is based on the picture that the transition is localized on the dividing surface and is independent each other. Compared the correlation times τ_k (in Table 4.9) with the averaged crossing intervals (in Table 4.9(b)), one can find that τ_k is longer than the crossing interval for the two conformers. This means that these conformers survive at the transition region for longer time than the average crossing intervals, and consequently the transition cannot be separated each other. The basic assumption of the TST is broken for these conformers. For the other seven isomers, the assumption seems to be satisfied at least and the TST seems to give an upper limit of the rate. In order to clarify the origin of the deviation, we will discuss the time-dependent behavior of the transition. The reaction kernel of the TST approximation $k_{tcf}^{TST}(t)$ is expressed as follows:

$$k_{tcf}^{TST}(t) = \frac{2}{3\hbar^2} Re < J^2 \exp(\frac{i}{\hbar}\Delta U t) >, \tag{4.34}$$

and we compared it with the original reaction kernel $k_{tcf}(t)$ in Fig. 4.11. We found that the TST approximation $k_{tcf}^{TST}(t)$ reproduces the original $k_{tcf}(t)$ quite well except the long-time tail. This implies that the rapid decay within $20fsec$ seen in the reaction kernel $k_{tcf}(t)$ is reproduced only by the statistical dephasing in the thermal equilibrium. The effect of dynamics is not important within the short time range but governs the long-time behavior of the reaction kernel. According to Fig. 4.11, it is clear that the deviation comes from the long-time tail of the reaction kernel $k_{tcf}(t)$. In the actual $k_{tcf}(t)$ the tail decays after $20fsec$, while in the static $k_{tcf}^{TST}(t)$ the long-time tail retains until about $100fsec$. On the other hand, the Fig. 4.10 shows that $\psi_U^{TST}(t)$ has smaller values than the original $\psi_U(t)$ in the range $t = 20 \sim 100fsec$; which is the opposite situation to the reaction kernel. Therefore, one can find that the deviation of the long-time behavior in the reaction kernel is derived from the dynamics effect of the SOC element $\vec{J}(t)$. The correlation decay of the SOC element actually suppresses the long-time tail. Thus the overestimation of the TST rate constants comes from the fact that the coupling element $\vec{J}(t)$ is not constant during the time of transition. Usually this effect is not considered explicitly as a drawback of the TST, because the survival time at the transition region is quite short in many reactions involving electronic transitions. It should be noted that the drawback of TST is usually attributed to the neglect of recrossing effect in the TST, but it is not the case because the coupling element is quite small in the present case.

4.5.2 Solvent Effect.

Several experiments have been carried out to elucidate the solvent effect on the ISC rate of the Norrish type II diradicals. We will also consider it from a microscopic viewpoint. In order to examine the effect of solvent dynamics,

we have calculated the force-force correlation function acting on the solute atoms defined as

$$\Psi_F(t) = \sum_{i=1}^{N_a} \frac{1}{M_i} < \vec{F}_i(0)\vec{F}_i(t) >; \tag{4.35}$$

where $N_a = 13$, the number of atoms in the solute molecule, and M_i is the mass of the atom i. $\vec{F}_i(t)$ is the force vector that the solvent molecules exert on the atom site i of the solute in the laboratory frame. The $\vec{F}_i(t)$ is regarded as the random force originated from the solvent fluctuation and is related to the solvent friction on the basis of the fluctuation-dissipation theorem. It plays an important role in determining the solute dynamics in solution. Figure 4.12 shows the power spectra $\tilde{\Psi}_F(\omega)$ obtained by the Fourier transformation of $\Psi_F(t)$, where we displayed the average of the spectra of nine solute isomers because all the spectra shapes exhibited a similar behavior. As seen in Fig. 4.12(a), the spectrum has a large component at the low frequency region below $200cm^{-1}$. The high-frequency component up to $800cm^{-1}$ is consequent on the hydrogen bonding between the solute and methanol molecules. Small peaks near $1000cm^{-1}$ are apparently derived from the intramolecular vibration of the solute (see Fig. 4.12(b) discussed below).

The force component with the frequency ω couples with the solute motion characterized by the same frequency. Figure 4.12(b) shows the power spectrum $\tilde{\Psi}_v(\omega)$ of the solute velocity correlation function $\Psi_v(t)$;

$$\Psi_v(t) = \sum_{i=1}^{N_a} M_i < \vec{v}_i(0)\vec{v}_i(t) > . \tag{4.36}$$

The high-frequency peaks observed above $800cm^{-1}$ correspond to the bending vibrations. The two broad peaks at the regions of $0 \sim 400cm^{-1}$ and $400 \sim 800cm^{-1}$ are attributed to the translation-rotation and the flexible chain vibrations of the solute, respectively. It is noted that the spectra do not contain the contribution from the stretching vibrations, because the MD calculations were carried out under the constraint to fix all the bond lengths. Comparing the power spectrum of $\tilde{\Psi}_F(\omega)$ with that of $\tilde{\Psi}_v(\omega)$, it is evident that the solvent motions affect mainly the translational and rotational motions of the solute and the effect on the chain vibration is small even in the protic methanol solvent.

The dynamic solvent effect on the ISC rate manifests itself through changing the time profile of the reaction kernel (see Eq. (4.27), which is determined by the propagation of the singlet-triplet energy splitting $\Delta U(t)$ as well as the SOC element $\vec{J}(t)$. The solvent dynamic effect on the solute translational-rotational motions does not affect the energy splitting or the SOC because they are only the functions of the internal coordinates in the present case. (One may understand that the vector orientation of the SOC element changes with the rotation, but it has no influence to the reaction rate

under no magnetic field, considering the derivation of Eq. (4.8) in Sec. 4.2.) Moreover, as discussed in Sec. 4.4, the correlation time of the reaction kernel τ_k is quite short about $20 fsec$, which corresponds to the period of oscillation with the frequency of about $1700 cm^{-1}$. In such a short time scale, the solvent motion can be regarded as nearly frozen as easily observed from the power spectra of $\tilde{\Psi}_F(\omega)$.

Experimentally it has been found that the lifetimes of the triplet diradicals are generally longer in polar solvents than those in nonpolar solvents [6, 7]. We presume that the solvent effect on the ISC rate mainly comes from the static characters rather than the dynamics. The solvent can influence the free energy surface of the system and consequently the equilibruim population of each conformer. Such effect in turn leads to a change of the averaged ISC rate. Unfortunately the MD trajectory method employed here is not suitable to estimate the equilibrium populations among the conformers. We need to perform another calculation such as Monte-Carlo simulation to be conclusive about the relative populations among the isomers. Another probable factor of the static solvent effects is an influence on the singlet-triplet energy splitting ΔU or the SOC element $\vec{J}$. It is expected that the singlet state is more polarizable than the triplet state in the diradical, because there is another singlet state with the ion-pair character but no other triplet state under the simple diradical picture of the two valence electron system. Since the singlet state tends to be lower in its energy than the triplet state as seen in Table 4.9, the perturbation of the electronic field of the polar solvent may stabilize the singlet state more and enhance the energy splitting. However, in order to estimate the difference of the polarizations, more accurate *ab initio* calculation with a larger basis set will be required. Further, it should be noted that the systems used in the actual experiments are not the same as the simple diradical C_4H_8O treated in the present work. Usually they have a phenyl ring instead of the 6-th hydrogen atom of the diradical $\dot{C}H_2CH_2CH_2\dot{C}\underline{H}OH$, and the substituted phenyl ring is connected directly to one of the radical carbons. This may be an important difference to consider the polarization. We think that the extensive electronic calculation as well as the detailed discussion of the free energy surface will throw light upon the mechanism of the solvent effect on the ISC rate of the Norrish type II diradicals.

4.6 Conclusion

We studied theoretically the ISC of diradical intermediates involved in the Norrish type II reactions in solution. In the diradicals the singlet and triplet states are nearly degenerated each other, and it is not obvious whether the treatment based on the localized transition is applicable for the systems. Thus we calculated the ISC rate using the time-dependent perturbation the-

ory with *ab initio* MO calculations and MD simulation.

First we carried out the *ab initio* calculation for a simple 1,4-diradical $\dot{C}H_2CH_2CH_2\dot{C}HOH$ to obtain the potential energy surfaces of the singlet and triplet states and the SOC elements between them. The singlet-triplet energy splitting and the SOC element vary with the solute geometry in a rather complicated manner, and have *no* correlation to the distance between the two radical sites because of the strong through-bond interaction. Nevertheless, these behaviors were represented with the analytic functions by considering the orbital interaction explicitly.

Using the potential energy surfaces and the SOC elements obtained, the MD calculations were performed for the diradical C_4H_8O in methanol solvent. The MD trajectories show that the surface crossing is not an activated process and occurs at all the accessible energy range. The ISC rate constant was calculated on the basis of the MD trajectories using Eq. (4.8), and the rate constant for each conformer was found to be consistent with the experiments. Analyzing the ISC rate for each isomer, the localized transition is apparently not realized for some conformers. Though the transition is not neccessarily localized, the ISC rate is reproduced fairly well by the TST approximation, which is derived as a limiting case that the molecular motions are frozen during the transition. The deviation from the TST is not due to the recrossing effect as commonly discussed, but from the fact that the coupling element varys with time during the transition.

The solvent effect on the ISC rate was also discussed on the basis of the present MD results. By analyzing the simulation result, we found that the solvent dynamics has little influence to the ISC rate even in protic methanol. We presume that the static effects give a dominant contribution to the solvent effect. Such factors to affect the rate as the static perturbation on the free energy surface or on the singlet-triplet energy splitting will be discussed more extensively in a further stage.

4.7 Acknowledgment.

Numerical calculations were carried out at the IMS Computer Center and Data Processing Center of Kyoto University. This work was supported by the Grants in Aid for Scientific Research from the Ministry of Education in Japan.

4.8 Appendix

The potential function consists in 7 components and and is represented as the sum (see Eq. (4.12)):

$$U = U_{stret} + U_{bend} + U_{vdW} + U_{tors} + U_{wag} + U_{rot} + U_{CH_2}.$$

The first four terms have been explained in Sec. 4.3 (a). The parameters in these terms are tabulated in Table 4.9 (a)~(d). In the following we describe the last three terms.

(1) Out-of-plane wagging of the 6-th hydrogen U_{wag}

$$U_{wag} = A(2\sin\frac{\omega_1}{2})^4 - 2A(2\sin\frac{\omega_1^{(0)}}{2})^2(2\sin\frac{\omega_1}{2})^2;$$

where ω_1 is 6-(2,1,3) out-of-plane angle (see Fig. 4.13(a)).
$A = 0.0258 hartree$. $\omega_1^{(0)} = 0.4247 rad$.

It is noted that the equilibrium position of the wagging angle $\omega_1^{(0)}$ is not zero.

(2) OH rotation U_{rot}

$$U_{rot} = P\cos^2\tau_O + Q\cos\tau_C + R\cos\tau_H;$$

where $P = 3.433 \times 10^{-3} hartree$, $Q = 3.564 \times 10^{-3} hartree$, $R = 3.100 \times 10^{-3} hartree$.

Refering to Fig. 4.13(b), τ_C, τ_H, and τ_O are the torsional angles between OH bond and 2-3 (τ_C), 2-6 (τ_H), and the orbital orientation of the unpaired electron (τ_O), respectively. The direction of the unpaired orbital was defined so as to divide equally the 3-1-6 angle, as seen in Fig. 4.13(c). Each term was derived by considering the bond-bond or bond-radical repulsion.

(3) CH_2 wagging and torsion U_{CH_2}

$$U_{CH_2} = \frac{1}{2}B(2\sin\frac{\omega_2}{2})^2 + CS^2;$$

where ω_2 is 4-(5,11,12) out-of-plane angle (see Fig. 4.13(a)), and

$$S = \frac{\vec{e}_1 \cdot \vec{e}_2}{\mid \vec{e}_1 \mid\mid \vec{e}_2 \mid},$$

as seen in Fig. 4.13(d). $\vec{e}_1 = \vec{LM}$, $\vec{e}_2 = \vec{JK} \times \vec{IK}$.
$B = 0.0149 hartree$. $C = -1.241 \times 10^{-3} hartree$.

The potential energy along the CH_2 wagging and torsion is represented by the two terms. The first term expresses the out-of-plane wagging around the minimum position $\omega_2^{(0)} = 0$. The second term is based on the attractive interaction between the unpaired electron orbital of the 5-th carbon and 3-4 antibonding localized orbital, which expresses the potential along the torsion as well as the wagging. The actual equlibrium position of the wagging angle w_2 deviates slightly from zero because of the second term.

4.9 Figures and Tables

Figure 4.1: Schematic picture of the diradical C_4H_8O with the serial numbers of the atoms. Two torsional angles τ_1 and τ_2 to characterize the isomers were also shown. The 14-th atom (X) is virtual utilized to describe the SOC elements (see Sec. 4.3(c)). It is connected to the oxygen atom O_1 in the opposite side of the 13-th hydrogen H_{13}, and the O_1-X_{14} distance is 1/10 of the O_1-H_{13}. The 33 internal coordinates to define the conformation were given in Table 4.9.

Figure 4.2: Potential energy surface for the averaged state as a function of the two torsional angles τ_1 and τ_2. unit: $kcal/mol$. The other internal coordinates were determined by interpolating the equilibrium geometries, as described in Sec. 4.3(a). The energy level $U = 0$ was defined by the optimized g^+t conformation (see Table 4.9), which has the lowest potential energy. The contour spacing is $1.0kcal/mol$, and the real lines indicate the levels of 5.0 and $10.0kcal/mol$. The nine equilibrium geometries $g^-g^- \sim tt$ were indicated in the figure.

Figure 4.3: Correlation between the square of the GVB orbital overlap S_{ab}^2 and the singlet-triplet energy splitting ΔU. The 144 points displayed in the figure refer to the geometries interpolating the optimized ones.

Figure 4.4: Comparison between the *ab initio* values and the fitted ones. (a) The singlet-triplet energy splitting ΔU. unit: $kcal/mol$. (b) The root mean square of the SOC elements $\sqrt{|\vec{J}|^2}$. unit: cm^{-1}.

Figure 4.5: Contour map of the singlet-triplet energy splitting $\Delta U = U_T - U_S$. The contour spacing is $0.5kcal/mol$. The thick lines show $\Delta U = 0$; the real lines and the broken lines correspond to the regions of $\Delta U > 0$ and $\Delta U < 0$, respectively.

Figure 4.6: Contour map of the root mean square $\sqrt{|\vec{J}|^2}$ of the SOC elements. The contour spacing is $0.1cm^{-1}$.

Figure 4.7: Time profiles of a typical MD trajectory in methanol solvent as a function of (a) τ_1 and (b) τ_2. The regions near 300°, 60°, 180° indicate gauche$^-$, gauche$^+$, and trans configurations of each torsional angle, respectively.

Figure 4.8: Time profiles of the reaction kernel $k_{tcf}(t)$ and their spectra $\tilde{k}(\omega)$. (a) and (b) represent $k_{tcf}(t)$ for the isomers g^-t and g^+t, respectively, and (c) and (d) refer to $\tilde{k}(\omega)$ for the isomers g^-t and g^+t. For the definition of comformers, see Table 4.9.

Figure 4.9: Comparison of the characteristic function $\psi_U(t)$ to its truncated form of the cumulant expansion $\psi_U^{cum}(t)$. (a) refers to the isomer g^-t and (b) to the isomer g^+t. The real line is for $\psi_U(t)$ (see Eq. (4.31)), and the broken line for $\psi_U^{cum}(t)$ (see Eq. (4.32)), respectively.

Figure 4.10: Comparison of the characteristic function $\psi_U(t)$ to its static approximation $\psi_U^{TST}(t)$ The real line is for $\psi_U(t)$ (see Eq. (4.31)), and the broken line for $\psi_U^{TST}(t)$ (see Eq. (4.33)), respectively. The above functions were obtained by averaging those of the nine isomers.

Figure 4.11: The reaction kernel and its TST approximation. The real line is for $\frac{1}{<|\vec{J}|^2>} Re < \vec{J}(0)\vec{J}(t) \exp(\frac{i}{\hbar}\int_0^t \Delta U(\tau)d\tau) >$, the dashed-bar line for $\frac{1}{<|\vec{J}|^2>} Re <\mid \vec{J} \mid^2 \exp(\frac{i}{\hbar}\Delta U t) >$, respectively. The above functions correspond to $k_{tcf}(t)/k_{tcf}(0)$ (see Eq. (4.27)), $k_{tcf}^{TST}(t)/k_{tcf}^{TST}(0)$ (see Eq. (4.34)), respectively. These functions were obtained by averaging those of the nine isomers.

Figure 4.12: Spectra of (a) solute-solvent force $\tilde{\Psi}_F(\omega)$ [a] and (b) intramolecular vibration $\tilde{\Psi}_v(\omega)$.

Figure 4.13: Geometric parameters defining U_{wag}, U_{rot} and U_{CH_2}. (a) the out-of-plane angle w represented as $I-(J,K,L)$. (b), (c) τ_C, τ_H and τ_O for the term of U_{rot}. (d) $\vec{e}_1$ and $\vec{e}_2$ for the term of U_{CH_2}.

Figure 4.1

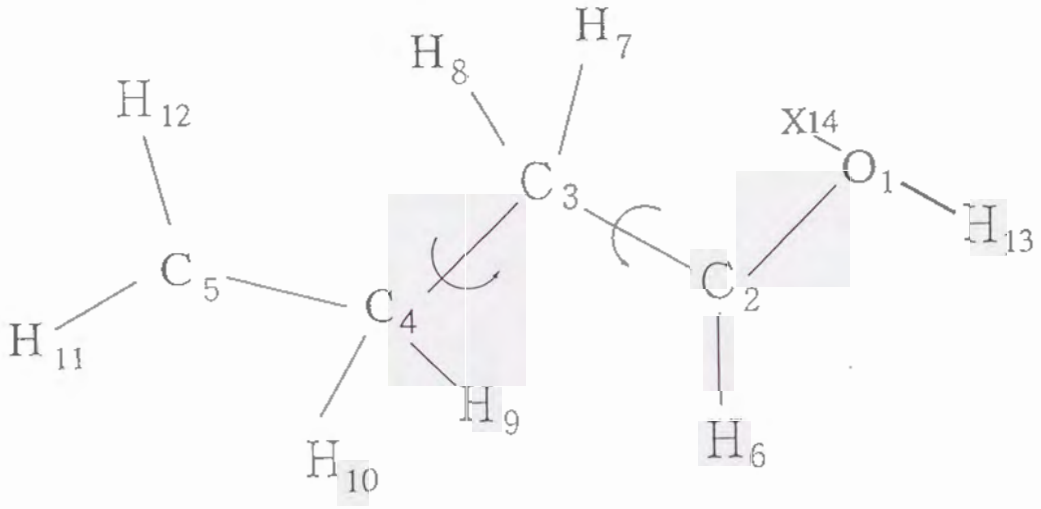

Figure 4.2

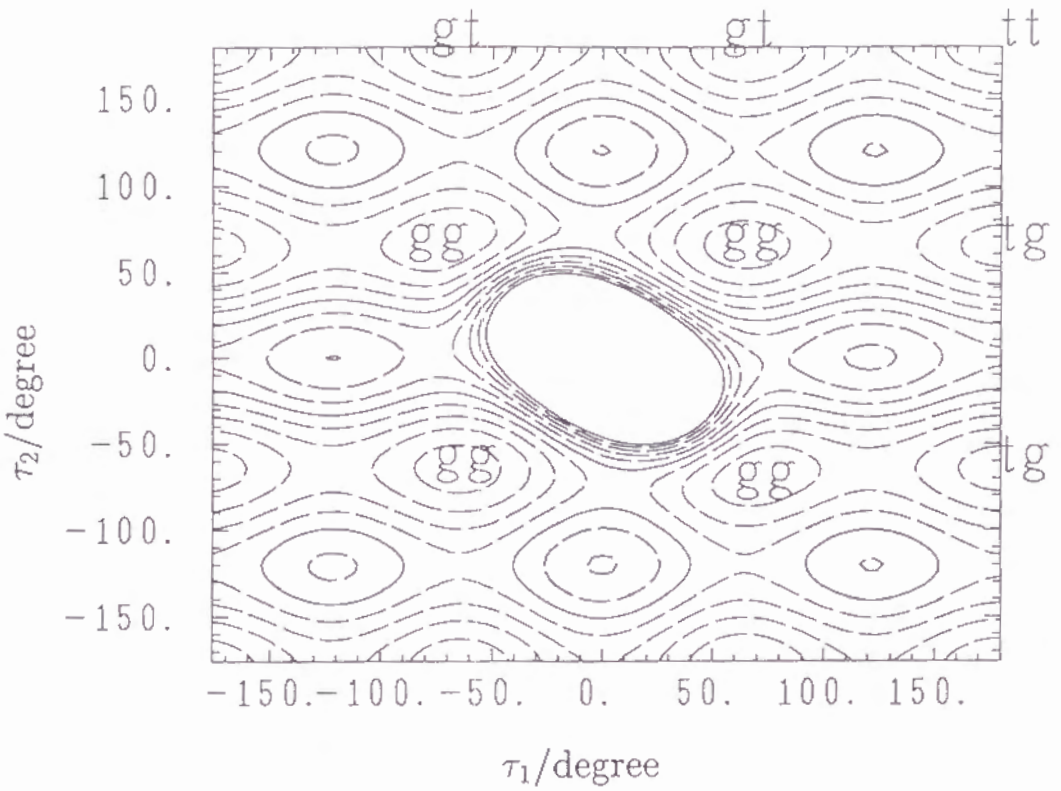
gt
gt
tt
150.
100.
50.
0.
-50.
-100.
-150.
gg
gg
tg
gg
gg
tg
-150.-100. -50. 0. 50. 100. 150.
τ_2/degree
τ_1/degree

Figure 4.3

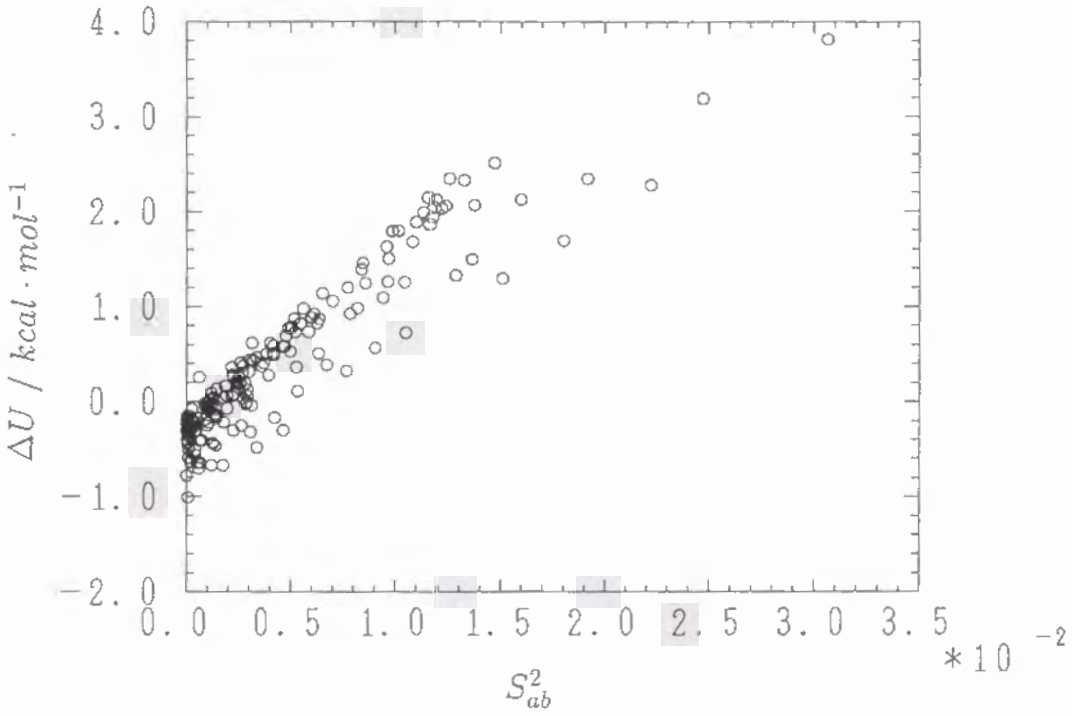

Figure 4.4(a)

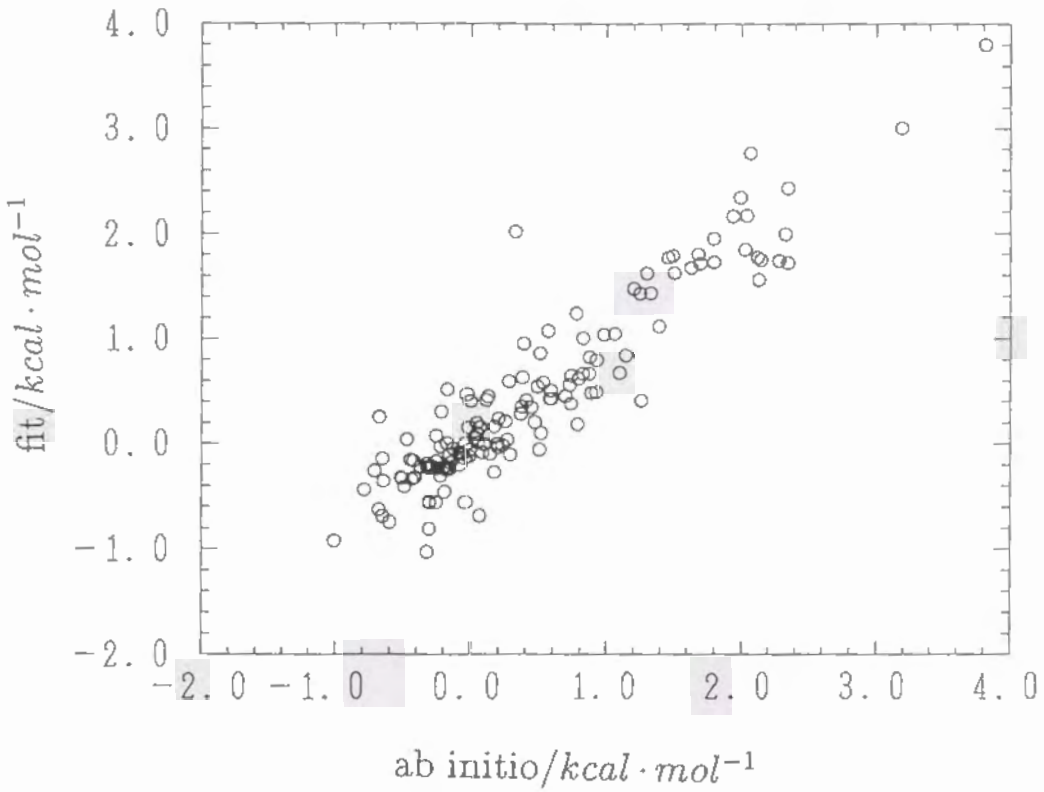
4.0
3.0
2.0
1.0
0.0
−1.0
−2.0
−2.0 −1.0 0.0 1.0 2.0 3.0 4.0
fit/$kcal \cdot mol^{-1}$
ab initio/$kcal \cdot mol^{-1}$

Figure 4.4(b)

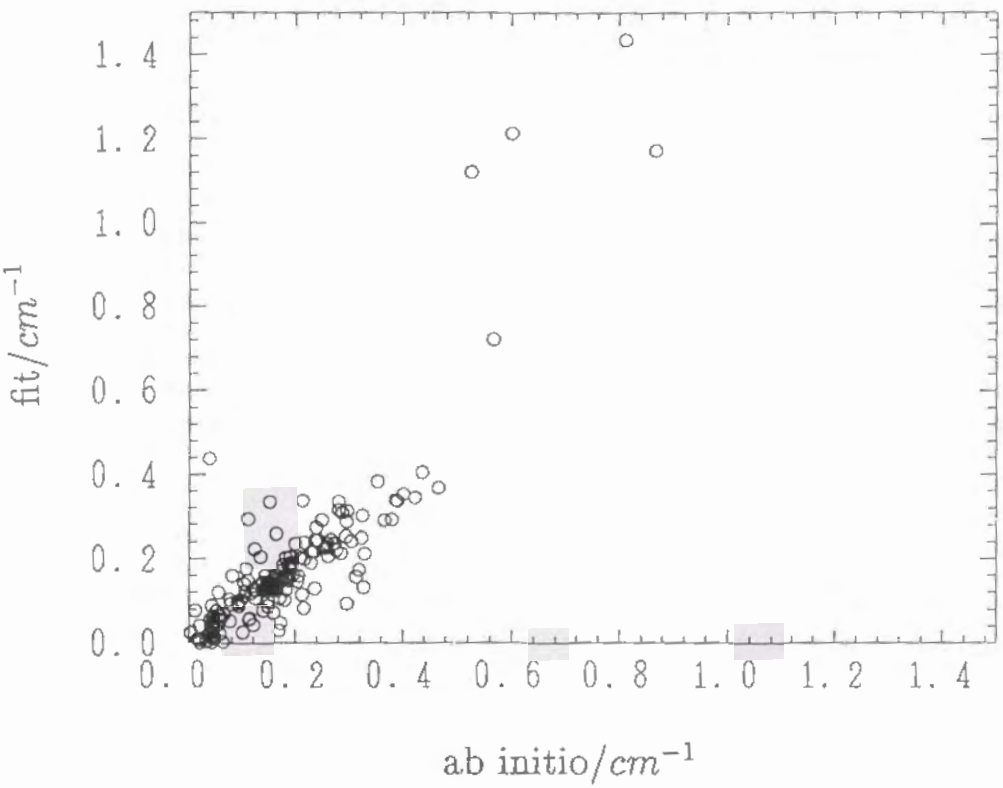

Figure 4.5

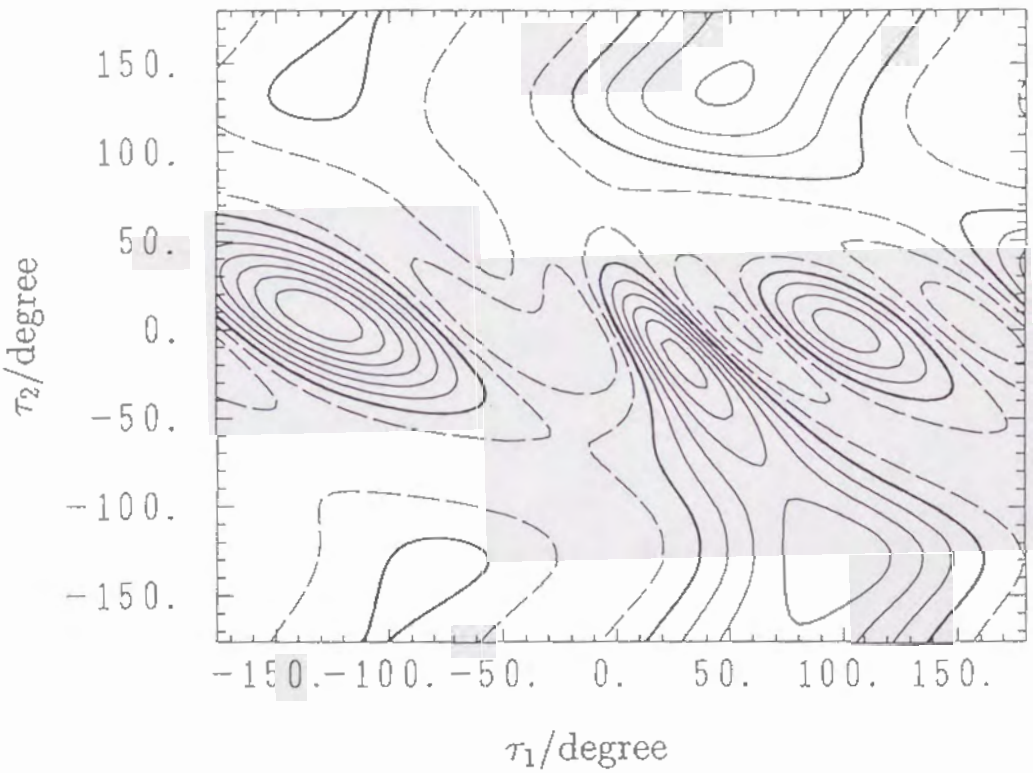
150.
100.
50.
0.
-50.
-100.
-150.
τ_2/degree
-150.-100. -50. 0. 50. 100. 150.
τ_1/degree

Figure 4.6

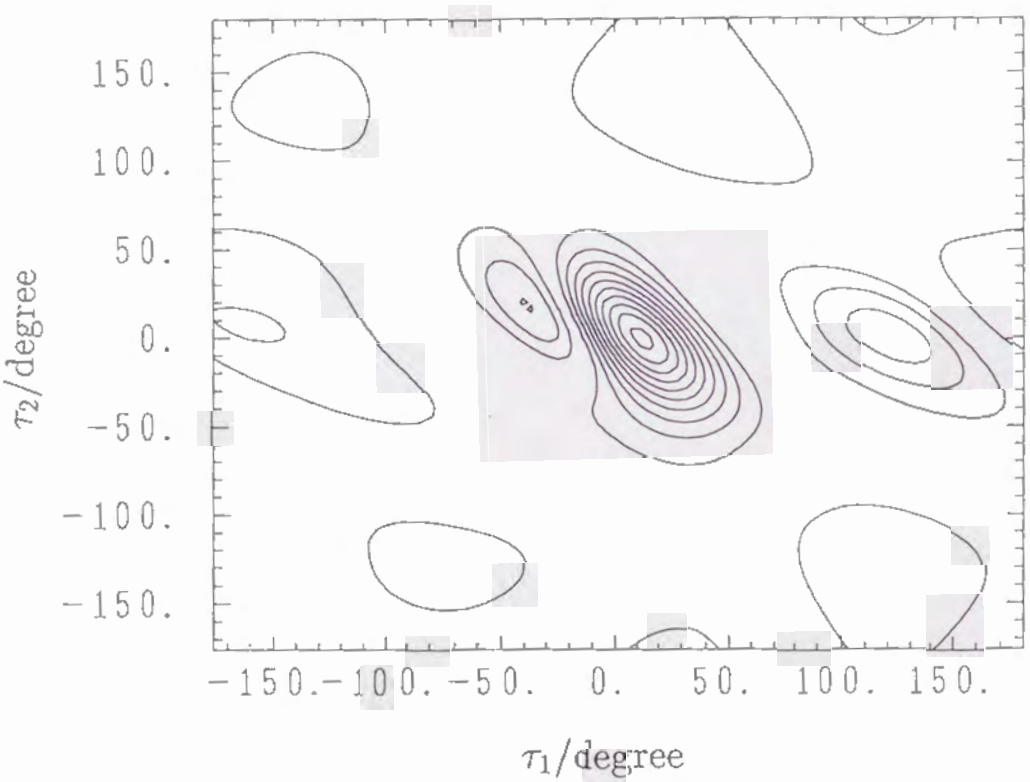
150.
100.
50.
0.
-50.
-100.
-150.
τ_2/degree
-150.-100.-50. 0. 50. 100. 150.
τ_1/degree

Figure 4.7(a)

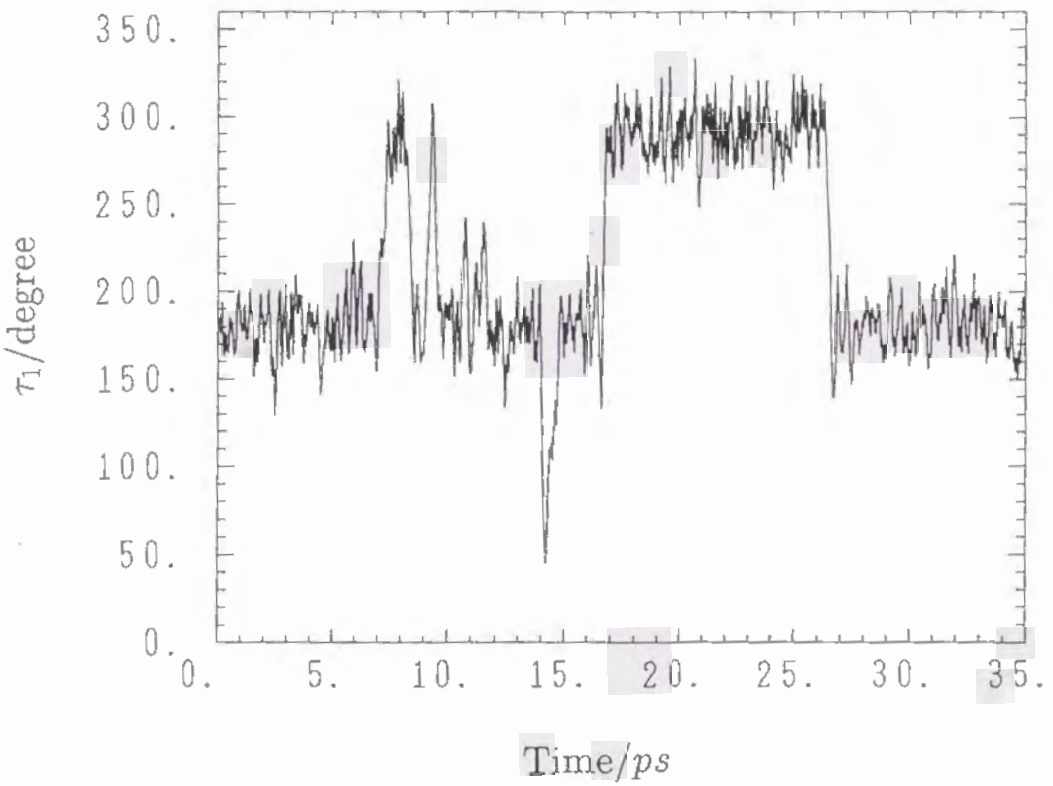
350.
300.
250.
200.
150.
100.
50.
0.
0.
5.
10.
15.
20.
25.
30.
35.
τ_1/degree
Time/ps

Figure 4.7(b)

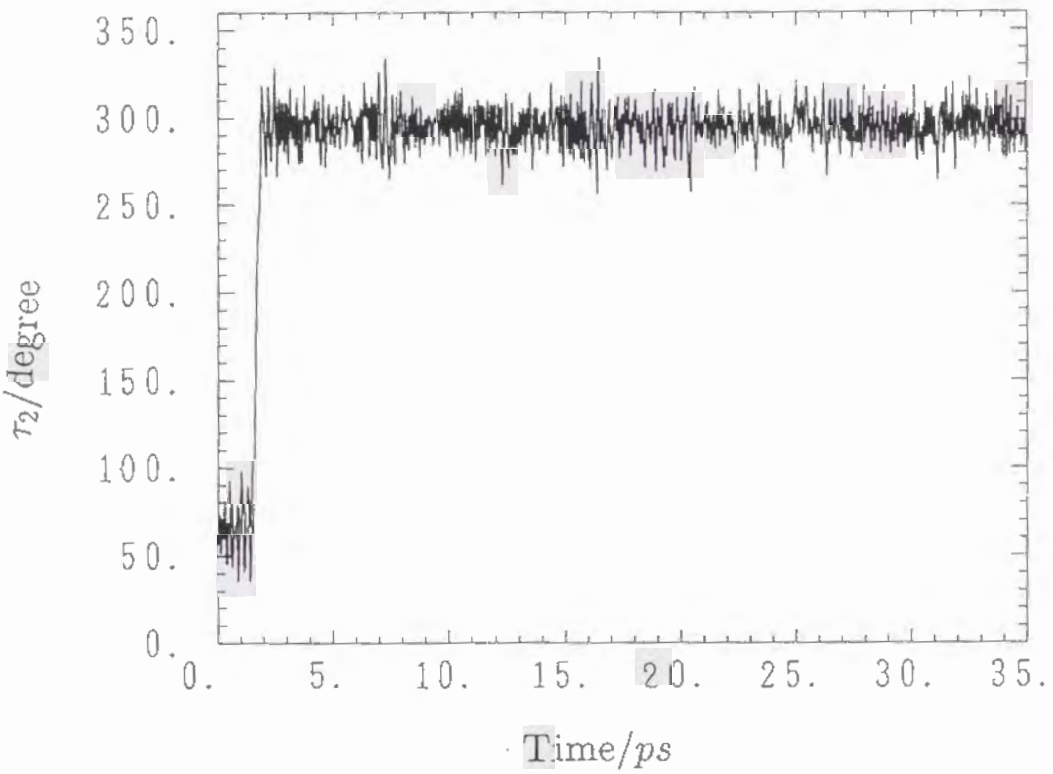
350.
300.
250.
200.
150.
100.
50.
0.
0.
5.
10.
15.
20.
25.
30.
35.
τ_2/degree
Time/ps

Figure 4.8(a)

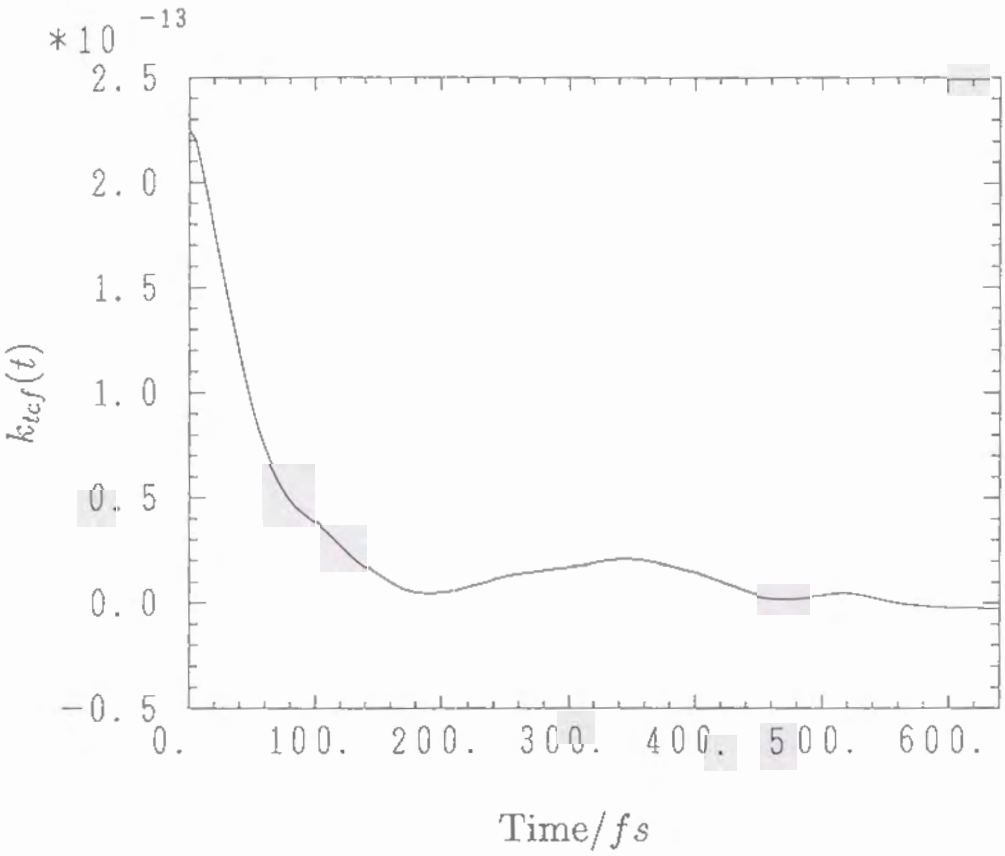

Figure 4.8(b)

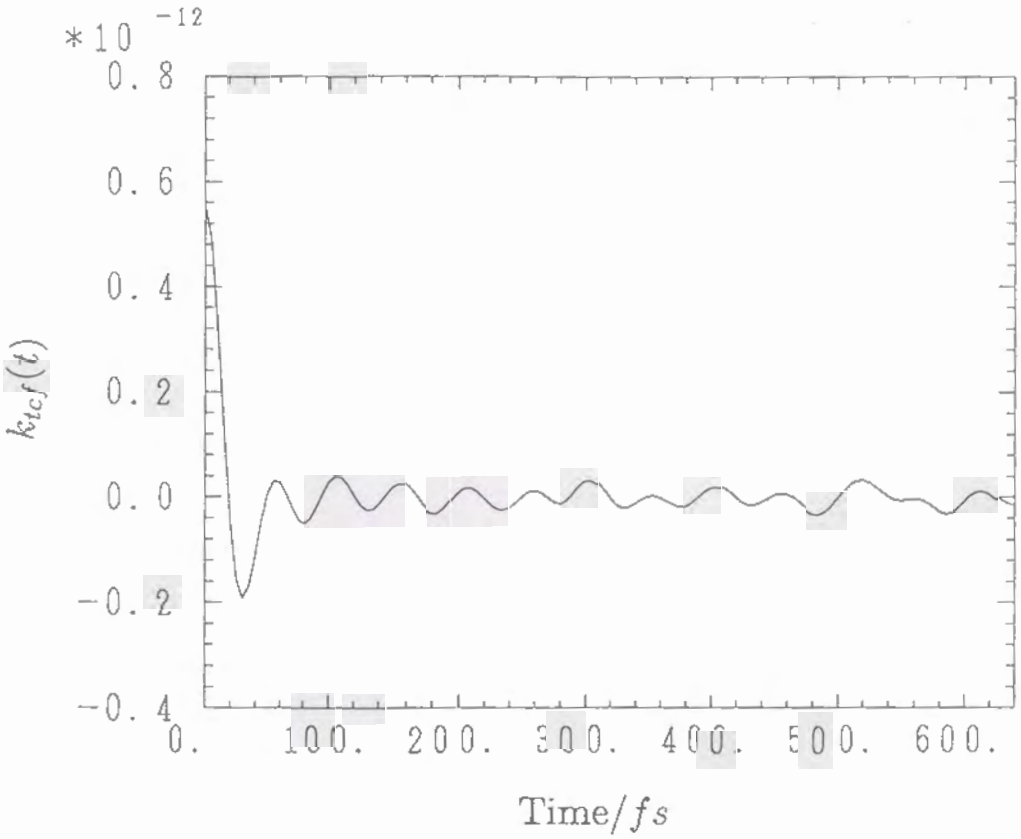

Figure 4.8(c)

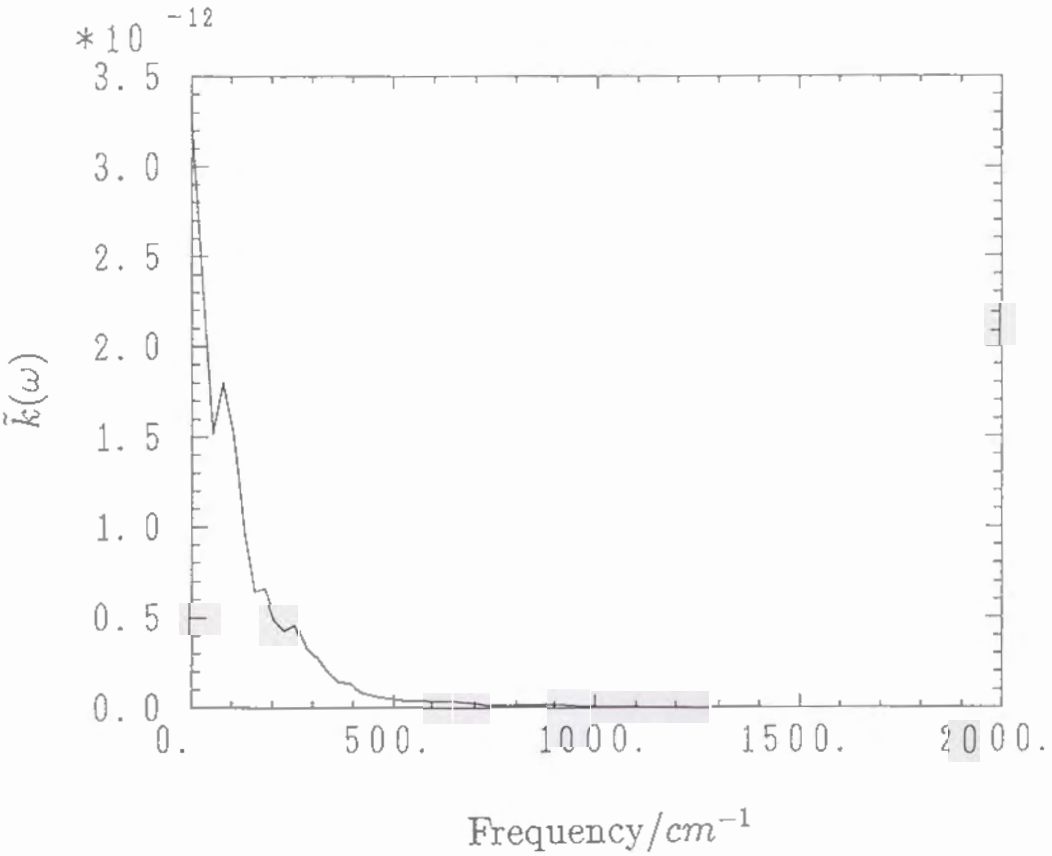
*10 -12
3.5
3.0
2.5
2.0
1.5
1.0
0.5
0.0
0.
500.
1000.
1500.
2000.
$\tilde{k}(\omega)$
Frequency/cm^{-1}

Figure 4.8(d)

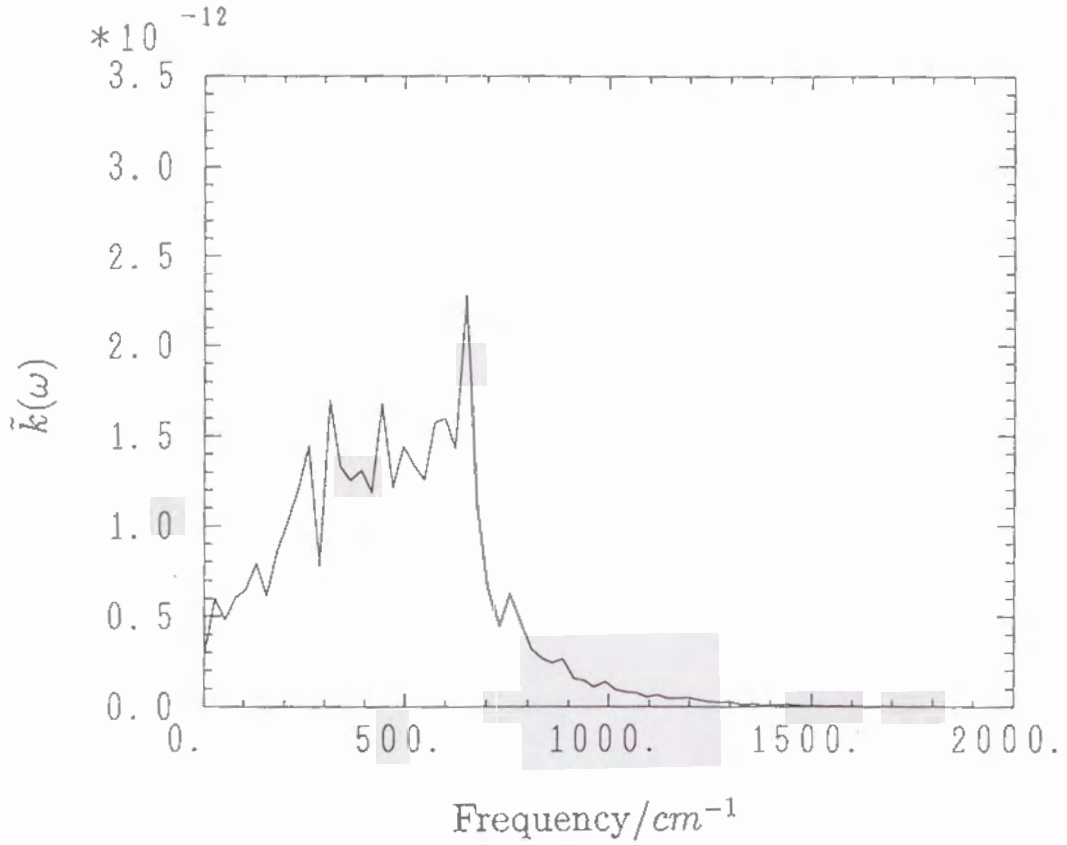
*10 -12
3.5
3.0
2.5
2.0
1.5
1.0
0.5
0.0
0.
500.
1000.
1500.
2000.
$\tilde{k}(\omega)$
Frequency/cm^{-1}

Figure 4.9(a)

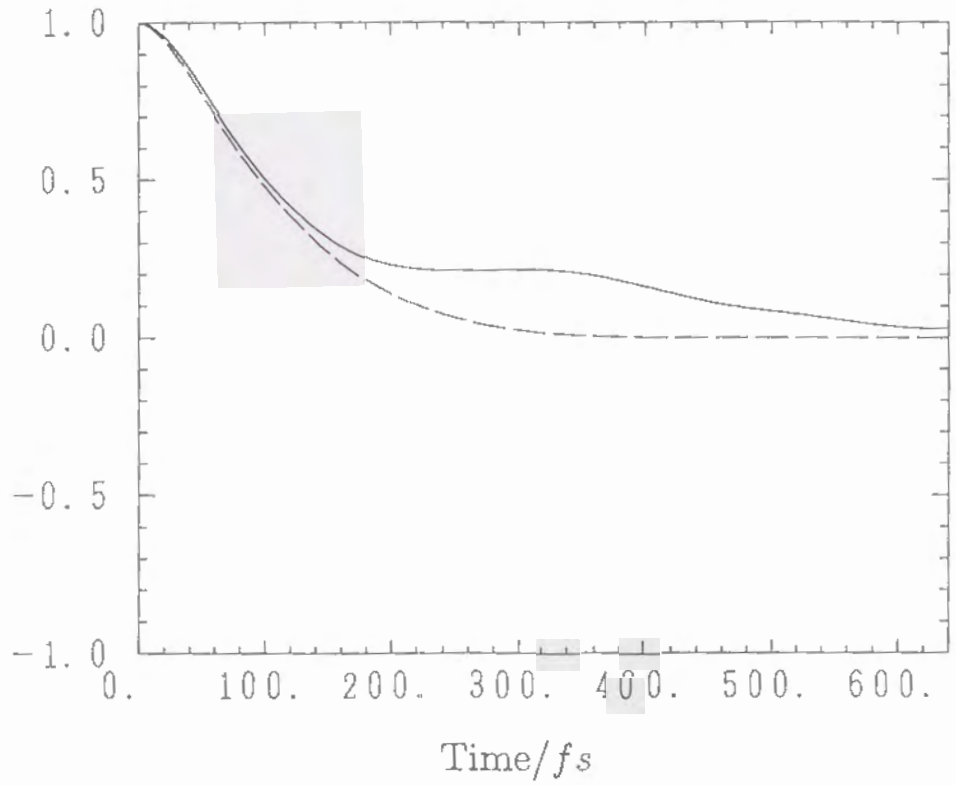

Figure 4.9(b)

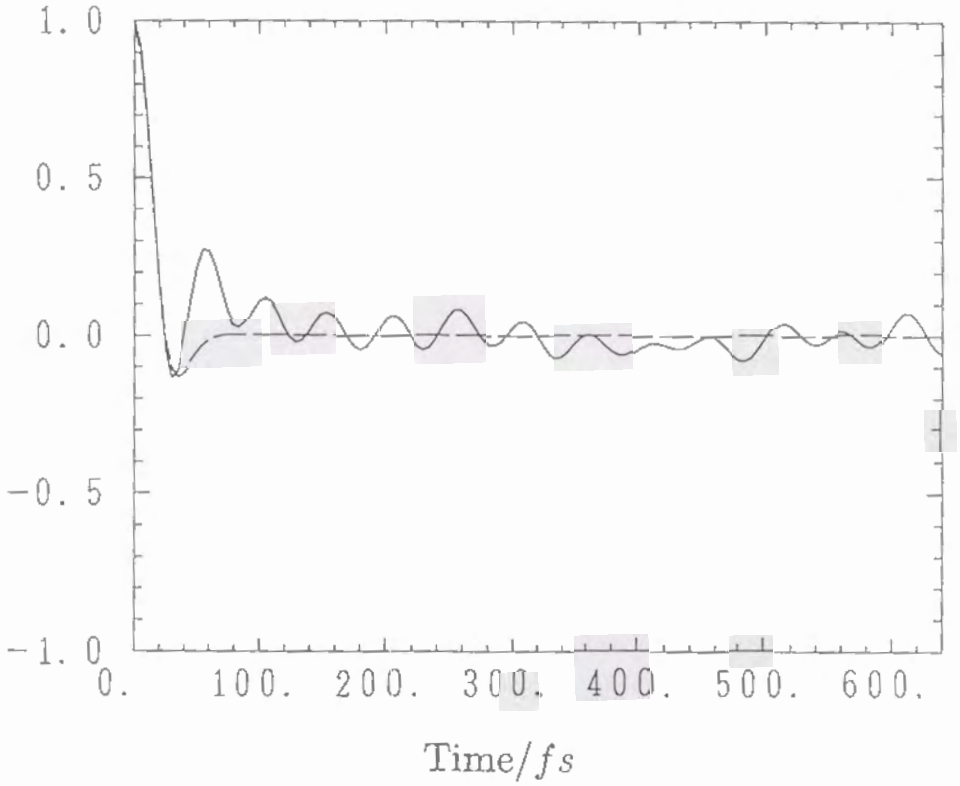

Figure 4.10

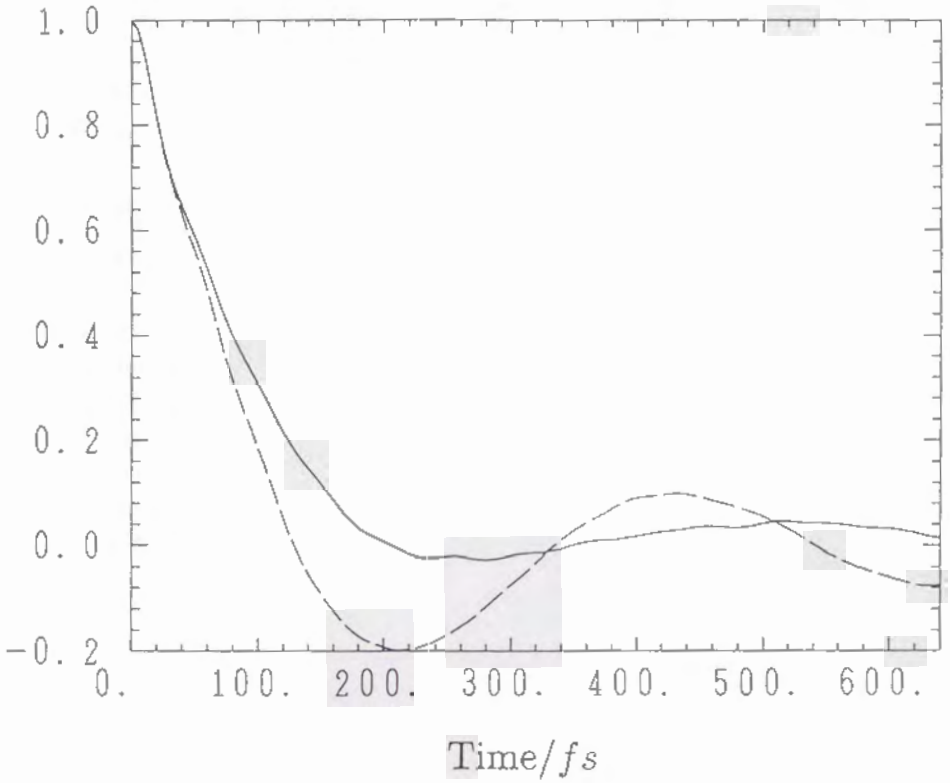

Figure 4.11

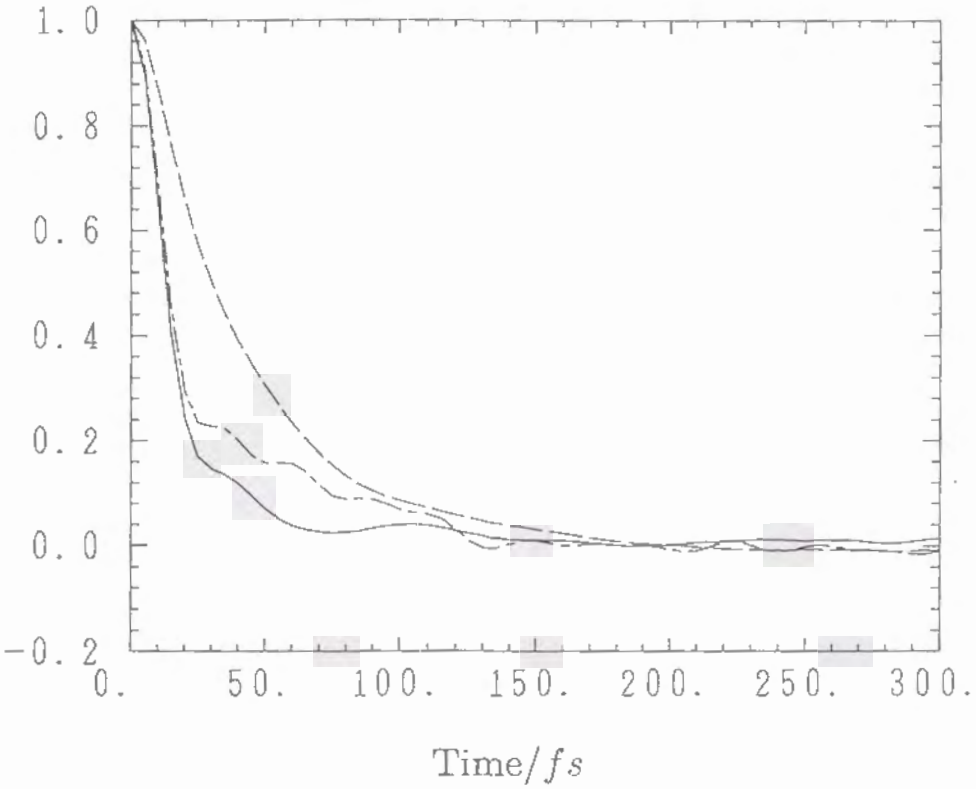

Figure 4.12(a)

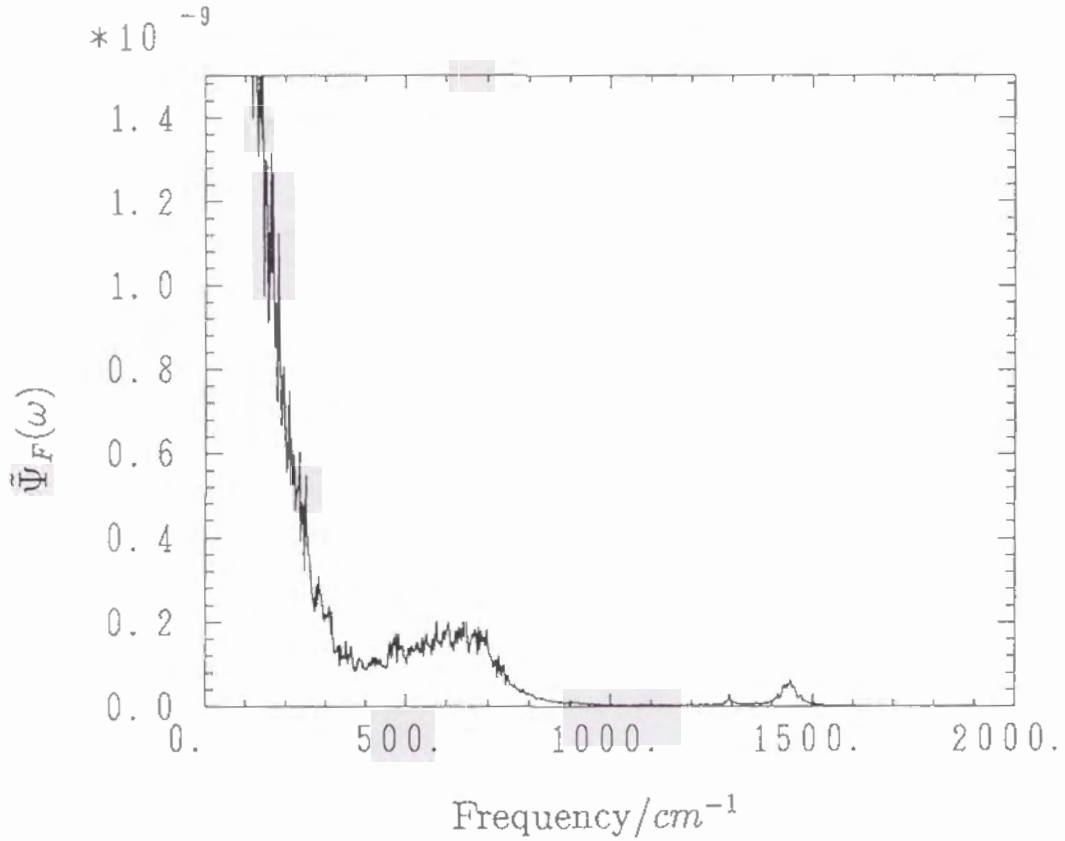
*10 -9
1. 4
1. 2
1. 0
0. 8
0. 6
0. 4
0. 2
0. 0
0.
500.
1000.
1500.
2000.
$\tilde{\Psi}_F(\omega)$
Frequency/cm^{-1}

Figure 4.12(b)

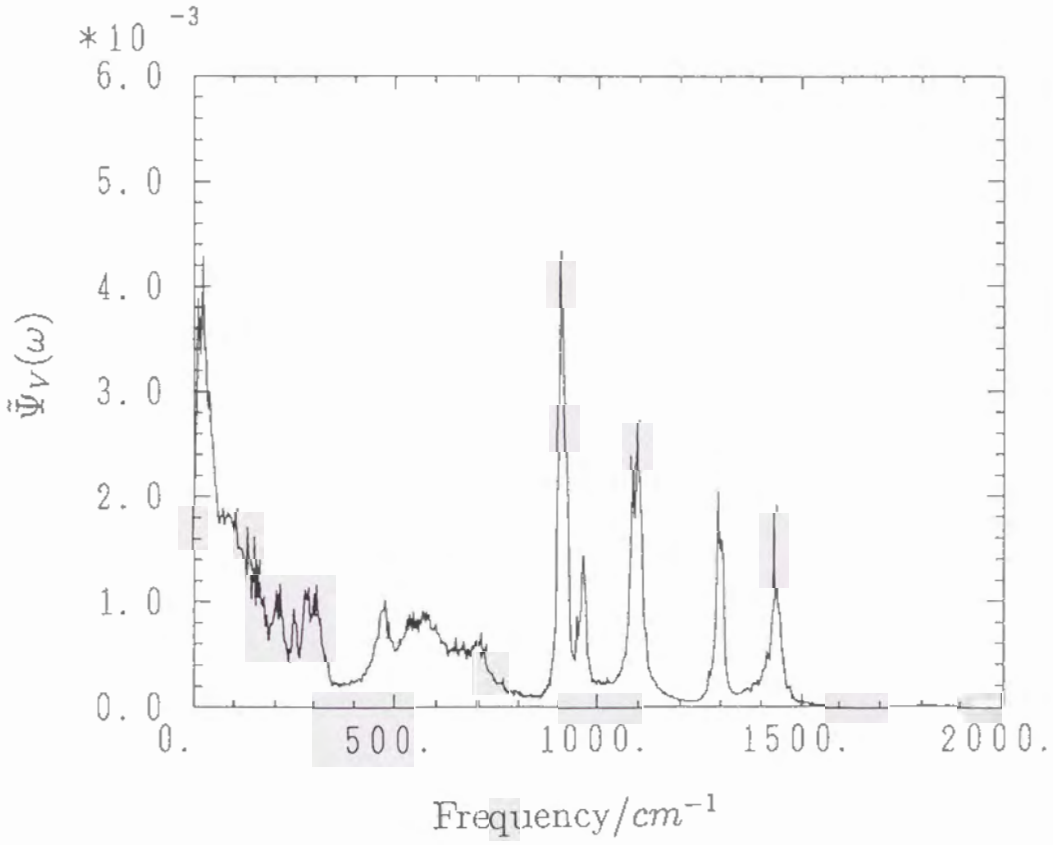
*10 -3
6.0
5.0
4.0
3.0
2.0
1.0
0.0
0.
500.
1000.
1500.
2000.
$\tilde{\Psi}_V(\omega)$
Frequency/cm^{-1}

Figure 4.13(a)

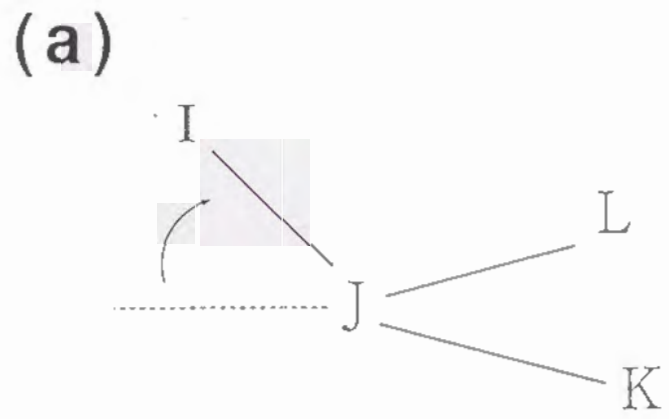

Figure 4.13(b)

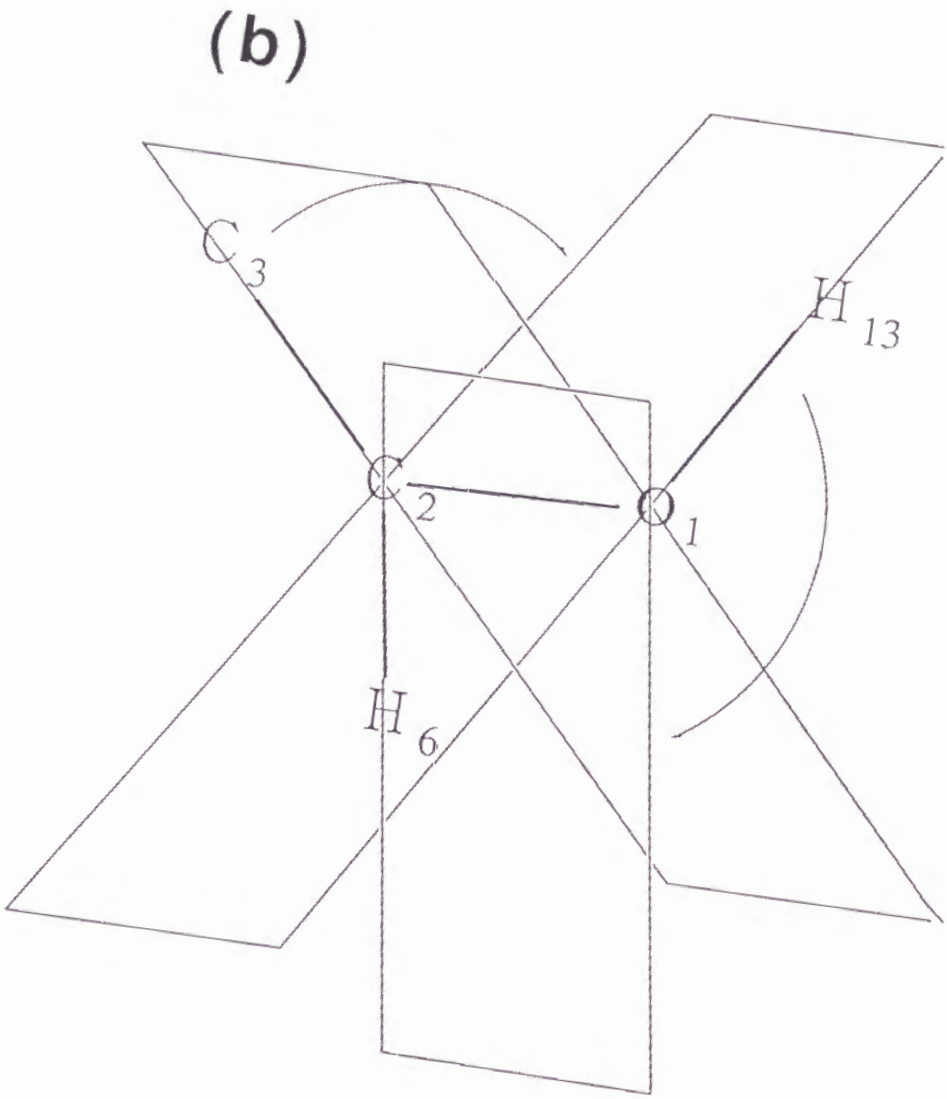

Figure 4.13(c)

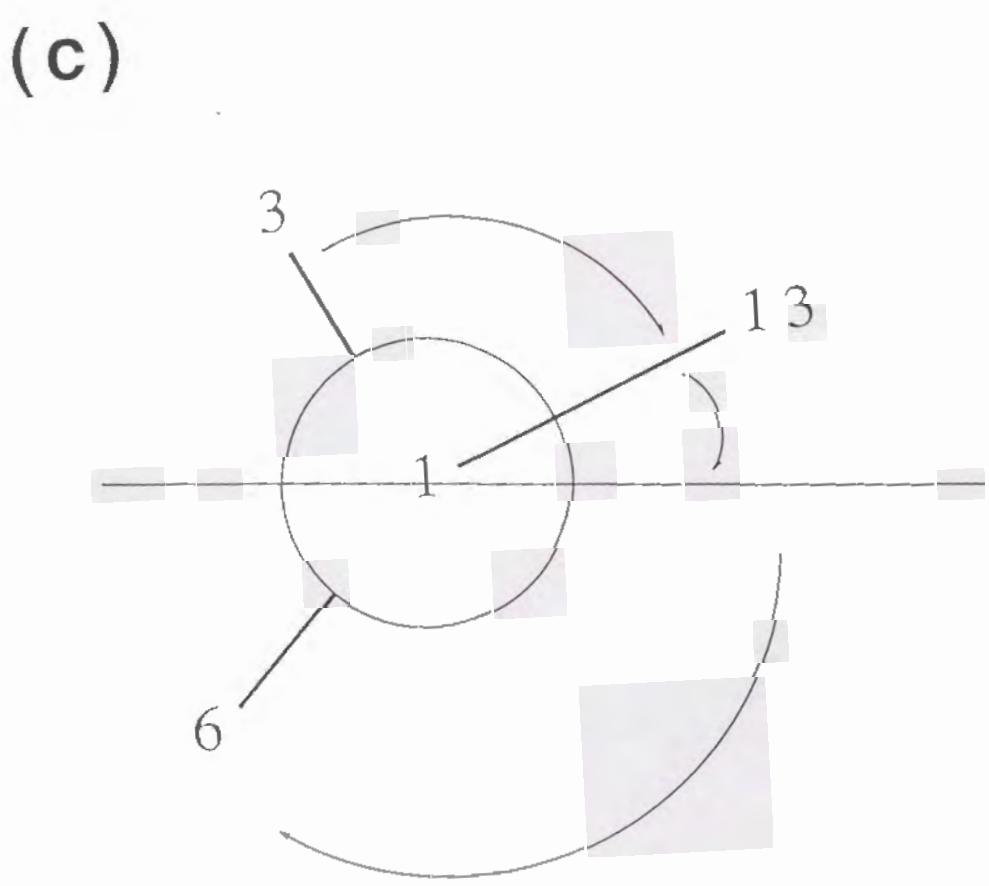

Figure 4.13(d)

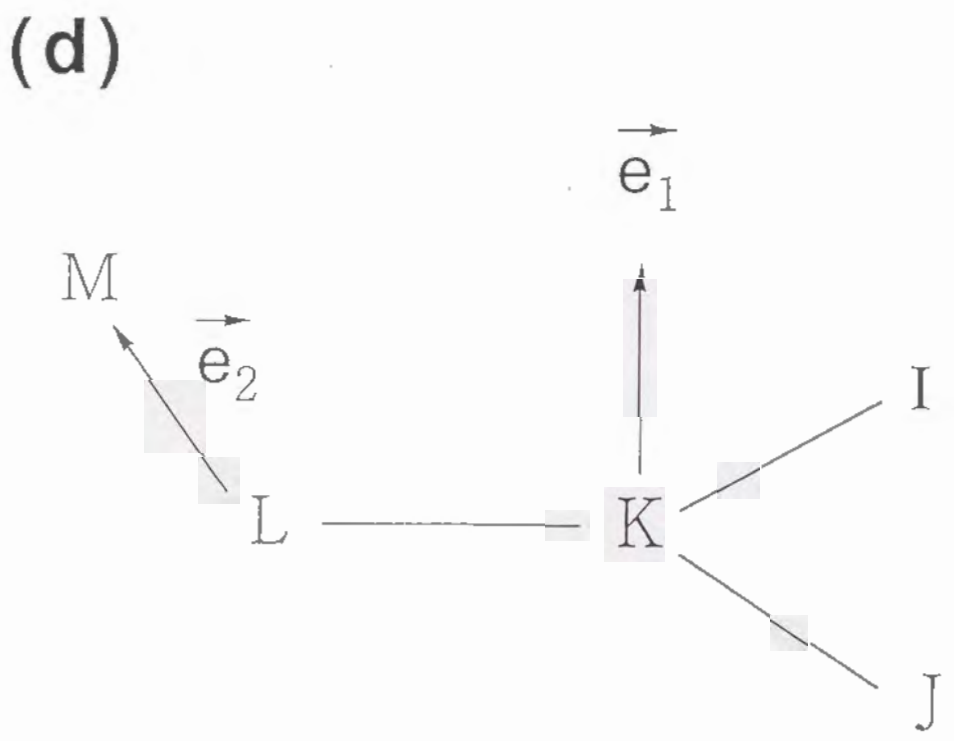

Table 4.1: Nine optimized geometries and their *ab initio* energies

(a) Optimized geometries [c]

	g^-g^-	g^-g^+	g^-t	g^+g^-	g^+g^+	g^+t	tg^-	tg^+	
stretch [a]									
1-2	1.401	1.397	1.400	1.400	1.400	1.399	1.399	1.397	1.39
2-3	1.499	1.501	1.501	1.501	1.499	1.501	1.500	1.498	1.50
3-4	1.554	1.551	1.552	1.555	1.557	1.553	1.552	1.550	1.55
4-5	1.506	1.508	1.507	1.509	1.507	1.510	1.509	1.507	1.50
2-6	1.078	1.078	1.078	1.078	1.077	1.078	1.077	1.078	1.07
3-7	1.084	1.085	1.084	1.083	1.085	1.084	1.089	1.088	1.08
3-8	1.089	1.088	1.088	1.085	1.084	1.084	1.084	1.085	1.08
4-9	1.082	1.088	1.086	1.085	1.085	1.082	1.085	1.085	1.08
4-10	1.085	1.083	1.082	1.085	1.081	1.085	1.086	1.085	1.08
5-11	1.073	1.074	1.075	1.071	1.074	1.074	1.074	1.074	1.07
5-12	1.074	1.072	1.074	1.074	1.074	1.074	1.074	1.073	1.07
1-13	0.964	0.965	0.965	0.964	0.965	0.964	0.964	0.964	0.96
bend [b]									
1-2-3	112.5	113.8	112.5	114.1	112.3	112.5	112.3	113.5	113
2-3-4	112.3	113.7	112.1	113.7	112.2	112.5	112.5	111.2	111
3-4-5	112.4	113.6	110.9	112.7	112.3	111.3	112.9	112.3	111
3-2-6	119.9	119.1	119.4	119.6	119.8	119.9	119.6	119.4	119
2-3-7	109.5	108.1	109.5	108.5	108.7	108.7	109.5	109.5	110
2-3-8	108.9	109.4	109.3	108.6	109.5	109.4	108.1	109.1	109
3-4-9	107.9	107.4	108.6	108.8	108.3	108.1	108.9	108.9	108
3-4-10	107.9	108.8	108.0	108.2	108.1	109.1	108.3	108.4	108
4-5-11	120.2	119.7	119.7	119.7	120.2	120.6	120.6	119.7	119
4-5-12	120.2	121.5	120.7	119.4	120.5	120.2	120.1	120.4	119
2-1-13	112.5	112.4	112.4	112.3	112.4	112.4	112.4	111.9	112
torsion [b]									
1-2-3-4(τ_1)	-56.3	-67.7	-52.0	71.2	61.2	63.9	-173.9	180.0	-179
2-3-4-5(τ_2)	-60.9	70.0	177.2	-66.1	60.0	177.8	-64.3	59.2	-176
4-3-2-6	160.2	148.7	165.9	-74.4	-81.9	-80.0	43.7	35.1	36
1-2-3-7	-178.7	171.2	-173.9	-50.3	-58.9	-56.5	63.5	58.9	59
1-2-3-8	63.7	54.1	68.4	-167.5	-177.0	-174.2	-52.8	-58.0	-57
2-3-4-9	60.9	-169.1	-61.8	56.3	-178.6	-60.3	57.8	-178.9	61
2-3-4-10	177.5	-53.2	55.0	172.5	-61.8	56.4	174.2	-62.7	-54
3-4-5-11	84.0	59.0	73.6	78.1	78.5	82.0	89.8	71.2	80
3-4-5-12	-83.0	-113.9	-91.4	-80.6	-89.1	-85.4	-78.0	-92.6	-82
3-2-1-13	-179.3	178.7	180.0	177.5	179.5	178.3	-178.6	177.6	-179

[a] unit: $\mathring{A}$. [b] unit: *degree*. [c] using UHF for triplet with 3-21G basis set.

see the text.

Table 4.2: Parameters of the potential function

(a) Stretch U_{stret} [a]

	atoms	k_i [b]	$r_i^{(0)}$ [c]
o i=1	1-2	0.410778	2.6430
2	2-3	0.307572	2.8410
3	3-4	0.273123	2.9350
4	4-5	0.304202	2.8496
5	2-6	0.376615	2.0317
6	3-7	0.363768	2.0529
7	3-8	0.363768	2.0529
8	4-9	0.367888	2.0495
9	4-10	0.367888	2.0495
10	5-11	0.391516	2.0618
11	5-12	0.391516	2.0618
12	1-13	0.549851	1.8233

$$^{a}U_{stret} = \sum_{i=1}^{12} U_{stret}^{(i)} = \sum_{i} \frac{1}{2} k_i (r_1 - r_i^{(0)})^2.$$

[b] unit: *hartree/a.u.*^{2}. [c] unit: *bohr*.

(b) *Ab initio* energies [f]

	triplet U_T [d]	singlet U_S [d]	diff. $U_T - U_S$ [e]
g^-g^-	-230.791258	-230.790538	-0.452
g^-g^+	.788092	.789076	0.617
g^-t	.788972	.788330	-0.403
g^+g^-	.788758	.791765	1.887
g^+g^+	.791488	.790466	-0.641
g^+t	.791054	.794328	2.054
tg^-	.790506	.791200	0.435
tg^+	.790200	.791764	0.981
tt	.791183	.790692	-0.308

[d] unit: *hartree*. [e] unit: *kcal/mol*.

[f] ROHF for triplet, TCSCF for singlet using 6-31G basis set.

(b) bending U_{bend} [d]

	atoms	k_i' [e]	$\theta_i^{(0)}$ [f]
o i=1	1-2-3	0.2538	g
2	2-3-4	0.1032	0.964
3	3-4-5	0.1032	1.955
4	3-2-6	0.1032	2.089
5	2-3-7	0.0826	1.907
6	2-3-8	0.0826	1.907
7	3-4-9	0.0826	1,894
8	3-4-10	0.0826	1.894
9	4-5-11	0.1410	2.096
10	4-5-12	0.1410	2.096
11	2-1-13	0.1960	1.957
12	1-2-6	0.1574	h
13	4-3-7	0.0826	1.904
14	4-3-8	0.0826	1.904
15	7-3-8	0.0734	1.877
16	5-4-9	0.0826	1.921
17	5-4-10	0.0826	1.921
18	9-4-10	0.0734	1.876
19	11-5-12	0.0825	2.062

$$^{d}U_{bend} = \sum_{i=1}^{19} U_{bend}^{(i)} = \sum_{i} \frac{1}{2} k_i'(\theta_i - \theta_i^{(0)})^2.$$

[e] unit $hartree/rad^2$. [f] unit: rad.
[g] $\theta_1^{(0)} = 2.024 + 0.052\cos\tau + 0.014\sin\tau$;
where τ is 13-1-2-3 torsional angle.
[h] $\theta_{12}^{(0)} = 2.009 + 0.072\cos\tau' + 0.046\sin\tau'$;
where τ' is 13-1-2-6 torsional angle.

The equilibrium positions of the above two bending angles g and h vary significantly with the OH rotation.

(c) van der Waals Interaction U_{vdW} [i]

	atoms	ϵ_i [j]	σ_i [k]
o i=1	1-4	2.120×10^{-2}	4.860
2	1-5	5.310×10^{-3}	7.252
3	2-5	2.050×10^{-3}	5.100

$$^{i}U_{vdW} = \sum_{i=1}^{3} U_{vdW}^{(i)} = \sum_{i} \epsilon_i [(\frac{\sigma_i}{r_i})^{12} - (\frac{\sigma_i}{r_i})^{6}].$$

[j] unit: *hartree*. [k] unit: *bohr*.

(d) Torsion U_{tors} [l]

	atoms	a_i [m]	b_i [m]	c_i [m]
o i=1	1-2-3-4	5.02×10^{-4}	5.27×10^{-4}	1.82×10^{-3}
2	2-3-4-5	1.32×10^{-3}	8.58×10^{-4}	3.45×10^{-3}

$$^{l}U_{tors} = \sum_{i=1}^{2} U_{tors}^{(i)} = \sum_{i} (a_i \cos \tau_i + b_i \cos 2\tau_i + c_i \cos 3\tau_i).$$

[m] unit: *hartree*.

Table 4.3: Parameters of solute C_4H_8O for intermolecular interaction

(a) Lennard-Jones parameters

		ϵ [a]	σ [b]
1	OH	0.305	3.216
2	$\dot{C}H$	0.115	3.800
3,4	CH_2	0.140	3.850
5	$\dot{C}H_2$	0.118	3.905

(b) Partial charge [c]

1	O	-0.69
2	C	+0.08
3	C	-0.04
4	C	-0.22
5	C	-0.23
6	H	+0.09
7,8	H	+0.09
9,10	H	+0.09
11,12	H	+0.10
13	H	+0.46

[a] unit: $kcal/mol$. [b] unit: $\mathring{A}$. [c] unit: $a.u.$

Table 4.4: Statistics of the MD trajectories

(a) Histgrams of potential energy

	energy range[a]	ratio of the staying time	mean free time of crossing[b]	average SOC[c]
1	0.0 ~ 2.0	0.026392	52.38	0.1237
2	2.0 ~ 4.0	0.269460	78.18	0.1644
3	4.0 ~ 6.0	0.439726	82.70	0.1776
4	6.0 ~ 8.0	0.213017	80.76	0.1853
5	8.0 ~ 10.0	0.045789	83.97	0.1912
6	10.0 ~ 12.0	0.005231	76.74	0.2243
7	12.0 ~ 14.0	0.000356	120.00	0.2218
8	14.0 ~ 16.0	0.000015	-	0.6452
9	16.0 ~ 18.0	0.0	-	-

[a] unit: $kcal/mol$; the energy level is defined as the minimum potential energy (of g^+t configuration).

[b] unit: $fsec$.

[c] root mean square value $\sqrt{<|\vec{J}|^2>}$; unit: cm^{-1}.

(b) Crossing interval for each isomer

g^-g^-	77.7	$fsec$
g^-g^+	43.3	
g^-t	76.0	
g^+g^-	75.9	
g^+g^+	78.7	
g^+t	182.8	
tg^-	82.2	
tg^+	84.3	
tt	85.3	

Table 4.5: ISC rates and some relevant properties

	$k_{tcf}(t)$			$< \Delta U >$ [c]	$< \delta\Delta U(0)\delta\Delta U(t) >$	
	k [a]	τ_k [b]	$\sqrt{<\mid \vec{J} \mid^2>}$ [c]		$\sqrt{< \delta\Delta U^2 >}$ [d]	τ_U [e]
g^-g^-	1.40×10^7	14.6	0.201	0.0774	0.620	14.6
g^-g^+	3.47×10^7	102.3	0.119	0.00242	0.305	29.4
g^-t	2.80×10^7	72.6	0.128	0.0599	0.234	71.5
g^+g^-	2.97×10^6	4.5	0.166	0.840	0.812	181.1
g^+g^+	6.13×10^6	12.1	0.146	0.0447	0.493	38.7
g^+t	2.32×10^6	2.4	0.200	0.970	0.746	105.8
tg^-	6.73×10^6	13.9	0.143	-0.115	0.435	33.4
tg^+	1.05×10^7	8.0	0.236	0.390	0.725	57.1
tt	9.60×10^6	25.2	0.127	0.0101	0.365	100.1

[a] unit: sec^{-1}; see Eq. (4.8).
[b] unit: $fsec$; see Eq. (4.28).
[c] unit: cm^{-1}. [d] unit: $kcal/mol$.
[e] unit: $fsec$; see Eq. (4.30).

Table 4.6: ISC rates estimated with the transition state theory

	k^{TST} [a]	τ_k^{TST} [b]	k^{TST}/k
g^-g^-	1.94×10^7	20.3	1.39
g^-g^+	1.72×10^7	51.0	0.50
g^-t	2.06×10^7	53.4	0.74
g^+g^-	3.27×10^6	5.0	1.10
g^+g^+	1.55×10^7	30.7	2.53
g^+t	4.83×10^6	5.1	2.08
tg^-	1.45×10^7	30.0	2.15
tg^+	1.19×10^7	9.0	1.13
tt	1.41×10^7	36.8	1.47

[a] unit: sec^{-1}.

[b] The correlation time of the TST reaction kernel

$$\tau_k^{TST} = \frac{1}{<\mid \vec{J} \mid^2>} \int_0^\infty < J^2 \exp(\frac{i}{\hbar}\Delta U t) > dt.$$

unit: $fsec$.

Bibliography

[1] W. T. Borden, Ed.; *Diradicals*; Wiley; New York, 1982.

[2] R. G. W. Norrish, Trans. Faraday. Soc. **33**, 1521 (1939).

[3] N. J. Turro, in *Modern Molecular Photochemistry*; Benjamin / Cummings; Menlo Park, 1978.

[4] L. J. Salem, J. Am. Chem. Soc. **96**, 3486 (1974).

[5] C. Doubleday, Jr., N. J. Turro, and J. -F. Wang, Acc. Chem. Res. **6**, 199 (1989).

[6] J. C. Scaiano, Acc. Chem. Res. **15**, 252 (1982).

[7] M. B. Zimmt, C. Doubleday, Jr. and N. J. Turro, Chem. Phys. Lett. **134**, 549 (1987).

[8] M. B. Zimmt, C. Doubleday, Jr., and N. J. Turro, J. Am. Chem. Soc. **107**, 6726 (1985).

[9] R. A. Caldwell, S. N. Dhawan, and T. Majima, J. Am. Chem. Soc. **106**, 6454 (1984).

[10] R. A. Caldwell, S. N. Dhawan, and D. E. Moore, J. Am. Chem. Soc. **107**, 5263 (1985).

[11] G. L. Closs and C. Doubleday, Jr., J. Am. Chem. Soc. **94**, 9248 (1972).

[12] F. J. J. de Kanter and R. Kaptain, J. Am. Chem. Soc. **104**, 4759 (1982).

[13] G. L. Closs, R. J. Miller, and O. D. Redwine, Acc. Chem. Res. **18**, 196 (1985).

[14] H. -J. Werner, Z. Schulten, and K. Schulten, J. Chem. Phys. **67**, 646 (1977).

[15] K. Schulten and R. Bittl, J. Chem. Phys. **84**, 5155 (1986).

[16] R. Bittl and K. Schulten, Chem. Phys. Lett. **146**, 58 (1988).

[17] F. J. J. de Kanter, J. A. den Hollander, A. H. Huizer, and R. Kaptain, Mol. Phys. **34**, 857 (1977).

[18] J. T. Hynes, in *The Theory of Chemical Reaction Dynamics;* ed. M. Baer, CRC, Boca Raton; FL, 1985, Vol. 4, p. 171.

[19] R. A. Kuharski, J. S. Bader, D. Chandler, M. Sprik, and M. L. Klein, J. Chem. Phys. **89**, 3248 (1988).

[20] J. K. Hwang and A. Warshell, J. Am. Chem. Soc. **109**, 715 (1987).

[21] S. Kato and A. Amatatsu, J. Chem. Phys. **92**, 7241 (1990).

[22] D. Borgis and J. T. Hynes, J. Chem. Phys. **94**, 3619 (1991).

[23] D. C. Borgis, S. Lee, and J. T. Hynes, Chem. Phys. Lett. **162**, 19 (1989).

[24] B. J. Gertner, K. R. Wilson, and J. T. Hynes, J. Chem. Phys. **90**, 3537 (1989).

[25] S. B. Zhu, J. Lee, and G. W. Robinson, J. Phys. Chem. **92**, 2401 (1988).

[26] J. E. Straub, M. Borkovec, and B. J. Berne, J. Chem. Phys. **89**, 4833 (1988).

[27] for example, L. I. Schiff, *Quantum Mechanics;* McGraw-Hill; New York, 1949.

[28] N. H. March, W. H. Young, and S. Sampanthar, in *The Many-Body Problem in Quantum Mechanics;* Cambridge University; Cambridge, 1967.

[29] see for example, S. Kato, J. Chem. Phys. **1988**, 3045 (1988).

[30] We used HONDO7 program; M. Dupuis, J. D. Watts, H. O. Villar, and G. J. Hurst, HONDO Ver. 7.0; QCPE 544, 1987.

[31] F. W. Bobrowicz and W. A. Goddard III, in *Modern Theoretical Chemisty;* Ed. H. F. Schaefer III, Plenum, New York, 1977, Vol. 3.

[32] (a) W. J. Hehre, R. Ditchfield, and J. A. Pople, J. Chem. Phys. **56**, 2252 (1972). (b) J. B. Binkley, J. A. Pople, and W. J. Hehre, J. Am. Chem. Soc. **102**, 939 (1980).

[33] R. Hoffmann, Acc. Chem. Res. **4**, 1 (1971).

[34] S. R. Langhoff, in *Modern Theoretical Chemistry;* Ed. H. F. Schaefer III, Plenum, New York, 1977, Vol. 4.

[35] H. F. King and T. R. Furlani, J. Comp. Chem. **9**, 771 (1988).

[36] L. Carlacci, C. Doubleday, Jr., T. R. Furlani, H. F. King, and J. W. McIver, Jr., J. Am. Chem. Soc. **109**, 5323 (1987).

[37] T. R. Furlani and H. F. King, J. Chem. Phys. **82**, 5577 (1985).

[38] H. F. King, R. E. Stanton, H. Kim, R. E. Wyatt, and R. G. Parr, J. Chem. Phys. **47**, 1936 (1967).

[39] L. Salem and C. Rowland, Angew. Chem. internat. Edit. **11**, 92 (1972).

[40] W. L. Jorgensen, J. Phys. Chem. **90**, 1276 (1986).

[41] W. L. Jorgensen, J. D. Madura, and C. J. Swenson, J. Am. Chem. Soc. **106**, 6638 (1984).

[42] S. L. Mayo, B. D. Olafson, and W. A. Goddard III, J. Phys. Chem. **94**, 8897 (1990).

[43] M. P. Allen and D. J. Tildesley, *Computer Simulation of Liquids*, Clarendon Press, Oxford, 1987.

[44] H. C. Andersen, J. Comp. Phys. **52**, 24 (1983).

[45] W. F. van Gunsteren and M. Karplus, Macromolecules **15**, 1528 (1982).

[46] D. J. Evans and S. Murad, Mol. Phys. **34**, 327 (1977).

[47] D. J. Adams, E. H. Adams, and G. J. Hills, Mol. Phys. **38**, 387 (1979).

Chapter 5

Excited State Characterization of Propenium Cation using Electron-Hole Potential Method and its Energy Gradient

The first excited state of propeniminium cation $CH_2CHCHNH_2^+$, a simple protonated Schiff base, was characterized by electon-hole potential method and its energy gradient. The potential energy surface and the optimized geometries on the excited state were obtained. Though a planar geometry is stable on the ground state, it has two out-of-plain modes with imaginary frequencies on the excited state. The isomerization dynamics following photoabsorption was also discussed. This method, especially its energy gradient technique, is applicable and suitable to a larger molecule in order to characterize the potential energy surfaces of excited states.

5.1 Introduction

Energy gradient method has been proved to be a powerful tool to characterize the potential energy surfaces of polyatomic systems [1, 2]. The geometry optimization of transition state as well as reactant and product and the harmonic analyses at these points provide useful information to understand the reaction mechanisms. Although the gradient method with Hartree-Fock (HF) approximation has been routinely applied to complex chemical reactions of large molecular systems on the ground state surface, the application to excited state reactions is rather scarce [3, 4, 5, 6]. One of the reason is that the restricted open-shell HF method cannot be applied to the excited state with the same symmetry as the ground state, and MCSCF method requires

a large amount of computer time. Considering these circumstances, it would be useful to develop the gradient methods for excited state wavefunctions which are equivalent to the HF method for the ground state. One of the possible ways is the singly-excited CI (SECI) method [7].

In the present paper, we have developed the energy gradient of electron-hole potential (EHP) method and applied it to the excited state of propeniminium cation $CH_2CHCHNH_2^+$. This compound is isoelectronic with 1,3-butadiene, whose excited states have been extensively studied by *ab initio* calculations [8, 9, 10]. Both molecules have small systems of conjugated π electrons, and the isomerization channels following the out-of-plain torsions are not one-dimensional. The propeniminium cation is also regarded as a model compound of protonated Schiff base; the photoisomeriztion of the protonated Schiff base of retinal has been recognized as an essential primary process of vision [11]. Du et al. [12, 13] have carried out MRSD-CI calculations on the propeniminium cation and the protonated Schiff base of retinal. They have shown that the $\pi\pi^*$ first excited state of these compounds can be reasonably described by a single electronic configuration.

The purpose of present work is to test the feasibility of EHP energy gradient method to characterize the excited state potential energy surface. The present paper is the first step of our studies on the photochemical reaction of large polyatomic molecules such as the protonated Schiff base of retinal. In the following section, we give a brief description of EHP gradient method. The potential energy surface, as well as the results of geometry optimization and harmonic analyses, of thl excited-state propeniminium cation are given in Sec. 5.3, and the isomerization dynamics is discussed. The applicability of the present method and further treatment are also mentioned.

5.2 Energy gradient for EHP wave function

Electron-hole potential (EHP) method developed by Morokuma and Iwata [14] is regarded as an extention of Hartree-Fock (HF) method to describe a certain kind of electronically excited states. This method is particularly useful for the system where the excited state has the same symmetry as the ground state and can be reasonably described by one singly excited electronic configuration. For this method, the potential energy of excited state from an occupied orbital α to a virtual μ is given by:

$$^{1,3}E(\alpha \rightarrow \mu) = E_0 + F_{\mu\mu} - F_{\alpha\alpha} - P_{\alpha\alpha,\mu\mu}; \tag{5.1}$$

where E_0 is the closed-shell HF energy of the corresponding ground state; $F_{\mu\mu}$ and $F_{\alpha\alpha}$ are diagonal elements of the Fock matrix. $P_{\alpha\alpha,\mu\mu}$ indicates electron-hole interaction expressed in terms of the following notation:

$$P_{pq,rs} \equiv (pq \mid rs) - (pr \mid qs) \mp (pr \mid qs) \tag{5.2}$$

(- for singet, + for triplet).

The energy $^{1,3}E(\alpha \rightarrow \mu)$ is determined variationally for the singly excited wavefunction

$$^{1,3}\Psi(\alpha \rightarrow \mu) = \frac{1}{\sqrt{2}}[\|\phi_1^2 \cdots \phi_\alpha \overline{\phi_\mu} \cdots \phi_n^2\| \pm \|\phi_1^2 \cdots \phi_\mu \overline{\phi_\alpha} \cdots \phi_n^2\|] \quad (5.3)$$
$$(1 \leq \alpha \leq n, \mu > n)$$

(+ for singlet, - for triplet).

$\{\phi\}$ is the optimized EHP orbital set, determined by unitary transformation of the canonical orbital set $\{\psi\}$ as

$$\phi_r = \sum_j \psi_j C_{jr}; \quad (5.4)$$

where C_{jr} refers to a unitary matrix and has no cross-term between occupied and virtual spaces. This feature confirms equivalent description with both orbital sets for the ground state. The variational condition to determine C_{jr} is given by the following two equations;

$$\sum_k^{\text{occ HF}} (F_{ii}\delta_{ik} + P_{ik,\mu\mu})C_{k\alpha} = \epsilon_\alpha C_{k\alpha} \quad (5.5)$$

$$\sum_w^{\text{vir HF}} (F_{\nu\nu}\delta_{\nu w} - P_{\alpha\alpha,\nu w})C_{w\nu} = \epsilon_\nu C_{w\nu}; \quad (5.6)$$

where i, k refer to the occupied canonical HF orbitals and ν, w to the virtual, respectively. Eqs.(5.5) and (5.6), are solved iteratively.

The gradient of the EHP energy is expressed as

$$\frac{\partial^{1,3}E(\alpha \rightarrow \mu)}{\partial R} = \frac{\partial E_0}{\partial R} + \frac{\partial F_{\mu\mu}}{\partial R} - \frac{\partial F_{\alpha\alpha}}{\partial R} - \frac{\partial P_{\alpha\alpha,\mu\mu}}{\partial R}. \quad (5.7)$$

The first term is the energy gradient of ground state, and the latter three terms are newly added to the EHP gradient. Provided that derivatives of EHP MO coefficients are represented with a matrix V in the following:

$$\frac{\partial C_{jr}}{\partial R} = \sum_s^{\text{EHP MO}} C_{js}V_{sr}, \quad (5.8)$$

the additional three terms can be expressed using V:

$$\frac{\partial F_{\mu\mu}}{\partial R} = \sum_r^{\text{vir EHP}} 2F_{\mu r}V_{r\mu} + \sum_i^{\text{vir HF}} C_{i\mu}^2 \frac{\partial F_{ii}}{\partial R}, \quad (5.9)$$

$$\frac{\partial F_{\alpha\alpha}}{\partial R} = \sum_r^{\text{occ EHP}} 2F_{\alpha r}V_{r\alpha} + \sum_i^{\text{occ HF}} C_{i\alpha}^2 \frac{\partial F_{ii}}{\partial R}, \quad (5.10)$$

$$\frac{\partial P_{\alpha\alpha,\mu\mu}}{\partial R} = \sum_r^{\text{vir EHP}} 2P_{\alpha\alpha,\mu r}V_{r\mu} + \sum_r^{\text{occ EHP}} 2P_{\alpha r,\mu\mu}V_{r\alpha} + P'_{\alpha\alpha,\mu\mu}; \quad (5.11)$$

where

$$P_{\alpha\alpha,\mu\mu} = (\alpha\alpha \mid \mu\mu)' - (\alpha\mu \mid \alpha\mu)' \mp (\alpha\mu \mid \alpha\mu)'$$

(- for singlet, + for triplet).

$(\ \mid\ )'$ denotes a MO representation of derivative integrals, obtained by differentiating the two-electron integrals with a nuclear coordinate and further transforming them with MO coefficients. Applying the variational conditions, Eq.(5.5) and (5.6), and the orbital orthogonarity condition, *i.e.*

$$V_{rs} + V_{sr} = 0, \tag{5.12}$$

to Eq.(5.9) $\sim$ (5.11), one can derive that all the terms including V cancel each other. The final form of the EHP gradient is in the following:

$$\frac{\partial^{1,3}E(\alpha \rightarrow \mu)}{\partial R} = \frac{\partial E_0}{\partial R} + \sum_i^{\text{vir HF}} C_{i\mu}^2 \frac{\partial \epsilon_i^0}{\partial R} - \sum_i^{\text{occ HF}} C_{i\alpha}^2 \frac{\partial \epsilon_i^0}{\partial R} - P'_{\alpha\alpha,\mu\mu}; \tag{5.13}$$

where ϵ_i^0 denotes an orbital energy of the canonical HF MO, *i.e.* $\epsilon_i^0 = F_{ii}$. In order to obtain the derivatives of the orbital energies, $\frac{\partial \epsilon_i^0}{\partial R}$, one has to solve the coupled perturbed HF (CPHF) equation [15] for the closed-shell ground state. This usually requires integral transformation, which is the rate-determining step. However, efficient use of extended storage will dramatically expedite the step.

5.3 Propeniminium Cation

In this section, we characterize the first excited states of propeniminium cation $CH_2CHCHNH_2^+$ as a model compound of protonated Schiff bases using the EHP and its energy gradient. The electronic structures of this compound are expressed with 90 basis by the standard Dunning's double-zeta-plus-polarization (DZP) (9s5p1d/3s1p)/[3s2p1d/2s1d] basis set [16]. The exponents of the polarization functions were taken to be 0.8 and 0.75 for d functions of N and C atoms, respectively, and 1.0 for p function of H atom. It is worth noting that the excited state has to be represented essentially with singly excited one configuration for the EHP method. Thus in order to confirm the applicability of EHP, we first examined the electronic structures of low-lying states by a 6-in-5 average CASSCF calculation before perfoming EHP. This calculation was performed at the trans geometry of the ground state optimized by HF (see Figure 5.1). In the preliminarily CASSCF, the active space consists of five orbitals, four π-orbitals $\pi_1 \sim \pi_4$ and one σ-orbital. The latter refers to anti-symmetric combination of CH σ bonds. Since the lowest three singlet states were calculated simultaneously with even weight, the average coefficient of the density matrices was taken to

be 0.33 : 0.33 : 0.33 for the three states. The result of CASSCF corroborates the adequate description by EHP; the first excited state, which lies $6.75eV$ above the ground state, was found to be an ionic $\pi_2 \rightarrow \pi_3$ state, and the CI coefficient of the $\pi\pi^*$ configuration was 0.915. By the way, the second excited state is doubly excited ^1A_g-type, characteristic to the conjugated π-electron systems, and it locates $1.24eV$ further above the first excited state. The energy difference between ^1B_u- and ^1A_g-type excited states is larger than that of trans 1,3-butadiene, since the ionic $-NH_2$ moiety of the propenium cation stabilizes the ionic ^1B_u-type state. We will focus on the first excited state hereafter. The total energies of the ground and first excited states calculated by HF and EHP are -171.33431 and -171.06217 Hartree, respectively. The vertical excitation energy is thus 7.40eV according to the EHP. We also performed singly-excited CI (SECI) calculation generated from the closed-shell configuration with the same basis set and geometry, obtaining the excitation energy to be $6.58eV$. By comparing this value to 6.75eV from CASSCF, 6.58eV from SECI or 5.67eV from MRCI [12], qualitative accuracy of EHP can be evaluated. The excitation energy of the conjugated π-electron system is not so quantitative for EHP instead of its simplicity. This comes from neglection of σ-polarization effect. The transition moment between the two states was estimated from EHP to $\overline{\mu} = \frac{1}{3}\sqrt{\mid \mu \mid^2} = 3.55$ Debye. This value implys strongly allowed transition.

Next the EHP gradient was utilized for geometry optimization and harmonic analysis on the first excited state of the propenium cation. The geometry was at first optimized within the planar symmetry like the optimized ground-state structure. However, it was proved to be unstable by harmonic analysis, demonstrating the presence of two unstable modes of out-of-plain vibrations: -CH_2 torsion ($945.9i\ cm^{-1}$) and the central C-C torsion ($423.1i\ cm^{-1}$). Another out-of-plain mode of -NH_2 torsion was found to be stable ($201.3cm^{-1}$). Therefore, the two unstable modes seems to be relevant to the dynamics on the first excited state; we display the potential energy surfaces in Fig. 5.2 as a function of the two torsional angles. Figure 5.2(b) shows three stable isomers on the first excited state: $(X, Y) \approx (180°, 90°)$, $(0°, 90°)$, and $(90°, 30°)$. The first two isomers denote trans and cis configurations with twisted -CH_2 moiety. These two configurations are directly accessible from the planar trans or cis geometry through the -CH_2 torsion. The last isomer is twisted in the central C-C torsional angle, but the potential well is so shallow ($\sim$ 5kcal/mol) that more accurate calculation will be required to confirm the existence of this isomer. The optimized geometries of the first two isomers and the EHP energies are tabulated in Table 5.5. In these two isomers, the ground and first-excited states are found to be nearly degenerated in energy levels, which is a common feature to conjugated π-electron systems at twisted geometries. The two electronic states corresponds to the diradical and ion-pair states, respectively. In such twisted geometries, the

diradical state is usually located lower than the ion-pair state [17]. Thus the energy ordering would be inappropriately reversed in EHP, since EHP predicts that the closed-shell state (ion-pair) is invariantly lower in energy than the open-shell state (diradical). However, this defect is insignificant for the global feature of the potential energy surface. It is also noted that the twisted NH_2 moiety was found to be unstable on the excited state besides the ground state.

On the basis of the potential energy surface of the first excited state, we will briefly discuss the isomerization dynamics following the photoabsorption. The photoexcitation at both the trans and cis configurations of the initial planar geometries principally leads to the vibrational excitation of the CH_2 torsion. However, Figure 5.2 shows that the other unstable mode, the central C-C torsion, is accompanied with the CH_2 torsional motion to some extent. The steepest descent direction indicates that the two torsional motions correlate with co-rotatory manner, because the energy reduction can be achieved by efficient destruction of the conjugated π-electron system. The counter-rotatory motion, namely "kink" motion of $C_3 - H_8$ moiety, little reduces the potential energy and forms the ridge in Figure 5.2. When the velocity along the central C-C torsion is large enough, cis $\longleftrightarrow$ trans isomerization can be realized, although the quantum yield of the isomerization is predicted to be fairly small initiated by the photoabsorption. Most of the excited species will be trapped in the twisted CH_2 configurations before reaching the cis-trans isomerization. The third optimized does not seem to play an important role in the photoisomerization dynamics.

5.4 Discussion

As demonstrated for the propeniminium cation, EHP and its energy gradient are useful to characterize potential energy surfaces of excited states because of its simplicity and moderate accuracy. In particular, the advantage can be exploited for a molecule too large that it is difficult to carry out another kind of *ab initio* calculation such as MCSCF. The principal disadvantage is that they can be applied only for monoconfigurational excited states. Since the first excited state of the protonated Schiff base of retinal is implied to be monoconfigurational according to E.R.Davidson [13], it is actually possible to apply these methods to the system. It is also easy to take into account the triplet state, although it might have little importance to the isomerization of the protonated Schiff base [11]. We are now in progress with these methods to grasp the global character of the potential energy surface of the excited state and to obtain more detailed information about the photoisomerization mechanism.

5.5 Figures and Tables

Figure 5.1: Schematic picture of propeniminium cation $CH_2CHCHNH_2^+$ with serial numbers of the atoms. Equilibrium distances and angles for the ground state are also displayed. The units are $\mathring{A}$ for distances and degree for angles, respectively.

Figure 5.2: Potential energy surfaces of (a) ground state and (b) first excited state of propeniminium cation as a function of the central C-C torsion (X-axis) and CH_2 torsion (Y-axis). The other coordinates were fixed to the values of optimized trans ground-state geometry. The contour spacing is 0.5eV, and the energy level was determined by the lowest energy of the ground state.

Figure 5.1

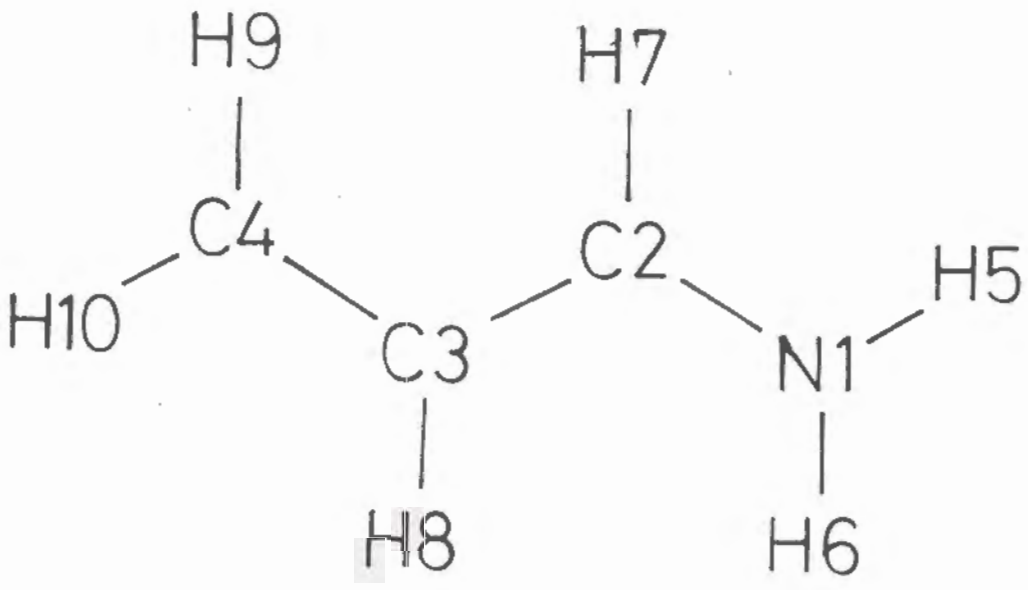

Figure 5.2(a)

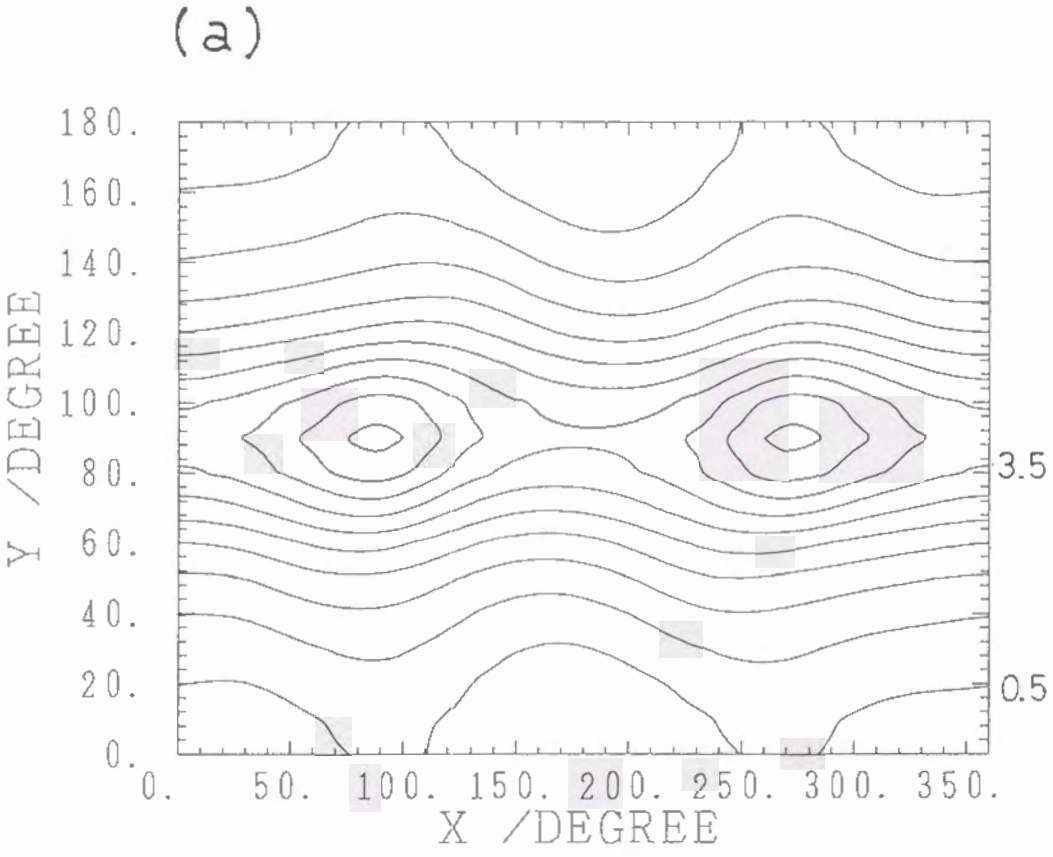
(a)
180.
160.
140.
120.
100.
80.
60.
40.
20.
0.
Y /DEGREE
0.
50.
100.
150.
200.
250.
300.
350.
X /DEGREE
3.5
0.5

Figure 5.2(b)

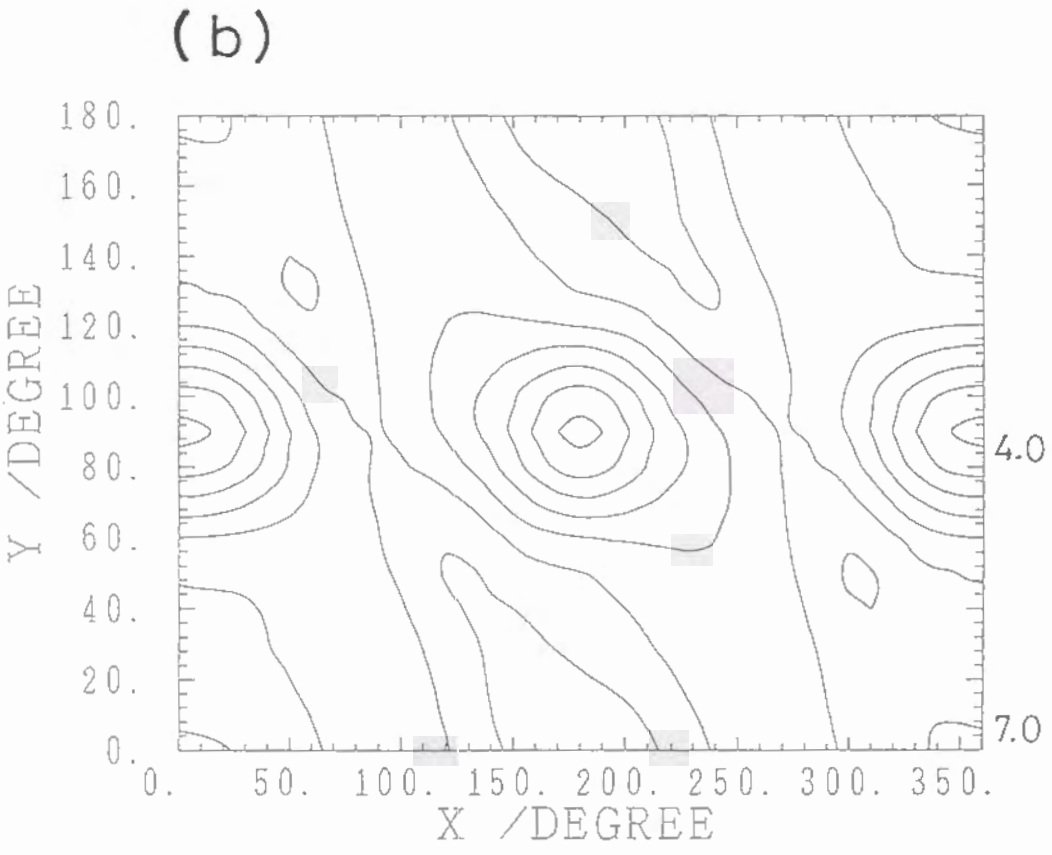
(b)
180.
160.
140.
120.
100.
80.
60.
40.
20.
0.
Y /DEGREE
0.
50.
100.
150.
200.
250.
300.
350.
X /DEGREE
4.0
7.0

Table 5.1: Optimized geometries and energies for the ground and first excited states using EHP.

internal coordinates[a]		equilibrium values[b]			
		ground state		excited state	
1. stretch	1-2	1.288	1.287	1.294	1.292
2. stretch	2-3	1.438	1.451	1.439	1.441
3. stretch	3-4	1.339	1.337	1.410	1.411
4. stretch	1-5	1.001	1.001	1.000	1.000
5. stretch	1-6	1.001	1.000	1.001	1.000
6. stretch	2-7	1.077	1.077	1.074	1.076
7. stretch	3-8	1.075	1.073	1.082	1.079
8. stretch	4-9	1.076	1.076	1.077	1.077
9. stretch	4-10	1.074	1.075	1.077	1.077
10. bend	3-2-1	124.0	127.1	123.2	124.4
11. bend	4-3-2	119.3	124.4	122.4	124.1
12. bend	5-1-2	121.3	120.6	120.9	120.7
13. bend	6-1-2	121.6	122.8	122.0	121.7
14. bend	7-2-3	119.4	117.4	119.5	118.6
15. bend	8-3-2	119.0	115.0	116.0	114.1
16. bend	9-4-3	122.1	123.8	121.4	121.2
17. bend	10-4-3	120.9	120.2	121.4	121.2
18. torsion	4-3-2-1	180.0	0.0	180.0	0.1
19. torsion	5-1-2-3	180.0	180.0	180.0	180.0
20. torsion	6-1-2-3	0.0	0.0	0.0	0.0
21. pla.bend	7-2-(1,3)	0.0	0.0	0.0	0.0
22. pla.bend	8-3-(2,4)	0.0	0.0	0.0	0.2
23. torsion	9-4-3-2	0.0	0.0	94.4	95.5
24. torsion	10-4-3-2	180.0	180.0	94.4	95.5
total energy[c]		-171.3343	-171.3258	-171.2004	-171.2014

[a] The serial numbers of the atoms were indicated in Figure 5.1.

[b] unit: $\mathring{A}$ for stretch, degree for bend, planar bend and torsion.

[c] The first two columns refer to the ground state, and the other to the first excited state. unit: Hartree.

Bibliography

[1] P.Pulay, *"Modern Theoretical Chemistry"* ed. H. F. Schaefer III, Vol.4, Plenum, New York, 1977.

[2] P.Pulay Adv. Chem. Phys. 69 (1987) 241.

[3] S. Kato and K. Morokuma, Chem. Phys. Lett. 65 (1979) 19.

[4] J. D. Goddard, N. C. Handy and H. F. Schaefer III, J. Chem. Phys. 71 (1979) 1525.

[5] (a) B. R. Brooks, W. D. Laidig, P. Saxe, J. D. Goddard, Y. Yamaguchi and H. F. Schaefer III, J. Chem. Phys. 72 (1980) 4652. (b) Y. Osamura, Y. Yamaguchi and H. F. Schaefer III, J. Chem. Phys. 75 (1980) 2919.

[6] R.Krishnan, H. B. Schlegel and J. A. Pople, J. Chem. Phys. 72 (1980) 4654.

[7] J. B. Foresman, M. H.-Gordon, J. A. Pople, and M. J. Frisch, J. Phys. Chem. 96 (1992) 135.

[8] V. B.-Koutechky, M. Persico, D. Döhnert, and A. Sevin, J. Am. Chem. Soc. 104 (1982) 6900.

[9] R. J. Cave and E. R. Davidson, J. Phys. Chem. 91 (1987) 4481.

[10] M. Aoyagi and Y. Osamura, J. Am. Chem. Soc. 111 (1989) 470.

[11] C. Sandorfy and D. Vocelle, Can. J. Chem. 64 (1986) 2251.

[12] P. Du, S. C. Racine and E. R. Davidson, J. Phys. Chem. 94 (1990) 3944.

[13] P. Du and E. R. Davidson, J. Phys. Chem. 94 (1990) 7013.

[14] K. Morokuma and S. Iwata, Chem. Phys. Lett. 16 (1972) 192.

[15] J. Gerrati and I. M. Mills, J. Chem. Phys. 49 (1968) 1719.

[16] T. H. Dunning, Jr. and P. J. Hay, *"Modern Electronic Structure Theory"*, ed. H. F. Schaefer, Plenum, New York, 1977.

[17] L. Salem, *"Electrons in Chemical Reactions"*, John Wiley, New York, 1982.

Chapter 6

An MD study on the long-time dielectric solvation dynamics of aqueous solution to examine the solute size dependence and the Onsager's snowball picture

We studied the effect of the slow motion of solvent on the solvation dynamics with long-time molecular-dynamics simulation with varying size of the solute, by making special attention to obtain the correct long-time (or low-frequency) dynamics. The small solute exhibited a remarkable difference in the relaxation dynamics with enhanced slow component, and that was attributed to the characteristic molecularity of liquid water in the dielectric property. In the small solute the particular low-frequency component emphasizes incomplete shielding, which necessarily makes the distant solvent slow. For the medius or large solute, the result partly supports the Onsager's snowball picture. Complete breakdown of the snowball picture in the aqueous solution should not be elucidated until the nonlinear response is incorporated. The basic assumption of the dynamical MSA theory and the role of translational motion were considered on the basis of the MD results.

6.1 Introduction

In the last few decades the dielectric relaxation dynamics in solution has been extensively studied as one of the primary issues in solution chemistry [1, 2, 3, 4, 5, 6, 7, 8, 9, 10, 11, 12, 13, 14, 15, 16, 17, 18, 19, 20, 21, 22, 23, 24, 25, 26]. This is because the phenomenon has a fundamental importance in the microscopic solvation dynamics, and is particularly amenable to the recent techniques, both experimental and theoretical, involving time-resolved

spectroscopy with ultrafast pulse lasers [27, 1, 2, 3, 4] and molecular-dynamics (MD) simulation [5, 6, 7, 25, 26]. A typical subject to be studied with these methods is the dielectric relaxation process of solvent that is induced by a sudden change of the solute charge or its charge distribution. One of the current problems has been how to explain the realistic feature of the relaxation function

$$C(t) = \frac{E(t) - E(\infty)}{E(0) - E(\infty)}, \tag{6.1}$$

where $E(t)$ is the excessive solvation energy as a function of time. The time-resolved experiments [1, 2, 3, 4, 8] showed considerable deviation from the exponential decay with the time constant of the longitudinal dielectric relaxation time τ_L of solvent, which is a consequence of the Debye-type dielectric continuum model [28]. Thus a number of theories have been proposed by considering the solvent molecularity [9, 10, 11, 12, 13].

A basic picture to deal with the solvent molecularity was proposed by Onsager [29, 30], namely the "snowball picture". This came from his conjecture that the dielectric relaxation occurs more quickly in the outer region from the solute than in the nearby region, and this counterintutive prediction brought about many arguments. Although some of the early theories supported the snowball picture [9, 11, 15], recent MD simulations as well as theoretical studies mostly denied it [5, 7, 25, 26, 20, 31]. We note that some successful theories, including the dynamical mean spherical approximation (MSA) [12, 14, 15, 16], were largely influenced by the snowball picture to incorporate the solvent molecularity, though they do not necessarily predict explicitly the slower relaxation in the vicinity. The dynamical MSA regards the cavity radius in the Born formula as frequency-dependent through frequency-dependent dielectric constant. Since the high-frequency dielectric constant is generally smaller than the low-frequency one, the effective cavity radius is expanded relatively in the high-frequency region on the basis of MSA, which in turn reduces the high-frequency component of the solvation energy in the nearby region. In the current tendency against the snowball picture, it is worthwhile not only to compare the dynamical MSA theory to simulation results, but also to reconsider the basic assumption of the theory. Recently, Bagchi et al. emphasized the importance of the translational motion to explain the breakdown of the snowball picture on the basis of the generalized Smoluchowski equation [18, 19, 20, 21, 22, 23, 24]. Their theory provoked following MD studies for examination, though the contraversial results have not yet been resolved [26, 25]. In order to obtain a further insight into these current problems, our concern is mainly devoted to the rather slow (or low-frequency) dynamics in the order of the Debye dielectric relaxation time τ_D ($\simeq$ 9.33 ps by experiment for water at $20°C$ [32], and $\simeq$ 18.7 ps by the present simulation discussed later). While the short-time relaxation dynamics has been thoroughly examined with MD simulation, the slow dy-

namics has not been studied so well by the simulation. It is well known that liquid water has two characteristic frequencies in its dielectric dynamics, *i.e.* the Debye frequency ω_D corresponding to τ_D and the other frequency about 600cm^{-1}. The latter high frequency is attributed to the librational motion, and the inertial effect in the short-time dynamics has come to be well understood. The former frequency involves another interesting effect, since the dielectric property of water drastically changes around the frequency. This effect on the solvation dynamics deserves further investigation, and the principal purpose of this article is to demonstrate the effect of low frequency motion on the solvation dynamics using MD simulation. We will show that such information is useful to consider the above-mentioned problems, *e.g.* about the basic assumption of the dynamical MSA or the importance of the translational motion.

In order to discuss the long-time behavior through MD simulation, we have to confirm the possibility to perform such an attempt with a unit cell of a finite scale, because the long-time dynamics might be affected by the artificial boundary more seriously than the short-time dynamics might be. Such simulation involves a subtle problem about the long-range force; the dielectric property was found to be quite sensitive to the boundary and cut-off conditions [33, 34]. There has been much work to study the dielectric property of water using MD simulation, with taking great care of these conditions [35, 36, 34, 37, 38]. Many studies sought adequate methods and conditions to reproduce the property through computer simulation to achieve a considerable success, and their results are available at the present. For example, the above-mentioned dynamical feature of liquid water, that the frequency-dependent dielectric constant drastically changes around the Debye dielectric frequency ω_D between 0.1cm^{-1} and 10cm^{-1}, was also reproduced through MD simulation [39, 35]. Most of these previous work dealt with the bulk dielectric property, but we applied their methods to investigate the solvation dynamics around solute molecules. We studied the dielectric solvation dynamics of aqueous solution, mainly focusing on the crucial time scale of the Debye dielectric relaxation time.

The remainder of this paper are as follows. The next section delineates our method to obtain valuable information on the slow solvation dynamics through the MD simulation. In Sec. 6.3, we present the results of the simulation about the pure water to provide a basis to consider the solvation dynamics. We show the results about the aqueous solution with varying size of the solute in Sec. 6.4 to discuss the effect of the slow component on the solvation dynamics as well as to examine the several assumptions in the currently available theories. The conclusion follows in Sec. 6.5.

6.2 Outline of the Method

In order to examine the low-frequency behavior of the dielectric relaxation as slow as 0.1cm^{-1}order, the usual procedure of the simulation, where the nonequilibrium relaxation process is pursued after a sudden change of the solute charge, does not seem to be adequate. That is because most of the relaxation process completes within a few picoseconds and thus the signal of the longer-time behavior is too weak to be detected clearly. Furthermore, in this situation the finite scale of the simulation cell causes an obscure artifact for the long-time behavior.

Many previous studies on the dielectric property of water demonstrated that the reaction field method reproduces the frequency-dependent dielectric constant of the bulk water fairly well with a moderate number of water molecules about 256 and sufficient time steps of simulation [39, 35]. We applied the reaction field method to examine the dynamics of solvent polarization around the solute molecule. In the reaction field method, the dipole-dipole part of the intermolecular interaction is modified in the followings [40]:

$$u^{DD}_{water-water}(i,j) = \begin{cases} \frac{\vec{\mu}_i \cdot \vec{\mu}_j}{r_{ij}^2} - \frac{3(\vec{\mu}_i \cdot \vec{r}_{ij})(\vec{\mu}_j \cdot \vec{r}_{ij})}{r_{ij}^5} - \frac{2(\epsilon_{RF}-1)}{2\epsilon_{RF}+1} \cdot \frac{\vec{\mu}_i \cdot \vec{\mu}_j}{r_C^3} & (r_{ij} < r_C), \\ 0 & (r_{ij} > r_C); \end{cases} \tag{6.2}$$

where $\vec{\mu}_i$ and $\vec{\mu}_j$ are the dipole moment vectors of the i-th and j-th molecules, respectively; $\vec{r}_{ij}$ is the vector of the center-of-mass separation; r_{ij} is its norm; r_C denotes the cut-off length, and ϵ_{RF} is the reaction field dielectric constant. Note that the potential of eqn.(6.2) is pairwise additive and that other interactions such as Lennard-Jones interaction should be added to form the total interaction potential. The first two terms of eqn.(6.2) represent the usual dipole-dipole interaction, and the last term including r_C and ϵ_{RF} describes the average interaction with the bulk continuum. The interaction beyond the cut-off length r_C is not explicitly count as indicated by eqn.(6.2), but instead it is properly involved in the third term. The treatment of eqn.(6.2) is derived on the crucial assumption of dielectric uniformity [40]. An advantage of the reaction field method lies in the consistent treatment between the relatively short-range interaction within the distance of r_C and the long-range one beyond r_C. The consistency, however, is of rather delicate character; if the consistency is broken by introducing a smoothing function, the outcome was found to deteriorate sensitively [34]. We have to be careful enough to the condition where eqn.(6.2) is justified to incorporate the long-range force, when we later discuss the condition to apply this method to the solvation dynamics. The successful results of the previous work indicate that the adequate treatment of the long-range force permits us to study the dielectric properties using the MD simulation performed even in a finite cell.

Before examining the solution, we first carried out a simulation of pure water to obtain the dielectric constant of the bulk water. The model potential we employed is the SPC model [41, 42], which is known to give a reliable value of the static dielectric constant (~ 70) on the reaction field method [34]. The cubic unit cell of the simulation constists of 256 water molecules with the density of 1.0g/cm^3, and consequently the box length was 34.25 Bohr. The periodic boundary condition was employed with the cut-off length r_C, which is the half of the box length. The dielectric constant for the reaction field ϵ_{RF} was assumed to be 67.8 [34]. The time step of the simulation was 1 fs, and the time development was performed on the 4-th order Gear predictor-corrector integrator [43] with quarterion parameters [44]. The MD run was carried out at the temperature T=300K during 3×2^{18} steps, 786 ps, except the preceeding equilibriation procedure during 3000 steps. The interaction to the reaction field causes heatup in the simulation cell, and accordingly the kinetic energy was scaled to adjust to the temperature when the total kinetic energy exceeded 1.3 times of the ideal value. The interval turned out to be about 3.9 ps on the average. We calculated the frequency-dependent dielectric constant of water, which was utilized to analyze the simulation of the solution in the next stage.

In the simulation of the solution, the condition is similar to the above except for a few important points. The simulation cell consisted of one solute molecule and 255 water molecules with the same box length. We employed a spherical atom with *no* charge as the solute. Only the Lennard-Jones interaction between the solute and solvent was assumed:

$$u_{solute-water} = 4\epsilon_{sw} \cdot \left\{ (\frac{\sigma_{sw}}{r})^{12} - (\frac{\sigma_{sw}}{r})^{6} \right\}, \tag{6.3}$$

with $\epsilon_{sw} = 7.96 \times 10^{-4}$Hartree fixed. σ_{sw} was given as the geometrical average,

$$\sigma_{sw} = \sqrt{\sigma_{solute} \cdot \sigma_{water}}, \tag{6.4}$$

with varying size of the solute σ_{solute}; $\sigma_{solute} = 3.59$, 4.79, and 5.98 Bohr, which correspond to $0.6\sigma_{water}$, $0.8\sigma_{water}$, and $1.0\sigma_{water}$, respectively. r is the distance between the solute and the oxygen atom of the water. The number of time steps was 2^{18}, and thus the total length was 262 ps. The other conditions were the same as those of the pure solvent simulation described above. The chargeless solute has several advantages to discuss the polarization dynamics of the solvent. First, even through no charge and equilibrium situation, the linear response theory provides the equivalent information on the relaxation process. Further, the present situation is more preferable to avoid such additional complication as the dielectric saturation. Thirdly, the present situation with no charged solute influences little perturbation on the surrounding solvent except for the local region near the solute. This is an important merit to resolve the problem on the long-range force, by retaining

the condition where the reaction field method is applicable to reproduce the dielectric property of the bulk water including the low-frequency dielectric dynamics. If the solute should have a substantial charge on the contrary, the situation would not be so simple any more, because the charge would destroy the dielectric uniformity, a crucial basis of eqn.(6.2), around the solute. The breakdown of the dielectric uniformity would thus invoke a complicated problem on the long-range force and probably require another consistent treatment. In order to obtain a proper solution for the use of simulation, the correction due to the long-range interaction beyond the simulation cell must be small enough to be regarded as a perturbation, since we do not explicitly consider the dielectric dynamics in the peripheral bulk region. This requirement calls for a sufficiently large cell within which the influence of the solute charge should be mostly damped, but such a cell is too large for a practical handling with the simulation at present. The situation with no charge enables us to discuss the solvation dynamics in the same manner as many previous studies on the dielectric properties.

The primary quantity to be investigated in the present work is the radial (longitudinal) component of the solvent polarization from the solute. The essential difference of the present work from the previous studies on the bulk dielectric properties is that we investigated the dielectric dynamics through projecting it onto the longitudinal component. The system in question is nearly spherically symmetric around the solute, and accordingly only the longitudinal polarization was dealt with as a function of the radical distance. Such a treatment reduces the whole dynamics into a spatially one-dimensional problem, which makes the following analysis rather simple. The longitudinal polarization as a function of the radial distance derives the electric potential at the solute center at every time. The time correlation function of the electric potential was interpreted to discuss the relaxation dynamics of solvation with the help of the linear response theory. We can neglect the fluctuation of the polarization in the bulk continuum beyond the cut-off length, and hence neglect the influence of the bulk continuum on the dynamic component of the electric potential. Since the dynamics of the longitudinal polarization was analyzed as a function of the radial distance, we obtained some information on the difference in the solvation dynamics between the nearby region and the distant region. When we observed the difference from the viewpoint of the frequency domain, the difference clearly manifests itself as discussed later. The frequency region around the Debye frequency, where the dielectric constant drastically changes, is particularly interesting to consider the solvation dynamics. The solute size dependence was demonstrated to be remarkable on the slow dynamics. Since the present result has a good statistical accuracy compared to the nonequilibrium simulation, this provided valuable information about the subtle problem to what extent the snowball picture actually holds. These analyses were utilized to

examine the current problems mentioned in Sec. 6.1.

6.3 Dielectric property of pure water

The dielectric property of water has been studied by many researchers with computer simulation, and some methods of the simulation to bring reliable results have been established [35, 36, 34, 37]. A remarkable consequence is that even the low-frequency behavior of the dielectric response can be well described if the long-range force is properly treated using the Ewald summation or the reaction field. It has been also verified that about 256 molecules per one cell are enough, while the number of the time steps is rather demanding to obtain a converged result. Therefore we have to take care of the convergence behavior; some early works obtained erroneous values due to the shortness of data accumulation. Fugure 6.1 shows the convergence behavior of $< M^2 >$, average square dipole moment of the cell, which is later used to derive the static dielectric constant. The result indicates that the total number of the time steps, 3×2^{18}, is sufficient to converge and to obtain the frequency resolution about $0.1\text{cm}^{-1}$of the frequency-dependent dielectric constants. The static dielectric constant of water ϵ_0 was calculated using the following modiefied Kirkwook formula [40]:

$$\frac{4\pi}{3}\frac{< M^2 >}{3Vk_BT} = \frac{(\epsilon_0 - 1)(2\epsilon_{RF} + 1)}{3(2\epsilon_{RF} + \epsilon_0)}; \tag{6.5}$$

where V is the volume of the cell; ϵ_{RF} is the dielectric constant of the reaction field (see eqn.(6.2)); k_B and T are the Boltzmann constant and the temperature. The calculated value of ϵ_0 is 70.93, which is consistent to the previous work with the SPC potential, 67.8 [34], and the experimental value, 77.65 at 300K [45].

The frequency-dependent dielectric constant $\epsilon(\omega) = \epsilon_r(\omega) - i\epsilon_i(\omega)$, was calculated from the equilibrium time correlation function,

$$\Psi(t) = \frac{< \vec{M}(0) \cdot \vec{M}(t) >}{< M^2 >}. \tag{6.6}$$

These are related by the linear response theory [46] in the following [47, 39]:

$$\begin{aligned} -\int_0^\infty dt e^{-i\omega t}\frac{d\Psi(t)}{dt} &= 1 - i\omega\int_0^\infty dt e^{-i\omega t}\Psi(t) \\ &= \frac{\{\epsilon(\omega) - 1\}(2\epsilon_{RF} + \epsilon_0)}{(\epsilon_0 - 1)\{2\epsilon_{RF} + \epsilon(\omega)\}}. \end{aligned} \tag{6.7}$$

The obtained results of the real part $\epsilon_r(\omega)$ and the imaginary part $\epsilon_i(\omega)$ were displayed in Figure 6.2. The figure exhibits a distinct transition in the dielectric quality between $0.1\text{cm}^{-1}$and 10cm^{-1}. There is also detected another

transition about 600cm^{-1}, which is attributed to the librational motion, but we omitted it and focused on the former transition to discuss the solvation dynamics. Excluding the second small transition, the frequency-dependent dielectric constants were well expressed by the Debye formula,

$$\begin{aligned} \epsilon(\omega) &= \epsilon_r(\omega) - i\epsilon_i(\omega) \\ &= \epsilon_\infty + \frac{\epsilon_0 - \epsilon_\infty}{1 + i\omega\tau}. \end{aligned} \tag{6.8}$$

Therefore,

$$\epsilon_r(\omega) = \epsilon_\infty + \frac{\epsilon_0 - \epsilon_\infty}{1 + \omega^2\tau^2}, \tag{6.9}$$

$$\epsilon_i(\omega) = \frac{(\epsilon_0 - \epsilon_\infty)\omega\tau}{1 + \omega^2\tau^2}. \tag{6.10}$$

The optimized parameters in the present work are as follows: $\epsilon_0 = 70.93$, $\epsilon_\infty = 2.57$, $\tau = 0.559/\text{cm}^{-1}$. Note that eqn.(6.8) does not take account of the second transition about 600cm^{-1}, and hence it is applicable roughly up to that frequency. The obtained result of eqn.(6.8) is also consistent to the experimental value [32] as well as the previous work [35, 36].

6.4 Solvation dynamics around the solute

In this section we deal with the aqueous solution instead of the pure water; the dielectric dynamics discussed above is considered as the solvation dynamics around the solute by projected onto the longitudinal component. Before discussing the solvation dynamics, we give a brief discussion about the static solvation structure around the solute molecule. Figure 6.3 shows the radial distribution function of the oxygen atoms of water from the solute in the case of the small solute. The first peak lies at 5.2 Bohr, and the first solvation shell was estimated to contain about 9-10 solvent molecules on the average. Though the broad second peak is observed about 10 Bohr, the fluctuation from the average density is attenuated fairly fast to seemingly vanish beyond the distance of 15 Bohr. However, with regard to the asymptotic behavior to approach bulk quantities, the dielectric property exhibited quite a different behavior, which is one of our main points in the later discussion. Based on Figure 6.3, we introduce a set of the concentric solvation shells with the thickness of 3.6 Bohr to distinguish the distance in the following analysis. To check the statistical convergence is a necessary procedure before full investigation of our results, like the simulation in the preceeding section. We displayed in Figure 6.4 the convergence behavior of the longitudinal polarization of the solvent $P_r(r)$ in the first solvation shell. Figure 6.4 indicates that the duration of the simulation is sufficient to obtain the converged result.

The discussion below is to clarify the role of the low-frequency component in the solvation dynamics based on the results of the MD simulation. The present MD simulation provided the electric potential at the solute center $A(t)$ as a function of time. If the solute has an hypothetical small charge $e(t)$, the electric solvation energy,

$$H' = -A(t) \cdot e(t), \tag{6.11}$$

is regarded as the perturbation Hamiltonian in the conventional linear response theory [46], where A and e corresponds to the displacement and the external force, respectively. Note that the linear relation of eqn.(6.11) seems to hold up to the actual unit charge in some solutes [5, 6, 26]. We calculated the time correlation function of $A(t)$,

$$S(t) = \frac{< (A(0) - \bar{A})(A(t) - \bar{A}) >}{< \delta A^2 >}, \tag{6.12}$$

with varying cut-off range R_{max}, within whose radius from the solute $A(t)$ was calculated. $S(t)$ is equivalent to $C(t)$ in eqn.(6.1) within the linear response theory. The results of $S(t)$ are displayed in Figs. 6.5 $\sim$ 6.7 with varying size of the solute. These results exhibit distinct difference in the small solute, where the slow component is quite enhanced. When we observe the relaxation rate against the distance from the solute, only the small solute apparently contradicts the snowball picture. In the other solutes, the order of the rate is rather complicated. Though the nearest solvent is slowest like the snowball picture, the other shells except the nearest one are slightly but obviously opposite to the snowball prediction. The tendency in the medium or large solutes was implied by previous nonequilibrium MD studies [25, 26], and the present result corroborated it with sufficient statistical accuracy as well as the reliable long-time behavior. It is hard for the nonequilibrium simulation to gain such statistical convergence, while the nonequilibrium simulation involves the nonlinear effect which lacks in the present work.

We will further analyze the unusual solvation dynamics in the small solute mainly from frequency domain. The time correlation function $S(t)$ derives the admittance $\chi_e(\omega)$ in the following [46]:

$$\chi_e(\omega) = \frac{< \delta A^2 >}{k_B T} \{1 + i\omega \int_0^\infty dt e^{i\omega t} S(t)\}. \tag{6.13}$$

The complex admittance $\chi_e(\omega)$ means the degree of the response of the electric potential to the solute charge in the frequency domain, *i.e.*

$$\tilde{A}(\omega) = \chi_e(\omega)\tilde{e}(\omega), \tag{6.14}$$

where $\tilde{A}(\omega)$ and $\tilde{e}(\omega)$ are the Fourier transformation of $A(t)$ and $e(t)$, respectively. Let us introduce the longitudinal polarization $P_\tau(r,t)$ as a function of

the distance from the solute r and time t. Provided that $P_r(r,t)$ is spherically symmetric, the electric potential at the center of the solute A is given as

$$A(t) = \int_{R_{min}}^{R_{max}} \frac{P_r(r,t)}{r^2} 4\pi r^2 dr = \int_{R_{min}}^{R_{max}} 4\pi P_r(r,t) dr. \tag{6.15}$$

R_{max} in eqn.(6.15) should be infinite in the ideal situation, and R_{min} refers to the cavity radius of solvation. We also introduce $\tilde{P}_r(r,\omega)$ as the Fourier transformation of $P_r(r,t)$ in time. If we employ the bulk electrostatic theory, $R_r(r,\omega)$ should be given with the frequency-dependent dielectric constant of the solvent $\epsilon(\omega)$ as

$$\tilde{P}_r(r,\omega) = -\frac{1}{4\pi}(1 - \frac{1}{\epsilon(\omega)})\frac{\tilde{e}(\omega)}{r^2}. \tag{6.16}$$

Using eqns.(6.15) and (6.16), the following is derived:

$$\tilde{A}(\omega) = \int_{R_{min}}^{R_{max}} \tilde{P}_r(r,\omega) 4\pi dr = (1 - \frac{1}{\epsilon(\omega)})(\frac{1}{R_{min}} - \frac{1}{R_{max}})\tilde{e}(\omega). \tag{6.17}$$

Therefore,

$$\chi_e(\omega) = (1 - \frac{1}{\epsilon(\omega)})(\frac{1}{R_{min}} - \frac{1}{R_{max}}). \tag{6.18}$$

Eqn.(6.18) was utilized to define the effective cavity radius R_{min} as a function of ω (and R_{max}), since $\chi_e(\omega)$ and $\epsilon(\omega)$ were obtained in the present work.

We will briefly consider the meaning of R_{min}. It is apparent that R_{min} defined in eqn.(6.18) is not necessarily identical to the geometrical radius of the solvation cavity, if the bulk dielectric theory of eqn.(6.16) is not adequate near the solute [10, 11, 22]. Eqn.(6.18) attributes the deviation entirely to the effective cavity radius R_{min} with the bulk dielectric constant $\epsilon(\omega)$ intact, along the spirit of the DMSA theory. An alternative way is that the bulk dielectric constant $\epsilon(\omega)$ is modified to consider the response in microscopic dimensions. The wavenumber-dependent dielectric constant $\epsilon(k,\omega)$ has been studied and applied to describe the solvation dynamics. Inhomogeneous dielectric model was also proposed to incorporate this effect phenomenologically [13, 22]. In order to evaluate the deviation in the small solute, we displayed both the effective cavity radius R_{min} and the effective dielectric constant ϵ in Fig. 6.8 as a function of ω and R_{max} (Note that the axes of ordinates refer to $1/R_{min}$ and $1/\epsilon$). Both figures show unusual features below $\sim 10\text{cm}^{-1}$. Figure 6.8(a) shows that the effective cavity radius is abnormally smaller than the geometrical radius in the low-frequency region, though we do not give the exact definition of the geometrical radius at present. In the higher frequency region, on the contrary, the effective radius is close to the solute radius, $\sigma_{solute}/2 = 1.8\text{Bohr}$. We note that it is closer to the solute

radius $\sigma_{solute}/2$ rather than the contract distance between the solute and solvent, $\sigma_{sw} = 4.6$Bohr. This result is based on the cancellation between the solvent molecularity and incomplete shielding.

The effective dielectric constant of Fig. 6.8(b) was determined on the basis of eqn.(6.18) with the cavity radius R_{min} being $\sigma_{solute}/2$. This figure exhibits strongly negative region below $\sim 10\text{cm}^{-1}$. It has come to be known that $1/\epsilon_L(k)$ has a negative peak about $kr_s \sim 2\pi$, where $\epsilon_L(k)$ denotes the wavenumber-dependent static longitudinal dielectric constant, and r_s refers to the diameter of a solvent molecule. This is probably the most distinguished feature of the solvent molecularity in the dielectric property, and the feature clearly emerges in the case of the small solute [48]. The static solvation free energy is represented using $\epsilon_L(k)$ as [49]

$$F = -\frac{q^2}{\pi}\int_0^\infty (1 - \frac{1}{\epsilon_L(k)})(\frac{\sin kr_c}{kr_c})^2 dk, \tag{6.19}$$

where r_c is the cavity radius, and q denotes the solute charge. When we evaluate the facter $(\sin kr_c/kr_c)^2$ at the negative peak $k \sim 2\pi/\sigma_{solute}$, the small solute with $\sigma_{solute} = 0.6\sigma_{water}$ and the medium one with $0.8\sigma_{water}$ are considerably different: $(\sin kr_c/kr_c)^2 \simeq 0.25$ for the small one and 0.05 for the medium. The present results clearly demonstrate that the small solute efficiently excites this particular dielectric mode.

The results of Fig. 6.8 bring further information about this peculiar solvation. First, the effective radius R_{min} as well as the effective dielectric constant ϵ deviates in the low-frequency region more exceedingly with expanding size of the system R_{max}, while the high-frequency components of both quantities are relatively insensitive to R_{max}. This implies the difference in the asymptotic behavior to the bulk dielectric polarization between the two frequency regions. In the bulk region the longitudinal polarization $P_r(r)$ behaves $\sim 1/r^2$ like eqn.(6.16) provided the spherical symmetry, and consequently R_{min} should be little affected by R_{max} as indicated by eqns.(6.16) - (6.18). Therefore, this result shows that the deviation from the bulk polarization is not yet attenuated within the range of R_{max} in the low-frequency region, though we did not confirm the asymptotic limit due to the restriction of the simulation cell. We point out that this enhancement of the slow component necessarily makes the distant solvation slow as shown in Figs. 6.5 and 6.6(a), because the slow component becomes more emphasized with expanding size of the system R_{max}. The frequency dependence of $R_{min}(\omega)$ in Fig. 6.8(a) is not apparently inconsistent with the dynamical MSA theory, since $R_{min}(\omega)$ increases with frequency ω. However, the present result does not support the assumption of the dynamical MSA in this case; the effective cavity does not expand from the solute radius, but rather contract from it in the low-frequency region.

We also note that the particular mode is restricted to low frequency

region below $\sim 10\text{cm}^{-1}$. Such slow component is translational in character, according to the frequency analysis of liquid water [50]. Bagchi et al. claimed the role of the translational motion to explain the breakdown of the snowball picture on the basis of a generalized diffusion equation [18, 19, 20, 21, 22, 23, 24]. Our present results are consistent to their theory at this point. We further emphasize that the snowball picture does not completely breakdown in the solutes with medium or large size, within the range of the linear response. Previous MD studies reported that the nearest shell is fastest as a consequence of the enhancement of the initial decay in the nonequilibrium simulation, but they also detected the characteristic slow component in the nearest solvation shell [26, 25]. Complete breakdown of the snowball picture in the relatively large solutes has to be elucidated beyond the linear response assumption.

6.5 Concluding Remark

We examined the solute size dependence and the meaning of the Onsager's snowball picture directly through the MD simulation. Instead of the usual simulation which pursues the dielectric relaxation dynamics following a sudden change of the solute charge, we employed another method capable of treating long-time dielectric dynamics beyond the Debye dielectric relaxation time, since we believe that the low-frequency dynamics is crucial to examine the snowball picture. A key to gain the correct result about the long-time dynamics lies in the manipulation of the long-range force. Previous MD studies on the dielectric property of water demonstrated that the reaction field method can reproduce the accurate frequency-dependent dielectric constant involving the low-frequency region by the MD simulation in a finite unit cell. The successful result is derived from the fact that the reaction field method can properly manage the long-range force on condition that the dielectric uniformity holds in the system. Though the previous studies dealt with the bulk dielectric property, we applied the method to investigate the long-time (or low-frequency) dynamics through projecting the polarization dynamics onto the longitudinal component. In order to retain the dielectric uniformity of the solution, we performed an equilibrium MD simulation of the aqueous solution with a solute molecule carrying no charge, since a substantial charge of the solute would destroy the dielectic uniformity around the solute. The equilibrium result with varying size of the solute was translated into the information on the solvation dynamics on the basis of the linear response theory.

The present results clearly demonstrated the solute size dependence in the relaxation profiles. The small solute with $\sigma_{solute} = 0.6\sigma_{water}$ exhibits particularly slower solvation than the other two cases, and this case obviously contradicts the snowball picture. The peculiarity was derived on the charac-

teristic dielectric property of water, which involves strongly negative response about the wavenumber of the solvent molecular diameter. The small solute efficiently excites this singularity. Further analysis indicated that this special influence is restricted in the low-frequency dynamics below $\sim 10\text{cm}^{-1}$. Such slow dynamics is translational in character, which is consistent to the importance of the translational motion. The analysis also showed that the singular effect is not yet attenuated within the distance in the simulation cell. This asymptotic behavior necessarily makes the distant solvation slow, contrary to the snowball assumption. In this situation, the assumption of the dynamical MSA also breaks down.

In the medium or large solutes, the solvation rate against the distance from the solute behaves rather complicated. The nearest solvent is slowest in accordance with the snowball picture, but the other solvation shells except the nearest one show slightly but obviously the reverse order to the snowball assumption. The origin of the slow component in the nearest shell should be elucidated in further work. Considering previous nonequilibrium MD studies that implied the completely reverse order, we suggest that the complete breakdown of the snowball picture has to be explained beyond the linear response assumption.

6.6 Acknowledments

We thank to Prof. Fumio Hirata for valuable comments. Numerical calculations were carried out at the IMS Computer Center and Deta Processing Center of Kyoto University. This work was supported by the Grand in Aid for Scientific Research from the Ministry of Education in Japan.

6.7 Figures and Tables

Figure 6.1: Convergence behavior the square dipole moment of the cell $< M^2 >$ as a function of the number of the time steps. Note that one time step corresponds to 1 fs and the volume of the cell is $(34.25\text{Bohr})^3$. The unit of $< M^2 >$ is a.u.

Figure 6.2: Frequency-dependent dielectric constants of water at T=300K. The real part $\epsilon_r(\omega)$ and the imaginary part $\epsilon_i(\omega)$ are represented by real and broken lines, respectively.

Figure 6.3: Normalized radial distribution function of the oxygen atoms of water from the solute atom in the small solute, $\sigma_{solute} = 0.6\sigma_{water}$.

Figure 6.4: Convergence behavior of the longitudinal polarization of solvent water $P_r(r)$ in a shell with the radius 3.58 - 7.17 Bohr in the case of the small solute. The average values of $P_r(r)$ are displayed against the number of the accumulated time steps. The unit of $P_r(r)$ is a.u.

Figure 6.5: Time correlation function of the electric potential at the solute center $S(t)$ defined in eqn.(6.12) with varying size of the system R_{max}. The solid line refers to $R_{max} = 7.17$ Bohr; dashed line to 10.75 Bohr; dotted line to 14.34 Bohr; dashed-dotted line to 17.92 Bohr.

Figure 6.6: Time correlation function $S(t)$ with each size of the solute atom. (a) refers to $\sigma_{solute} = 0.6\sigma_{water}$, (b) to $0.8\sigma_{water}$, and (c) to $1.0\sigma_{water}$. The solid line denotes the case of $R_{max} = 7.17$ Bohr; dashed line to 10.75 Bohr; dotted line to 14.34 Bohr; dashed-dotted line to 17.92 Bohr.

Figure 6.7: Time correlation function $S(t)$ with each solvation shell to compare the different solute size. (a) refers to $R_{max} = 7.17$ Bohr, and (b) to 17.92 Bohr. The solid line denotes the case of $\sigma_{solute} = 0.6\sigma_{water}$; dashed line to $0.8\sigma_{water}$ dotted line to $1.0\sigma_{water}$.

Figure 6.8: (a) Inverse of (a) the real part of the effective cavity radius $1/R_{min}$ and (b) the real part of the effective dielectric constant $1/\epsilon$ as a function of the frequency in the case of the small solute with varying system size R_{max} (see the text). The solid line denotes $R_{max} = 7.17$ Bohr; dashed line 10.75 Bohr; dotted line 14.34 Bohr; dashed-dotted line 17.92 Bohr.

Figure 6.1

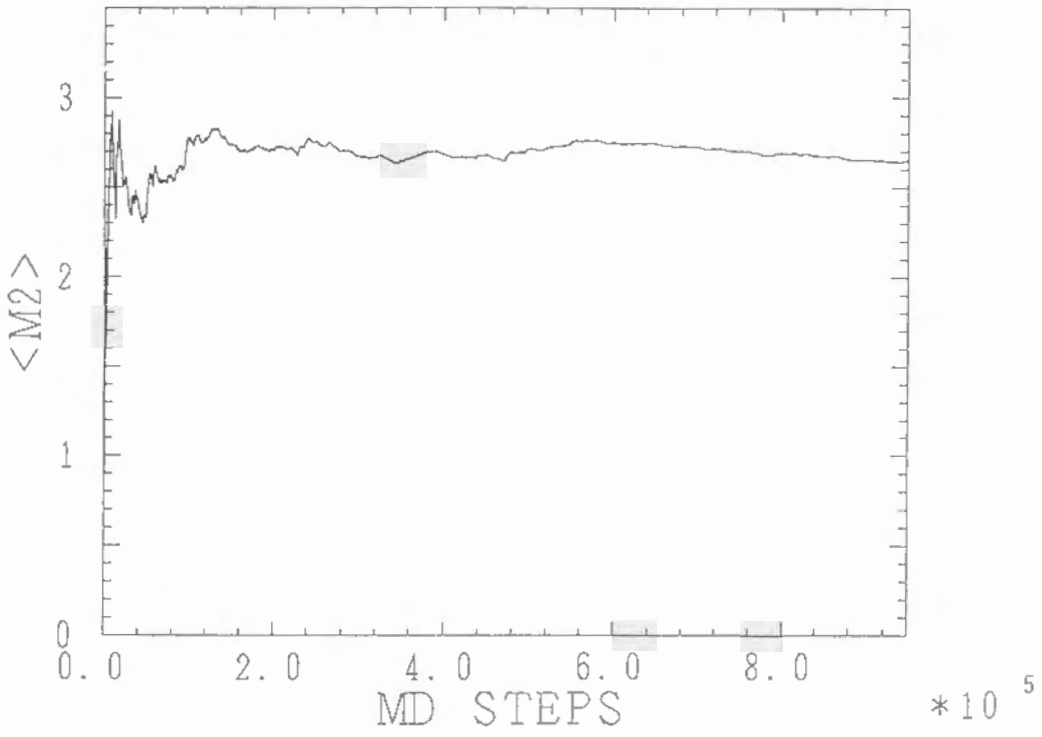

Figure 6.2

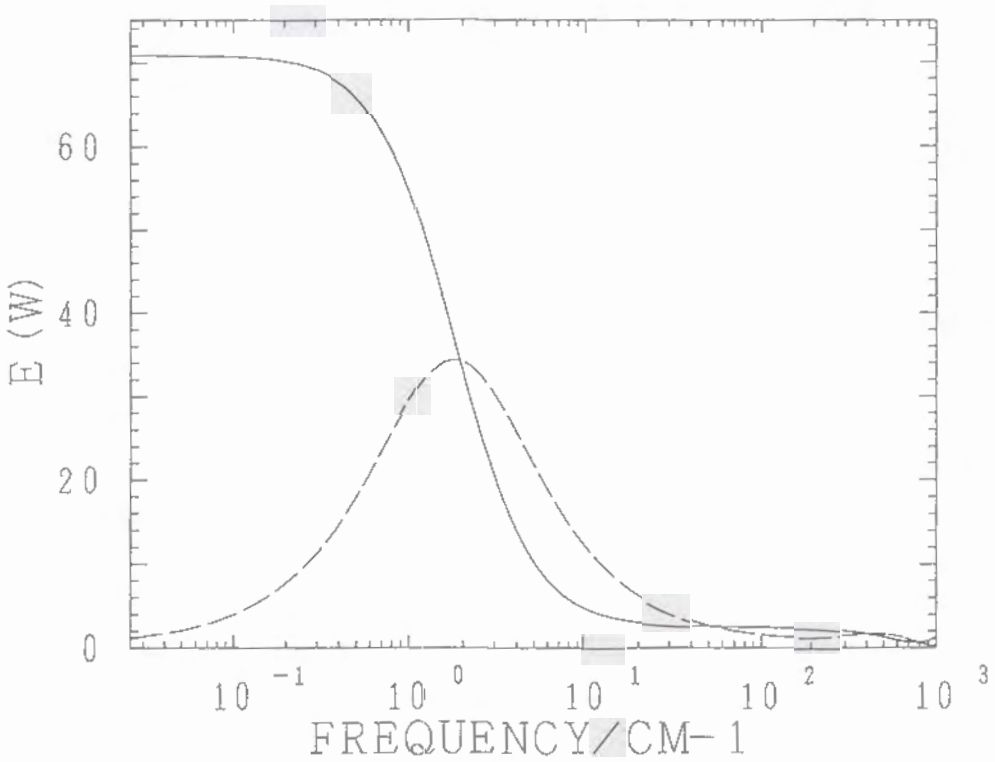

Figure 6.3

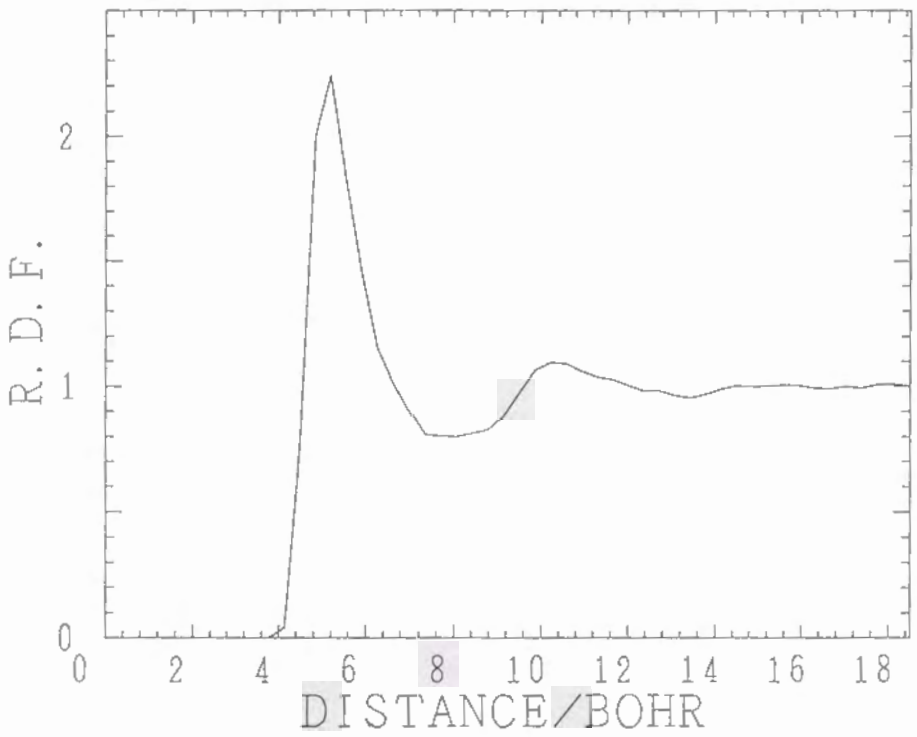

Figure 6.4

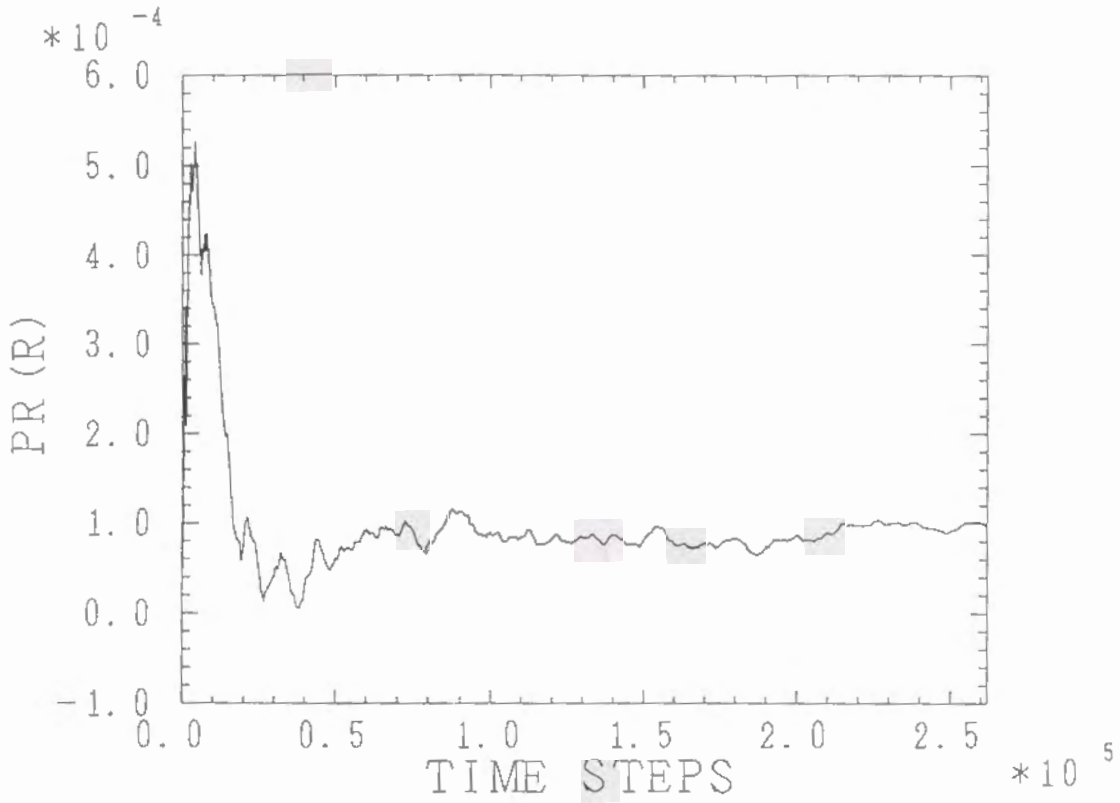

Figure 6.5

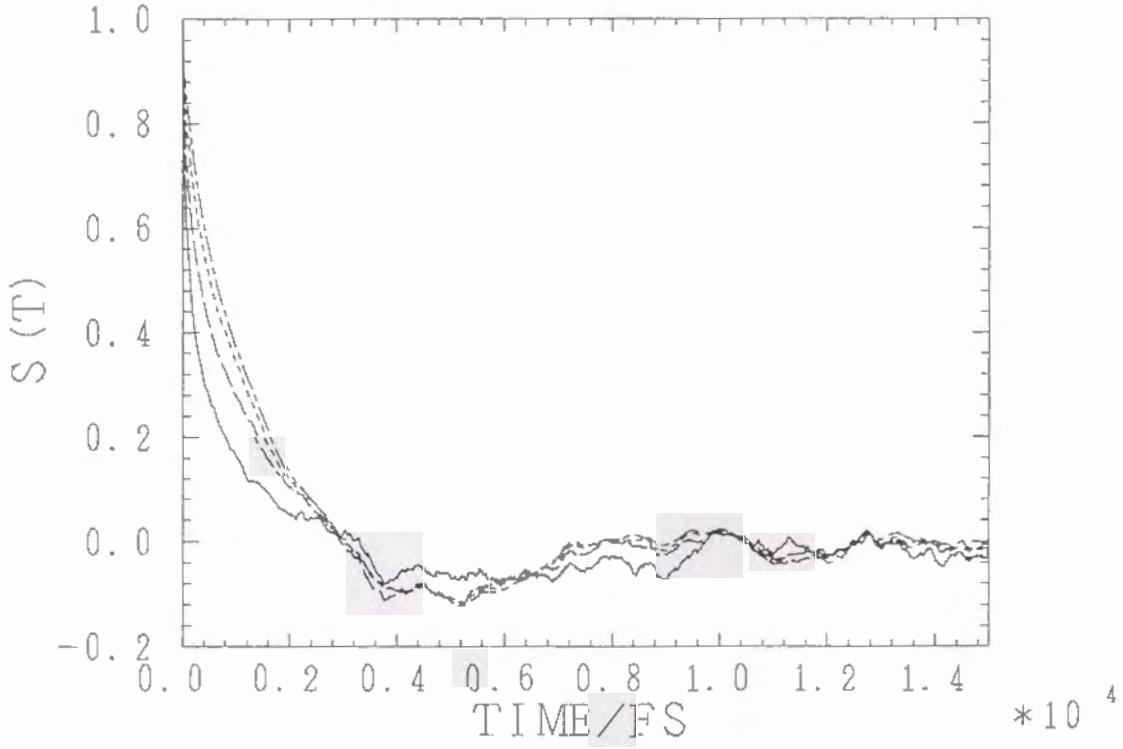

Figure 6.6(a)

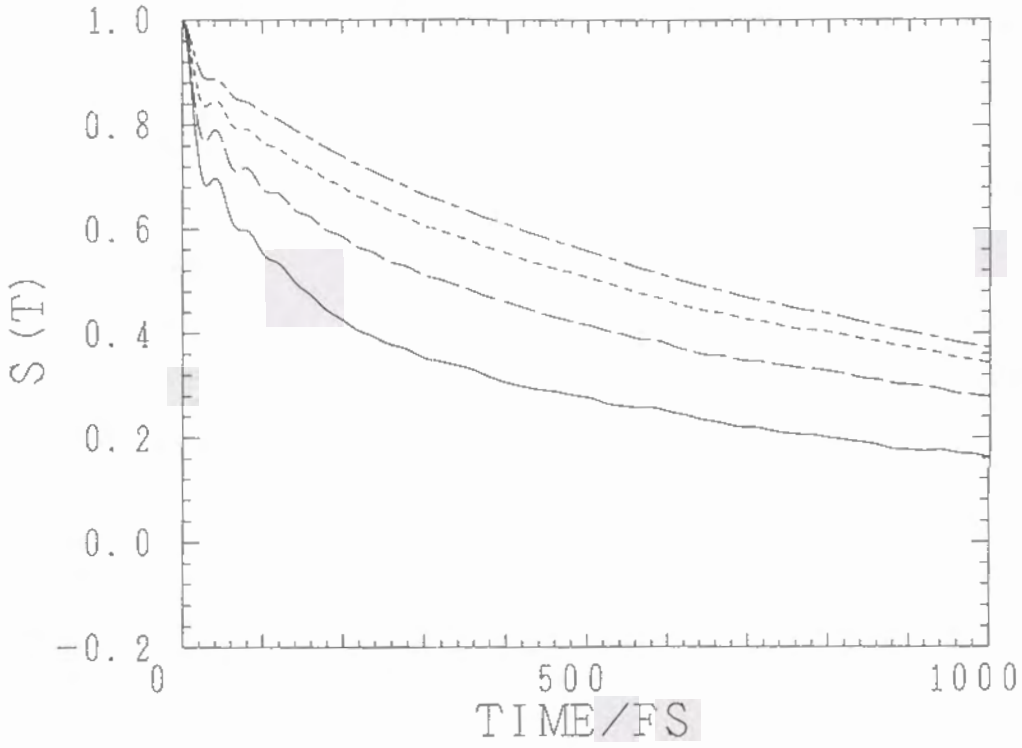

Figure 6.6(b)

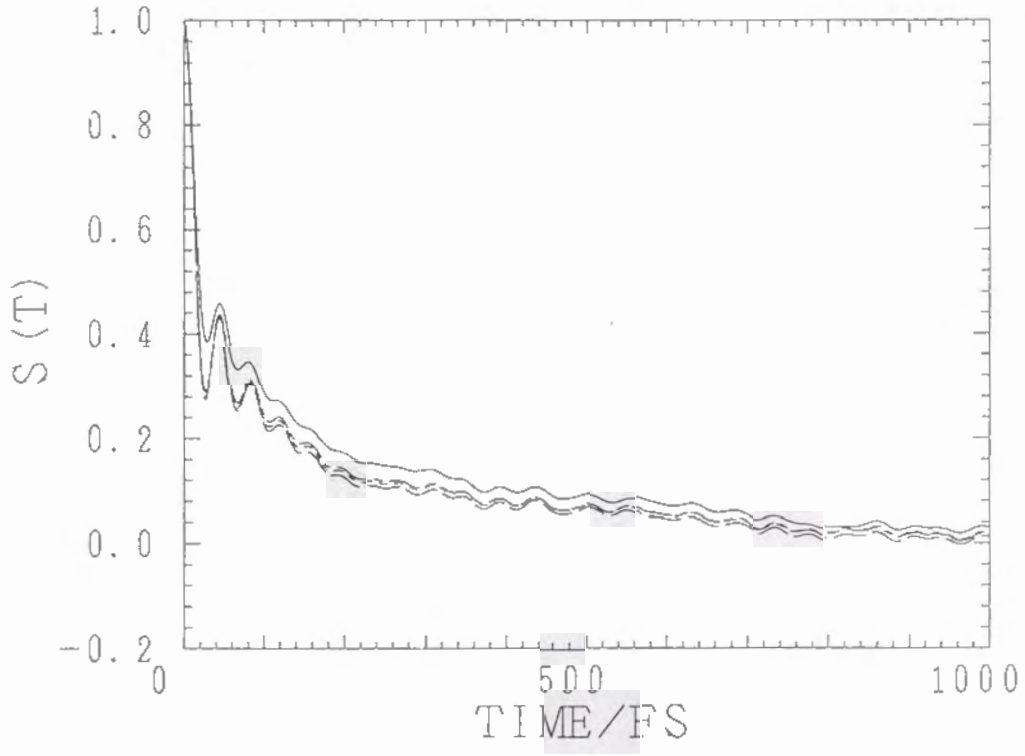

Figure 6.6(c)

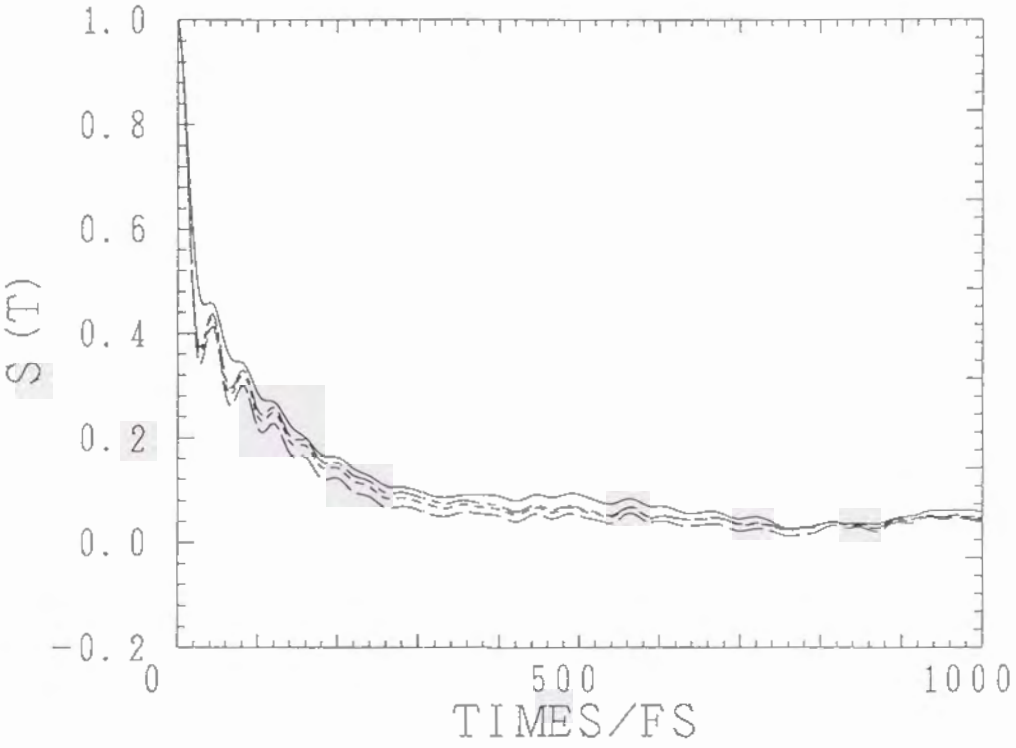

Figure 6.7(a)

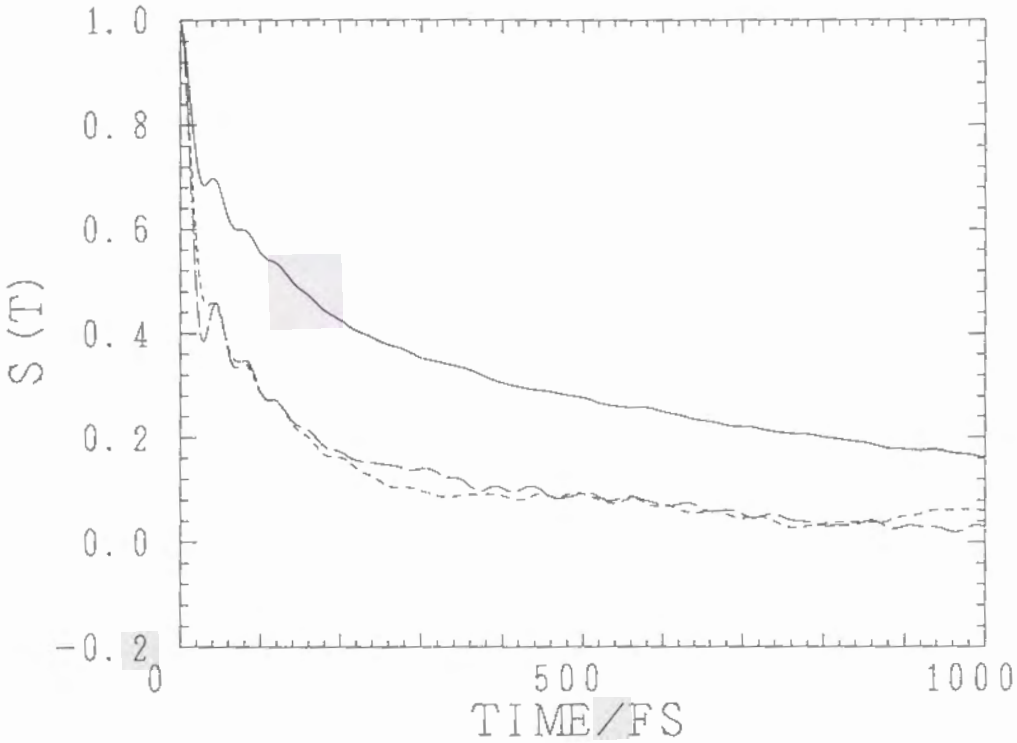

Figure 6.7(b)

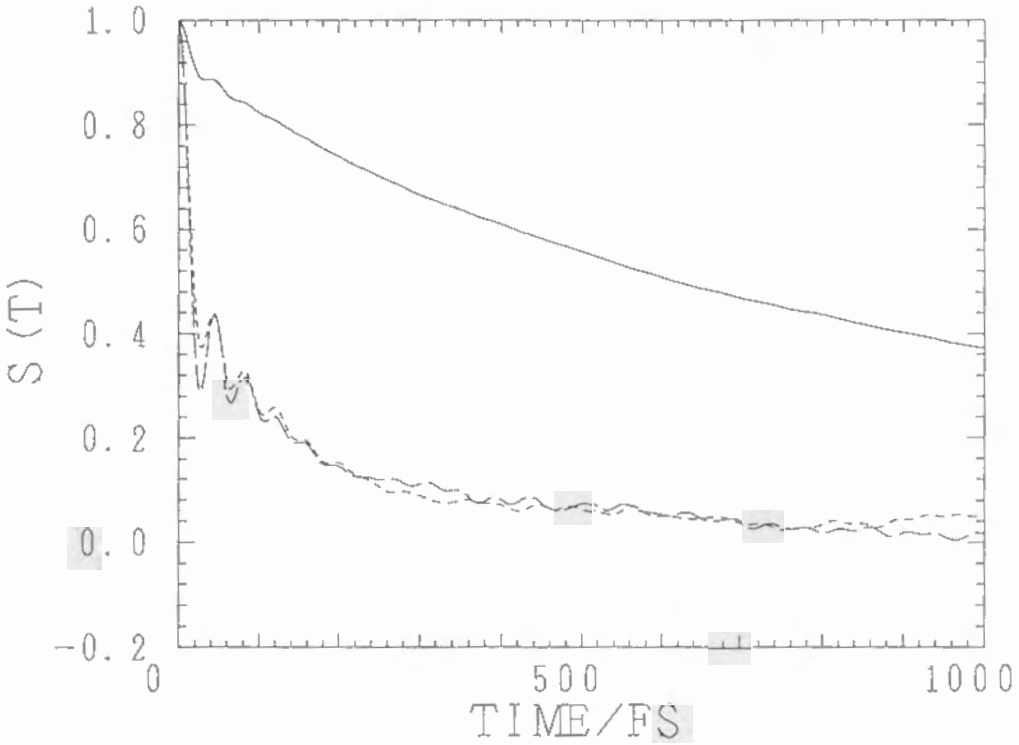

Figure 6.8(a)

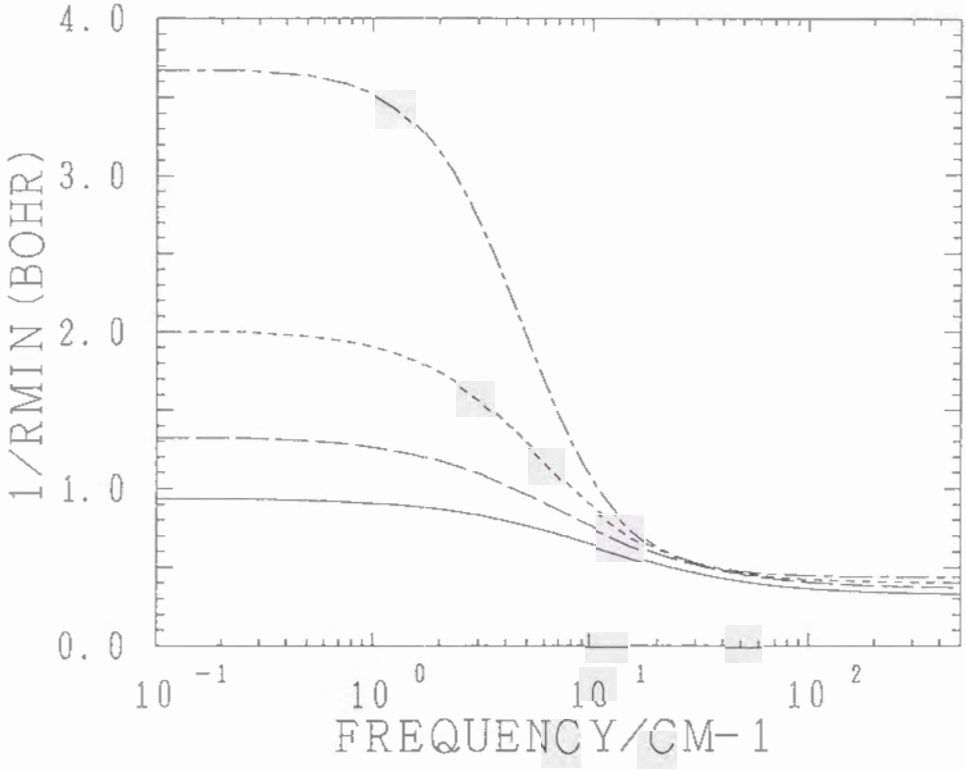

Figure 6.8(b)

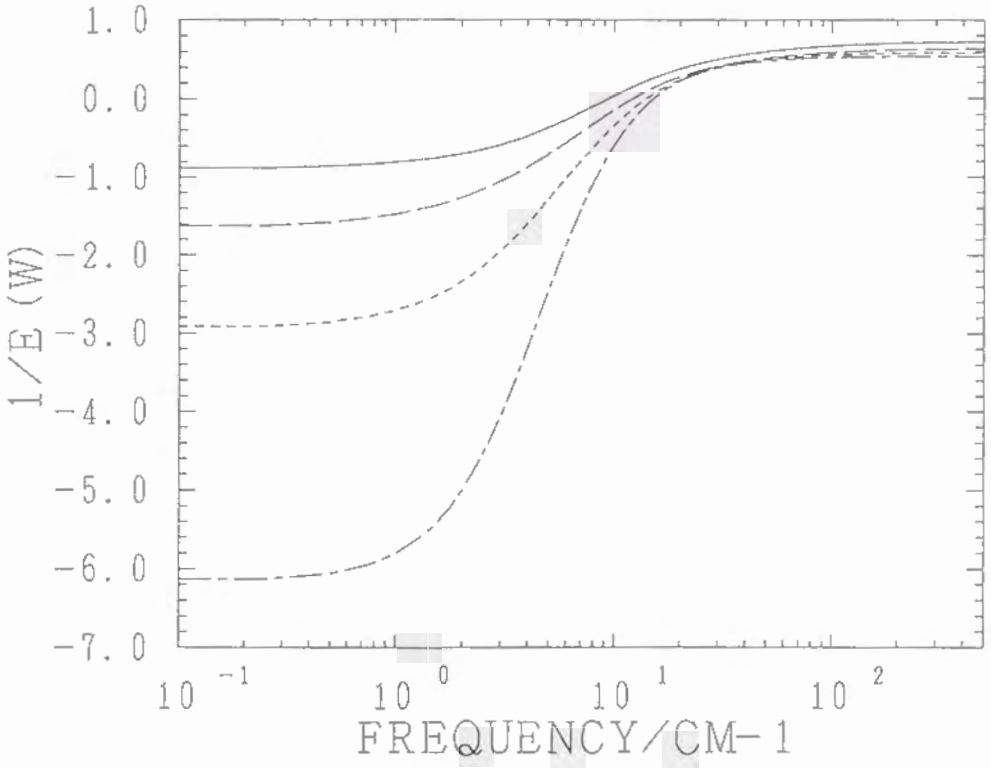

Bibliography

[1] J. D. Simon. Acc. Chem. Res., **21**, 128, (1988).

[2] S. G. Su and J. D. Simon. J. Phys. Chem., **91**, 2693, (1987).

[3] N. Nagarajan, A. M. Brearley, T. J. King, and P. F. Barbara. J. Chem. Phys., **86**, 3183, (1987).

[4] W. Jarzęba, G. C. Walker, A. E. Johnson, M. A. Kahlow, and P. F. Barbara. J. Phys. Chem., **92**, 7039, (1988).

[5] M. Maroncelli and G. R. Fleming. J. Chem. Phys., **89**, 5044, (1988).

[6] M. Maroncelli. J. Chem. Phys., **94**, 2084, (1991).

[7] K. Ando and S. Kato. J. Chem. Phys., **95**, 5966, (1991).

[8] M. Maroncelli and G. R. Fleming. J. Chem. Phys., **86**, 6221, (1987).

[9] D. Calef and P. G. Wolynes. J. Chem. Phys., **78**, 4145, (1983).

[10] V. Friedrich and D. Kivelson. J. Chem. Phys., **86**, 6425, (1987).

[11] R. F. Loring and S. Mukamel. J. Chem. Phys., **87**, 1272, (1987).

[12] P. G. Wolynes. J. Chem. Phys., **86**, 5133, (1987).

[13] E. W. Castner Jr., G. R. Fleming, B. Bagchi, and M. Maroncelli. J. Chem. Phys., **89**, 3519, (1988).

[14] I. Rips, J. Klafter, and J. Jortner. J. Chem. Phys., **88**, 3246, (1988).

[15] I. Rips, J. Klafter, and J. Jortner. J. Chem. Phys., **89**, 4288, (1988).

[16] A. L. Nichols III and D. F. Calef. J. Chem. Phys., **89**, 3783, (1988).

[17] M. Maroncelli and G. R. Fleming. J. Chem. Phys., **89**, 875, (1988).

[18] B. Bagchi. Ann. Rev. Phys. Chem., **40**, 115, (1989).

[19] B. Bagchi and A. Chandra. J. Chem. Phys., **90**, 7338, (1989).

[20] A. Chandra and B. Bagchi. J. Chem. Phys., **91**, 2594, (1989).

[21] A. Chandra and B. Bagchi. J. Chem. Phys., **91**, 7181, (1989).

[22] A. Chandra and B. Bagchi. J. Phys. Chem., **93**, 6996, (1989).

[23] A. Chandra and B. Bagchi. J. Phys. Chem., **94**, 1874, (1990).

[24] A. Chandra and B. Bagchi. J. Chem. Phys., **92**, 6833, (1990).

[25] L. Perera and M. L. Berkowitz. J. Chem. Phys., **96**, 3092, (1992).

[26] E. Neria and A. Nitzan. J. Chem. Phys., **96**, 5433, (1992).

[27] G. R. Fleming. Ann. Rev. Phys. Chem., **37**, 81, (1986).

[28] H. Frohlich. *Theory of Dielectrics*, chapter 3. Oxford University Press, Oxford, (1949).

[29] L. Onsager. Can. J. Chem., **55**, 4145, (1977).

[30] J. Hubbard and L. Onsager. J. Chem. Phys., **67**, 4850, (1977).

[31] M. Tachiya. Chem. Phys. Lett., **203**, 164, (1993).

[32] P. R. Mason, J. B. Hasted, and L. Moore. Adv. Mol. Relaxation Processes, **6**, 217, (1974).

[33] H. Frohlich. *Theory of Dielectrics*, chapter Appendix A. Oxford University Press, Oxford, (1949).

[34] H. E. Alper and R. M. Levy. J. Chem. Phys., **91**, 1242, (1989).

[35] M. Neumann. J. Chem. Phys., **82**, 5663, (1985).

[36] M. Neumann. J. Chem. Phys., **85**, 1567, (1986).

[37] R. D. Mountain and D. Thirumalai. Comp. Phys. Commu., **62**, 352, (1991).

[38] X. Ni and R. M. Fine. J. Phys. Chem., **96**, 2718, (1992).

[39] M. Neumann, O. Steinhauser, and G. S. Pawley. Mol. Phys., **52**, 97, (1984).

[40] M. Neumann. Mol. Phys., **50**, 841, (1983).

[41] H. J. C. Berendsen, J. P. M. Postma, W. F. von Gunsteren, and J. Hermans. *Intermolecular Forces*. Reidel, Dordrecht, Holland, (1981).

[42] W. L. Jorgensen, J. Chandrasekhar, J. D. Madura, R. W. Impey, and M. L. Klein. J. Chem. Phys., **79**, 926, (1983).

[43] C. W. Gear. *Numerical Initial Value Problems in Ordinary Differential Equations.* Prentice-Hall, Englewood Cliffs, (1971).

[44] M. P. Allen and D. J. Tildesley. *Computer Simulation of Liquids.* Clarendon Press, Oxford, (1987).

[45] Chemical Sciety of Japan, editor. *Kagaku Binran (Japanese)*, volume 2, page 501. Maruzen, Tokyo, (1984). We derived the dielectric constant at 300K using an experimental formula in the following

$$\epsilon = 87.740 - 0.40008t + 9.398 \times 10^{-4}t^2 - 1.410 \times 10^{-6}t^3,$$

where t is the Celsius temperature.

[46] R. Kubo, M. Toda, and N. Hashitsume. *Statistical Physics II.* Springer, Berlin, (1985).

[47] M. Neumann and O. Steinhauser. Chem. Phys. Lett., **102**, 508, (1983).

[48] F. O. Raineri, Y. Zhou, and H. L. Friedman. Chem. Phys., **152**, 201, (1991).

[49] R. R. Dogonadze and A. A. Kornyshev. J. Chem. Soc. Faraday Trans. II, **70**, 1121, (1974).

[50] M. Cho, G. R. Fleming, S. Saito, I. Ohmine, and R. M. Stratt. J. Chem. Phys., **100**, 6672, (1994).

Chapter 7

Acknowledgment

The author sincerely thanks to Professor Shigeki Kato for his valuable consultations and encouragements. The author also thanks to his collegues in the Prof. Kato's laboratory and other collegues. He wishes to express his gratitude to Professor Okitsugu Kajimoto for his early stage of the research and to Professor Fumio Hirata for valuable comments. His research is supported by the Fellowship of the Japan Society for the Promotion of Science for Japanese Junior Scientists. He would like to express his gratitude to his parents.